

DISS. ETH NO. 28040

METER-SCALE MICROWAVE QUANTUM NETWORKS
FOR SUPERCONDUCTING CIRCUITS

A thesis submitted to attain the degree of
DOCTOR OF SCIENCES of ETH ZURICH

(Dr. sc. ETH Zurich)

presented by

Paul Magnard

MSc ETH Physics, ETH Zurich

born on 31.03.1992

citizen of France

accepted on the recommendation of

Prof. Dr. Andreas Wallraff, examiner

Prof. Dr. Yiwen Chu, co-examiner

2021

I dedicate this thesis to my grandfather, Louis Magnard, who planted the seed from which my passion for physics grew. Merci, Papi Loulou, pour tous les récits que tu m'as contés sur l'univers. En retour, je te dédie cette thèse.

Abstract

A Bell test is a hardware agnostic experimental procedure which can reject classes of physical theories and be used to certify randomness or secure communications with untrusted devices. Violating a Bell inequality without any of the major loopholes - detection, freedom-of-choice, and locality - is an outstanding challenge which has been achieved only in a handful of experiments, using either NV centers, trapped ions, or optical photons. However, Bell tests with superconducting circuits, a top-contending quantum computing platform, have so far ignored the locality loophole due to the difficulty to entangle physically remote systems without an optical photon interface.

In this thesis, I report the work we have done at the Quantum Device Lab towards realizing a loophole-free Bell test using superconducting qubits entangled using microwave photons. To minimize the distance required between the two Bell parties to close the locality loophole, we have developed a new readout parameter optimization procedure enabling the discrimination of a transmon qubit state with high fidelity in a record speed. We have also designed and realized a modular cryogenic link technology to connect superconducting circuits housed in separate dilution refrigerators and separated by a distance of up to 30 m with a milli-Kelvin temperature, lossless waveguide, which acts as a microwave quantum bus between the remote quantum systems. Using a microwave-activated sideband transition, we demonstrate the possibility to transfer qubit excitation via the successive emission and absorption of a single microwave photon with time-reversal-symmetric envelope, propagating within the cryogenic link. We also demonstrate a simple method to unconditionally reset the transmon qubits in record time and fidelity using this very sideband emission. Using the photon transfer scheme, we transfer qubit states, generate entangled states, and violate Bell's inequality with predetermined measurement settings, using two transmon qubits separated by up to 30 m.

In the same experimental setup, we demonstrate random measurement-basis choice in less than 30 ns, and high-fidelity qubit readout in 50 ns. Therefore, this setup should be able to realize a significant loophole-free Bell test, with repetition rates exceeding 10 kHz. This would put yet-unachieved device-independent tasks within reach and would demonstrate the potential to use microwave photons for realizing local area quantum networks.

Résumé

Un test de Bell est une procédure expérimentale permettant de rejeter certaines classes de théories de la physique de manière robuste, et avec un minimum d'hypothèse sur le fonctionnement interne du dispositif utilisé. Un tel test permet notamment de certifier le caractère aléatoire d'une source de nombres ou d'encrypter une communication de façon fiable, sans postuler le bon fonctionnement du dispositif. La violation d'une inégalité de Bell sans échappatoires - échappatoires de détection, de choix libre, et de localité - est un défi exceptionnel qui n'a été accompli que rarement dans des expériences utilisant des centres NV, des ions piégés ou des photons optiques. Cependant, les tests de Bell conduits jusqu'à présent avec des circuits supraconducteurs, une des plateformes de calcul quantique les plus prometteuses, omettent l'échappatoire de localité. En effet, en l'absence d'une interface cohérente entre les circuits supraconducteurs et les photons optiques, il est difficile d'intriquer des systèmes distants.

Dans cette thèse, je présente le travail que nous avons effectué au Quantum Device Lab, dans le but de réaliser un test de Bell sans échappatoire, avec des qubits supraconducteurs intriqués par le biais de photons radiofréquences. Afin de minimiser la distance requise entre les qubits pour clore l'échappatoire de localité, nous avons développé une nouvelle procédure d'optimisation des paramètres de mesure afin déterminer fidèlement l'état d'un qubit transmon en un temps record. Nous avons également conçu et réalisé une technologie de lien cryogénique modulaire, permettant de connecter des circuits supraconducteurs, refroidis dans des réfrigérateurs à dilution distants de plusieurs dizaines de mètres, avec un guide d'ondes à moins de 50 mK. Ce guide d'onde fait office de bus quantique radiofréquence, sans perte, entre les systèmes quantiques qu'il relie. En induisant une transition de bande latérale par une impulsion radiofréquence externe, nous réalisons un transfert d'excitation d'un qubit à l'autre via l'émission et l'absorption successives d'un photon radiofréquence singulier d'enveloppe temporelle symétrique, se propageant dans le guide d'onde. Nous présentons également une méthode simple pour l'initialisation rapide, fidèle et inconditionnelle de qubits transmons, grâce à cette même transition à bande latérale. Le protocole de transfert de photon, appliqué à des qubits distants de 30 m, en état de superposition, nous permet de transférer l'état quantique d'un qubit à l'autre, d'intriquer les deux qubits de façon déterministe, et d'utiliser cet état intriqué pour violer l'inégalité de Bell, en utilisant des axes de mesures prédéterminés.

Nous démontrons qu'il est possible de sélectionner les axes de mesure de chaque qubit en moins de 30 ns, et de mesurer l'état des qubits fidèlement en 50 ns, dans ce même dispositif, prouvant ainsi que ce dernier permettrait de violer significativement

et sans échappatoire l'inégalité CHSH, avec des taux de répétition supérieurs à 10 kHz. Un tel résultat ouvrirait la voie à la réalisation inédite d'expériences d'auto-certification quantique, et constituerait une démonstration sans appel des atouts uniques des photons radiofréquences pour la réalisation de réseaux quantiques.

Contents

Abstract	v
Résumé	vii
Contents	ix
1 Introduction	1
2 Circuit QED and quantum communication	7
2.1 Quantum information with superconducting circuits	8
2.1.1 Harmonic Oscillator	8
2.1.2 Josephson Junctions	13
2.1.3 The Transmon qubit	16
2.1.4 Qubit Control and Coherence	22
2.1.5 Jaynes-Cummings Hamiltonian	30
2.1.6 Purcell decay	37
2.1.7 Tunable light-matter interaction	40
2.1.8 Remote entanglement generation	43
2.2 Bell test with Superconducting circuits	49
2.2.1 Bell test formalism	50
2.2.2 Loopholes	56
2.2.3 Bell violation with a realistic error model	62
2.2.4 Toward a loophole-free Bell test with superconducting circuits	65
3 Parameter optimization for fast dispersive readout	69
3.1 Quantifying qubit readout with the SNR	70
3.2 Readout parameter optimization in the weak drive limit	74
3.3 Including the Purcell filter in the SNR optimization	79
3.4 SNR reduction due to experimental parameter uncertainty	80

3.5	Considering non-linear effects for readout	82
3.6	Parameter optimization procedure	84
4	Prototyping of a Cryogenic Link Technology	87
4.1	Dilution Refrigerator	88
4.2	General Design of the Cryogenic Link	90
4.3	Heat Transfer	92
4.3.1	Between Radiation Shields	92
4.3.2	Waveguide Field	95
4.4	Design Considerations to Optimize Heat Transfer	97
4.5	Cryogenic Link Prototypes	98
4.6	Achievable lengths for cryogenic links	102
4.7	Discussion and outlook	104
4.8	Characterizing the properties of individual parts	106
4.8.1	Mechanical and thermal properties of the mechanical support posts	106
4.8.2	Thermal conductivity of copper	110
4.8.3	Thermal resistance of the nodes	113
4.8.4	Thermal resistance of link and braid modules	117
4.8.5	Radiative heat load on the 50K stage	119
4.8.6	Waveguide attenuation constant	122
5	Unconditional, All-Microwave Reset	125
5.1	Literature Overview	126
5.2	Experimental setup and concept	128
5.3	Calibration	130
5.4	Reset operating regimes	133
5.5	Experimental results	134
5.6	Qubit measurement and population extraction	137
5.7	Discussion and outlook	140
6	Inter-Cryogenic Microwave Quantum Communication	143
6.1	Connecting superconducting circuits located in different cryogenic systems with a cold waveguide	144
6.2	Experimental cQED setup	147
6.3	Emission and absorption of shaped photons	153
6.4	Qubit State Transfer from one cryostat to another	156

6.5	Bell state generation	157
6.6	Bell test	160
6.7	Random basis choice	162
6.8	Closing the locality loophole	167
6.8.1	Experimental setup	167
6.8.2	Rapid Single-Shot Readout	170
6.8.3	Quantum communication over 30 meters	174
6.9	Conclusion	177
7	Outlook	179
A	External Coupling	183
A.1	LC-Resonator	183
A.2	CPW $\lambda/4$ resonator	184
A.2.1	Galvanic coupling	185
A.2.2	Capacitive coupling	186
A.3	Practical considerations for capacitive external coupling	188
B	Photon shaping	189
B.1	Emitting photons of arbitrary shapes	189
B.2	Optimal photon shape	192
B.3	Design considerations	193
C	SNR expressions for arbitrary readout circuitries in the weak-drive limit	197
D	Derivation of Reset Operating Regimes	201
E	Master Equation Simulations	205
E.1	Reset	205
E.2	Quantum Communication	207
	Bibliography	211
	List of Publications	259
	Acknowledgements	261
	Curriculum Vitae	263

Chapter 1

Introduction

*I think I can safely say that nobody understands
quantum mechanics.*
— Richard Feynman

Quantum information processing has fundamentally changed the way we understand what information *is* by questioning what physical form it can take in a world governed by quantum mechanics [Feynman82, Deutsch85]. Its framework embeds information in the wavefunction of quantum objects, which, in their most abstract version, take the form of two-level systems known as quantum bits, or *qubits*. A quantum computer is a system of multiple qubits whose joint wavefunction can be manipulated and measured to execute algorithms [Deutsch89]. The exponential growth of the Hilbert space spanned by the wavefunction with the number of qubits enables an exponential speed-up of some quantum algorithms over their most-efficient classical counterparts. Therefore, the possibility to implement a physical quantum computer has major implications in the science of information. On a fundamental aspect, quantum computers violate the strong [Vergis86] and extended [Bernstein93] Church-Turing theses, which assert that any physical computing machine can be efficiently simulated by a probabilistic Turing machine. A thesis which used to be widely believed among computer scientists [Vergis86] until Peter Shor found a polynomial-time quantum algorithm for prime factorization [Shor97]. On a practical end, thanks to the subsequent development of many quantum algorithms displaying a speed-up, quantum computers promise a revolution in many computational fields such as cryptography [Shor97, Bernstein09], linear algebra [Harrow09], machine learning [Lloyd13], quantum chemistry and many-body simulations [Reiher17, Babbush18a], protein-folding simulations [Robert21, Casares21],

finance [Rebentrost18], optimization [Grover96, Farhi01, Brassard02], and many other fields [Montanaro16, Clader13].

It is widely believed that this quantum *speed-up* in information processing comes from the quintessential quantum property of entanglement [Penrose98, Jozsa03]: the existence of multi-qubit superposition states which cannot be described by the state of the individual qubits. As argued by R. Penrose [Penrose98] and R. Jozsa [Jozsa03], the dimension of the Hilbert space spanned by non-entangled quantum states increases only linearly with the number of qubits. Therefore, a quantum computer without entanglement can be efficiently simulated by a classical one, and loses its exponential speed-up. A striking example of the role of entanglement in quantum computing is the one-way computing framework developed by R. Raussendorf and H. Briegel, in which arbitrary quantum circuits can be implemented efficiently with single-qubit measurements performed on a highly-entangled initial cluster state [Raussendorf01]. Another example is the recent work by Y. Zhou *et al.*, which highlights the direct connection between the amount of entanglement in a quantum circuit and the possibility to simulate it efficiently on a classical computer thanks to a compression into matrix product states [Zhou20]. Finally, entangled states are direct resources in many crucial quantum information primitives such as the quantum Fourier transform [Shor97], the teleportation of quantum states [Bennett93, Bouwmeester97] or gates [Gottesman99, Eisert00, Chou18], quantum error correction [Shor95, Bennett96b, Knill98, Steane96, Kitaev03], or super-dense coding [Bennett92, Mattle96].

Beyond its computational properties, entanglement has intrigued physicist ever since it has been highlighted by A. Einstein, B. Podolski and N. Rosen (EPR) in 1935 [Einstein35, Schrödinger35]. In this famous *gedanken experiment*, EPR considered an entangled state between two physically remote systems A and B. They highlighted that a projective measurement of subsystem B with one of two incompatible observables \hat{B}_1 and \hat{B}_2 would instantaneously reduce the wavefunction of subsystem A into an eigenvector of two incompatible observables \hat{A}_1 or \hat{A}_2 , irrespective of the physical distance between the two subsystems. Therefore if the wavefunction representation of quantum mechanics is *real*, which EPR defined as the wavefunction capturing at least some *elements of reality* of our world, then an action taken locally (measuring B) can *instantaneously* change elements of reality on a remote place (system A), be it at the other side of the universe, in apparent contradiction with special relativity. In other words, the wavefunction description of quantum mechanics is either not *realistic* (complete), or not *local*.

In 1964, John Bell gave a generic description of realistic models, in which all

elements of reality are captured by a variable λ , which is potentially multi-dimensional, and whose structure and value can be partially or totally hidden to the observers. He then showed that further assuming locality, *i.e.* that λ cannot be influenced by future or space-like-separated events, leads to predictions, called “Bell’s inequalities”, which are violated by quantum mechanics [Bell64]. In other words, John Bell gave an experimental procedure to prove that the models describing our world must either be non-local, or non-realistic. As Clauser and Shymony put it: “the conclusions are philosophically startling: either one must totally abandon the realistic philosophy of most working scientists, or dramatically revise out concept of space-time.”

A few years later, Stuart Freedman and John Clauser reported the first experimental evidences to reject local realism [Freedman72]. However, the value which they used to violate Bell’s inequality was calculated indirectly from correlation measurements and auxiliary measurements, leaving room for criticism [Clauser78]. Ten years later, a team lead by Alain Aspect demonstrated an experimental violation of Bell’s inequality, directly calculated from the correlation measurements [Aspect82b], and with a fast switching of the measurement settings [Aspect82a]. However, the conclusion of this experiment suffered from loopholes stemming from assumptions made in addition to local realism [Larsson14, Brunner14]. The remaining loopholes were first closed individually, in independent experiments using entangled photon pairs [Weihs98] and trapped ions [Rowe01], and then simultaneously in three landmark experiments performed in 2015 at TU Delft [Hensen15], TU Vienna [Giustina15] and NIST [Shalm15], thereby providing compelling statistical evidences against local realism.

Bell tests also turn out to have a practical relevance in quantum information processing. For instance, a successful Bell test guarantees finite amount of secrecy in quantum cryptography [Ekert91]. In general, because loophole-free Bell tests rely on a minimal set of assumptions, they can be used to certify many properties of a quantum protocol, such as security in quantum key distribution [Mayers98, Barrett05, Pironio09, Vazirani14, McKague09, Arnon-Friedman18, Murta19], measurement incompatibility [Chen21a], entanglement [Verstraete02, Bowles18, Arnon-Friedman19], or randomness [Colbeck09, Vazirani12, Colbeck12, Nieto-Silleras14, Kessler17], even if the used devices are untrusted [Gallego10, Reichardt13]. Therefore, loophole-free Bell tests lead to the most trustworthy benchmarks one can do of a quantum computing network [Reichardt13].

In most physical implementations of qubits, quantum information is carried in the state of a single quantum particle, like the polarization of an optical photon [Aspect82a, Kok07], or an electronic or nuclear spin in a single atom [Saffman16, Reiserer15],

in a trapped ion [Cirac95, Monroe95a, Leibfried03], in a molecule [Gershenfeld97, Tseng99, Vandersypen01], in a localized solid-state defect in diamond [Jelezko04, Wolfowicz21], or in a quantum dot [Hanson07, Urbaszek13]. In 1999, Nakamura *et al.* demonstrated the first quantum bit encoded in a mesoscopic system, the Cooper-pair box [Nakamura99], in which quantum states are defined by the coherent oscillations of a superconducting phase (or current) across a Josephson junction [Josephson62, Josephson74], involving the coherent motion of many electrons. This experiment marked the birth of quantum information processing with superconducting circuits. In the following decades, Ramsey interference [Vion02], two-qubit gates [Pashkin03, Yamamoto03], and prototypical quantum algorithms [DiCarlo09] were demonstrated using superconducting circuits. The demonstration of strong coherent coupling between superconducting qubits and microwave resonators [Wallraff04] enabled the study of controlled light matter interaction in superconducting circuits. A setting known as circuit quantum electrodynamics [Blais04, Blais21] which enabled flexible multi-qubit architectures [Schuster08, DiCarlo09], and quantum non-demolition readout protocols [Blais04, Reed10a]. The steady increase of coherence times [Koch07, Reagor13, Paik11, Somoroff21, Wang21] and of the number of controllable qubits [Steffen13, Barends16, Arute19, Jurcevic20, Blok21] in superconducting quantum processors enabled the realization of landmark experiments, such as the demonstration of a quantum computational advantage [Arute19] and quantum error correction [Ofek16, Andersen20a, Campagne-Ibarcq20, Chen21b].

Nowadays state-of-the-art superconducting quantum processors contain a few dozens qubits, and might find application in noisy-intermediate scale quantum computing application [Preskill18, O'Malley16, Kandala17, Kandala19, Lacroix20]. Efforts in qubit integration and packaging [Béjanin16, Das18, Foxen18, Lei20] will likely extend the scale of these processors to thousands of qubits in the foreseeable future. A scale at which such processors might encode a single, error-corrected logical qubit [Chen21b]. However, the most frugal yet provably useful quantum algorithms require orders of magnitude more qubits: 10^{6-8} to simulate nitrogen fixation by nitrogenase, 10^{5-7} to encode the electronic spectra of correlated electrons [Babbush18a], and 10^8 for Shor's factorization of a 2000 bits number. To reach such scale, it appears unavoidable that a superconducting quantum computer will require to be built as a network, connecting multiple processors housed in different cryogenic systems to each other [Awschalom21, Krinner19]. However, because superconducting qubits lack of a natural interface with optical photons, they cannot be entangled at a distance in the same fashion as single atoms [Moehring07], trapped ions [Hofmann12], or defects in

diamond [Bernien13]. Realizing such superconducting quantum network is therefore a challenging task.

In this thesis, we present the work we have conducted over the last five years to realize the first superconducting quantum network, in the aim to violate Bell's inequality free of any loophole. This network consists of two superconducting circuits, housed in distinct dilutions refrigerators, separated by several meters, and connected to each other with a superconducting waveguide cooled to cryogenic temperatures, through which itinerant microwave photons carry quantum information. In chapter 2, we give a detailed introduction to quantum information processing with superconducting circuits and to the Bell test formalism. In chapter 3, we provide an analytical study of dispersive transmon qubit readout at short integration times, which leads to a clear parameter optimization procedure for the design of the readout circuitry, and concludes on the possibility to perform a Bell test closing the locality loophole in a quantum network spanning a few tens of meters. In chapter 4, we give a detailed presentation and characterization of the cryogenic link technology which we developed to connect qubits with cold waveguides over distances of up to 30 m. In chapter 5, we present a fast and high-fidelity qubit reset scheme based on microwave pumping of a transmon-resonator system. We have used this reset scheme in all subsequent experiments presented in this thesis. In chapter 6, we report the experimental demonstration of quantum communication protocols, including a Bell test, between two superconducting circuits housed in two cryogenic systems, separated by 5 and 30 m, and connected to each other by the cryogenic link presented in chapter 4. We also demonstrate how this unique setup is geared to perform the first loophole-free Bell test using superconducting circuits.

Chapter 2

Circuit QED and quantum communication

*The besson is a true particle, unlike the Transmon,
which is just a chunk of metal.*

— Christopher Eichler

This chapter introduces concepts of electrical superconducting circuits and of quantum information which are essential to understand the results presented in the rest of the thesis. In the first section, we will give an introduction to superconducting circuits applied for quantum information processing. We will present the elementary circuits implementing quantum harmonic oscillators and quantum bits, then show how to manipulate the quantum states of such circuits, and describe a small subset of the rich phenomena which arise when combining these two elementary circuits, with a particular focus on quantum communication and entanglement generation between remote circuits. In the second section, we will describe the formalism of Bell tests and detail the requirements to perform a loophole-free Bell test using superconducting qubits and microwave photons.

2.1 Quantum information with superconducting circuits

2.1.1 Harmonic Oscillator

Perhaps the simplest example of a quantum system is that of a quantum harmonic oscillator. Such a system is described by the Hamiltonian

$$\hat{H}_{\text{ho}} = \frac{\hat{p}^2}{2m} + \frac{1}{2}m\omega^2\hat{x}, \quad (2.1)$$

where m is the particle's mass, ω is the resonance frequency of the harmonic oscillator, and \hat{x} and \hat{p} are the conjugate quantum operators for position and momentum, which obey the commutation rule $[\hat{x}, \hat{p}] = i\hbar$. The simplest electrical circuit implementing a harmonic oscillator is the lumped-element LC circuit, where the only node of the circuit is connected to ground via a capacitor and an inductor in parallel [Fig. 2.1 (a,b)]. The classical Hamiltonian of the system amount to the total energy stored in the circuit

$$H_{\text{LC}} = \frac{CV^2}{2} + \frac{LI^2}{2} \quad (2.2)$$

$$= \frac{Q^2}{2C} + \frac{\Phi^2}{2L}, \quad (2.3)$$

where C is the capacitance to ground, L is the inductance of the inductor, V is the node voltage, and I the current flowing in the inductor. In the second line of Eq. (2.3), we have introduced the capacitor's charge $Q = \int I(t)dt = CV$ and the flux $\Phi = \int V(t)dt = LI$ threaded through the inductor. Since Φ and Q are canonical conjugate

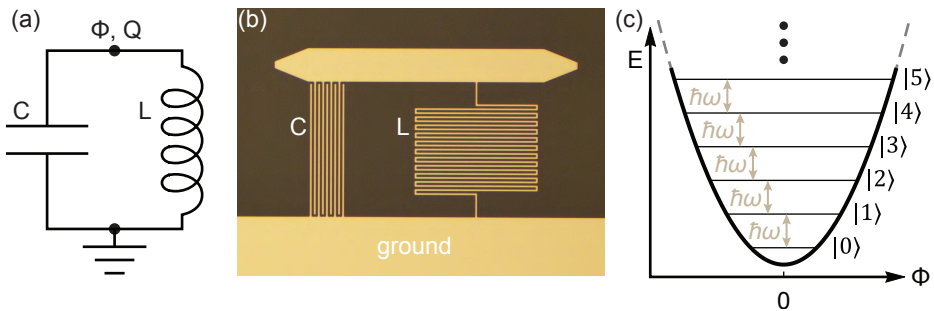


Figure 2.1 (a) LC-circuit electrical diagram. (b) Optical photograph of a planar LC-circuit pattern via photolithography (credits: A. Potočník). The dark and clear part are sapphire and niobium, respectively. (c) Potential landscape and energy levels of a quantum harmonic oscillator.

variables, the canonical quantization of Eq. (2.3) leads to the quantum Hamiltonian

$$\hat{H}_{\text{LC}} = \frac{\hat{Q}^2}{2C} + \frac{\hat{\Phi}^2}{2L}, \quad (2.4)$$

where the canonically conjugate operators $\hat{\Phi}$ and \hat{Q} follow the commutation rule $[\hat{\Phi}, \hat{Q}] = i\hbar$. Identifying flux to position and charge to momentum, the quantum LC oscillator is analogous to a harmonic oscillator with mass C and resonance frequency $\omega = 1/\sqrt{LC}$. In the second quantization formalism, one introduces the creation and annihilation operators

$$\hat{a} = \frac{1}{2} \left(\frac{\hat{\Phi}}{\Phi_{\text{zpf}}} + i \frac{\hat{Q}}{Q_{\text{zpf}}} \right), \quad \text{and} \quad \hat{a}^\dagger = \frac{1}{2} \left(\frac{\hat{\Phi}}{\Phi_{\text{zpf}}} - i \frac{\hat{Q}}{Q_{\text{zpf}}} \right), \quad (2.5)$$

where $\Phi_{\text{zpf}} = \sqrt{\hbar Z_r/2}$ and $Q_{\text{zpf}} = \sqrt{\hbar/2Z_r}$ are the flux and charge zero-point fluctuations, and $Z_r = \sqrt{L/C}$ is the characteristic impedance of the resonator [Girvin14]. These operators obey the bosonic commutation rule $[\hat{a}, \hat{a}^\dagger] = 1$, and can be used to express the Hamiltonian as

$$\hat{H}_{\text{LC}} = \hbar\omega(\hat{a}^\dagger \hat{a} + 1/2). \quad (2.6)$$

The bosonic commutation rule leads to two important properties of the quantized harmonic oscillator. First, the eigenenergies of $\hat{a}^\dagger \hat{a}$ are positive integers $n \in \mathbb{N}$. The corresponding eigenstates, typically labelled $|n\rangle$, are called Fock states. Second, the annihilation (creation) operator acts on a Fock state $|n\rangle$ as $\hat{a}|n\rangle = \sqrt{n}|n-1\rangle$ ($\hat{a}^\dagger|n\rangle = \sqrt{n+1}|n+1\rangle$). Therefore annihilation (creation) operator removes (adds) one quanta of energy $\hbar\omega$ from (to) the oscillator. These quanta of energies are plasmon-polariton particles, *i.e.* they involve both the electronic field via the collective motion of electron charges (as a plasma) and the electromagnetic field it generates. However, because of the linear and the electro-magnetic nature of the LC circuit, it's elementary excitations are typically called *microwave photons* [Girvin14]. Third, the energy levels are spaced evenly, by $\hbar\omega$ [Fig. 2.1 (c)]. Therefore, it is not possible to drive one transition selectively. Instead, driving the resonator with a classical drive, *e.g.* a coherent tone, will map the harmonic oscillator to a classical state, such as a coherent state.

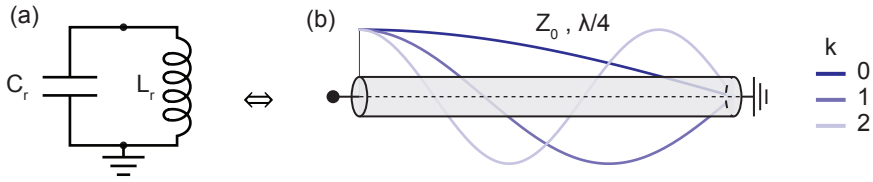


Figure 2.2 Electrical circuit diagram of, (a) an LC-circuit, and (b), a $\lambda/4$ resonator. The blue curves in (b) represent the voltage profile inside the $\lambda/4$ resonators for modes $k = 0, 1, 2$.

Lumped-element LC resonator

In typical circuit QED experiments, LC-resonators are fabricated from a thin film of superconducting metal, such as niobium or aluminum, deposited on top of a clean substrate, such as silicon or sapphire. A metal pad and a meandering inductor shunting it to ground is then patterned in the film through a photolithographic step [Fig. 2.1 (b)]. The metal pad constitutes a natural capacitor to ground. The capacitance and inductance of the system are defined by the specific geometry of the metal pad and the inductor, and typically lead to frequencies in the range of 1 to 10 GHz and impedances of 20 to 200 Ohms [McKay15, McRae20].

However, the typical size of these circuits is just an order of magnitude below the typical millimeter-long resonant wavelength. These systems are therefore not strictly lumped-elements and we must consider the parasitic inductance (capacitance) of the capacitor (inductor) to estimate the systems parameters precisely [Pozar12, McRae20].

$\lambda/4$ resonator

Alternatively, microwave resonators can be built from distributed electrical elements (Fig. 2.2). For instance, a transmission line terminated with a short-circuit on one end, and an open-circuit on the other end, can support standing waves with a current node on the short-circuited end and a voltage node on the open one [Fig. 2.2 c]. Such a resonator is called a $\lambda/4$ resonator, because its fundamental mode, of frequency

$$\omega_0 = \frac{\pi v_p}{2l},$$

supports a standing wave which spans the transmission line with a quarter of its wavelength. Here, l is the length of transmission line, and $v_p = c/\sqrt{\epsilon_{\text{eff}}}$ is the phase velocity in the transmission line, with c the speed of light in vacuum, and $\epsilon_{\text{eff}} \geq 1$ the effective dielectric constant of the transmission line. Harmonic modes appear at each

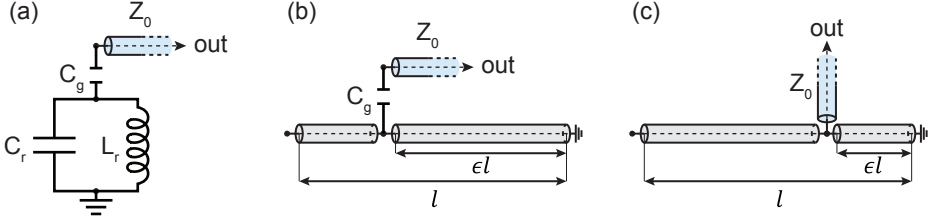


Figure 2.3 Electrical circuit diagram of, (a) an LC-circuit capacitively coupled to an output port, (b), a $\lambda/4$ resonator capacitively coupled to an output port, and (c), a $\lambda/4$ resonator galvanically coupled to an output port. The output port transmission line is in blue.

frequency compatible with the boundary conditions, *i.e.*

$$\omega_k = (2k + 1)\omega_0, \quad \text{for } k \in \mathbb{N}.$$

To first order, a $\lambda/4$ resonator is well approximated near resonance by a parallel LC-circuit with parameters [Pozar12]

$$C_k = \frac{\pi}{4Z_0\omega_0}, \quad L_k = \frac{Z_0}{\omega_0} \frac{4}{\pi(2k+1)^2}, \quad \text{and} \quad Z_{r,k} = Z_0 \frac{4}{(2k+1)\pi}, \quad (2.7)$$

with Z_0 the characteristic impedance of the transmission line.

External coupling

In order to control or characterize the parameters of a resonator, the resonator should couple to a drive port. In this sub-section, we present useful formulae to derive the impedance Z_r , the resonance frequency ω_r , the output coupling rate κ_{ext} , and the corresponding quality factor $Q_{\text{ext}} := \omega_r / \kappa_{\text{ext}}$ of resonators coupled in various ways to an output port. A detailed derivation of these formulae can be found in appendix A.

For a parallel LC-resonator coupled via a capacitance $C_g \ll C_r$ to an output port of constant impedance Z_0 [Fig. 2.3 (a)], the external coupling rate is [Göppl08, Houck08]

$$\kappa_{\text{ext}} \simeq C_g^2 Z_r Z_0 \omega_r^3, \quad (2.8)$$

where the resonance frequency $\omega_r \simeq 1/\sqrt{L_r C_\Sigma}$ and the impedance $Z_r \simeq \sqrt{L_r/C_\Sigma}$ are shifted by the coupling capacitor by substituting C_r with the total capacitance $C_\Sigma := C_r + C_g$.

For a $\lambda/4$ resonator of length l , and whose coupling capacitor is located at a distance ϵl from the shorted end [Fig. 2.3 (b)], we show in appendix A that Eq. (2.8) generalizes

to

$$\kappa_{\text{ext}} \simeq \sin^2\left(\epsilon \frac{\pi}{2}\right) C_g^2 Z_r Z_0 \omega_r^3, \quad (2.9)$$

where the resonance frequency $\omega_r \simeq 1/\sqrt{L_r C_\Sigma}$ and the impedance $Z_r \simeq \sqrt{L_r/C_\Sigma}$ are shifted by the coupling capacitor by substituting the equivalent circuit capacitance C_r with the total capacitance $C_\Sigma := C_r + C_g \sin^2(\epsilon\pi/2)$. Here again, we assumed that $C_g \ll C_r$. Such a *capacitive* output coupling is convenient when high quality factors are needed because it requires a small coupling capacitance. Indeed small capacitances can be easily implemented in a planar geometry, and the lumped-element coupling approximation $C_g \ll C_r$ stays valid in this regime.

Alternatively, a distributed resonator can be coupled with arbitrary rate to an output port by contacting the center conductor of the latter to that of the resonator, in a T-junction located at a distance ϵl from the shorted end [Fig. 2.3 (c)]. As derived in appendix A, the resonance frequency and the impedance of the resonator are unchanged, and the external coupling is

$$\kappa_{\text{ext}} = \omega_r \frac{4}{\pi} \sin^2\left(\epsilon \frac{\pi}{2}\right). \quad (2.10)$$

The output coupling rate is proportional to the square of the voltage fluctuation at the coupling port. Equivalently, the external quality factor is simply $\pi/[4 \sin^2(\epsilon\pi/2)]$. From this expression, we see that any quality factor can be reached, from very high quality factors, with $\epsilon \ll 1$, to a complete destruction of the resonance for $\epsilon = 1$. Such a *galvanic* output coupling is convenient when low quality factors are desired. Indeed, we have seen in the last paragraph that a low-Q capacitive port would break the lumped element approximation $C_g \ll C_r$, whereas Eq. (2.10) is correct for any quality factor.

CPW geometry

In this thesis, we realized all transmission lines, including those used in distributed resonators, using a coplanar waveguide (CPW) geometry [Wen69, Pozar12, Simons01]. In a CPW transmission line, the inner conductor is a metal strip of width s and thickness t , separated from the in-plane ground plane by a gap of width w [Fig. 2.4 (a)]. The fabrication of a CPW line is therefore compatible with standard photolithography, as described above for LC lumped-element resonators [Göppl08]. When the film thickness t is very small compared to w and s , then half of the electric field lives in the vacuum above the chip, and the other half in the substrate below the metal film. As a result, the effective dielectric constant of a CPW transmission line is the mean between

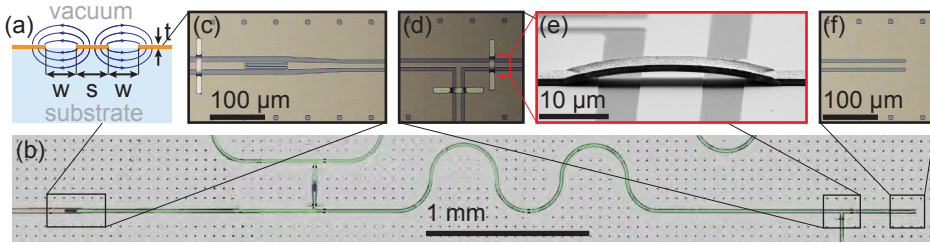


Figure 2.4 (a) Schematic cross-sectional-view of a CPW transmission line. The metal is in orange and electric field lines going from the center conductor to the ground plane are represented with blue arrows. (b) False-color optical image of a $\lambda/4$ resonator (green) used in [Magnard20]. Microscope image of, (c) the input capacitor, (d) the galvanic output port tee-junction, and (f), the shorted end of the resonator shown in (b). The images shown in (c,d,f) have the same scale. (e) Scanning electron microscope image of the airbridge shown in panel (d), taken at an angle of 85 deg from the axis normal to the plane.

that of the two media $\epsilon_{\text{eff}} \simeq (1 + \epsilon_{\text{sub}})/2$. An important feature of CPW transmission lines is that their characteristic impedance is determined by the ratio s/w , rather than by the absolute values of s and w , in stark contrast to other planar geometries like strip lines and microstrip line. Conveniently, for a typical substrate dielectric constant $\epsilon_{\text{sub}} = 10$, the standard 50Ω characteristic impedance is obtained for $s = 2w$. CPW transmission lines can therefore be easily miniaturized while being impedance matched with standard RF components.

For instance, the device which we will present in chapter 6 [Magnard20], possesses a CPW 4.7 GHz $\lambda/4$ resonator with film thickness $t \simeq 150$ nm, length $l \sim 4.5$ mm and planar dimensions $s = 10.5 \mu\text{m}$ and $w = 5.5 \mu\text{m}$, leading to a footprint as small as 0.1mm^2 [Fig. 2.4 (b)]. Conveniently, the resonator can be coupled using simple geometries to implement lumped-element capacitors and tee-junctions [Fig. 2.4 (c,d)]. The CPW center conductor splits the ground plane into two parts whose voltage we equalized at critical places such as bends and tee-junctions with an Al/Ti/Al airbridges to suppress unwanted slotline modes [Lee99], see Fig. 2.4 (e). Finally, the shorted end of the resonator simply consists in merging the center conductor with the ground plane just next to it [Fig. 2.4 (f)].

2.1.2 Josephson Junctions

Harmonic oscillators and linear circuit elements play an essential role in quantum information processing. However, because the energy levels of a harmonic oscillator are evenly spaced, it is not possible to selectively drive a single-transition. Instead, a classi-

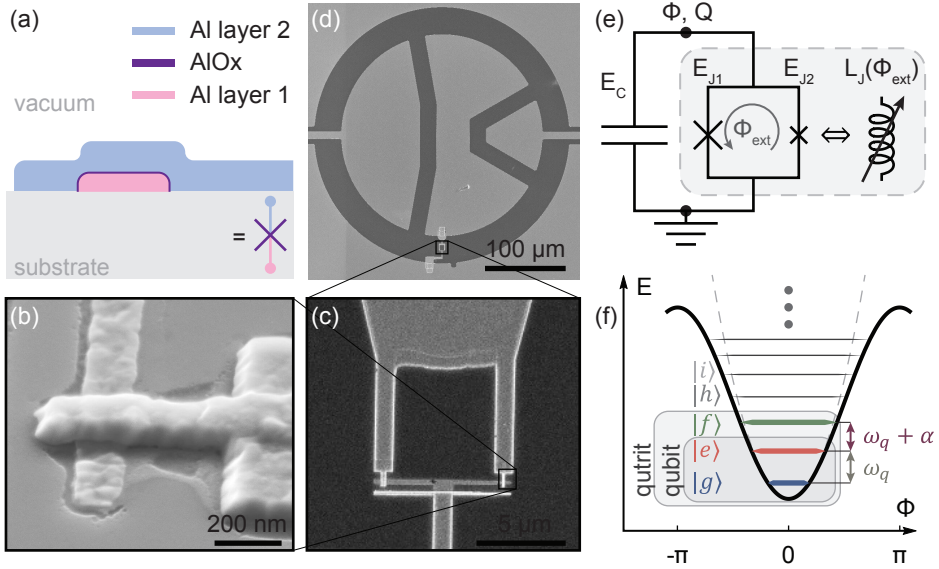


Figure 2.5 (a) Schematic cross-sectional-view a Josephson junction consisting of two layers of aluminum separated by an aluminum oxide insulating barrier. Scanning electron microscope images of, (b) an Al/AlOx/Al Josephson junction, (c) a SQUID loop, and (d), a flux-tunable transmon qubit. In (b-d) the colors from darkest to brightest are the silicon substrate, the niobium film, and the aluminum electrodes of the Josephson junctions, respectively. (e) Electrical diagram of a transmon qubit. The equivalence between the SQUID loop and a flux tunable nonlinear inductor is enclosed in the gray box. (f) Cosine potential energy and first energy levels of the transmon qubit. The grey dashed line is the quadratic expansion of the potential energy.

cal drive will generate a particular type of superposition of multiple Fock states known as a coherent state. Such state can be well described classically as the coherent oscillation of the classical variables Φ and Q . To generate non-classical states and harness the advantages of quantum information processing, one needs to add a non-linear lossless element to the electrical circuit toolbox: the Josephson junction [Josephson62].

The Josephson junction

A Josephson junction consists of two superconducting leads separated by a thin insulating or normal metal barrier. The Josephson junctions presented in this thesis consist of two layers of aluminum deposited with double-angle evaporation using a Dolan bridge technique [Dolan77], and separated by a ~ 1 nm thick aluminum oxide barrier grown in between the two deposition steps [Fig. 2.5 (a,b)].

The tunnelling effect of supercurrent through the barrier leads to the non-linear

Josephson relation [Josephson62]

$$I = I_0 \sin\left(\frac{\Phi}{\Phi_0}\right) \quad (2.11)$$

where $\Phi_0 = \hbar/2e$ is the flux quantum, and the critical current I_0 is the maximum current which can flow through the junction before it turns into a normal resistor. Integrating the right-hand-side of Eq. (2.11) leads to an expression of the potential energy associated with a Josephson junction

$$U(\Phi) = -I_0\Phi_0 \cos\left(\frac{\Phi}{\Phi_0}\right) = -E_J \cos(\varphi), \quad (2.12)$$

where we introduced the dimensionless flux $\varphi = \Phi/\Phi_0$, and the Josephson energy $E_J = I_0\Phi_0$. The Josephson energy is proportional to the area of the Josephson junction and decreases exponentially with the barrier thickness, with prefactors which depend on the junction materials. It can be conveniently estimated from a measurement of the normal state junction's resistance R_n at room temperature, with the Ambegaokar-Baratoff formula [Ambegaokar63b]

$$E_J = \frac{\Phi_0 \pi \Delta}{2eR_n},$$

where e is the electron charge, and Δ the superconducting gap of the superconductor.

SQUID loop as a tunable Josephson junction

A superconducting quantum interference device (SQUID) is a circuit consisting of two Josephson junctions in parallel [Fig. 2.5 (c)], which behaves effectively as a single Josephson with tunable Josephson energy. To see that we first consider the potential energy of a SQUID,

$$U_{\text{SQUID}} = -E_{J,1} \cos \varphi_1 - E_{J,2} \cos \varphi_2,$$

where $E_{J,i}$ and φ_i are the energy of, and the dimensionless flux across, each of the two junctions. Because the two junctions form a loop, Faraday's law constrains the phase drops across the two junctions

$$\Phi_{\text{ext}}/\Phi_0 = \varphi_2 - \varphi_1, \quad (2.13)$$

where Φ_{ext} is the external magnetic flux threaded through the SQUID loop. Using Eq. (2.13), we can eliminate a variable and re-write the potential energy of a SQUID as

$$U_{\text{SQUID}}(\varphi) = -E_{\Sigma} \sqrt{d^2 + (1-d^2) \cos^2\left(\frac{\Phi_{\text{ext}}}{2\Phi_0}\right)} \cos(\varphi), \quad (2.14)$$

with $E_{\Sigma} = E_{J,1} + E_{J,2}$ the total Josephson tunnelling energy, $d = (E_{J,1} - E_{J,2})/E_{\Sigma}$ the SQUID asymmetry, and $\varphi = (\varphi_1 + \varphi_2)/2 - \arctan(d \tan(\Phi_{\text{ext}}/2\Phi_0))$ [Vool17]. Identifying Eq. (2.14) with Eq. (2.12), we see that the SQUID loop is an element which behaves like a single Josephson junction with a Josephson energy

$$E_J = E_{\Sigma} \sqrt{d^2 + (1-d^2) \cos^2\left(\frac{\Phi_{\text{ext}}}{2\Phi_0}\right)}$$

tunable between a maximum value of $E_{\Sigma} = E_{J,1} + E_{J,2}$ for $\Phi_{\text{ext}} = 2n\pi\Phi_0$ and a minimum value of $dE_{\Sigma} = |E_{J,1} - E_{J,2}|$ for $\Phi_{\text{ext}} = (2n+1)\pi\Phi_0$, where $n \in \mathbb{Z}$.

2.1.3 The Transmon qubit

Electrical circuits consisting of a Josephson junction or a SQUID loop in parallel with a combination of, a shunt inductor, a shunt capacitors and/or a Josephson junction array, will exhibit a complex level structure which typically allows to address transitions between quantum energy levels individually. Such circuits behave as artificial atoms who can be treated as qubits. Different types of qubits can be obtained, depending the choice of elements shunting the Josephson junction, and the relative energy associated with each element. All the experiments which we will present in this thesis use transmon qubits, which consist of a Josephson junction shunted by a large capacitor. Therefore this section and the next ones focus solely on this type of qubit. We refer the reader interested in other types of superconducting qubits to specific reviews [Kjaergaard20, Wendin17].

Hamiltonian

A Josephson junction can also be viewed as a non-linear inductor. This becomes explicit when inverting Eq. (2.11)

$$\begin{aligned}\Phi &= \Phi_0 \arcsin(I/I_0) \\ &= \frac{\Phi_0}{I_0} \left[\underbrace{1 + \frac{1}{6} \left(\frac{I}{I_0}\right)^2 + O\left(\left(\frac{I}{I_0}\right)^4\right)}_{L_J(I/I_0)} \right] I,\end{aligned}\quad (2.15)$$

which corresponds to the $I - V$ relation of an inductor with current-dependent Josephson inductance $L_J \sim \Phi_0/I_0 = \Phi_0^2/E_J$. Therefore, the circuit consisting of a Josephson junction (or a SQUID loop) in parallel with a capacitor, also called a Cooper-pair box (CPB) [Shnirman97, Nakamura99], acts as a non-linear LC-circuit [Fig. 2.5 (d,e)]. We see from Eq. (2.15) that, as long as $\Phi < \Phi_0$, the inductance of the CPB increases with increasing power. Therefore the resonance frequency $\omega(\Phi) = 1/\sqrt{L(\Phi)C}$ of the Cooper-pair box decreases with power.

Similar to the quantization of the harmonic oscillator [Eq. (2.4)], we use canonical quantization to obtain the quantum Hamiltonian of the CPB [Bouchiat98, Girvin09],

$$\hat{H}_{\text{CPB}} = 4E_C(\hat{n} - n_g)^2 - E_J \cos(\hat{\varphi}), \quad (2.16)$$

where we introduced the Coulomb charging energy $E_C = e^2/2C_\Sigma$, the total capacitance of the CPB C_Σ , the charge number operator $\hat{n} = \hat{q}/2e$, and the gate offset charge number $n_g = q_t/2e$.

Identifying again charge with momentum and phase with position, we see that in the *transmon* regime where $E_J \gg E_C$, adding charges to the CPB island adds little “kinetic energy” to the system relative to the depth of the “potential well”. Therefore we expect the lowest energy eigenstates to be deep in the potential well of the Josephson junction, and that the boundary condition $\psi(\varphi) = \psi(\varphi + 2\pi)$ can be lifted [Koch07]. The cosine term can then be expanded to fourth order in φ , and the gate offset charge number n_g neglected, to give the transmon Hamiltonian

$$\hat{H}_t = 4E_C \hat{n} + E_J \frac{\varphi^2}{2} - E_J \frac{\varphi^4}{24} + O(\varphi^6), \quad (2.17)$$

where we omitted a global energy offset. Similar to the case of the harmonic oscillator, we go through a second quantization by introducing the bosonic creation and

annihilation operators for the transmon

$$\hat{b} = \sqrt[4]{\frac{E_J}{32E_c}}\hat{\varphi} + i\sqrt[4]{\frac{2E_c}{E_J}}\hat{n}, \quad \text{and} \quad \hat{b}^\dagger = \sqrt[4]{\frac{E_J}{32E_c}}\hat{\varphi} - i\sqrt[4]{\frac{2E_c}{E_J}}\hat{n}. \quad (2.18)$$

The bosonic commutation rule $[\hat{b}, \hat{b}^\dagger] = 1$ can be easily verified. Up to leading order, neglecting operators which do not conserve the number of excitations, and omitting a global energy offset, we obtain

$$\hat{H}_t = (\sqrt{8E_J E_c} - E_c)\hat{b}^\dagger\hat{b} - \frac{E_c}{2}\hat{b}^\dagger\hat{b}^\dagger\hat{b}\hat{b}. \quad (2.19)$$

Similar to the case of the harmonic oscillator, we find that \hat{H}_t has a discrete set of eigenstates which we label $|k\rangle$, with $k \in \mathbb{N}$ in increasing order of energy, and on which the creation and annihilation operators act as

$$\hat{b}|k\rangle = \sqrt{k}|k-1\rangle, \quad \hat{b}^\dagger|k\rangle = \sqrt{k+1}|k+1\rangle, \quad \text{and} \quad \hat{b}^\dagger\hat{b}|k\rangle = k|k\rangle. \quad (2.20)$$

Using Eq. (2.19) and Eq. (2.20), we can find the eigenenergies E_k and transition frequencies $\omega_{k,k+1}$ of the transmon circuit ($\hbar = 1$)

$$E_k = \langle k|\hat{H}_t|k\rangle = k(\sqrt{8E_J E_c} - E_c) - \frac{k(k-1)}{2}E_c \quad (2.21)$$

$$\omega_{k,k+1} = E_{k+1} - E_k = (\sqrt{8E_J E_c} - E_c) - kE_c. \quad (2.22)$$

We see that the levels of the transmon circuit are not evenly spaced, and that the transition frequency gets smaller and smaller as we climb the energy ladder [Fig. 2.5 (f)]. This picture is the quantized version of the classical interpretation which we made earlier, of the transmon circuit being a non-linear resonator whose resonant frequency decreases with power [see Eq. (2.15)].

Remarkably, because each transition has a different frequency, it is possible to address them selectively. Therefore, if the transmon circuit is initialized in its ground state, it can be used as a quantum object with a finite number of dimensions $d + 1$ by addressing only the transitions from $|0\rangle$ to $|d\rangle$. For $d = 2$ or 3 , we will refer to the transmon circuit as a *transmon qubit* or *qutrit*. In this case, we will label the three lowest energy states $|g\rangle$, $|e\rangle$ and $|f\rangle$ [Fig. 2.5 (f)]. The qutrit transition frequencies

are then given by ($\hbar = 1$)

$$\omega_q := \omega_{ge} = \sqrt{8E_J E_C} - E_C, \quad (2.23)$$

$$\text{and } \omega_{ef} = \omega_q + \alpha, \quad (2.24)$$

$$\text{with } \alpha = -E_C. \quad (2.25)$$

We specify the anharmonicity α even though we intend to use the transmon circuit as a qubit because this quantity has a practical impact in quantum information processing. For instance, as we will see in Sec. 2.1.4 and chapter 3, it sets an upper limits to transition drive rates [Motzoi09] and the measurement speed [Walter17]. The anharmonicity of the transmon qubit is negative, but we will often omit the negative sign and refer implicitly to its modulus from here on.

From Eq. (2.25), it seems that α is determined by the total capacitance of the transmon qubit C_Σ . However, the transition frequencies given by Eq. (2.25) are asymptotic limits as $E_J/E_C \rightarrow +\infty$. As soon as $E_J/E_C > 50$, this asymptotic limit is a very accurate approximation of the exact qubit frequency ω_q obtained by diagonalizing the CPB Hamiltonian [Fig. 2.6 (a)]. However, for typical values of E_J/E_C ranging from 30 to 150 [Koch07, Magnard18], Eq. (2.25) underestimates α by more than 10% [Fig. 2.6 (a)]. It is also useful to notice that the relative anharmonicity $\alpha_r := \alpha/\omega_q \simeq 1/(\sqrt{8E_J/E_C} - 1)$ is a decreasing function of E_J/E_C , which is below 10% for $E_J/E_C > 25$ [Fig. 2.6 (b)].

At this point, we need to make three important remarks about the perturbative treatment we have made to derive Eq. (2.19). First, a rigorous perturbative derivation of the eigenstates of the transmon circuit yields a perturbed creation (and annihilation) operator, and we decided to omit this part for conciseness and clarity. The reader may find a complete perturbative analysis to first order in Ref. [Koch07] and to arbitrary order in Ref. [Didier18]. Second, because the transmon approximation holds only if the phase of the wavefunction is focused deep inside the cosine potential well, it necessarily breaks down at high enough excitation number. In particular, the negative transition frequencies obtained from Eq. (2.22) for $n + 1 > \sqrt{8E_J/E_C}$ indicate that the transmon approximation is already invalid for these high excitation numbers. Last but not least, the perturbative treatment of the CPB Hamiltonian simply removes any dependence on the gate offset charge number n_g .

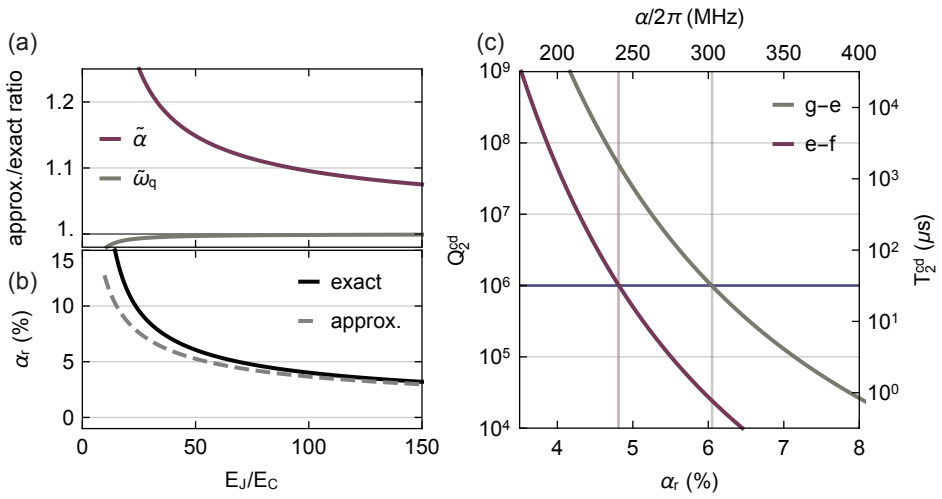


Figure 2.6 (a) Ratio between the approximate [Eq. (2.25)] and exact value for the qubit frequency and the anharmonicity, vs E_J/E_C ratio. (b) Absolute value of the relative anharmonicity $\alpha_r := \alpha/\omega_q$ vs E_J/E_C ratio calculated with an exact diagonalization of the CPB Hamiltonian, and with the approximate transmon formulae (2.25). (c) Worst case scenario charge dispersion quality factor Q_2^{cd} of the g - e and e - f transitions vs relative transmon anharmonicity α_r . The ticks in the top and right axis show the corresponding anharmonicity α and Ramsey coherence limit T_2^{cd} for a nominal qubit frequency $\omega_q/2\pi = 5$ GHz. The pink and the gray vertical grid lines at 5% and 6% correspond to the relative anharmonicity at which the charge dispersion quality factor is 10^6 (blue line), for the e - f and g - e transitions, respectively.

Charge dispersion suppression

Understanding the dependence of the CPB energy levels on n_g is important however, because the charge noise in the environment of the CPB translate in random fluctuations of n_g which then leads to random fluctuation of the qubit frequency, or qubit dephasing. To do so, one needs to solve the eigenenergies from the CPB Hamiltonian Eq. (2.16). This can be done analytically by expressing Schrödinger's equation in the phase basis and using Mathieu's characteristic functions, or numerically by using a truncated charge basis [Koch07]. One then finds that eigenenergies, and therefore transition frequencies, are 1-periodic in n_g with extrema at $n_g = 0$ and $n_g = 1/2$. Using the asymptotics of Mathieu characteristic values, one can approximate the charge dispersion $\epsilon_k = E_k(n_g = 1/2) - E_k(n_g = 0)$ of level k with [Koch07]

$$\epsilon_k \simeq (-1)^k E_C \frac{2^{4k+5}}{k!} \sqrt{\frac{2}{\pi}} \left(\frac{E_J}{2E_C} \right)^{\frac{k+3}{2}} e^{-\sqrt{8E_J/E_C}}. \quad (2.26)$$

The charge dispersion is exponentially suppressed in $\sqrt{E_J/E_C}$ and increases exponentially with k . To determine the maximum amount of Ramsey dephasing induced by this charge dispersion, we consider the worst case scenario where the charge offset alternates randomly between $n_g = 0$ and $n_g = 1/2$. This induces the k -($k+1$) transition frequency to randomly alternate between its two extrema

$$\omega_{k,k+1}(n_g = 0 \text{ or } 1/2) \simeq \omega_{k,k+1}(n_g = 1/4) \pm \frac{\epsilon_{k+1} - \epsilon_k}{2}, \quad (2.27)$$

which implies that the coherence between states $|k\rangle$ and $|k+1\rangle$ depends on time t as $\cos((\epsilon_{k+1} - \epsilon_k)t/2)$. Defining the Ramsey dephasing time T_2^* as the time it takes for the coherence to reach $1/e$, we find that the worst case scenario T_2^* limit imposed by charge noise is

$$T_2^{\text{cd}} = \frac{2}{\epsilon_{k+1} - \epsilon_k} \arccos(e^{-1}) \simeq \frac{2.4}{\epsilon_{k+1} - \epsilon_k}. \quad (2.28)$$

Equations (2.25), (2.26) and (2.28) highlight the most important feature of the transmon qubit: for a fixed qubit frequency, the dephasing effect of charge noise is exponentially suppressed in $\sqrt{E_J/E_C}$ whereas the anharmonicity of the transmon $\alpha \simeq -E_C$ decreases inversely proportionally to $\sqrt{E_J/E_C}$. Thanks to this feature, it is possible to set $\sqrt{E_J/E_C}$ high enough to virtually suppress charge noise dephasing, while maintaining high enough qubit anharmonicity. Indeed, by expressing $\sqrt{E_J/E_C}$ as a function of the relative anharmonicity α_r [see Fig. 2.6 (b)], we see that the quality factor

$Q_2^{\text{cd}} := \omega_q T_2^{\text{cd}}$ associated with charge dispersion, can exceed 10^6 for $\alpha_r < 6\%$ and even 10^9 for $\alpha_r < 4\%$ [Fig. 2.6 (c)]. For a typical qubit frequency $\omega_q/2\pi = 5$ GHz, the anharmonicity can be as high as 300 MHz (240 MHz), corresponding to a minimum qubit gate time of $\sim 2 \times 2\pi/\alpha = 6.6$ ns (8.3 ns) [Motzoi09, Gambetta11b], before the charge noise coherence limit on the g - e (e - f) transition drops below $30 \mu\text{s}$ [Fig. 2.6 (c)].

2.1.4 Qubit Control and Coherence

Initialization

To control the quantum state of a transmon qubit, the circuit should first be initialized in a pure, fiducial state [DiVincenzo00]. This is typically achieved by letting the transmon qubit thermalize to its cryogenic environment. Then the qubit ends up in its ground state, with a residual thermal excitation $n_{\text{th}} = \exp(-\hbar\omega_q/k_b T)$, which is negligible if the thermal energy of the environment is small enough, *i.e.* $T \ll \hbar\omega_g/k_b$. Here k_b is the Boltzmann constant. Noting that,

$$\frac{\hbar}{k_b} \simeq 48 \text{ mK/GHz},$$

this condition corresponds to $T \ll 250$ mK for a qubit with a typical transition frequency $\omega_q/2\pi = 5$ GHz. For this reason superconducting circuits need to be operated at temperatures of a few dozens mK, far below the critical temperature of the superconducting metals.

The dynamics of initialization by passive thermalization are governed by qubit decay, and one should wait for a thermalization time that is several times the qubit decay time to reach good ground state with this scheme. Alternatively, it is possible to actively initialize the transmon qubit to its ground state with tunable dissipation or using measurement and feedback. We will discuss this topic in details in chapter 5, in which we present a demonstration of our own reset scheme.

Rabi oscillations

To perform qubit rotations, the qubit needs to be coupled to a drive line: a dedicated transmission line whose open end couples capacitively to the transmon qubit island. Applying a microwave tone with carrier frequency ω_d through the drive line effectively modulates the gate charge offset n_g in Eq. (2.16), which leads to an additional time-

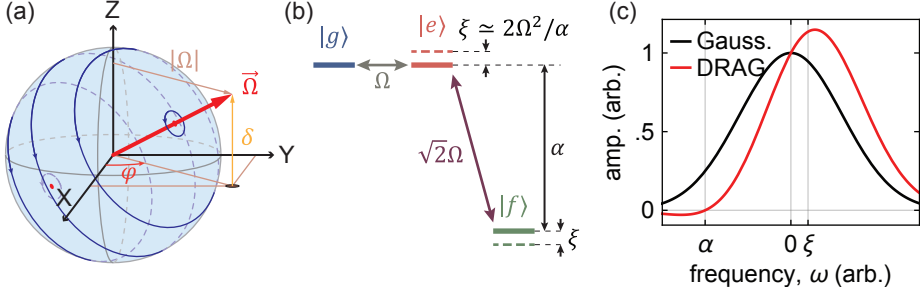


Figure 2.7 (a) Bloch sphere representation of a qubit rotation (dark blue circling arrows) around the Bloch vector $\vec{\Omega}$ (red arrow) induced by a drive of amplitude $|\Omega|$ (teal) and phase φ (orange), detuned from the qubit frequency by δ (yellow). (b) Qutrit energy level diagram in the frame rotating at the qubit frequency, in the presence of a resonant g - e drive. The dashed blue and green lines are the $|e\rangle$ and $|f\rangle$ states dressed by the off-resonant drive-induced e - f coupling term (purple arrow), and ac-stark-shifted by $\pm\xi \simeq \pm 2\Omega^2/\alpha$ in the weak drive limit $\Omega \ll \alpha$. (c) Real amplitude spectrum of a Gaussian, and Gaussian DRAG pulse, in the frame rotating at the qubit frequency. The vertical ticks and gridlines denote the e - f transition ($\omega = \alpha$), the bare g - e transition ($\omega = 0$) and the dressed g - e transition [$\omega = \xi$, see panel (b)], respectively.

dependent drive term to the Hamiltonian

$$\hat{H}_d = \Omega e^{i\omega_d t} \hat{b} + h.c.,$$

where the Rabi drive rate Ω is a complex quantity whose phase and amplitude are given by that of the drive tone. In the frame rotating at the drive frequency, the total Hamiltonian becomes

$$\hat{H} = \hat{H}_t + \hat{H}_d(t) = \delta \hat{b}^\dagger \hat{b} + \frac{\alpha}{2} \hat{b}^\dagger \hat{b}^\dagger \hat{b} \hat{b} + (\Omega \hat{b} + \Omega^* \hat{b}^\dagger), \quad (2.29)$$

where $\delta = \omega_q - \omega_d$ is the detuning between the drive and qubit frequencies. Assuming that the drive is detuned far enough from the e - f transition frequency, we can omit the $|f\rangle$ level and consider the transmon circuit as a qubit, *i.e.* express the bosonic operators in terms of the Pauli operators: $\hat{b}^\dagger \hat{b} \rightarrow \sigma_z/2$ and $\hat{b}^{(\dagger)} \rightarrow \sigma^\pm = (\sigma_x \pm i\sigma_y)/2$. Then Hamiltonian 2.29 takes the form of a qubit experiencing Rabi oscillations: a periodic rotation of the wavefunction on the Bloch sphere around the Bloch vector $\vec{\Omega} = (\text{Re}(\Omega), \text{Im}(\Omega), \delta)$ at rate $|\vec{\Omega}| = \sqrt{|\Omega|^2 + \delta^2}$ [Nielsen11], see Figure 2.7 (a). Therefore, any arbitrary qubit rotation $R_{\vec{u}, \theta}$ of angle θ around the Bloch unit axis \vec{u} , can be performed by driving the qubit with a Rabi rate Ω and a detuning δ for a time t_g such

that

$$\frac{\vec{\Omega}}{\sqrt{|\Omega|^2 + \delta^2}} = \vec{u}, \quad (2.30)$$

and $t_g \sqrt{|\Omega|^2 + \delta^2} = \theta.$

In particular one can perform rotations around the X or Y axis of the Bloch sphere by driving the qubit resonantly ($\delta = 0$) with a drive phase of 0 or $\pi/2$. The rotation angle θ is set by the drive amplitude and the gate duration. We will often refer to the pulse which induce the rotations $R_{X/Y}^{\pi/2}$ and $R_{X/Y}^{\pi}$ as $\pi/2$ and π pulses, respectively. Z axis rotations can be performed virtually, by changing the phase of the rotating frame. This abstract change of referential is instantaneous and its effect in the lab reference frame consists in updating the phase of all subsequent control pulses [McKay17].

To calibrate the amplitude of the $\pi/2$ and π pulses, we initialize the qubit in its ground state and apply a resonant Gaussian-envelope pulse of fixed duration of which we sweep the amplitude A_{ge} . We then fit the measured $|e\rangle$ population with a cosine to extract the amplitudes yielding $\pi/2$ and π rotations [Fig. 2.8 (a)].

DRAG pulses

The gate duration t_g is inversely proportional to the Bloch vector amplitude, and Eq. (2.30) seems to indicate that it can be decreased arbitrarily by increasing the drive amplitude. However when the Rabi amplitude starts to be comparable to the detuning $\delta + \alpha$ between the drive and the e - f transition frequencies, the $|f\rangle$ level cannot be neglected any more. This is well explained by considering a resonant drive ($\delta = 0$), and rewriting Hamiltonian 2.29 in the form of a matrix in the $\{|g\rangle, |e\rangle, |f\rangle\}$ basis,

$$\hat{H} = \begin{pmatrix} 0 & \Omega & 0 \\ \Omega^* & 0 & \sqrt{2}\Omega \\ 0 & \sqrt{2}\Omega^* & \alpha \end{pmatrix}. \quad (2.31)$$

The drive term couples states $|e\rangle$ and $|f\rangle$ non-resonantly [Fig. 2.7 (b)]. If $\sqrt{2}\Omega \ll \alpha$, then $|e\rangle$ and $|f\rangle$ are coupled dispersively, *i.e.* there is only negligible population transfer from $|e\rangle$ to $|f\rangle$, but the dressed $|e\rangle$ -level energy is ac-stark shifted by $\xi \simeq 2\Omega^2/\alpha$ [Stark14, Tamarat95]. The drive is therefore detuned by ξ from the dressed g - e transition instead of being resonant, which leads to a *phase error* in the qubit rotation [Fig. 2.7 (b)]. If $\sqrt{2}\Omega$ is comparable or bigger than α then the drive will

induce non-negligible population transfer from $|e\rangle$ to $|f\rangle$, leading to leakage of the population outside of the computational subspace, referred to as *leakage errors*.

These detrimental effects of the $|f\rangle$ level can be mitigated by shaping the drive pulse appropriately. This can be done using numerical methods [Khaneja05, Werninghaus21], or a sub-optimal but analytical approach called derivative removal by adiabatic gates (DRAG) [Motzoi09]. The Gaussian DRAG method consists in parametrizing the Rabi drive as

$$\begin{aligned} \Omega(t) &= G(t) + i \frac{q}{\alpha} \dot{G}(t) \\ \text{with } G(t) &= \begin{cases} \Omega_0 \left(e^{-\frac{1}{2}(\frac{t}{\sigma})^2} - e^{-\frac{1}{2}(\frac{t_g}{2\sigma})^2} \right) & -\frac{t_g}{2} \leq t \leq \frac{t_g}{2} \\ 0 & \text{otherwise.} \end{cases} \end{aligned} \quad (2.32)$$

The pulse consists of a truncated Gaussian pulse in-phase, with width σ and total duration t_g , and its derivative in quadrature scaled with a factor q/α . Looking at the expression of the drive in Fourier space (assuming no truncation)

$$\begin{aligned} \hat{\Omega}(\omega) &= \hat{G}(\omega) + i \frac{q}{\alpha} \hat{G}'(\omega) \\ &= \hat{G}(\omega) + i \frac{q}{\alpha} (-i\omega \hat{G}(\omega)) \\ &= \hat{G}(\omega) \left(1 + \frac{q}{\alpha} \omega \right), \end{aligned} \quad (2.33)$$

we see that the frequency component which is resonant with the e - f transition ($\omega = \alpha$) cancels for $q = -1$, thereby suppressing the leakage errors [Fig. 2.7 (c)]. The phase error is also mitigated because the mean frequency of the pulse is shifted upwards, in the same direction as the ac-stark shift, see Fig. 2.7 (c). The rest of the phase error can be independently mitigated with an appropriate change of the instantaneous drive frequency [Motzoi09, Gambetta11b, McKay17, Chen16]. The DRAG correction typically reduces the rotation error by more than an order of magnitude, down to 10^{-3} for gate durations longer than $t_{\min} = 2 \times 2\pi/\alpha$ [Motzoi09, Gambetta11b]. For an anharmonicity $\alpha/2\pi = -300$ MHz, representative of the transmon qubits used in this thesis, the corresponding minimum gate time is $t_{\min} = 5.3$ ns.

In this thesis, we used a simplified, though less optimal, pulse shape parametrization, where the instantaneous drive frequency is fixed and only the phase error is minimized by optimizing the DRAG parameter q [Lucero10, Chow10]. To do so, we initialize the qubit in its ground state, then apply an $R_X^{\pi/2}$ rotation followed by either R_X^π , $R_Y^{-\pi}$ or R_Y^π , and measure the qubit state. We repeat the experiment multiple times,

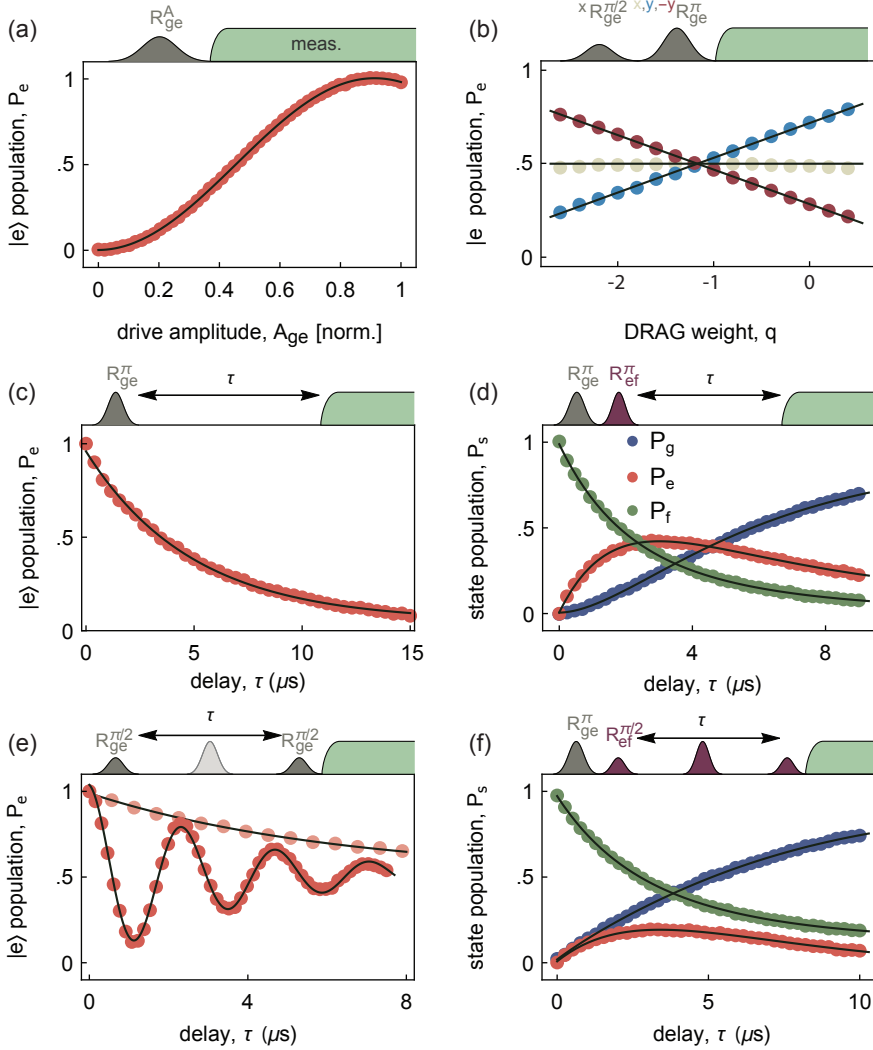


Figure 2.8 (a) Rabi calibration: excited state population vs amplitude of a fixed-duration resonant gaussian DRAG pulse (dots), fitted with a cosine (line). (b) DRAG parameter calibration. (c,d) T_1 measurement of levels $|e\rangle$ and $|f\rangle$, respectively. (e) Ramsey (red dots) and Hahn echo measurement (clear red dots). (f) Measurement of the e - f Ramsey dephasing time. For each calibration measurement, the pulse scheme is shown on the top axis. In (e), the optional Hahn echo π pulse is shown in light gray. These calibrations were performed on the qubit labelled A in Ref. [Kurpiers18].

sweeping the parameter q , and select the value of q for which the average excited population is the closest to 0.5 for all three sequences [Fig. 2.8 (b)].

To manipulate higher levels of the transmon qubit, we use DRAG pulses which are resonant with higher transitions [Bianchetti10].

Qubit Decay

As for all qubits, the transmon qubit is not perfectly isolated from the environment, which leads to finite coherence of its quantum state.

Qubit decay is a process by which the the state of the transmon qubit spontaneously decays from $|k\rangle$ to $|k-1\rangle$. It can emerge from the transverse coupling of the electric field generated by the transmon qubit to lossy elements of the environment, such as: infinite, or semi-infinite transmission lines [Houck08], pieces of normal metal in the package surrounding the transmon qubit chip [Huang21a], or the thin oxide layers which typically grow at the substrate-air, substrate-metal, and metal-air interfaces on the chip [Wenner11, Wang15, Dial15, Woods19]. The probability of a qubit decay event is given by the exponential law

$$P[|\psi(\tau)\rangle = |\psi(0)\rangle = |k\rangle] = e^{-\tau/T_1^{k-1,k}}, \quad (2.34)$$

characterized by the *characteristic decay time* $T_1^{k-1,k}$. To probe decay from $|e\rangle$ to $|g\rangle$ experimentally, we initialize the qubit in $|e\rangle$ with a π pulse and wait for a time τ before measuring the qubit state. The average qubit population in $|e\rangle$ then follows the exponential law of Eq. (2.34), from which we can retrieve T_1^{ge} [Fig. 2.8 (c)]. The T_1 time of higher energy levels can be obtained by running a similar experiment with the qubit initialized in $|k\rangle$, with $k > 1$ [Fig. 2.8 (d)].

Qubit Dephasing

Interactions between the qubit and the environment can also suppress the quantum coherence of the qubit. We have seen earlier that the transmon qubit frequency ω_q can depend on external quantities, such as the gate offset charge n_g applied to the transmon qubit, or the external magnetic flux Φ_{ext} threaded through its SQUID loop. Classical noise in these quantities translate into random fluctuation of the qubit frequency, and therefore, of the qubit phase. Let's take an example with a qubit initialized in the equal superposition pure state $(|0\rangle + |1\rangle)/\sqrt{2}$. As it idles, the qubit frequency differs from it's mean by the randomly fluctuating term $\delta\omega_q(t)$, and after a time τ , the qubit is in state $|\phi\rangle = (|0\rangle + e^{i\phi}|1\rangle)/\sqrt{2}$, where $\phi = \int \delta\omega_q dt$. Because the process is random, the final state is described by a density matrix which is the mixture of all possible final

states

$$\begin{aligned}\rho &= \int |\phi\rangle \langle\phi| f_\phi(\phi) d\phi \\ &= \frac{1}{2} \begin{pmatrix} 1 & \mathcal{V} \\ \mathcal{V}^* & 1 \end{pmatrix},\end{aligned}\tag{2.35}$$

with $f_\phi(\phi)$ the probability density function of the random variable ϕ , and the qubit coherence $\mathcal{V} = \int f_\phi(\phi) e^{i\phi} d\phi$. If the phase fluctuation is small, then $f_\phi(\phi)$ is narrowly peaked around 0, and $\mathcal{V} \simeq 1$. By contrast if the phase fluctuation is large, then $f_\phi(\phi)$ is close to uniform over $[0, 2\pi]$, and $\mathcal{V} \simeq 0$. In other words, the coherence \mathcal{V} of the qubit decreases with increasing uncertainty of ϕ . This is why this decoherence process is often referred to as *qubit dephasing*.

Assuming that the phase ϕ follows a centered Gaussian distribution with standard deviation σ , then integrating Eq. (2.35) leads to

$$\mathcal{V} = e^{-\frac{1}{2}\sigma^2}.$$

Using the fact that

$$\sigma^2(\tau) = \text{Var}\phi = \int_0^\tau \int_0^\tau \langle \delta\omega_q(t), \delta\omega_q(t') \rangle dt dt',$$

we find that $\sigma^2 \propto \tau$, in the case of white frequency noise (i.e. $\langle \delta\omega_q(t), \delta\omega_q(t') \rangle \propto \delta(t, t')$), and that $\sigma^2 \propto \tau^2$ in the case of low-frequency noise (i.e. $\langle \delta\omega_q(t), \delta\omega_q(t') \rangle = \text{cst}$). As a result, in the more general case that $\delta\omega_q$ fluctuates with a combination of white and low-frequency noise, we find that

$$\mathcal{V} = \exp\left[-\frac{\tau}{T_2^{\text{wn}}}\right] \times \exp\left[-\left(\frac{\tau}{T_2^{\text{wn}}}\right)^2\right],$$

where T_2^{wn} and $T_2^{1/f}$ are the characteristic dephasing times associated with white and low-frequency noise, respectively.

Another source of dephasing comes from entanglement between the qubit and the environment. This can be modeled with the general unitary performing the following map

$$|0\rangle_q |E_i\rangle \mapsto |0\rangle_q |E_0\rangle, \quad \text{and} \quad |1\rangle_q |E_i\rangle \mapsto |1\rangle_q |E_1\rangle,$$

where $|E_i\rangle$ denote the initial state of the environment, and $|E_{0/1}\rangle$, it's final state after having interacted with the qubit initialized in $|0/1\rangle_q$. Starting with the qubit in $|+\rangle$, and tracing out the environmental degrees of freedom, the reduced density matrix of the qubit takes the form of Eq. (2.35), with

$$\mathcal{V} = \langle E_0 | E_1 \rangle.$$

If the qubit is not entangled with the environment at all, then $|E_0\rangle = |E_1\rangle$ and $\mathcal{V} = 1$: the qubit keeps a perfect coherence. But for maximal entanglement with the environment, $|E_0\rangle$ and $|E_1\rangle$ are orthogonal and $\mathcal{V} = 0$: the qubit is completely dephased. Up to a unitary transformation of the environment, we can rewrite $|E_0\rangle = |0\rangle_E$ as the vacuum state, and $|E_1\rangle = |\beta\rangle_E$. In many cases, including that of a continuous measurement of the qubit, $|\beta\rangle_E$ is a coherent state whose number of photons increases linearly with the interaction time $|\beta|^2 \propto \tau$. Then we obtain

$$\mathcal{V} = \langle 0 | \beta \rangle = e^{-\frac{1}{2}|\beta|^2} = e^{-\tau/T_2^{\text{ent}}}. \quad (2.36)$$

The qubit decoheres exponentially with the characteristic time T_2^{ent} , at which the qubit gets entangled with the environment. Because $|E\rangle$ can be considered as the pointer state in a Von Neumann measurement, we generally refer to this mechanism as *measurement-induced dephasing*.

To extract the dephasing time of the qubit, we perform a Ramsey measurement. We initialize the qubit in state $|+\rangle$ with a $\pi/2$ pulse and wait for a time τ . The qubit density matrix then has the form of Eq. (2.35). We then apply a second $\pi/2$ pulse, in phase with the first one and measure the qubit state. The average population in state $|e\rangle$ is then

$$P_e(\tau) = \frac{1}{2}(1 + \mathcal{V} \cos(\delta \tau)) = \frac{1}{2} \cos(\delta \tau) \left(1 + \cos(\delta \tau) e^{-\tau/T_2^{\text{exp}}} e^{-(\tau/T_2^{\text{lf}})^2} \right), \quad (2.37)$$

where δ is the detuning between the qubit and the drive frequency, and $1/T_2^{\text{exp}} = 1/T_2^{\text{ent}} + 1/T_2^{\text{wn}}$ is the overall characteristic exponential decoherence time. We use fits of Eq. (2.37) to Ramsey measurements to extract the dephasing time and frequency $\omega_q = \omega_d + \delta$ of the qubit [Fig. 2.8 (e)].

The Hahn echo sequence is an adaptation from the Ramsey sequence, where a π pulse is introduced in the middle of the two $\pi/2$ pulses [Fig. 2.8 (e)]. This extra π pulse generates a spin echo and effectively filters the frequency noise with a band pass centered at $\omega_c = 1/\tau$ [Bylander11]. As a result, the low-frequency noise is

filtered out, leading to exponential decay of \mathcal{V} with an improved decoherence time T_2^e [Fig. 2.8 (e)]. Similar to all the calibrations presented so far, it is possible to probe the transition frequency and the coherence times of the e - f (or higher) transition by performing a Ramsey or Hahn echo sequence with the transmon qubit initialized in $(|e\rangle + |f\rangle)/2$. The fit function then needs to be adapted from Eq. (2.37) to also account for decay towards $|g\rangle$ [Fig. 2.8 (f)].

2.1.5 Jaynes-Cummings Hamiltonian

In the previous section, we have seen how to build two essential tools of quantum information processing with superconducting circuits: a harmonic oscillator and an artificial atom. We shall now see how these two building blocks interact.

Coupling between two resonators

We will start with the simpler case of two LC-circuit coupled to each other with a capacitance C_g . This circuit, which is shown in Fig. 2.9 (a), implements the classical Hamiltonian

$$H_{2LC} = \frac{1}{2} \vec{\Phi}^\top \mathbf{L}^{-1} \vec{\Phi} + \frac{1}{2} \vec{Q}^\top \mathbf{C}^{-1} \vec{Q}, \quad (2.38)$$

where $\vec{\Phi} = (\Phi_1, \Phi_2)$ and $\vec{Q} = (Q_1, Q_2)$ are the flux and charge vectors of the system, and the inductance and capacitance matrices are

$$\mathbf{L} = \begin{pmatrix} L_1 & 0 \\ 0 & L_2 \end{pmatrix}, \quad \text{and} \quad \mathbf{C} = \begin{pmatrix} C_1 + C_g & -C_g \\ -C_g & C_2 + C_g \end{pmatrix}.$$

Assuming that the coupling capacitor is small ($C_g \ll C_1, C_2$), we can expand the inverse of the capacitance matrix to first order in $C_g/C_{1/2}$

$$\mathbf{C}^{-1} \simeq \begin{pmatrix} \frac{1}{C_1 + C_g} & \frac{C_g}{C_1 C_2} \\ \frac{C_g}{C_1 C_2} & \frac{1}{C_2 + C_g} \end{pmatrix},$$

and use this simpler form in Eq. (2.38) to obtain

$$H_{2LC} \simeq \underbrace{\frac{Q_1^2}{2C_1'} + \frac{\Phi_1^2}{2L_1}}_{\text{H.O. 1}} + \underbrace{\frac{Q_2^2}{2C_2'} + \frac{\Phi_2^2}{2L_2}}_{\text{H.O. 2}} + \underbrace{\frac{C_g}{C_1 C_2} Q_1 Q_2}_{\text{coupl.}}, \quad (2.39)$$

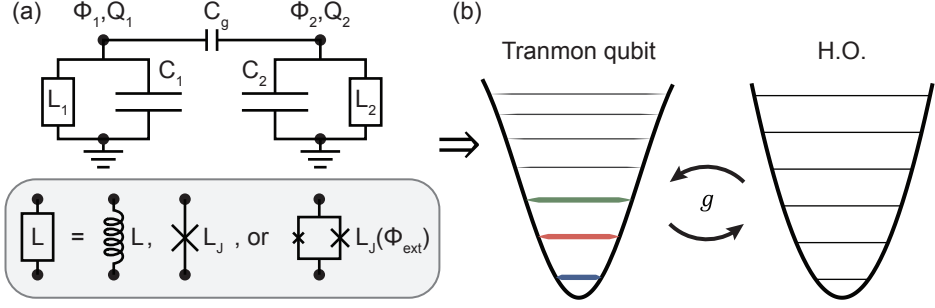


Figure 2.9 (a) Electrical circuit diagram of two LC-circuits coupled capacitively to each other. As indicated in the grey box, for each LC-circuit the inductance could stem from a linear inductor a Josephson junction or a SQUID loop. As shown in the main text, the quantization of circuit (a) leads to the three Hamiltonian terms of Eq. (2.42), graphically represented in (b).

where we introduced the total capacitances $C'_{1/2} = C_{1/2} + C_g$. As indicated by the brackets in Eq. (2.39), the Hamiltonian decomposes into three terms: the Hamiltonian of the two independent harmonic oscillator (H.O.) LC-circuits and a coupling term involving Q_1 and Q_2 . We go through first and second quantization by replacing all the charge and flux variables with their corresponding quantum operators, and by introducing the creation and annihilation operators

$$\hat{a}_k = \frac{1}{2} \left(\frac{\hat{\Phi}_k}{\Phi_{\text{zpf},k}} + i \frac{\hat{Q}_k}{Q_{\text{zpf},k}} \right), \quad \text{and} \quad \hat{a}_k^\dagger = \frac{1}{2} \left(\frac{\hat{\Phi}_k}{\Phi_{\text{zpf},k}} - i \frac{\hat{Q}_k}{Q_{\text{zpf},k}} \right),$$

where the flux and charge zero-point fluctuation are defined as in Eq. (2.5). The Hamiltonian in the second quantized form is then

$$\hat{H}_{2LC} \simeq \underbrace{\hbar\omega_1(\hat{a}_1^\dagger\hat{a}_1 + 1/2)}_{\text{H.O. 1}} + \underbrace{\hbar\omega_2(\hat{a}_2^\dagger\hat{a}_2 + 1/2)}_{\text{H.O. 2}} - \underbrace{\frac{\hbar C_g}{2} \omega_1\omega_2 \sqrt{Z_1 Z_2} (\hat{a}_1^\dagger - \hat{a}_1)(\hat{a}_2^\dagger - \hat{a}_2)}_{\text{coupl.}}, \quad (2.40)$$

where $\omega_k = 1/\sqrt{L_k C'_k}$ is the resonance frequency of the uncoupled harmonic oscillators, and $Z_k = \sqrt{L_k/C'_k}$ their characteristic impedance. Invoking the rotating wave approximation the coupling term can be reduced to

$$\hat{H}_{\text{coupl.}} \simeq \hbar \underbrace{\frac{C_g}{2} \omega_1\omega_2 \sqrt{Z_1 Z_2}}_g (\hat{a}_1^\dagger \hat{a}_2 + \hat{a}_1 \hat{a}_2^\dagger). \quad (2.41)$$

Therefore the circuit of Fig. 2.9 (a) can be interpreted as that of two quantum harmonic oscillators coupled with a photon-exchange term with rate $g = C_g \omega_1 \omega_2 \sqrt{Z_1 Z_2} / 2$ [Fig. 2.9 (b)].

Jaynes-Cummings Hamiltonian

To obtain the Hamiltonian of a transmon qubit capacitively coupled to a resonator, we can simply replace the inductor of one of the LC-resonators with a Josephson junction or a SQUID loop. The Hamiltonian then takes the form

$$\frac{\hat{H}_{qr}}{\hbar} = \underbrace{\omega_q \hat{b}^\dagger \hat{b} + \frac{\alpha}{2} \hat{b}^\dagger \hat{b}^\dagger \hat{b} \hat{b}}_{\hat{H}_q} + \underbrace{\omega_r \hat{a}^\dagger \hat{a}}_{\hat{H}_r} + \underbrace{g(\hat{a}^\dagger \hat{b} + \hat{a} \hat{b}^\dagger)}_{\hat{H}_{\text{int}}}, \quad (2.42)$$

where $\omega_r = 1/\sqrt{LC'}$ is the resonator frequency, $\omega_q = \sqrt{8E_J E_C} - E_C$ is the g - e transition frequency of the transmon, and $\alpha \simeq -E_C$ is the transmon anharmonicity [Fig. 2.9]. Here we have omitted several constant energy terms for simplicity. The coupling rate g in \hat{H}_{int} takes exactly the same form as for the two-resonator case [Eq. (2.41)], *i.e.*

$$\begin{aligned} g &\simeq \frac{C_g}{2} \omega_r \omega_p \sqrt{Z_r Z_q} \\ &= \sqrt{2} \frac{C_g}{C_\Sigma} e V_{\text{zpf}} \sqrt[4]{\frac{E_J}{8E_C}} \end{aligned} \quad (2.43)$$

where we used the plasma frequency $\omega_p = \sqrt{8E_J E_C} = 1/\sqrt{L_q C_\Sigma}$ and the impedance $Z_q = \sqrt{L_q/C_\Sigma}$ of the transmon circuit in the first line. The second line is obtained by using the expressions of ω_p and Z_q in terms of C_Σ , E_C , E_J and $V_{\text{zpf}} = \sqrt{\hbar \omega_r^2 Z_r / 2}$, and corresponds to the formula of Ref. [Koch07].

In practice, the coupling capacitance C_g is a small but non-negligible fraction of the transmon capacitance to ground C_q , therefore the assumption that $C_g \ll C_q$ is excessive and Eq. (2.43) can be significantly off. A more accurate estimate of g can be obtained by taking the exact inverse of the capacitance matrix \mathbf{C} .

The reader might have already recognised that, when truncating the transmon Hamiltonian \hat{H}_q to its first two levels, Hamiltonian (2.42) takes the form of the standard Jaynes-Cumming Hamiltonian [Jaynes63]

$$\frac{\hat{H}_{\text{JC}}}{\hbar} = \frac{\omega_q}{2} \sigma_z + \omega_r \hat{a}^\dagger \hat{a} + g(\hat{a}^\dagger \sigma^- + \hat{a} \sigma^+), \quad (2.44)$$

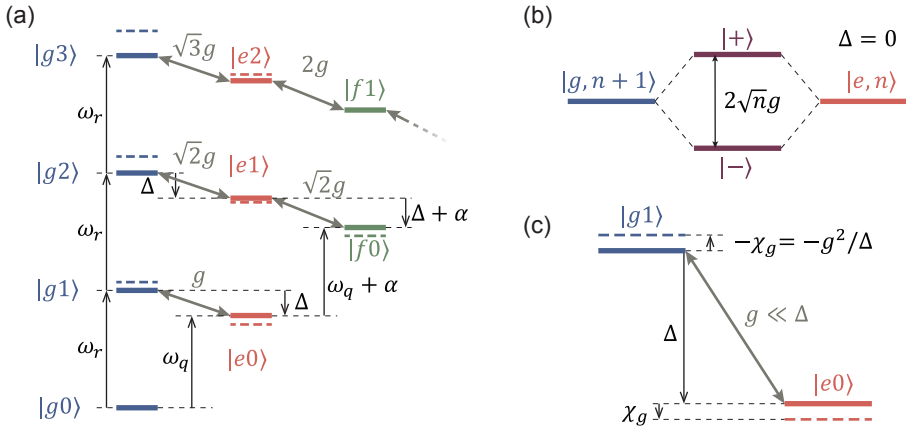


Figure 2.10 (a) Energy-level diagram of the transmon-resonator Jaynes-Cummings Hamiltonian (2.42), in the case where $\omega_q < \omega_r$. The gray double arrows represent the qubit resonator transverse coupling term arising from H_{int} . The black arrows highlight relevant detunings, with the direction of the arrow indicating the sign of the detuning. The dashed colored horizontal bars represent the dressed energy levels. (b) Dressing of states $|g, n + 1\rangle$ and $|e, n\rangle$ in the resonant case $\Delta = 0$. (c) Dressing of states $|g, 1\rangle$ and $|e, 0\rangle$ in the dispersive regime $g \ll \Delta$.

under the rotating-wave approximation. Therefore, the simple circuit shown in Fig. 2.9 (a) can reproduce the rich properties and phenomena captured by the Jaynes-Cumming model [Haroche89, Blais04]. In particular, it can implement the Jaynes-Cumming Hamiltonian (2.44) in the strong coupling regime, where the coupling strength g is much larger than the loss and dephasing rates of the qubit and the resonator [Haroche92, Wallraff04], thereby forming an electrical circuit analogue to the setting of cavity quantum electrodynamics (QED) [Mabuchi02, Hood00, Raimond01], which is often termed *circuit QED* [Blais04, Haroche20].

Jaynes-Cummings eigenenergies

In the Jaynes-Cumming Hamiltonian, the bare states of the individual systems are coupled pairwise, as indicated by the arrows in Fig. 2.10 (a) (ignoring higher transmon levels). Therefore, Hamiltonian (2.44) can be diagonalized by blocks of two dimen-

sional subspaces to obtain the exact exact expression of the dressed states [Blais04]

$$\begin{aligned} |\overline{e, n}\rangle &= \cos \theta_n |e, n\rangle + \sin \theta_n |g, n+1\rangle \\ |\overline{g, n+1}\rangle &= -\sin \theta_n |e, n\rangle + \cos \theta_n |g, n+1\rangle \\ \text{with } \theta_n &= \frac{1}{2} \arctan\left(\frac{2g\sqrt{n+1}}{\Delta}\right), \end{aligned} \quad (2.45)$$

and of their corresponding eigenenergies

$$\begin{aligned} \frac{E_{\overline{g/e, n}}}{\hbar} &= (n+1)\omega_r \pm \frac{1}{2} \sqrt{4g^2(n+1) + \Delta^2} \\ \frac{E_{\overline{g, 0}}}{\hbar} &= \frac{\Delta}{2}. \end{aligned} \quad (2.46)$$

Here we have introduced the detuning $\Delta = \omega_q - \omega_r$ between the qubit and the resonator.

Resonant regime

When the resonator is resonant with the qubit, *i.e.* $\Delta = 0$, the bare states $|e, n\rangle$ and $|g, n+1\rangle$ hybridize completely. The corresponding dressed states are equal symmetric and antisymmetric superpositions of the bare states [Eq. (2.45)], split by an energy difference $2\sqrt{n}g$ [Fig. 2.10 (b)]. An alternative interpretation is to see the coupling term as a resonant Rabi drive, which induces oscillations between the bare states $|e, n\rangle$ and $|g, n+1\rangle$ at a rate $\sqrt{n+1}g$ around the X axis. This Rabi oscillation can be interpreted as a that of a photon swapping back and forth between the qubit and the resonator. For finite detuning $\Delta = \omega_q - \omega_r$, the interaction leads to a non-resonant Rabi oscillation around the Bloch vector $(g, 0, \Delta)$.

Dispersive regime

In the limit of large detuning $g \ll \Delta$, also known as the *dispersive regime*, the transmon qubit and the resonator hybridize very little, but the dressed energies are pushed away from each other by $n\chi$ where $\chi = g^2/\Delta$ is the dispersive shift [Fig. 2.10 (c)]. Using a Schrieffer-Wolf transformation of the Hamiltonian, or Bogoliubov transformation of the bosonic operator, one can re-express the Jaynes-Cumming Hamiltonian in the approximate form of the dispersive Hamiltonian [Blais20]

$$\frac{\hat{H}_{\text{JC}}}{\hbar} \simeq \frac{\hat{H}_{\text{disp}}}{\hbar} = \frac{\omega_q + \chi}{2} \hat{\sigma}_z + \omega_r \hat{a}^\dagger \hat{a} + \chi \hat{a}^\dagger \hat{a} \hat{\sigma}_z. \quad (2.47)$$

This Hamiltonian has several important properties. First, the dispersive Hamiltonian commutes with both σ_z and $\hat{a}^\dagger \hat{a}$. As a consequence, the number of photons in the resonator and the qubit state population are constant with time, which is a mathematically rigorous way to say that population swaps between the qubit and the resonator can be neglected. Second, the frequency of the qubit is Lamb shifted by χ . Finally, factorizing the interaction term $\chi \hat{a}^\dagger \hat{a} \hat{\sigma}_z$ with the first term, the dispersive Hamiltonian reads

$$\frac{\hat{H}_{\text{disp}}}{\hbar} = \left(\frac{\omega_q + \chi}{2} + \chi \hat{a}^\dagger \hat{a} \right) \hat{\sigma}_z + \omega_r \hat{a}^\dagger \hat{a}.$$

The interaction term can be seen as a quantized ac-stark shift: a photon number dependent shift of the qubit frequency by $2\chi \hat{a}^\dagger \hat{a}$. Alternatively, the dispersive term can be factorized with the second term, to yield

$$\frac{\hat{H}_{\text{disp}}}{\hbar} = \frac{\omega_q + \chi}{2} \hat{\sigma}_z + (\omega_r + \chi \hat{\sigma}_z) \hat{a}^\dagger \hat{a},$$

and be interpreted as a qubit-state-dependent shift $\pm\chi$ of the resonator frequency.

Dispersive readout

This second interpretation highlights a convenient way to readout the state of the qubit by driving the resonator with a tone close to its resonance frequency. Indeed, the amplitude and phase of the signal escaping through the resonator output port will depend on the resonance frequency of the resonator, which itself depends on the state of the qubit via the dispersive interaction term [Fig. 2.11]. The amplification and detection of this qubit-state-dependent microwave signal therefore constitutes a measurement of the $\hat{\sigma}_z$ operator of the qubit [Blais04]. More details about this *dispersive readout* scheme can be found in chapter 3 of this thesis, where we demonstrate how to optimize the speed of this scheme.

It is also possible to measure an arbitrary Pauli observable $\vec{n} \cdot \vec{\sigma}$ of the qubit, with \vec{n} a unit vector of \mathbb{R}^3 and $\vec{\sigma} := (\hat{\sigma}_x, \hat{\sigma}_y, \hat{\sigma}_z)$ the vector of Pauli matrices. Indeed, be R a unitary qubit rotation mapping state $(I + \vec{n} \cdot \vec{\sigma})/2$ to $|0\rangle \langle 0|$, we see from the identity $\vec{n} \cdot \vec{\sigma} = R^\dagger \cdot \hat{\sigma}_z \cdot R$ that such a measurement can be done by first applying the rotation R to the qubit, then measure its $\hat{\sigma}_z$ observable via dispersive readout, and finally applying the inverse rotation R^\dagger to map the projected states on the $(I \pm \vec{n} \cdot \vec{\sigma})/2$ basis. The final inverse rotation R^\dagger can be omitted if the qubit state is not re-used in the algorithm after the measurement.

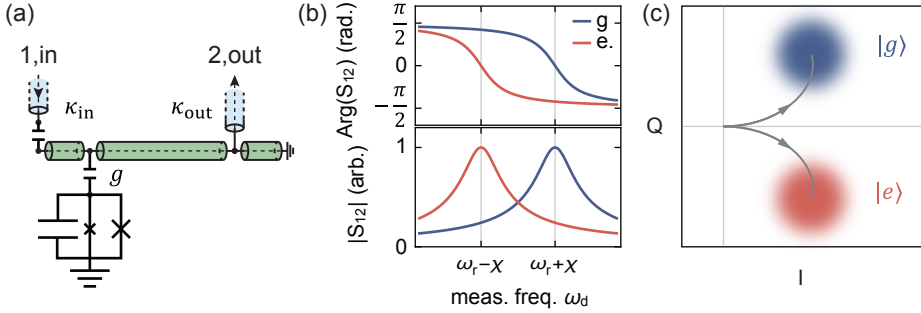


Figure 2.11 (a) Electrical circuit diagram of a qubit dispersively coupled to a $\lambda/4$ resonator. The resonator can be probed in transmission by applying a readout tone of frequency ω_d on its input port. (b) Amplitude (top) and (phase) of the signal transmitted through the output port vs readout frequency, when the qubit is in the ground, or excited state. (c) Path of the transmitted signal in the I-Q plane for $\omega_d = \omega_r$. The gaussian blob represent the probability distribution of the noisy signal.

Dispersive interaction and higher transmon levels

Hamiltonian (2.42) considers the full level structure of the transmon qubit, and thus cannot be diagonalized analytically. However, using the same methods as for the qubit case, it is possible to approximate it in the dispersive regime by

$$\frac{\hat{H}_{\text{disp}}}{\hbar} = \tilde{\omega}_q \hat{b}^\dagger \hat{b} + \frac{\alpha}{2} \hat{b}^\dagger \hat{b}^\dagger \hat{b} \hat{b} + (\omega_r + \chi_k |k\rangle \langle k|) \hat{a}^\dagger \hat{a} \quad (2.48)$$

$$\text{with } \chi_k = \begin{cases} -\frac{g^2}{\Delta} & \text{if } k = 0 \\ -\frac{kg^2}{\Delta + (k-1)\alpha} + \frac{(k+1)g^2\alpha}{(\Delta + (k-1)\alpha)(\Delta + k\alpha)} & \text{otherwise,} \end{cases} \quad (2.49)$$

where $|k\rangle$ denotes the k^{th} transmon level, and where the Lamb shift of the qubit frequency is already absorbed in $\tilde{\omega}_q = \omega_q + g^2/\Delta$. The transmon qubit state dependent dispersive shifts of Eq. (2.49) can be obtained by considering that each pair of bare states $|k, n+1\rangle$ and $|k+1, n\rangle$ is coupled with an interaction rate $g_{k,n} \simeq \sqrt{k+1}\sqrt{n+1}g$ much smaller than their detuning $\Delta_{k,n} = \Delta + (k-1)\alpha$ and repel each other by $\pm g_{k,n}^2/\Delta_{k,n}$ [see Fig. 2.10 (a)]. At $\Delta = -k\alpha$ for all $k \in \mathbb{N}$, states $|k+1, n\rangle$ and $|k, n+1\rangle$ are resonant and the dispersive approximation is invalid, which explains the non-physical divergence of the dispersive shifts χ_k at these points.

Returning to an effective 2-level approximation of the transmon qubit, we obtain

Hamiltonian (2.47), but where the dispersive shift

$$\chi = \frac{\alpha g^2}{\Delta(\Delta + \alpha)}, \quad (2.50)$$

is negative as long as Δ is not in the interval $[\alpha, 0]$, and is reduced by a factor $\alpha/(\Delta + \alpha)$ compared to the true qubit case. Here also, we will often omit the negative sign of χ and implicitly refer to its modulus. In the limit $\alpha \rightarrow 0$ where the transmon qubit is turned into a harmonic oscillator, Eq. (2.47) simplifies to

$$\frac{\hat{H}_{\text{disp,2LC}}}{\hbar} = \left(\omega_q + \frac{g^2}{\Delta} \right) \hat{b}^\dagger \hat{b} + \left(\omega_r - \frac{g^2}{\Delta} \right) \hat{a}^\dagger \hat{a}.$$

The two harmonic oscillator get an opposite Lamb shift of modulus $\frac{g^2}{\Delta}$ and the dispersive interaction disappears. In general, the larger the anharmonicity, the larger the dispersive shift.

As a last remark, we would like to note that a similar analysis can be conducted for the case of two transmon qubits coupled to each other [Fig. 2.9 (a)]. The results are similar, with the exception of the values of the dispersive shifts χ_k given in Eq. (2.49), which should account for the anharmonicity of the second transmon circuit.

2.1.6 Purcell decay

So far, we have only considered perfectly lossless and isolated circuits, which in a quantized setting lead to unitary evolution of the wavefunction describing the circuits. However, the different circuit elements need to be connected in some form to control and measurement apparatuses in order to manipulate their quantum states. However, coupling a quantum system to an output port creates a channel in which the quantum state can decay.

For instance, a transmon qubit of frequency ω_q and impedance Z_q , capacitively coupled to a dedicated drive line of characteristic impedance Z_0 with capacitance C_g decays into the drive transmission line with rate [Houck08]

$$\Gamma_d = C_g^2 Z_q Z_0 \omega_q^3. \quad (2.51)$$

This can be easily shown by considering the Josephson junction as a linear inductor, and calculating classically the external coupling of the resulting LC-oscillator [see Fig. 2.3 and Eq. (2.8)]. This decay rate is also the coupling rate of the drive line

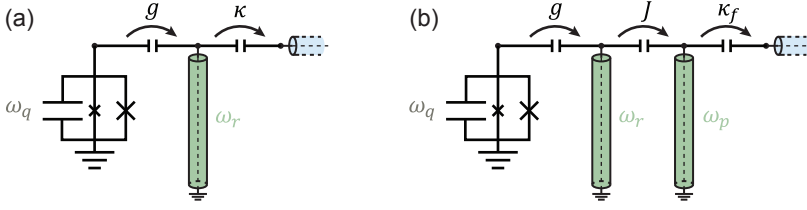


Figure 2.12 Electrical circuit diagram of a qubit of frequency ω_q coupled with rate g to a $\lambda/4$ resonator of frequency ω_r in the dispersive regime ($g \ll |\omega_q - \omega_r|$). The resonator couples to an output port, (a) directly with rate κ , or (b), with rate J to a Purcell filter resonator of frequency ω_p which itself couples with rate κ_f to the output port.

to the qubit: for a given Rabi rate, the required drive power is proportional to $1/\Gamma_d$. Therefore, C_g should be chosen in such a way that Γ_d is small enough that it does not limit the coherence of the qubit, while maintaining the ability to drive the qubit without excessive power. In this thesis, we typically chose C_g such that $1/\Gamma_d$ lies between 100 and 200 μs .

A second qubit decay channel comes from its hybridization with an output coupled resonator, a mechanism known as the *Purcell effect* [Purcell46, Haroche92, Blais04]. For instance, let us consider the system shown in Fig. 2.12 (a), consisting of a qubit of frequency ω_q , coupling with rate g to a resonator of frequency ω_r , and external coupling rate κ . A convenient way to account for the external loss is to consider the Jaynes-Cummings Hamiltonian (2.42) with an extra non-Hermitian term $-i\kappa\hat{a}^\dagger\hat{a}$. The subspace spanned by states $|e0\rangle$ and $|g1\rangle$ is coupled to no other states [see Fig. 2.10 (a)] so we can write the non-Hermitian Hamiltonian in this subspace only, yielding

$$\frac{H_{\text{NH}}}{\hbar} = \begin{pmatrix} \Delta & g \\ g & -i\kappa \end{pmatrix}, \quad (2.52)$$

in the frame rotating at the resonator frequency. The real and imaginary parts of the eigenvalues of H_{NH}/\hbar correspond to the dressed state frequency and amplitude loss rate respectively. From this, a simple diagonalization of H_{NH} yield the Purcell decay rate

$$\begin{aligned} \Gamma_p &= \frac{\kappa}{2} \left(1 - \text{Re} \left[\sqrt{\left(1 + i\frac{2\Delta}{\kappa}\right)^2 - \left(\frac{4g}{\kappa}\right)^2} \right] \right) \\ &\simeq \frac{g^2}{\Delta^2} \kappa \quad \text{assuming } (4g)^2 \ll \kappa^2 + (2\Delta)^2, \end{aligned} \quad (2.53)$$

which is valid in the dispersive regime. The Purcell decay is proportional to κ and the square of the small parameter g/Δ .

However, some applications require large values of both g/Δ and κ to improve speed and fidelity, such as qubit readout [Jeffrey14, Walter17, Heinsoo18], photon transfer [Kurpiers18] or single photon detection [Besse18, Kono18] via the resonator. In this case the Purcell decay can dominate, but fortunately, it can be further suppressed by introducing a Purcell filter at the output of the resonator. For instance, let us consider the circuit shown in Fig. 2.12 (b), where the resonator is coupled with rate J to a Purcell filtering resonator of frequency ω_p and external coupling rate κ_f . In the limit where $J^2 \ll (\kappa_f/4)^2 + (\delta/2)^2$, the Purcell filter resonator can be adiabatically eliminated and the system considered as a qubit coupled to a single, effective resonator with effective output coupling rate [Sete15]

$$\kappa \simeq \left(\frac{2J}{\kappa_f} \right)^2 \kappa_f \frac{1}{1 + \left(\frac{2\delta}{\kappa_f} \right)^2}, \quad (2.54)$$

with δ the detuning between the resonator and the filter. This expression highlights the Lorentzian dependence of κ on δ with a full width at half maximum of κ_f . For a fixed bandwidth κ_f , κ is maximized when the resonator is inside the bandwidth of the filter, $|\delta| \ll \kappa_f$, and increases with the ratio J/κ_f .

Using the same non-Hermitian Hamiltonian method as above, one can derive the qubit Purcell decay rate [Sete15]

$$\gamma_P \simeq \frac{g^2 J^2 \kappa_f}{\Delta^4} \quad (2.55)$$

$$\simeq \underbrace{\left(\frac{\kappa_f}{2J} \right)^4}_{\text{suppression factor}} \left(\frac{\kappa}{2\Delta} \right)^2 \frac{g^2 \kappa}{\Delta^2}, \quad (2.56)$$

where the second line is obtained from the first one by expressing J and κ_f as functions of the effective resonator output coupling rate κ and the ratio J/κ_f . Comparing Eq. (2.56) to Eq. (2.53), we see that for a fixed effective resonator linewidth κ , the filter suppresses the Purcell effect by a factor $(\kappa_f/2J)^4 (\kappa/\Delta)^2 \ll 1$.

The suppression is more effective with higher detuning Δ , and higher J/κ_f ratio. For high J/κ_f ratio, the approximation used to derive the effective decay rate in Eq. (2.54) breaks down, and the effective decay rate is only given by the exact

expression [Sete14]

$$\kappa = \frac{\kappa_f}{2} \left(1 - \operatorname{Re} \left[\sqrt{\left(1 + i \frac{2\delta}{\kappa_f} \right)^2 - \left(\frac{4J}{\kappa_f} \right)^2} \right] \right),$$

As a conclusion, we would like to give the reader an intuitive picture of the Purcell effect using the language of classical filter theory. From the point of view of the qubit, in the absence of a Purcell filter, the resonator acts as a first order Lorentzian, band-pass filter centered at ω_r . The transmission of signals at the qubit frequency from the qubit to the output port is suppressed by a factor $(g/\Delta)^2$, which corresponds to 20 dB suppression per decade in Δ . In the presence of the Purcell filter, the qubit couples to the output through two filters in series, which act together as a second order bandpass filter. Transmission of signals at the qubit frequency from the qubit to the output port is therefore suppressed by a factor $g^2 J^2 / \Delta^4$, corresponding to 40 dB suppression per decade. Following this reasoning, using a n^{th} order bandpass filter behind the resonator, the Purcell effect should decrease exponentially with the filter order as $\propto \Delta^{-2(n+1)}$. By contrast, the resonator is in the bandpass of the filter. The output coupling rate of the resonator is therefore only limited by the filter linewidth. So arbitrarily large external coupling of the resonator can be obtained with arbitrarily low Purcell decay rate by employing higher order Purcell filters [Cleland19, Kim21, Chamberland20]. Alternatively, the Purcell effect can be also suppressed by using a bandstop filter before the output port, with the qubit (resonator) frequency being inside (outside) the stop band of the filter [Bronn15b, Bronn15a, Lescanne20].

2.1.7 Tunable light-matter interaction

The ability to exchange quantum states on-demand between two sub-elements of a circuit is a primary task of quantum information processing [Nielsen05]. This can be done in multiple ways by engineering the Jaynes-Cumming Hamiltonian. For instance, using a flux tunable qubit, the transition frequency can be tuned to switch between a resonant ($\Delta = 0$) and a dispersive ($|\Delta| \gg g$) Jaynes-Cummings interaction. This leads to Rabi oscillation between $|e, 0\rangle$ and $|g, 1\rangle$ around the time-varying Bloch vector $(g, 0, \Delta(t))$ [Mariantoni11a]. Control over more degrees of freedom of the resonator-qubit Bloch vector can be obtained using tunable-couplers [Yin13, Zhong19], parametric drives [Besse20a, Naik17, Leung19] or strong microwave drives [Leek09, Gasparinetti16, Zeytinoğlu15].

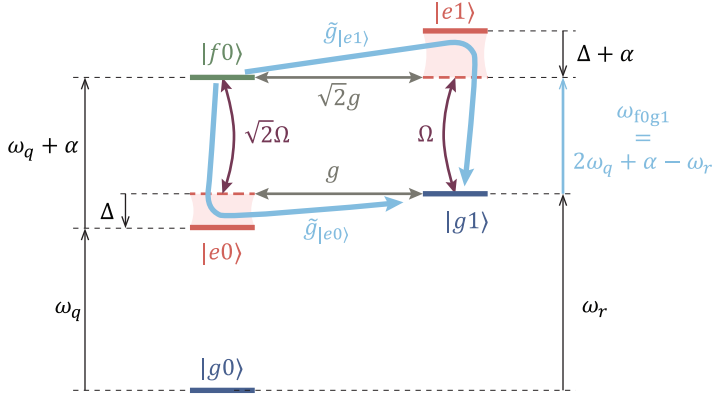


Figure 2.13 Energy level diagram of the transmon Jaynes-Cummings Hamiltonian under a drive resonant with the $f0$ - $g1$ transition. The qubit-resonator coupling terms, the transmon qubit drive coupling terms, and the two effective Raman coupling terms are represented by gray, purple and light blue arrows, respectively. The horizontal, dashed, red line represents the virtual $|e0\rangle$ and $|e1\rangle$ levels which are resonant with the drive and the qubit-resonator transverse coupling.

In the following, we will focus exclusively on one type of microwave-activated qubit-resonator interaction between states $|f, n\rangle$ and $|g, n+1\rangle$ [Zeytinoğlu15, Pechal14, Gasparinetti16, Rosenblum18], which has been used in all experiments presented in this thesis [Kurpiers18, Magnard18, Magnard20]. When applying a microwave tone of carrier frequency $\omega_{f0g1} = 2\omega_q + \alpha - \omega_r$ on the transmon qubit, one effectively drives the g - e transition with rate Ω detuned by $\Delta + \alpha$ and the e - f transition with rate $\sqrt{2}\Omega$ detuned by Δ (purple arrows in Fig. 2.13). In addition, the coupling term of the Jaynes-Cummings Hamiltonian (2.42) can effectively be seen as drives acting on the $e0$ - $g1$ and $f0$ - $e1$ transitions, with rates g and $\sqrt{2}g$ detuned by Δ and $\Delta + \alpha$, as indicated by the gray arrows in Fig. 2.13. The Hamiltonian therefore presents two simultaneous Raman transitions between states $|f0\rangle$ and $|g1\rangle$, going through the intermediate state $|e0\rangle$ and $|e1\rangle$, respectively, as indicated by the light blue arrows in Fig. 2.13. Focusing on the first Raman transition (via $|e0\rangle$), in the limit where $\sqrt{2}\Omega, g \ll |\Delta|$, the intermediate level $|e0\rangle$ can be eliminated adiabatically and the Hamiltonian simplifies to a single coupling term [Gerry90, Alexanian95, Wu97]

$$\hat{H}_{\text{Ram},|e0\rangle} = \tilde{g}_{|e0\rangle} |f0\rangle \langle g1| + h.c.,$$

with $\tilde{g}_{|e0\rangle} = \frac{\sqrt{2}\Omega 2g}{2\Delta}$.

Similarly, the adiabatic elimination on the second Raman transition (via $|e1\rangle$) leads to an effective coupling term

$$\hat{H}_{\text{Ram},|e1\rangle} = \tilde{g}_{|e1\rangle} |f0\rangle \langle g1| + h.c.$$

$$\text{with } \tilde{g}_{|e1\rangle} = \frac{\sqrt{2}\Omega 2g}{2(-\Delta - \alpha)}.$$

Adding the coupling terms of both Raman path, and rewriting $|f0\rangle \langle g1| \rightarrow \hat{b}^\dagger \hat{b}^\dagger \hat{a}$, we obtain a single effective coupling term [Zeytinođlu15]

$$\hat{H}_{f0g1} = \tilde{g} \hat{b}^\dagger \hat{b}^\dagger \hat{a} + h.c.$$

$$\text{with } \tilde{g} = \tilde{g}_{|e0\rangle} + \tilde{g}_{|e1\rangle} = \Omega \frac{g\alpha}{\sqrt{2}\Delta(\Delta + \alpha)}.$$

Driving the transmon at the $f0$ - $g1$ transition frequency therefore induces Rabi oscillation between state $|f, n\rangle$ and $|g, n+1\rangle$. The drive rate $\sqrt{n}\tilde{g}$ of this transition is proportional to the complex amplitude Ω of the qubit drive, and the effective detuning is set by the qubit drive frequency. Therefore, all three components of the Bloch vector can be controlled in time with a single microwave drive. Because for each Raman transition, one of the coupling term stems from the transverse qubit-resonator coupling, we call this $f0$ - $g1$ transition a *cavity-assisted Raman transition* [Zeytinođlu15, Alexanian95]. The conditions for the validity of the adiabatic elimination lead to $\tilde{g} \ll \Omega, |\alpha|$. Therefore $f0$ - $g1$ drive rate is more than an order of magnitude smaller than the transmon qubit anharmonicity α and the transmon drive rate Ω , as expected from the second-order nature of this transition.

The off-resonant qubit drive will also lead to an ac-Stark shift of the qubit, (see Sec. 2.1.4). In the limit $\Omega \ll \Delta$, one can approximate the $f0$ - $g1$ drive induced ac-Stark shift with

$$\Delta_{f0g1}(\Omega) \simeq \Omega^2 \frac{\alpha(2\Delta + \alpha)}{\Delta(\Delta^2 - \alpha^2)}, \quad (2.57)$$

by adding the ac-Stark shift $\Omega^2/(\Delta + \alpha)$ induced by the g - e drive term on state $|g\rangle$ and the opposing ac-Stark shifts $2\Omega^2/\Delta$ and $3\Omega^2/(\Delta - \alpha)$ induced by the e - f and f - h drive terms on state $|f\rangle$. The ac stark shift is a quadratic and decreasing function of the drive amplitude Ω , in the typical case where $|\alpha| < |\Delta|$ and $\alpha < 0$.

2.1.8 Remote entanglement generation

Photon shaping schemes

Such a tunable light-matter coupling can be used in conjunction with the output coupling of the resonator to emit itinerant photons with precisely defined quantum state and envelope inside the output transmission line [Pechal14, Pfaff17, Morin19]. For instance, as shown by M. Pechal *et al.* [Pechal14] this can be done by first initializing the transmon qubit in state $|f\rangle$ and applying a strong drive on the $f0$ - $g1$ transition with precise shape. As shown in [Morin19] and in appendix B, it is possible to emit a fraction $a^2 \leq 1$ of a photon with arbitrary real amplitude time-envelope $f(t)$ and detuning $\delta(t)$ from the resonator frequency by driving the $f0$ - $g1$ transition with the time-dependent complex drive rate $\tilde{g} \exp[-i\varphi]$ of amplitude and instantaneous frequency

$$\tilde{g}(t) = \sqrt{\frac{(\dot{f} + \frac{\kappa}{2}f)^2 + (\delta f)^2}{\kappa(\frac{1}{a^2} - F_2) - f^2}},$$

$$\dot{\varphi} = \omega_{f0g1}(\tilde{g}) + \frac{\delta}{\kappa(\frac{1}{a^2} - F_2) - f^2} \left(f^2 + \frac{f\ddot{f} - \dot{f}^2}{\tilde{g}^2} \right).$$

Here we constrain the photon envelope to have unit \mathcal{L}_2 norm

$$\int_{-\infty}^{+\infty} f^2(t) dt = 1$$

and introduced the short notation

$$F_2(t) := \int_{-\infty}^t f^2(\tau) d\tau.$$

The quantity $a^2 F_2(t)$ is the fraction of a photon which has been emitted at time t . We account for ac-Stark shifts induced by the strong $f0$ - $g1$ drive with the drive-amplitude-dependent $f0$ - $g1$ resonant frequency $\omega_{f0g1}(\tilde{g})$ [Pechal14, Zeytinoğlu15, Kurpiers18, Magnard18], see also Eq. (2.57). Any photon shape f can be emitted under the constraint that \tilde{g} does not diverge, *i.e.*

$$\forall t \in \mathbb{R}, \quad \kappa(1 - a^2 F_2) > a^2 f^2,$$

whose physical meaning is that, at any time t , the power $a^2 f^2$ of the emitted photon cannot be bigger than the resonator external coupling rate κ times the amount of

excitation $1 - a^2 F_2$ left in the transmon-resonator system.

Using this formula, it is possible to emit single photons ($a^2 = 1$) with time-symmetric envelope $f(t) = f(-t)$, such as $f \propto \cos(\Gamma t/2)$ [Pechal14], or $f \propto \text{sech}(\Gamma t/2)$ [Kurpiers18, Magnard20]. This case is particularly interesting, because it gives a simple mean to absorb the itinerant wavepacket with unit fidelity, when it impinges on a second, identical chip. Indeed, as pointed out by I. Cirac *et al.* in 1997 [Cirac97] and illustrated in Fig. 2.14 (a), from the point-of-view of the receiving chip, absorbing a quantum wavepacket with time-envelope $f(t)$ is simply the time-reversed problem of emitting the same wavepacket with envelope $f(-t) = f(t)$. In principle, qubit B can therefore absorb the incoming photon with unit fidelity by applying the time-dependent drive of amplitude $\tilde{g}(-t)$ and instantaneous frequency $\dot{\varphi}(-t)$.

Such a photon shaping technique was used in three landmark experiments by P. Kurpiers, P. Magnard *et al.* [Kurpiers18], C. Axline, L. Burkhardt, W. Pfaff *et al.* [Axline18], and P. Campagne-Ibarcq, E. Zalys-Geller *et al.* [Campagne-Ibarcq18], to demonstrate the first fully deterministic protocols to transfer qubit states and generate entanglement between physically remote qubits. All three experiments were carried out at the same time, but used a different type of light-matter coupling scheme. Our demonstration, whose setup is illustrated in Fig. 2.14 (b), made use of the $f0$ - $g1$ transition and photon shaping method presented above to perform the following map

$$|g0\rangle \mapsto |g0\rangle, \quad |e0\rangle \mapsto |e0\rangle, \quad \text{and} \quad |f0\rangle \mapsto |g1\rangle \quad (2.58)$$

where the first and second labels in $|k, n\rangle$ denote the transmon qubit state, and the state of the itinerant photon in the mode of envelope f [see Fig. 2.14 (a) and Fig. 2.15 (a)]. The absorption process is simply the reverse of Eq. (2.58). Using these maps, it is possible to transfer any qubit state from qubit A to qubit B by initializing qubit B in $|g\rangle$, applying an e - f π pulse and an emission pulse on qubit A, absorbing the incoming photon with a matched absorption pulse and applying a final e - f π pulse on qubit B [Fig. 2.15 (b,c)]. Indeed, such a sequence of pulse maps $|gg\rangle$ to $|gg\rangle$, and $|eg\rangle$ to $|ge\rangle$. Similarly, by preparing qubit A in $(|e\rangle + |f\rangle)/\sqrt{2}$ and qubit B in $|g\rangle$, then applying the emission and absorption pulses, followed by a final e - f π pulse on qubit B, one can in principle obtain the pure Bell state $|\Psi^+\rangle = (|ge\rangle + |eg\rangle)/\sqrt{2}$ [Fig. 2.15 (d,e)].

Accounting for errors which arise from finite qubit coherence and the finite probability $(1 - \eta_A)$ that the photon is either not emitted, or lost while travelling from chip A to chip B, or not absorbed by qubit B, the joint state shared by the two qubits is of

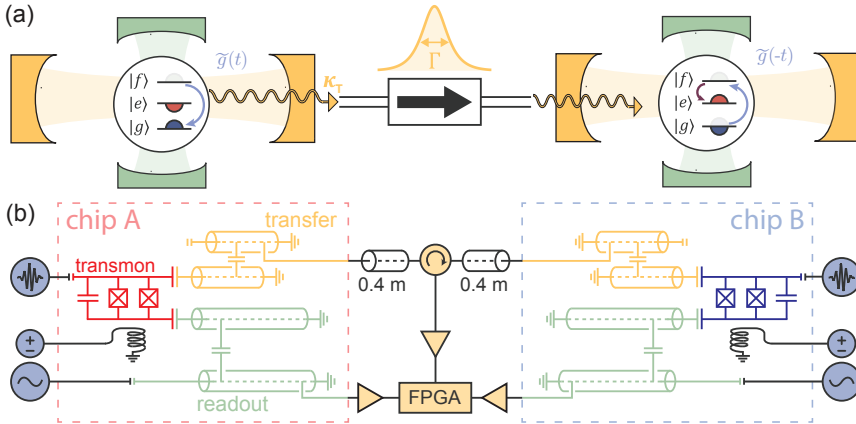


Figure 2.14 (a) Quantum optical schematic of a deterministic unidirectional entanglement protocol between two cavity QED nodes of a quantum network. At the first node, a three-level system is prepared in its second excited state $|f\rangle$ (grey half-circle) and coherently driven ($\tilde{g}(t)$, blue arrow) to $|g\rangle$ (blue half-circle) creating the transfer cavity field $|1\rangle$ (light yellow). The cavity field couples into the directional quantum channel with rate κ_T as a single photon wavepacket of bandwidth Γ (yellow hyperbolic secant shape). In the second quantum node, the time reversed drive $\tilde{g}(-t)$ transfers the excitation from $|g\rangle$ to $|f\rangle$ in the presence of the transferred photon field $|1\rangle$. Finally, the protocol is completed with a transfer pulse between $|f\rangle$ and $|e\rangle$ (red half-circle) to return to the qubit subspace. Additionally, each three level system is coupled to a readout cavity (green). (b) Implementation of the system depicted in (a) in a planar, chip-based, circuit QED architecture. At each node, a transmon (red and blue) is capacitively coupled to two $\lambda/4$ coplanar waveguide resonators and Purcell filter circuits [Walter17] acting as the transfer (yellow) and readout (green) cavities, respectively. The output transmission lines are galvanically coupled to the corresponding circuit. A directional quantum channel is realized using a semi-rigid coaxial cable and circulator connecting to the output port of the transfer circuit Purcell filter at each node. Figure adapted from [Kurpiers18], see reference for more details.

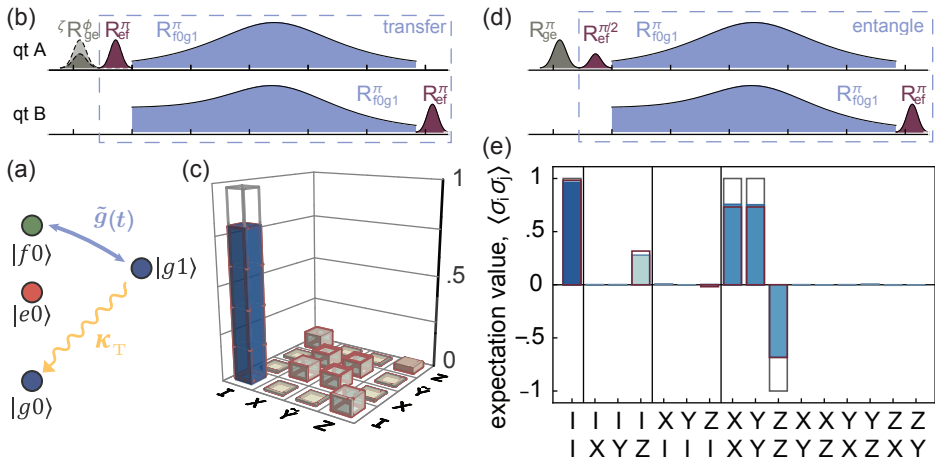


Figure 2.15 (a) Energy level diagram of the qutrit-transfer resonator system. The blue arrow indicates the f - g_1 drive, and the yellow arrow represents the resonator coupling to the waveguide. (b) Pulse scheme used to transfer a qubit state from qubit A to qubit B. (c) Absolute value of the process matrix χ of the qubit state transfer. (d) Pulse scheme used to generate entanglement. (e) Expectation value of the Pauli operators of the resulting two-qubit entangled state. In (c) and (e), the solid blue bars, the red wireframes and the gray wireframes indicate the measured, the simulated and the ideal values, respectively. Figure adapted from [Kurpiers18], see reference for more details.

the form

$$\rho_{AB} = \frac{\nu}{2} \begin{pmatrix} 2 - (\eta_A + \eta_B) & 0 & 0 & 0 \\ 0 & \eta_A & \mathcal{V}\sqrt{\eta_A\eta_B} & 0 \\ 0 & \mathcal{V}\sqrt{\eta_A\eta_B} & \eta_B & 0 \\ 0 & 0 & 0 & 0 \end{pmatrix}, \quad (2.59)$$

where η_B results from decay of qubit B, $\mathcal{V} < 1$ results from dephasing, and $\nu \leq 1$ is the fraction of the population that has not leaked to higher levels of the transmon qubits. Such a leakage to higher levels can for instance happen due to decay from $|f\rangle$ to $|e\rangle$ before the final e - f pulse on qubit B, and is witnessed in the fact that $\langle II \rangle < 1$ in Fig. 2.15 (e). Using this parametrization, the fidelity to the target state,

$$\langle \Psi^+ | \rho_{AB} | \Psi^+ \rangle = \frac{\nu}{4} (\eta_A + \eta_B + 2\mathcal{V}\sqrt{\eta_A\eta_B}),$$

is proportional to ν , decreases with increasing photon and qubit loss η_A and η_B and decreases with the coherence term \mathcal{V} .

To characterize the amount of entanglement, it is convenient to calculate the concurrence, which is defined for 2×2 states as

$$\mathcal{C}(\rho_{AB}) = \max[0, \lambda_1 - \lambda_2 - \lambda_3 - \lambda_4],$$

where λ_i are the eigenvalues of

$$\sqrt{\sqrt{\rho_{AB}}(\sigma_y \otimes \sigma_y)\rho_{AB}^*(\sigma_y \otimes \sigma_y)\sqrt{\rho_{AB}}},$$

in increasing order, and ρ_{AB}^* is the conjugate of ρ_{AB} when expressed in the standard basis [Wootters98]. Indeed, the concurrence is an increasing function of the entanglement of formation [Bennett96b], is 0 for separable states, non-zero for entangled states, and 1 for maximally entangled states: it is therefore a measure of entanglement of its own [Hill97]. For states ρ_{AB} of the form of Eq. (2.59), the concurrence is simply given by two times the off-diagonal term of ρ_{AB}

$$\mathcal{C}(\rho_{AB}) = \nu\mathcal{V}\sqrt{\eta_A\eta_B}. \quad (2.60)$$

As long as ν , \mathcal{V} , η_A and η_B are non-zero, the concurrence is above 0 and the state is genuinely entangled.

In Refs. [Kurpiers18, Axline18, Campagne-Ibarcq18], the fidelity to the target Bell state is on the 80% level. The dominant source of error comes from $\eta_A \sim 0.7$, where

$\sim 10\%$ infidelity comes from qubit decay during the protocol, and $20 - 25\%$ comes from photon loss in the transmission line, which includes $10 - 15\%$ insertion loss from the circulator used to make the transfer line unidirectional.

Resonant mode schemes

To reduce photon loss and improve the protocol's fidelity, N. Leung, Y. Lu *et al.* [Leung19] developed an alternative scheme which bypasses the need for a lossy circulator in between the two chips. Without a circulator, the transfer transmission line behaves like a lossy multi-mode resonator with free-spectral range

$$\text{FSM} = v_p/2l \simeq 100 \text{ MHz},$$

for a length $l \simeq 1 \text{ m}$ of transfer line. If the transfer resonators have matched frequencies, they hybridize in a mode which has zero amplitude in the lossy cable mode. The authors then used a parametric drive-based tunable light-matter coupling scheme to transfer excitations from qubit A to qubit B via the shared, low-loss mode, and generate entanglement with this scheme [Leung19]. Following the idea of [Leung19], several circulator-free schemes were developed, where an excitation can be transferred via a low-loss mode of the transfer line. Concomitant efforts to reduce loss, *e.g.* by using low-loss superconducting cables connected directly to the chip, bypassing lossy connectors and printed-circuit boards, further improved the fidelity to the 90% level [Burkhart21, Zhong21]. Alternatively, it is possible to avoid populating the lossy bus mode using stimulated Raman adiabatic passage [Chang20] or far-detuned Raman transition [Burkhart21]. We refer to this category of schemes as *resonant-mode* quantum communication protocols.

Higher fidelities can be achieved in both photon-shaping and resonant-mode schemes by detecting photon loss errors, using either a time-bin [Kurpiers19b] or a bosonic encoding [Axline18, Burkhart21]. Note that, in all remote entanglement schemes which we have presented in this section, the entangled state can be well parametrized as Eq. (2.59) with $\eta_A < \eta_B \sim 1$, up to local basis changes. This parametrization is therefore a useful tool to understand the limitations of each protocol which we will re-use throughout this thesis.

Effect of bus length

In general, resonant-mode schemes are more favorable than photon-shaping schemes when the bus length l is less than a few meters. In this regime, high coupling rates to the mode can be achieved, without being limited by the free-spectral range of the transfer line. In addition, the absence of a circulator decreases the photon loss and allows bi-directional communication. Finally, unlike photon-shaping schemes, resonant-mode schemes do not necessarily require frequency matching of the transfer resonators, or complex calibration of the control-pulse shape.

However, for larger lengths l , the speed of resonant-mode protocols might be limited by the low free-spectral range of the bus, because only one mode should be utilized. By contrast, the duration of photon-shaping methods just increases by the propagation delay $\tau_{AB} = l/v_p$. Moreover, because no emitted field can come back to the emitter for a time $2\tau_{AB}$, the transfer line can be considered as a Markovian environment for this duration even in the absence of a circulator. Therefore, photon shaping schemes could in principle work the same way, with or without a circulator, as long as l is large enough for $2\tau_{AB}$ to be longer than the emission duration.

2.2 Bell test with Superconducting circuits

In the previous section, we have discussed how superconducting circuits could be used to process quantum information. In particular, we have shown how these circuits can be used to generate entangled states between physically remote quantum bits, which can be locally measured along any Pauli observable. Therefore, a natural direction is to use such remote entangled states to verify the “spooky action at a distance” experienced by one of the qubits when the other one is measured locally [Einstein35, Eintein71] by carrying out the experimental test proposed by John Bell for this purpose [Bell64]. In this section we describe what a Bell test is and how to perform one with superconducting circuits, following closely the review from N. Brunner *et al.* on the topic [Brunner14]. We first give an introduction to the formalism of Bell tests, give the definition of a local-hidden variable theory within this framework, and explain how this class of theories can be rejected experimentally by quantum mechanics with a Bell test. We then discuss loopholes in experimental Bell tests and the ways to close them. Then we work out useful formulas to quantify the expected violation of the Clauser-Horne-Shimony-Holt (CHSH) inequality [Clauser69], based on a realistic set of experimental error channels. Finally, we conclude this chapter by

summarizing the requirements which need to be fulfilled to perform a loophole-free Bell test with superconducting circuits, and the subsequent constraints these requirements put on the experimental setup. This last subsection serves as an outline to this thesis.

2.2.1 Bell test formalism

In a Bell experiment, we consider two physically separate parties, named Alice and Bob, which can interact before each measurement run [Fig. 2.16 (a)]. This "interaction" can take any form, such as communicating classical information, sharing a joint quantum state, or more generally do anything which could correlate future behaviors of Alice and Bob. At the beginning of a measurement run, all interactions between the parties are cut, and each party receives a classical input, x for Alice, and y for Bob, which is not to be communicated to the other party before the end of the measurement run. After a time Δt , each party locally returns an output, a for Alice and b for Bob, and interaction can resume. A Bell experiment estimates the probability $p(ab|xy)$ that Alice and Bob return the answer (a, b) , for a given input pair (x, y) . Many Bell scenarios can be considered depending on the number of possible values which can be taken by the inputs x and y , and the outputs a and b . Also, more than two parties can

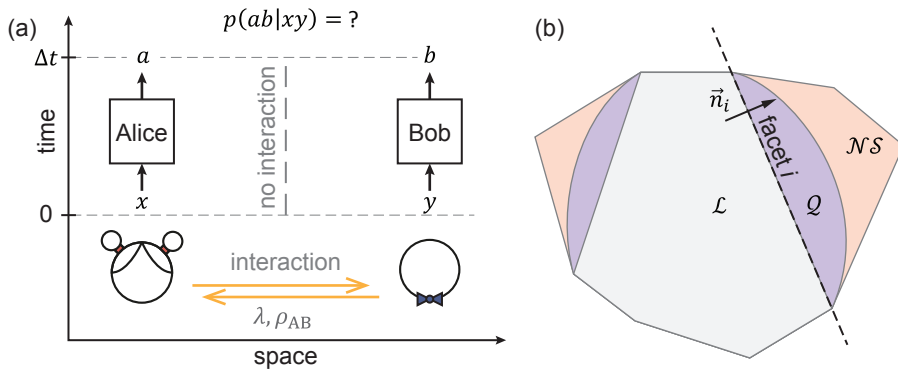


Figure 2.16 (a) Illustration of a generic Bell test experiment. Two physically separate parties, Alice and Bob, are represented by physically separated black-boxes each receive an input at time $t = 0$, and returning a classical output at time Δt to estimate the probabilities $p(ab|xy)$. The yellow arrows represent the interaction taking place before each measurement run. (b) Illustration of the convexity and strict inclusion of the local set \mathcal{L} (gray), the quantum set \mathcal{Q} (purple) and the non-signaling set \mathcal{NS} (red) to which the vector \vec{p} must belong, as well as the polytopic geometry of \mathcal{L} and \mathcal{NS} . The dashed line represents a facet of \mathcal{L} .

be considered to form a generalized multipartite Bell experiment [Brunner14]. We will focus exclusively on the bipartite, binary-input, binary-output scenario, where x and y take values in $\{0, 1\}$ and a and b in $\{-1, 1\}$. In this setting, the vector \vec{p} , whose 16 elements are the probabilities $p(ab|xy)$, evolves in the set \mathcal{P} defined by the positivity constraint

$$\forall a, b, x, y \quad p(ab|xy) \geq 0, \quad (2.61)$$

and the normalization constraints

$$\forall x, y \quad \sum_{a,b} p(ab|xy) = 1,$$

of probabilities. Because the 4 normalization constraint are linear, \mathcal{P} is included in a 12 dimensional subspace.

Mathematically, the constraint that the inputs are not communicated to the other party before the latter gives an output can be formalized as [Brunner14]

$$\begin{aligned} \forall b, y, x, x' \quad p(b|xy) &:= \sum_a p(ab|xy) = \sum_a p(ab|x'y) =: p(b|x'y) \\ \text{and } \forall a, x, y, y' \quad p(a|xy) &:= \sum_b p(ab|xy) = \sum_b p(ab|xy') =: p(a|xy'). \end{aligned} \quad (2.62)$$

In words, eqs. (Eq. (2.62)) states that the output a of Alice cannot be influenced by the input y asked to Bob (first line), and *vice versa* (second line). This means that no information can be communicated between the two parties during a single run of the Bell test. The *non-signaling* set \mathcal{NS} , defined as the set of points following constraints (2.62) is 8-dimensional and is strictly included in \mathcal{P} .

A tighter constraint can be obtained by assuming that the two parties live in a physical world governed by quantum mechanics. In this case, there must exist two Hilbert spaces \mathcal{H}_A and \mathcal{H}_B , each of dimensions greater than one, a quantum state ρ_{AB} of the joint Hilbert space $\mathcal{H}_A \otimes \mathcal{H}_B$, such that for any x, y , there exists measurement operators $M_{a|x}$ and $M_{b|y}$ [positive operator valued measure (POVM) elements] acting on \mathcal{H}_A and \mathcal{H}_B , which satisfy the relation

$$p(ab|xy) = \text{Tr}(\rho_{AB} M_{a|x} \otimes M_{b|y}). \quad (2.63)$$

The *quantum* set \mathcal{Q} is defined by constraint (2.63).

Finally, a general definition of a local-hidden variable (LHV) models can be given in terms of a constraint on \vec{p} . Indeed, in a LHV model, the output of one party should

not have any causal influence on the output of the other party. However, they can be correlated via their dependence on past classical events, which we group in the local hidden variable λ . Mathematically, the independence of a and b given a common hidden variable reads

$$p(ab|xy\lambda) = p(a|x\lambda)p(b|y\lambda) \quad (2.64)$$

Averaging over all possible values of λ , we obtain the constraint

$$p(ab|xy) = \int_{\mathcal{L}} p(a|x\lambda)p(b|y\lambda)q(\lambda)d\lambda, \quad (2.65)$$

which defines the *local* set \mathcal{L} , and where $q(\lambda)$ is the unknown probability density function of λ .

One can show that the non-signaling, the quantum and the local sets have the same number of dimensions [Pironio05], are all closed and convex [Pitowsky86], and follow a strict inclusion rule [Khalfin85, Popescu94, Rastall85]

$$\mathcal{L} \subsetneq \mathcal{Q} \subsetneq \mathcal{NS},$$

as illustrated in Fig. 2.16 (b).

The second inclusion has a profound meaning: if quantum mechanics is non-signalling, it prevents distant parties from communicating information without further interaction, even if they share an entangled state. A direct consequence is that superluminal communications cannot occur in a world governed by quantum mechanics: quantum mechanics is compatible with special relativity. The first inclusion might have an even more profound impact. It implies that, in a quantum world, it is possible to perform a Bell experiment where \vec{p} is incompatible with any LHV model. This can be used to experimentally refute all LHV theories. We will discuss how in the next paragraph.

Let \vec{p}_Q be a vector of \mathcal{Q} outside of \mathcal{L} . Because \mathcal{L} is closed, bounded and convex, invoking the hyperplane separation theorem [Boyd04], we can find a vector \vec{n} and a threshold value t such that

$$\forall \vec{p} \in \mathcal{L}, \vec{n} \cdot \vec{p} \leq c, \quad \text{and} \quad \vec{n} \cdot \vec{p}_Q > c. \quad (2.66)$$

Such a relation defines a Bell inequality, which must hold true for LHV models, but can be violated by a quantum mechanical setting. A Bell test is then a statistical null-hypothesis rejection test, with null hypothesis \mathcal{H}_0 : “*reality can be explained by a LHV*”

model". To reject this hypothesis, one prepares the shared state ρ_{AB} , and measure it's sub-system locally with operators $M_{a|x}$ and $M_{b|y}$ chosen such that $\vec{p} = \vec{p}_q$, runs the same experiment N times, and estimate the quantity $\bar{S} = \vec{n} \cdot \vec{p}_q$ with the average estimators

$$\bar{p}_{\square}(ab|xy) := \frac{N_{xyab}}{N_{xy}},$$

where $N_{xy(ab)}$ denotes the number of runs with inputs (and outputs) x, y (a, b). From the central limit theorem, assuming that the measurement runs are independent and identically distributed (i.i.d.), the probability law of \bar{S} is well approximated by a Gaussian law of mean $S := \vec{n} \cdot \vec{p}_q > c$ and variance s^2/N , with s^2 the variance of S for a single run of the Bell test. Suppose we observe $\bar{S} = c + \varepsilon$ with $\varepsilon > 0$, the probability that the outcome of \bar{S} is bigger than what is observed under the null hypothesis \mathcal{H}_0 is bounded by the *P-value*, formally defined as

$$\begin{aligned} P\text{-value} &:= \max_{\mathcal{H}_0} P(\bar{S} \geq c + \varepsilon | \mathcal{H}_0) \\ &\simeq \frac{1}{2} \operatorname{erfc} \left(\frac{\varepsilon \sqrt{N}}{s \sqrt{2}} \right) \\ &< \frac{1}{\sqrt{2\pi}} \frac{s}{\varepsilon \sqrt{N}} \exp \left[-\frac{1}{2} \frac{\varepsilon^2 N}{s^2} \right], \end{aligned} \tag{2.67}$$

and informally defined as the highest probability that a random variable compatible with LHV model violates the Bell inequality by a value equal or more extreme than that observed. The lower the *P-value*, the more confidently we can reject the null hypothesis. The approximate equality in Eq. (2.67) stems from the central limit theorem, and the last inequality originates from the asymptotically tight upper bound to the complementary error function erfc . Because the *P-value* tends towards zero for large N , the finite violation of a Bell inequality can in principle reject LHV theories with arbitrarily high statistical confidence.

The local set has other useful properties. First, it can be shown that the set of quantum correlations obtained from a separable state $\rho_{AB} = \rho_A \otimes \rho_B$ is included in \mathcal{L} [Brunner14]. The direct consequence is that a Bell inequality can be violated only if the shared quantum state ρ_{AB} is entangled. The reverse however is not true [Verstraete02, Hyllus05]. Second, \mathcal{L} can be shown to be a polytope: a closed, convex set whose boundaries are flat facets [Brunner14], as illustrated in Fig. 2.16 (b). According to Minkovski's theorem, \mathcal{L} can therefore be equivalently defined by a minimal and finite

set of Bell inequalities, known as *facet inequalities*

$$\vec{p} \in \mathcal{L} \iff \forall i \in \mathcal{J}, \quad \vec{n}_i \cdot \vec{p} \leq c_i, \quad (2.68)$$

where \mathcal{J} is the finite set of facets of \mathcal{L} , \vec{n}_i is the normal vector of facet i pointing outwards, and b_i are real numbers [see Fig. 2.16 (b)]. Facets inequalities are tight Bell inequalities, in the sense that they are the minimal set of inequalities which define \mathcal{L} . By symmetry, a facet inequality is transformed into another facet inequality under any combination of the permutations $a \rightarrow -a$, $b \rightarrow -b$, $x \rightarrow (1-x)$, $y \rightarrow (1-y)$, $a \leftrightarrow b$ and $x \leftrightarrow y$. Such permutation relations define equivalence classes of Bell inequalities.

In the following, each Bell inequality will implicitly refer to its equivalence class. Also, some facets, called *trivial* facets, are shared between the local and quantum sets, *i.e.* their corresponding Bell inequalities also bound the quantum set and cannot be used to refute LHV models experimentally. A simple example of such a *trivial* facet is the facet defined by the positivity constraint (2.61) of $p(ab|xy)$.

A particularly well studied class of facet inequality is the Claude-Horne-Shimony-Holt (CHSH) inequality [Clauser69],

$$S_{\text{CHSH}} := \langle ab \rangle_{00} + \langle ab \rangle_{01} + \langle ab \rangle_{10} - \langle ab \rangle_{11} \leq 2, \quad (2.69)$$

where we introduced the correlators $\langle ab \rangle_{xy} := \sum_{ab} ab p(ab|xy)$. In fact, M. Froissart and A. Fine showed in independent works that in a bi-partite, binary-input, binary-output Bell scenario, the CHSH inequality is the only non-trivial facet inequality [Froissart81, Fine82], which means that any non-local quantum state must violate a CHSH inequality. This inequality, which can be easily proven from Eq. (2.65), is maximally violated when using the pure singlet Bell state

$$|\Psi^-\rangle := \frac{1}{\sqrt{2}} (|01\rangle - |10\rangle),$$

between Alice and Bob [Fig. 2.19 (a)]. Let the input x correspond to the measurement axis $\vec{x} \in \mathbb{R}^3$ associated to the observable $\vec{x} \cdot \vec{\sigma}$, and equivalently for y . Then a simple calculation yields $\langle ab \rangle_{xy} = -\vec{x} \cdot \vec{y}$, from which one can show that S_{CHSH} is maximized when

$$\vec{x}_0 = \vec{e}_0, \quad \vec{x}_1 = \vec{e}_1, \quad \vec{y}_0 = -(\vec{e}_0 + \vec{e}_1)/\sqrt{2}, \quad \text{and} \quad \vec{y}_1 = (\vec{e}_1 - \vec{e}_0)/\sqrt{2},$$

where \vec{e}_0 and \vec{e}_1 can be any pair of orthonormal vectors in \mathbb{R}^3 . Such an optimal configu-

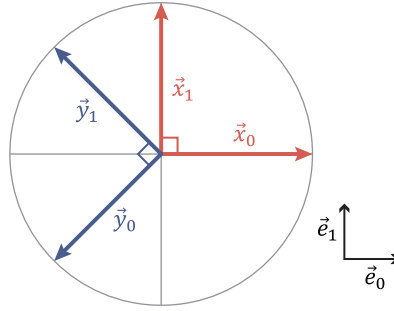


Figure 2.17 Measurement axes leading to a maximal violation of the CHSH inequality for $\rho_{AB} = |\Psi^-\rangle\langle\Psi^-|$. Here, \vec{e}_0 and \vec{e}_1 are two orthonormal vectors of \mathbb{R}^3 defining a plane cut in the Bloch sphere.

ration of measurement axes is represented in a 2D cut of the Bloch sphere in Fig. 2.17. Then we have $\langle ab \rangle_{00} = \langle ab \rangle_{01} = \langle ab \rangle_{10} = 1/\sqrt{2}$ and $\langle ab \rangle_{11} = -1/\sqrt{2}$, which leads to

$$S_{\text{CHSH}} = 2\sqrt{2} \simeq 2.828 > 2.$$

which saturates the quantum bound for CHSH type inequalities [Cirel'son80].

We have seen that a Bell inequality can only be violated if the joint state is entangled. In fact, the amount of CHSH violation gives a lower bound on the degree of entanglement of the joint state ρ_{AB} . Franck Verstraete and Michael Wolf showed that the CHSH value S gives a lower bound to the concurrence [Verstraete02]

$$\mathcal{C}(\rho) \geq \sqrt{\left(\frac{S}{2}\right)^2 - 1} \quad \text{for } S > 2.$$

This lower bound reaches 1 for $S = 2\sqrt{2}$, so reaching the CHSH quantum bound certifies that the joint state was maximally entangled.

The key aspect of the Bell test formalism is its agnosticism to hardware and theory: no assumption other than the null hypothesis is made on the the internal working principle of the two parties, or on the physical theory which governs reality. Instead, the two parties are treated as black-boxes, and a statistical analysis of their binary inputs and outputs suffices to reject entire classes of physical theory. Thanks to this agnosticism, Bell tests can be used to certify entanglement [Verstraete02, Bowles18, Arnon-Friedman19], secure communication [Mayers98, Barrett05, Pironio09, Vazirani14, McKague09, Arnon-Friedman18, Murta19] or randomness [Colbeck12, Nieto-Silleras14],

even when the experiment relies on untrusted devices, a property also known as *device independence* [Gallego10].

However, systematic errors, which can arise in an experimental setup without being noticed by the experimentalist, can significantly change the conclusions of a Bell test. For instance, cross-talk between the devices generating the input on one side, with the one generating the output on the other side can lead to a violation of the locality constraint (2.62), which could lead to a violation of Bell inequalities in a LHV model. So in practice, systematic errors lead to experimental loopholes, which should be all closed with a rigorous treatment. We will discuss the various loopholes which can arise in a Bell test in the following subsection.

2.2.2 Loopholes

To derive the condition defining the local set \mathcal{L} , and thus all Bell inequalities which stem from it, the following assumptions need to be valid: (i) Alice's output cannot be influenced by Bob's input, and vice versa, (ii) there is only two possible outcomes per party for each measurement run. However, most experimental setups cannot guarantee that these two conditions are met, without requiring extra assumptions on the inner workings of the device in addition to \mathcal{H}_0 . Making such an extra assumption breaks the agnosticity of the Bell test, and is said to open a *loophole*. Here we will describe the four main loopholes and the way they can be closed experimentally. Other loopholes, such as the coincidence loophole and the coincidence-postselection loophole, can be considered as particular cases of the four main ones. We will therefore not discuss them. The interested reader may find a complete discussion on loopholes in Bell tests in [Larsson14].

The freedom-of-choice loophole

In a practical experiment, the inputs x and y given to Alice and Bob at each run need to be generated by a physical setup. For assumption (i) to hold, one needs to assure that these numbers cannot be part of the LHV λ . To that end, Weihs *et al.* used quantum random number generators (QRNG) at each site to generate the input [Weihs98]. Then, because the inputs are generated at random, they are fully uncorrelated with both λ and the output of the remote party. This was considered as the first experiment to conclusively tackle this loophole, however without fully closing it. Indeed this reasoning still relies on a physical description and theory of the random number generators. If one assumes that physics is described by a LHV model, then so

do the QRNGs and one cannot affirm that the generated numbers are not correlated with λ without further assumptions.

Several other propositions were made to close this *freedom-of-choice* loophole [Scheid110]. One idea consists of choosing the input settings based on very remote sources of randomness, such as light emitted from stars or quasars at the opposite side of the universe. In such a setting, the LHV could still fake quantum correlations, but to influence or guess x and y , it would need to do it when the past light-cones of the randomness sources crossed each other, years, or billions of years in the past [Vaidman01, Larsson14]. This idea was implemented recently in two independent experiments by Rauch *et al.* [Rauch18] and Li *et al.* [Li18]. In such a case, an LHV model would need to “*conspire on the galactic scale*” to produce non-local correlations in a Bell test [Vaidman01]. It is *super-deterministic* in the sense that all events are included in λ , even those that appear truly random and occur very far in the future [Bell85, Brans88]. However, superdeterminism is in contradiction with an essential axiom of Physics: the idea that reality is governed by universal laws [Bell85]. A consequence is that superdeterminism cannot be tested. One can therefore argue that superdeterminism is not a Physical theory *per se*, and close the freedom-of-choice loophole by rejecting superdeterministic LHV models based on this philosophical reasoning [Bell85, Larsson14].

A third alternative is to invoke human free-will to justify that the hidden variable cannot predict or influence the input choices if they are made by humans [Bell04, Bell85, Vaidman01, BBT18].

In any case, the freedom-of-choice loophole can only be closed based on a philosophical argument to justify the existence of unpredictable events.

Finite predictability of the inputs

Before discussing another type of loophole, we first introduce the notion of finite predictability of the randomness sources. Indeed, a typical random number generation (RNG) process used to define the input x and y relies on the detection of light emitted from a random source with photo-detectors (PD) or single-photon detectors (SPD). However, a realistic random light source will have non-Dirac-like autocorrelation function, and realistic detectors suffer from classical local noise (*e.g.* dark counts in SPDs or voltage noise in PDs). Therefore, a LHV model can use the information it has about past RNG outcomes, and local classical noise sources in the detectors to increase the probability of guessing the inputs for the next run, and increase the CHSH value it can reach [Kofler06, Hall10].

Formally, we write the probability of guessing correctly the input z_n given to Alice ($z = x$) or Bob ($z = y$) at the n^{th} run of the experiment knowing the LHV λ_n as [Abellán15]

$$\max_i P(z_n = i | \lambda_n) := \frac{1}{2}(1 + \varepsilon_{z,n}). \quad (2.70)$$

The parameter $\varepsilon_{z,n}$ defines the *excess predictability* or the random number generator at round n . The apparently random input transitions from fully unpredictable to predictable with certainty to the LHV model, as $\varepsilon_{z,n}$ ranges from 0 to 1. Therefore the excess predictability is a measure of how random and predictable the inputs are to LHV models. In typical RNG processes, known as Santha-Varizani sources [Santha86], the excess predictability can be bounded by

$$\varepsilon_{z,n} \leq \varepsilon_z, \quad \forall n \in \mathbb{N}. \quad (2.71)$$

In the most paranoid scenario where the classical noise in each RNG process is fully correlated, the maximum probability of guessing the input pair $\{x_n, y_n\}$ is

$$P := \max_{i,j,n} P(x_n = i \wedge y_n = j | \lambda_n) \leq \frac{1}{4}(1 + \varepsilon_x)(1 + \varepsilon_y) \leq \frac{1}{4}(1 + \varepsilon)^2, \quad (2.72)$$

where we introduced $\varepsilon := \max[\varepsilon_x, \varepsilon_y]$. Jason Pope and Alastair Kay showed that for a given probability P , the maximal expectation value of the CHSH for a LHV model increases with the number of experimental Bell runs N and converges to the asymptotic value S given by [Pope13]

$$P = \left(\frac{4+S}{24} \right)^{(4+S)/8} \left(\frac{4-S}{8} \right)^{(4-S)/8}. \quad (2.73)$$

As shown in Fig. 2.18, the maximum mean CHSH value S that a LHV model can reach is an increasing function of the excess predictability ε . For $\varepsilon = 0$, we get $S = 2$, which is nothing else than the standard CHSH inequality in the ideal setting. Surprisingly, the best LHV model can reproduce all quantum correlations, with $S = 2\sqrt{2}$, when the excess predictability is as low as $\varepsilon \simeq 1.62\%$, or equivalently $P \simeq 0.258$. Beyond this threshold, no quantum settings can reject LHV models, and the best LHV model can even reproduce some post-quantum, non-signaling correlations. The RNG excess predictability should therefore be much lower than 1.62%. In this low excess predictability regime, the maximum CHSH violation for LHV models can be well approximated by the power law

$$S - 2 \simeq 6.866 \varepsilon^{0.49982} \simeq 6.866 \sqrt{\varepsilon}, \quad (2.74)$$

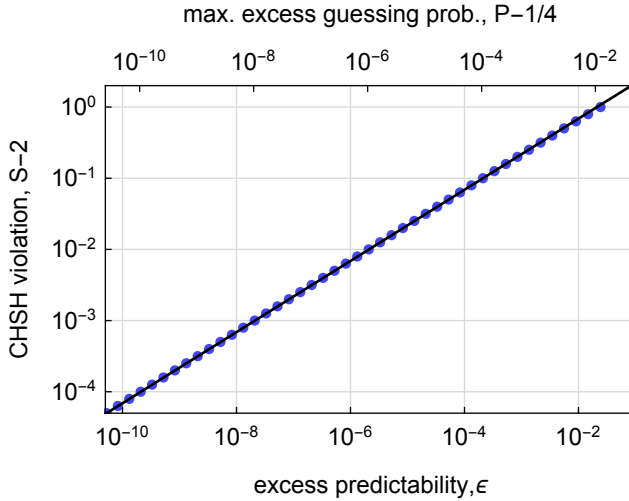


Figure 2.18 Maximum CHSH violation $S - 2$ allowed by a LHV model vs the maximum excess predictability ϵ of the two RNG sources, in the case of fully correlated RNG predictability, and in the limit of infinite number of Bell runs N . The blue dots are calculated from Eq. (2.73), and the black line is a power law fit to the points yielding expression (2.74).

as shown by the black solid line in Fig. 2.18. Reverting Eq. (2.74), we obtain that ϵ should be lower than $\sim 2.08(S - 2)^2$ for a given CHSH threshold S .

As discussed in Sec. 6.7, in the Bell test presented in this thesis, the QRNG have an excess predictability ϵ lower than 4.23×10^{-6} . According to Eq. (2.74), the corresponding CHSH threshold increases to $S > 2.015$ [Eq. (2.74)]. This is far below the maximum quantum bound $S = 2\sqrt{2}$ and should therefore be within experimental reach.

The locality loophole

Even if the freedom-of-choice loophole is closed, a LHV model could violate assumption (i) by communicating the outcome of x to Bob before he outputs his answer b , and *vice versa*. If the pairs of events x and b , and y and a , are space-like separated, like in Fig. 2.19, then assertion (i) is a consequence of the null hypothesis because no information can be transferred faster than at the speed of light in a local theory, and no extra assumption is needed. Otherwise, one needs to make an extra assumption about the internal working of the device to assert (i), which opens the *locality loophole*.

Note that closing the locality loophole requires to determine rigorously where the input generation and output events occur in space-time. However, defining the space-

time position of the input events comes back to closing the freedom-of-choice loophole, which we have seen earlier cannot be closed without an external, philosophically-backed, assumption. Similarly, defining the output event space-time position requires a model of wavefunction collapse, which creates a loophole here again [Kent05]. Closing this *collapse-locality* loophole therefore requires to define an acceptable event at which we consider the outputs to be classical. In the setting of a transmon qubit dispersively read out, such an event can be, in increasing order of paranoia: when the qubit is entangled with a measurement field, when the measurement field is first amplified, when the measurement field starts or stops being digitized, when the digitized signal is processed by a classical computer to generate the binary output, or when this output is read by a conscious human experimenter [Kent05].

One should always keep in mind that the locality loophole cannot be fully closed and state explicitly what assumptions are made to define the space-time positions of the input and output events.

The detection loophole

In an ideal Bell test, the experiment is to produce a pair of binary outputs each time it is ran, but this might not always be the case in a real experiment. For instance, in a photonic experiment, where the shared quantum state consists of a pair of entangled photons, there is a finite probability that at least one of the the measurement devices does not detect a photon, due to photon loss and detector inefficiencies. In the Bell

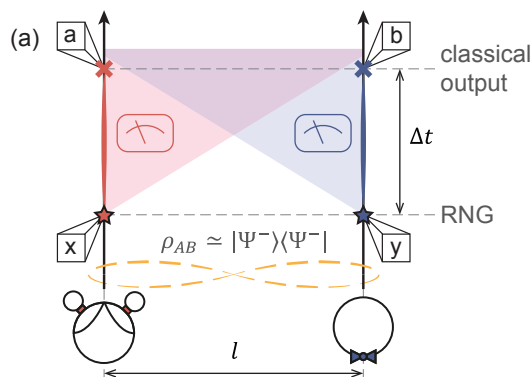


Figure 2.19 Space time diagram schematically representing a Bell experiment, in which the interaction prior to the experiment leads Alice and Bob to share the singlet state $\rho_{AB} = |\Psi^-\rangle\langle\Psi^-|$. The red and blue shaded regions correspond to the future light cone of events x and y , respectively.

formalism, these “no-click” events are to be recorded as a third output possibility, which violates assumption (ii). There are two ways of treating this third output possibility. The first one consists in *assuming* that “no-click” events happen independently from the hidden-variable, and that the subset of experimental runs where both photons were detected is statistically representative of the correlations which would be obtained in the absence of detection inefficiencies. This extra *fair-sampling* assumption creates the *detection loophole*. The second treatment consists in testing Bell inequalities derived for a ternary outputs scenario, or to consider assigning the “no-click” output to either 1 or -1 . However, as discovered by Philipp Pearle, accounting for these “no-click” events reduces the CHSH value, and Bell inequalities cannot be violated if the detection efficiency is below $\nu \simeq 82.84\%$ [Pearle70]. Indeed, as was shown two decades later, it is possible to construct explicit LHV models which perfectly reproduce the Bell correlations observed from a maximally entangled state in the subset of measurement runs where both photons are detected, if the detection probability is below a certain threshold [Santos96, ÅkeLarsson99, Gisin99].

In a Bell test using transmon qubits, the equivalent of such a “no-click” event would be that one of the transmon qubit has leaked outside of the qubit subspace, *e.g.* to state $|f\rangle$ or higher energy levels. These events are accounted for by the parameter ν in the parametrization (2.59) of ρ_{AB} . Typically, $1 - \nu \ll 1$, therefore the detection loophole can be systematically closed without significantly reducing the CHSH violation.

The memory loophole

The derivation of the P -value in Eq. (2.67) relies on the assumption that the random variables describing the experimental runs of the Bell test are independent and identically distributed (i.i.d.). This means that the LHV model has a hidden-variable λ which is not affected by the result of past Bell runs, *i.e.* which has no memory of the experiment. This assumption creates the *memory loophole* [Barrett02, Gill03a, Gill03b]. Fortunately, it is possible to derive an upper bound to the P -value without the i.i.d. assumption with a more complex statistical analysis. The CHSH value produced by a LHV model can be described by a supermartingale, whose probability to violate a Bell inequality by a given amount which can be bounded using Hoeffding’s or Bentkus’s inequalities [Gill03a, Elkouss16, Bentkus04]. For instance, assuming that the input x and y are uniformly distributed, one can obtain the simple bound for the CHSH

inequality based P -value [Gill03b]

$$P\text{-value} := \max_{\mathcal{J}_0} p(S \geq 2 + \varepsilon | \mathcal{J}_0) \leq \exp \left[-\frac{1}{2} \frac{\varepsilon^2 N}{16} \right], \quad \text{for } \varepsilon > 0. \quad (2.75)$$

Small corrections need to be made for the case of biased inputs x and y [Barrett02], and tighter upper bounds can be obtained using the methods described in [Elkouss16]. Compared to the i.i.d. case [Eq. (2.67)], the upper bound to the P -value decreases more slowly with respect to ε/\sqrt{N} , but it still holds that the P -value becomes arbitrarily small with increasing number of experimental run N for any finite amount of CHSH violation $\varepsilon > 0$. In other words, if LHV theories are rejected with the i.i.d. assumption, they will also be rejected when closing the memory loophole, at the cost of a relatively higher P -value.

2.2.3 Bell violation with a realistic error model

We have seen in Sec. 2.1.8 that several experiments demonstrated the possibility to generate entanglement between superconducting qubits fabricated on distinct chips, and physically separated by meter distances, using microwave photons. In these experiments, the entangled states are imperfect, with fidelity to the target pure Bell state ranging from 80% to 90%, limited mostly by two mechanisms: qubit decoherence and photon loss. Moreover, as we discuss in Secs. 3.1 and 5.6, the single-shot readout protocols in these experiments have errors: the measurement of a qubit initialized in state $|s\rangle$ is not always assigned correctly to the output s (see Secs. 3.1 and 5.6). How do these experimental imperfections affect the CHSH value that could be reached in a Bell test? What are the measurement axes \vec{x} and \vec{y} which maximize the CHSH value for these imperfect Bell states and measurement operations? This section is devoted to answer these two questions.

Part of the answer to the first question was given in 1995 by the Horodecki family [Horodecki95]. In this publication, the authors demonstrated that the maximum CHSH value which can be obtained from a joint state ρ_{AB} , maximized over all possible local measurement operators is

$$S_{\max} = 2\sqrt{s_1^2 + s_2^2} \quad (2.76)$$

where s_1 and s_2 are the two largest singular values of the 3×3 real matrix $\mathcal{J}_{\rho_{AB}}$, of

coefficients

$$\mathcal{T}_{\rho_{AB}ij} = \text{Tr}(\rho_{AB} \hat{\sigma}_i \otimes \hat{\sigma}_j), \quad \text{for } i, j \in \{x, y, z\}. \quad (2.77)$$

For imperfect entangled states ρ_{AB} of the form Eq. (2.59) generated with circuit QED photon-shaping or resonant-mode methods (see Sec. 2.1.8), we obtain the Horodecki matrix

$$\mathcal{T}_{\rho_{AB}} = \nu \begin{pmatrix} \mathcal{V}\sqrt{\eta_A\eta_B} & 0 & 0 \\ 0 & \mathcal{V}\sqrt{\eta_A\eta_B} & 0 \\ 0 & 0 & 1 - (\eta_A + \eta_B) \end{pmatrix}. \quad (2.78)$$

As a reminder, ν is the fraction of the population that stayed in the two-qubit computational subspace, \mathcal{V} is the phase coherence of the Bell state, $1 - \eta_B \sim 0$ accounts for decay of qubit B, and $1 - \eta_A \sim 0.1 - 0.3$ account for decay of qubit A and photon loss during the entanglement generation protocol. Because $\mathcal{T}_{\rho_{AB}}$ is diagonal, finding its singular values is trivial. From theorem (2.76) we see that

$$S_{\max} = \begin{cases} \nu\mathcal{V}\sqrt{\eta_A\eta_B} 2\sqrt{2} & \text{if } \nu^2 \geq \frac{(1 - \eta_A - \eta_B)^2}{\eta_A\eta_B}, \\ \nu\sqrt{\mathcal{V}^2\eta_A\eta_B/2 + (1 - \eta_A - \eta_B)^2/2} 2\sqrt{2} & \text{otherwise.} \end{cases} \quad (2.79)$$

A proper treatment of leakage outside of the 2-qubit subspace leads to an additional term $\epsilon < 2(1 - \nu)^2$, which we will neglect as it is very small for $\nu \sim 1$ [Brunner14].

Setting the measurement bases to

$$\vec{x}_0 = \vec{e}_0, \quad \vec{x}_1 = \vec{e}_1, \quad \vec{y}_0 = (\vec{e}_0 + \vec{e}_1)/\sqrt{2}, \quad \text{and} \quad \vec{y}_1 = (\vec{e}_0 - \vec{e}_1)/\sqrt{2}, \quad (2.80)$$

with \vec{e}_0 and \vec{e}_1 two orthogonal vectors in the XY plane of each party's Bloch sphere, the CHSH value for ρ_{AB} is

$$S_{XY} = \nu\mathcal{V}\sqrt{\eta_A\eta_B} 2\sqrt{2}. \quad (2.81)$$

Conversely, setting the measurement bases to

$$\vec{x}_0 = \vec{e}_0 = (0, 0, 1), \quad \vec{x}_1 = \vec{e}_1, \quad \vec{y}_{0/1} = \frac{\mathcal{V}\sqrt{\eta_A\eta_B}\vec{e}_1 \pm (1 - \eta_A - \eta_B)\vec{e}_0}{\sqrt{(1 - \eta_A - \eta_B)^2 + \mathcal{V}^2\eta_A\eta_B}}, \quad (2.82)$$

with \vec{e}_1 a unit vector in the XY plane, the CHSH value for ρ_{AB} is

$$S_Z = \nu\sqrt{\mathcal{V}^2\eta_A\eta_B/2 + (1 - \eta_A - \eta_B)^2/2} 2\sqrt{2}. \quad (2.83)$$

Comparing Eqs. (2.81) and (2.83) to Eq. (2.79), we find that

$$S_{\max} = \begin{cases} S_{XY} & \text{if } \mathcal{V}^2 \geq \frac{(1 - \eta_A - \eta_B)^2}{\eta_A \eta_B}, \\ S_Z & \text{otherwise.} \end{cases} \quad (2.84)$$

Therefore, Eqs. (2.80) and (2.82) yield an explicit optimization of the measurement bases for each case. As mentioned before, in practice, η_B is typically much closer to 1 than η_A and photon loss dominates over decoherence. We therefore have $\mathcal{V}^2 \geq \eta_A \simeq (1 - \eta_A - \eta_B)^2 / \mathcal{V} \eta_A \eta_B$ and $S_{\max} = S_{XY}$.

To account for readout classification errors, we first introduce the readout classification error probabilities

$$\epsilon_g := P(e|g) \quad \text{and} \quad \epsilon_e := P(g|e),$$

and remark that the expectation value of the σ_z operator under these readout assignment errors becomes

$$\langle \sigma_z \rangle \rightarrow \mathcal{F}_r \langle \sigma_z \rangle, \quad (2.85)$$

where we define the readout fidelity

$$\mathcal{F}_r := (1 - \epsilon_g - \epsilon_e).$$

As described earlier (Sec. 2.1.5), in typical circuit QED system, the other Pauli observables are measured by doing a pre-rotation and measuring the σ_z observable. Therefore the substitution (2.85) is also valid for the Pauli vector $\vec{\sigma}$. Doing this substitution in the Bell operator used in the demonstration of the Horodecki theorem [Horodecki95], we find that the maximum CHSH violation becomes

$$S_{\max} \rightarrow \mathcal{F}_{r,A} \mathcal{F}_{r,B} S_{\max}. \quad (2.86)$$

In conclusion, in a practical circuit QED implementation of a Bell test, we expect to obtain the CHSH value

$$\begin{aligned} S_{\max} &= \mathcal{F}_{r,A} \mathcal{F}_{r,B} \mathcal{V} \mathcal{V} \sqrt{\eta_A \eta_B} 2\sqrt{2} \\ &= \mathcal{F}_{r,A} \mathcal{F}_{r,B} \mathcal{C}(\rho_{AB}) 2\sqrt{2}, \end{aligned} \quad (2.87)$$

where we used Eq. (2.60) to get the second equality. As a consequence, the CHSH inequality can be violated if and only if the readout fidelities and the concurrence are

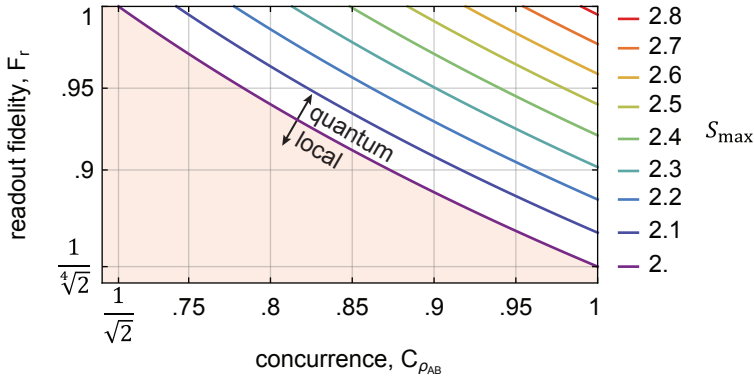


Figure 2.20 Expected experimental CHSH value vs the concurrence of the prepared state $\mathcal{C}(\rho_{AB})$ and the geometric mean of the readout fidelities \mathcal{F}_r , calculated using Eq. (2.87) and assuming that ρ_{AB} is of the form given in Eq. (2.59). The shaded region is the parameter space leading to local correlations, in which no Bell inequality can be violated.

large enough so that $\mathcal{F}_{r,A}\mathcal{F}_{r,B}\mathcal{C}(\rho_{AB}) > 1/\sqrt{2} \simeq 0.707$. We show in Fig. 2.20 a contour plot of the expected experimental CHSH values as a function of the concurrence, and of the geometric mean of the readout fidelities $\mathcal{F}_r = \sqrt{\mathcal{F}_{r,A}\mathcal{F}_{r,B}}$.

2.2.4 Toward a loophole-free Bell test with superconducting circuits

Now that we have presented all key aspects of circuit QED and Bell tests, we can assess the requirements to perform a Bell test using superconducting qubits and microwave photons, free of any loophole. Let us first see what requirements are added by the constraints of closing all loopholes.

To close the freedom-of-choice loophole, we intend to use a pair of quantum random number generators (QRNG) to generate the inputs. For instance, the QRNGs developed at ICFO [Abellán15] were used in the first three Bell test experiments to be considered loophole-free [Hensen15, Shalm15, Giustina15], and shall therefore lead to suitable assumptions to close the freedom-of-choice loophole and to conservatively define the space-time position of the input events. The detection loophole is systematically closed in a setup using superconducting circuits, because each time we run a dispersive measurement, we record a measurement trace which is systematically classified into either $a, b = -1$ or 1 [Ansmann09].

To close the locality loophole, we must first determine the time Δt which will elapse between the input and output events. This time can be divided into four contributions: the time Δt_1 to generate a low excess predictability random number, the time Δt_2 to

convert that number into a measurement basis, the measurement time Δt_3 needed to discriminate the qubit state with high readout fidelity, and the propagation time Δt_4 of all the signals which enter this critical timing path, from the QRNG to the digitization of the measurement signal on an analogue-to-digital (ADC) acquisition card. The QRNG of [Abellán15, Hensen15, Shalm15, Giustina15] was shown to generate random inputs in current-mode logic in 11 ns every 5 ns, with an excess predictability per bit bounded by $\varepsilon \simeq 0.1$. The successive bits need to be added modulo 2 to decrease the excess predictability to acceptable levels (see Sec. 2.2.2 and [Abellán15]). In Sec. 6.7, we present an adaptation of this QRNG which parallelizes the process to generate a random bit with $\varepsilon \simeq 4 \times 10^{-6}$ in time $\Delta t_1 \lesssim 17$ ns. Translating this random bit into a measurement basis requires to send a rotation pulse to the qubit conditioned on the QRNG output, to map the desired measurement axis to the z axis before the measurement of σ_z starts. In Sec. 6.7, we present a scheme allowing to do both in $\Delta t_2 \leq 12$ ns. The σ_z measurement consists of a dispersive readout scheme, which can reach fidelities higher than 98% for an integration time $\Delta t_3 \leq 50$ ns [Walter15]. Finally, propagation delay Δt_4 accounts for the time taken by: the control signal travelling from the QRNG output port to the switch control port, the rotation pulse travelling from the switch input port to the qubit, and the readout signal travelling from the readout resonator to the input port of the ADC. The optimized cabling scheme presented in chapter 4 is expected to reduce Δt_4 to 20 ns. Therefore, we expect the Bell test run to last $\Delta t = \Delta t_1 + \Delta t_2 + \Delta t_3 + \Delta t_4 \leq 100$ ns. To close the locality loophole, the two qubits should be separated by a distance strictly larger than $c(\Delta t_1 + \Delta t_2 + \Delta t_3) \simeq 24$ m. To be conservative, we decide to separate the two qubits by a distance $c\Delta t \simeq 30$ m.

The two qubits thus need to be connected via an approximately 30 m long transmission line or waveguide, for entanglement generation. This enforces two other constraints on the setup. First, in the absence of a circulator in the transmission line, the latter would form a multi-mode cavity with a free spectral range smaller than $1/2\Delta t \simeq 5$ MHz, which would limit the speed and hence the fidelity of a resonance-based entanglement protocol. Therefore we choose to resort to a photon shaping method. Second, to generate a joint state with high concurrence, the transmission line should be superconducting, to be low loss, and should have low thermal occupation [Xiang17], which require it to be held at cryogenic temperatures. Our Bell test therefore requires to build a 30 m long cryogenic link to cool the communication transmission line. As we detail in chapter 4, the electronics which define the start (QRNG) and stop (ADC) events of the Bell test should be positioned 1.1 m and 1.9 m

away from the centers of the two dilution refrigerators, respectively. This extra 3 m distance between the input and output events gives 10 ns extra margin to close the locality loophole [Fig. 2.21 (a)].

In conclusion, the experimental setup would consist of two transmon qubits housed in dilution refrigerators separated by 30 m and connected by a waveguide held at cryogenic temperature [Fig. 2.21 (a)]. A Bell test run then consists of two phases: a preparation phase during which the qubits are reset and entangled using a microwave photon shaping technique, and a Bell test phase of duration $\Delta t \leq 100$ ns in which the

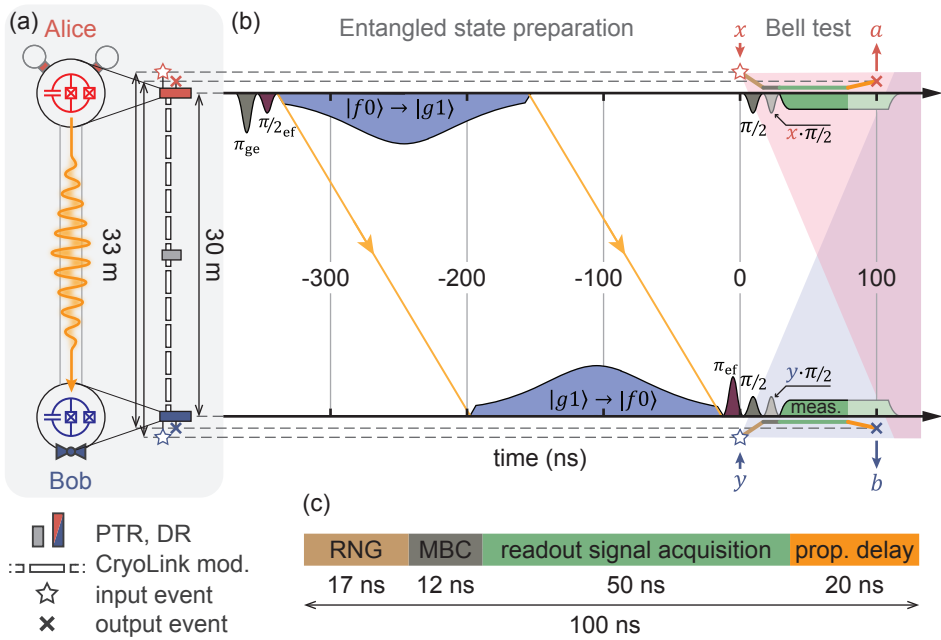


Figure 2.21 (a) Illustration of the setup, and (b) space-time diagram of the pulse scheme suggested to perform a loophole free Bell test with superconducting circuits [blue and red circuit elements in (a)] and microwave photons (yellow arrows). The future light cones of the input events x and y are shaded in red and blue, respectively. The rotation pulse implementing the measurement basis choice is colored in a lighter shade, and has an input-dependent rotation angle $x \times \pi/2$ for Alice and $y \times \pi/2$ for Bob. (a) and (b) display the spatial position, and the spatio-temporal position input (star) and output (cross) events, respectively. The former event is located at the drive input of the QRNG, and the latter at the input port of the ADC. The critical timeline for a single instance of the Bell test, represented in (b) as a line matching the input to the output, can be divided into four contributions detailed in (c): the random number generation process (RNG, brown), the qubit rotation implementing the measurement basis choice (MBC, gray), the readout signal acquisition (green) and the propagation delay of time critical signals in the cables (orange). PTR: pulse-tube refrigerator; DR: dilution refrigerator

two qubits are measured on local bases chosen at random [Fig. 2.21 (b,c)]. The key ingredients to perform a loophole-free Bell test with superconducting qubits entangled via microwaves are the following:

- a cryogenic link technology allowing to connect separate dilution refrigerators with a cold, lossless transmission line,
- a deterministic and high fidelity reset protocol,
- a high fidelity remote entanglement protocol,
- a fast and random measurement basis choice mechanism,
- and a readout scheme optimized for speed and fidelity.

In the remainder of this thesis, we discuss how we implement all these key aspects to converge toward the loophole-free experimental violation of Bell inequalities, using superconducting circuits.

Chapter 3

Parameter optimization for fast dispersive readout

Would you like to have your bed flipped?

— David van Woerkom

Distinguishing the state of a qubit with high fidelity is an essential tool for quantum information processing tasks such as quantum error correction [Shor95, Knill98, Kitaev03], teleportation [Bennett93, Gottesman99], distillation [Bennett96a, Bravyi05] or state initialization [Reed10a, Campagne-Ibarcq13, Salathé15]. The most popular method to measure superconducting qubits consists in measuring the signal transmitted through a coupled resonator, whose frequency is dispersively shifted conditioned on the qubit state [Blais04, Wallraff04, Mallet09, Reed10a]. The fidelity of qubit readout protocols is limited by qubit decay happening during the measurement, therefore minimizing the measurement time is key to improve on the readout quality [Jeffrey14, Walter17]. Moreover, optimizing readout speed can significantly reduce idling errors in quantum error correction codes [Andersen20b, Heinsoo18, Chen21b], or any algorithm requiring feedback or feedforward [Steffen14, Chou18, Córcoles21] and is necessary to close the locality loophole in a Bell test [Aspect82a, Hensen15, Giustina15, Shalm15]. See also Sec. 2.2. Theoretical studies so far have focused on optimizing the measurement speed assuming that the readout resonator field is in a steady-state regime [Gambetta08]. However, as we demonstrated in [Walter17], the information acquired during the transient regime of the readout, during which the resonator field gets populated, can be significant. A systematic optimization of the measurement speed should therefore account for the transient dynamics of the readout

resonator.

In this chapter, we detail a systematic procedure to optimize readout speed in the weak-drive dispersive regime, including the effects of the transient dynamics. We first define the signal-to-noise ratio (SNR) of the transmitted field and derive useful properties of the SNR in Sec. 3.1. In Sec. 3.2, we show how to optimize the SNR for a given measurement time in the case of a single resonator coupled to the qubit, from which we show how to minimize the measurement time. Section 3.3 extends the readout optimization to Purcell filtered circuits, and Sec. 3.4 provides a clear compromise between Purcell decay suppression and SNR tolerance to the experimental uncertainty of parameters. We discuss considerations on weak-drive and strong-drive non-linear effects in Sec. 3.5, and assess qualitatively how they can improve or limit readout performance. Section 3.6 will conclude with a generic protocol to optimize readout parameters for speed.

3.1 Quantifying qubit readout with the SNR

We consider a single transmon qubit with frequency ω_q and anharmonicity α , coupled with rate g to a resonator of frequency ω_r , which couples with rate κ to a single output port [Fig. 2.12 (a)]. We assume that the system is in the dispersive regime, where g is very small compared to the detuning $\Delta = \omega_q - \omega_r$, and that it has no internal loss. We consider that at $t = 0$, the transmon qubit is in the eigenstate $|k\rangle$, and the resonator is driven from the vacuum state by a drive tone of amplitude $\epsilon(t)$ and carrier frequency ω_d . To further simplify the problem, we consider the weak drive limit, where the mean number of photons n in the resonator is always much smaller than the critical photon number $n_c = \Delta^2/4g^2$, and the dispersive approximation is valid [Blais04].

In this regime, σ_z commutes with the dispersive Hamiltonian describing the motion of the qubit-resonator system [Eq. (2.47)]. Therefore the measurement is a quantum-nondemolition (QND) process, *i.e.* it does not affect the mean population of the qubit states. As a consequence, the qubit stays in state $|k\rangle$ during the whole process. The resonator behaves like a linear system, whose inner and output field can be described the input-output relations [Gardiner85]

$$\dot{a}_k = -i(\omega_k - \omega_d)a_k - \frac{\kappa}{2}a_k - \sqrt{\kappa}a_{\text{in}} \quad (3.1)$$

$$a_{\text{out},k} = \sqrt{\kappa}a_k + a_{\text{in}}, \quad (3.2)$$

expressed in the frame rotating at the drive frequency, and where $\omega_k = \omega_r - \chi_k$ is the dressed, qubit-state-dependent, resonance frequency of the resonator [see Eq. (2.49)], and the time-dependent operators a_{in} , a_k and $a_{\text{out},k}$ corresponding to the input, resonator and output fields are expressed in the Heisenberg picture. The drive amplitude is then defined as $\varepsilon := -i\sqrt{\kappa}\langle a_{\text{in}} \rangle$. Because the system is linear, if the drive input field $a_{\text{in}}|0\rangle$ is in a coherent state then so are the resonator and output fields. The system can be treated semi-classically and its evolution is determined by the quantum Langevin equation applied to the expectation values $\alpha := \langle a \rangle$ of the field operators

$$\dot{\alpha}_k = -i(\omega_k - \omega_d)\alpha_k - \frac{\kappa}{2}\alpha_k - i\varepsilon \quad (3.3)$$

$$\dot{\hat{\alpha}}_{\text{out},k} = \sqrt{\kappa}\alpha_k + \frac{i}{\sqrt{\kappa}}\varepsilon + \hat{\xi} \quad (3.4)$$

Here, the time-dependent output field $\hat{\alpha}_{\text{out},k}$ is treated as a random variable (which are specified by hats in this section) by the addition of the quantum noise term $\hat{\xi}$, which follows a proper, complex centered Gaussian distribution with white noise, $\langle \text{Re}[\hat{\xi}](t), \text{Re}[\hat{\xi}](t') \rangle = \langle \text{Im}[\hat{\xi}](t), \text{Im}[\hat{\xi}](t') \rangle = \delta(t - t')/4$. Without loss of generality, the qubit-state independent term $i\varepsilon/\sqrt{\kappa}$, which stems from direct reflection of the input field, can be set to zero via an abstract displacement operation on the output field. This way, our analysis generalizes to measurement geometries other than reflection measurements.

For a given measurement time $\tau > 0$, the output field $\hat{\alpha}_{\text{out},k}$ follows a multi-variate, complex, Gaussian distribution of mean $\sqrt{\kappa}\alpha_k$, covariance matrix $\Sigma(t, t') = \delta(t - t')/2$, and null pseudo-covariance matrix [Eriksson09], in the infinite-dimensional Hilbert space \mathcal{L}_2^τ of square integrable complex functions on the interval $[0, \tau]$. The means of the distributions followed by $\hat{\alpha}_{\text{out},g}$ and $\hat{\alpha}_{\text{out},e}$ are distant by $2\sqrt{\kappa}\|\alpha_e - \alpha_g\|_{2,\tau}$ standard deviations, so the corresponding power SNR between the two distributions is

$$\text{SNR} = 4\kappa\|\beta\|_{2,\tau}^2, \quad (3.5)$$

Here we define $\beta := \alpha_e - \alpha_g$, and introduced the \mathcal{L}_2^τ norm

$$\|u\|_{2,\tau}^2 := \int_0^\tau |u|^2 dt, \quad (3.6)$$

associated with the inner product

$$\langle u, v \rangle \equiv u^\dagger \cdot v := \int_0^\tau u^* v dt. \quad (3.7)$$

In steady-state, the intra-cavity field α_k are constant, Eq. (3.5) simplifies to the well know formula $\text{SNR} \simeq 4|\beta(+\infty)|^2 \kappa \tau$ [Gambetta08], and the SNR increases linearly with time.

Interestingly, all the information needed to distinguish between states $|g\rangle$ and $|e\rangle$ is encoded the real part of the component of the field along the unit vector

$$w(t) = \frac{\beta(t)}{\|\beta\|_{2,\tau}}.$$

Indeed one can show that the random variables $\hat{S}_{g/e} = \text{Re}[w^\dagger \cdot \hat{\alpha}_{\text{out},g/e}]$ follow marginal distributions which are Gaussian, real-valued, and single-variate with means that are distant by $\langle \hat{S}_e \rangle - \langle \hat{S}_g \rangle = \sqrt{\kappa} \|\beta\|_{2,\tau}$, and standard deviation $\sigma = \sqrt{w^\dagger \cdot \Sigma / 2 \cdot w} = 1/2$, so their relative SNR is the same as for the full multivariate distributions [Eq. (3.5)].

Therefore the following qubit state discrimination procedure given a measured trace $\sqrt{\kappa}\alpha$ is optimal [Gambetta08]. (i) Integrate $\sqrt{\kappa}\alpha$ with the weight function w to obtain the integrated trace $S = \sqrt{\kappa} \text{Re}[w^\dagger \cdot \alpha]$. (ii) Choose $k \in \{g, e\}$ such that the likelihood S is maximum for the distribution followed by \hat{S}_k . The second step is equivalent to a threshold discrimination rule which assigns the measurement outcome to g if $S < ((\langle \hat{S}_e \rangle) + \langle \hat{S}_g \rangle)/2$, and to e otherwise. Then the measurement fidelity is limited by the overlap error between the two Gaussian distributions

$$\mathcal{F} := 1 - P(e|g) - P(g|e) < \text{erf}\left(\sqrt{\text{SNR}/8}\right), \quad (3.8)$$

with $P(k|k')$ the probability to assign the measurement outcome to k when the qubit was in state $|k'\rangle$, and erf the error function. The readout fidelity is typically smaller due to initialization and qubit state-mixing errors. Table 3.1 links typical readout fidelities to their corresponding SNR.

There is a relation between the measurement SNR and the amount of dephasing the measurement induces on the qubit. Indeed, the measurement process has the effect of mapping $|s\rangle |0\rangle |E_0\rangle \mapsto |s\rangle |\alpha_s(\tau)\rangle |E_s\rangle$, where the first, second and third kets denote the qubit, resonator, and output field states, respectively. Because $|E_g\rangle$ and $|E_e\rangle$ are two propagating coherent states which differ from each other by $\kappa \|\beta\|_{2,\tau}^2$ photons, we find using Eq. (2.36) that the qubit coherence is reduced by the measurement process

to

$$\begin{aligned}
\mathcal{V} &= \langle \alpha_g(\tau) | \alpha_e(\tau) \rangle \langle E_g | E_e \rangle \\
&= \exp \left[-\frac{1}{2} |\beta(\tau)|^2 \right] \exp \left[-\frac{\kappa}{2} \|\beta\|_{2,\tau} \right] \\
&= \exp \left[-\frac{1}{2} |\beta(\tau)|^2 - \frac{\text{SNR}(\tau)}{8} \right].
\end{aligned} \tag{3.9}$$

We note that the left term in the exponential disappears if the drive pulse is finite and the resonator fields have returned to vacuum at time τ . Also, if the resonator stops being driven at time τ_f then the coherence \mathcal{V} stops decreasing, the field remaining in the resonator will eventually leak into the detection line leading to an increment in the SNR

$$\lim_{\tau \rightarrow +\infty} \text{SNR}(\tau) = \text{SNR}(\tau_f) + 4|\beta(\tau_f)|^2.$$

This formula is useful in order to estimate the SNR accumulated with a finite drive pulse, but semi-infinite acquisition window. In steady-state, the SNR is proportional to τ , therefore the right term of Eq. (3.9) dominates and the qubit coherence is approximately

$$\mathcal{V} \simeq \exp \left[-\frac{\text{SNR}(\tau)}{8} \right] \simeq \exp \left[-\frac{1}{2} |\beta|^2 \kappa \tau \right],$$

i.e. the qubit experiences an exponential *measurement-induced dephasing* at rate $\Gamma_m = |\beta|^2 \kappa / 2$.

So far, we have only considered the quantum limited SNR, *i.e.* the signal to noise ratio that the field leaving the chip carries with it. However, extra noise will be added to the signal during the amplification and measurement process leading to a reduction of the detected SNR by a factor η compared to the ideal SNR of Eq. (3.5). To limit the amount of added noise, most experiments use a near-quantum-limited Josephson parametric amplifier (JPA) as the first amplifier [Caves82, Yurke96, Castellanos-Beltran08, Clerk10], whose detection efficiency η must be below 1 if only one quadrature of the

$1 - \mathcal{F}$	SNR
5%	15.4
2%	21.6
1%	26.5
0.5%	31.5
0.1%	43.3

Table 3.1 Maximum readout fidelity that can be achieved for a given SNR [Eq. (3.8)].

signal is amplified (phase-sensitive mode), and below 1/2 if both quadratures are amplified (phase-preserving mode) [Caves82, Clerk10]. Because of extra inefficiencies, like signal loss or noise added before or after the JPA, typical detection efficiencies range between 0.15 and 0.35 for phase-preserving reflective [Roy15, Eichler14a], or traveling wave amplifiers [Macklin15, Planat19], and between 0.5 and 0.8 for phase-sensitive amplifiers [Ristè12b, Walter17, Eddins19].

The finite bandwidth of JPAs and other components in the detection line will also lead to time-correlations in the noise term $\hat{\xi}$. The noise covariance matrix $\Sigma(t, t')$ is no longer diagonal and therefore an orthogonal projection of the signal along u is no-longer SNR-preserving. However, because that $\sqrt{\Sigma^{-1}} \cdot \xi$ has a white noise matrix, projecting the signal along vector $\Sigma^{-1} \cdot u$ is SNR preserving, and the linear discrimination algorithm described above is optimal. Note that, unlike u , $\Sigma^{-1} \cdot u$ is not necessarily zero at negative times. Therefore, in order to preserve SNR, the integration window should start at a negative time $-\tau_{\text{BW}}$ which is several times the characteristic response time of the detection chain. More formally, $-\tau_{\text{BW}}$ should be large enough so that

$$\int_{-\infty}^{-\tau_{\text{BW}}} |\Sigma^{-1} \cdot u|^2 dt \ll \int_{-\tau_{\text{BW}}}^{\tau} |\Sigma^{-1} \cdot u|^2 dt.$$

3.2 Readout parameter optimization in the weak drive limit

To optimize the SNR for a given measurement time τ , we should first express it in terms of the readout circuit parameters. To that end we consider the weak-drive dispersive readout setting illustrated in Fig. 2.12 (a) and introduced in the beginning of Sec. 3.1, from which we derived Eq. (3.4). To keep the problem analytically tractable, we further assume that the drive rate ε is a unit-step pulse of constant amplitude. Then, solving Eq. (3.4) provides an analytical solution to Eq. (3.5) which shows that the SNR is proportional to the drive power $|\varepsilon|^2$. In practice, high drive powers lead to a breakdown of the dispersive approximation, and the linearity and QND-ness assumptions used to obtain Eq. (3.4) are no longer valid. While quantifying the limit on the applicable power is a on-going research topic [Boissonneault09, Boissonneault10, Sank16], a common way to parametrize the drive power is to relate the number of photons n it induces in the resonator in steady-state with the critical photon number n_c [Blais04, Gambetta08, Boissonneault09, Boissonneault10, Reed10a, Jeffrey14, Sank16, Walter17]. To be able to compare the SNR for different parameter choices and to restrict ourselves to the linear case, we set the drive power such that $n := \max(n_g, n_e)$ is set to a fixed, small

fraction of n_c . The SNR is maximized when $n_g = n_e = n$ which sets the optimal readout drive frequency to $\omega_d = (\omega_g + \omega_e)/2$ [Gambetta08]. The SNR can then be expressed as

$$\begin{aligned} \text{SNR}(\tau) = & \\ & \frac{4n}{(\kappa^2 + 4\chi^2)^2} \left[\right. \\ & 4\chi^2(2\kappa^3 + 8\kappa\chi^2)\tau + 8\chi^2(4\chi^2 - 11\kappa^2) \\ & + e^{-\kappa\tau/2}16\chi\kappa(4\chi\kappa\cos(\chi\tau) + (\kappa^2 - 4\chi^2)\sin(\chi\tau)) \\ & \left. + e^{-\kappa\tau}(-(\kappa^2 + 4\chi^2)^2 + \kappa^2(\kappa^2 - 12\chi^2)\cos(2\chi\tau) + \kappa\chi(8\chi^2 - 6\kappa^2)\cos(2\chi\tau)) \right], \end{aligned} \quad (3.10)$$

where $\chi := |\chi_g - \chi_e|/2$ is the amplitude of the effective dispersive shift of the transmon qubit [Eq. (2.50)].

At first glance, Eq. (3.10) looks barbaric, but several of its aspects are instructive. Indeed, noting that

$$n_c = 1/(4\chi) \times \alpha\Delta/(\Delta + \alpha),$$

Eq. (3.10) can be rewritten as

$$\text{SNR}(\tau) = 4 \frac{n}{n_c} \tilde{\alpha} \tau f(\kappa\tau, \chi\tau), \quad (3.11)$$

with f a function varying between 0 and 1 which depends only on $\chi\tau$ and $\kappa\tau$, and $\tilde{\alpha} := \alpha\Delta/(\alpha + \Delta)$ defining the modified anharmonicity. This expression is useful because it allows to write the SNR as a function of three independent terms which can be optimized separately, the relative readout power n/n_c , the modified anharmonicity $\tilde{\alpha} := \alpha\Delta/(\alpha + \Delta)$, and the time-dependent term $\tau f(\kappa\tau, \chi\tau)$.

Optimizing power

As expected from the linearity of Eq. (3.4), the SNR is proportional to the drive power n . Therefore, the drive power should be increased until measurement-induced state-mixing limits the readout fidelity. This step is typically done with an experimental sweep of drive power [Walter17].

Optimizing the modified anharmonicity

In typical transmon/resonator systems, $\alpha/\Delta \ll 1$, so the modified anharmonicity expands as

$$\tilde{\alpha} = \alpha \left(1 - \frac{\alpha}{\Delta} + \mathcal{O}\left(\frac{\alpha}{\Delta}\right)^2 \right)$$

with this small parameter, which highlights the linear dependence of the SNR on the anharmonicity α . Therefore, a large α is desirable to improve the SNR. However, the anharmonicity of a transmon qubit increases with charging energy E_c , therefore large values of α either come at the cost of a reduced E_J/E_c ratio, which leads to greater sensitivity to charge noise, or at the cost of a higher qubit frequency (see Fig. 2.6 and [Koch07]). Also, the spurious ZZ coupling rate between neighboring qubits is typically proportional to α [Krinner20]. These considerations must be accounted for by the experimenter to determine how large α can be. Choosing the frequency arrangements such that α and Δ have opposite signs leads to an increase of the SNR by a fraction $2|\alpha/\Delta|$ compared to the opposite situation. The detuning Δ only has minor effect on $\tilde{\alpha}$ and can therefore be chosen based on other constraints.

Optimizing $f(\kappa\tau, \chi\tau)$

The dependence of f on $\kappa\tau$ and $\chi\tau$ is instructive. To study it, we first introduce the variables $\theta := \arctan(2\chi/\kappa)$ and $\tilde{\tau} := \sqrt{\kappa^2 + 4\chi^2}\tau$. These variables are the modulus and argument of the complex quantity $(\kappa + i2\chi)\tau$, with the argument θ ranging from 0 to $\pi/2$ as the ratio χ/κ increases. We find that f is zero for $\tau = 0$ and for $\theta = 0$ ($\iff \chi = 0$) or $\pi/2$ ($\iff \kappa = 0$), and increases with integration time $\tilde{\tau}$ [Fig. 3.1 (a)] to reach the asymptotic steady-state value

$$\lim_{\tilde{\tau} \rightarrow +\infty} f(\theta, \tilde{\tau}) = \sin(2\theta), \quad (3.12)$$

A consequence is that f varies between 0 and 1. It can therefore be seen as a scaling factor to the maximum SNR possible $\text{SNR}_{\max} = 4(n/n_c)\tilde{\alpha}\tau$. Equation (3.12) corroborates the well-established result that the SNR in steady-state is maximum when $2\chi = \kappa$ ($\iff \theta = \pi/4$) [Gambetta08]. In practice this steady-state regime is reached for $\tilde{\tau} \gtrsim 30$. For a fixed $\tilde{\tau} < 30$, the optimal $\theta_0(\tilde{\tau})$ is close, but not equal to $\pi/4$, as indicated by the black line in Fig. 3.1. However, for a fixed $\chi\tau$ (light blue lines in Fig. 3.1), there is a single optimal value of $\kappa\tau$ (thick blue line) which is typically such that $\kappa > 2\chi$. Conversely, for a fixed $\kappa\tau$ (light red lines in Fig. 3.1), there is a single optimal value of $\chi\tau$ (thick red line) which is typically such that $\kappa < 2\chi$.

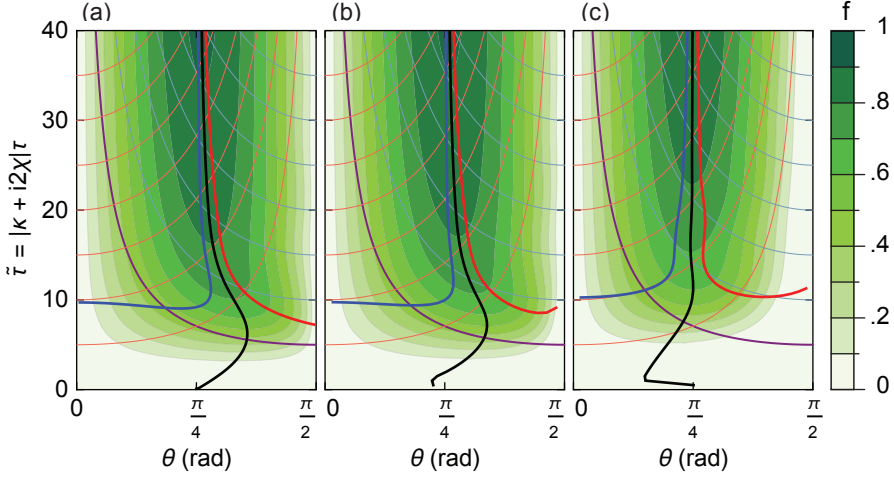


Figure 3.1 Normalized SNR $f(\kappa\tau, \kappa\tau)$ vs the variables $\theta = \arctan(2\chi/\kappa)$ and $\tilde{\tau} = \sqrt{\kappa^2 + 4\chi^2}\tau$, in the case of (a), a single resonator coupled to the transmon qubit and (b,c), a Purcell filtered resonator coupled to the qubit with a J/κ_f ratio of 1/10 and 1/3, respectively. For (b,c), δ is set to zero and κ is calculated from J and κ_f with Eq. (2.54). The black, red and blue line correspond to the argument maximizing f for fixed $\tilde{\tau}$, $\kappa\tau$ and $\chi\tau$, respectively. The thin light blue and light red lines correspond to fixed values of $\kappa\tau$ and $\chi\tau$, respectively. The purple line corresponds to $2\chi\tau = 5$.

To maximize the SNR, and therefore f , with a fixed, short integration time, one needs to increase the absolute value of χ and κ , to increase $\tilde{\tau}$. Qualitatively, this corresponds to shortening the transient period of the readout. In principle, κ can be arbitrarily high as long as the corresponding increase in Purcell decay is suppressed with Purcell filters. However, noting that $\chi = \tilde{\alpha}(g/\Delta)^2$, and that $\tilde{\alpha}$ is already maximized, there is a limit $\chi_{\max} = \tilde{\alpha}(g/\Delta)_{\max}^2$ to how large χ can be set by the requirement $g/\Delta < (g/\Delta)_{\max} \lesssim 0.1$ for the dispersive approximation to hold.

The SNR scaling function f should therefore be optimized under the constraint $\chi\tau \leq \chi_{\max}\tau$. This is done by setting $\chi\tau = \chi_{\max}\tau$ and maximizing f with respect to κ . Graphically speaking, let the purple line in Fig. 3.1 be $\chi\tau = \chi_{\max}\tau$, we want to find the maximum of f in the region on the bottom left of that line. The optimal solution is then at the crossing between the purple and the blue lines. We note $f_{\chi_{\max}}^{\text{opt}}(\tau)$ the value of f at this point. If $2\chi_{\max}\tau < 7.5$, this optimal solution leads to $f < 1/2$, and corresponds to κ significantly bigger than $2\chi_{\max}$ [Walter17]. In the opposite case $2\chi_{\max}\tau \geq 7.5$, setting $\kappa = 2\chi$ is close to optimal.

Optimizing τ

The optimization procedure detailed above for a given τ gives a simple mean to choose the minimum integration time τ . Defining $\text{SNR}_{\text{target}}$ as the minimum SNR needed for the application, and η the measurement efficiency, we find that the integration time should be greater than a value τ_{min} which fulfils the relation

$$\tau_{\text{min}} f_{\chi_{\text{max}}}^{\text{opt}}(\tau_{\text{min}}) = \frac{\text{SNR}_{\text{target}}}{4\eta(n/n_c)\tilde{\alpha}}.$$

To illustrate the optimization routine, we use the external constraints and parameters which apply for the realization of a Loophole-free Bell test with superconducting circuits, as devised in chapter 2. The same optimization procedure can be applied to different contexts by considering the particular constraints on τ , α and Δ .

We have seen in Sec. 2.2.4, closing the locality loophole requires to measure the qubit state with high fidelity in less than 50 ns. Therefore we restrict our study of the SNR to an integration time $\tau = 50$ ns. We set an upper-limit of -350 MHz to $\alpha/2\pi$, after which we judge that the charge noise on the e-f transition becomes too important, and set α to this upper-limit. Indeed, for a qubit frequency of 7.2 GHz, this leads to a limit of $19 \mu\text{s}$ on the e-f dephasing time in the worst-case scenario [Eq. (2.28)]. We set the target detuning between the qubit and the resonator to $\sim +1.5$ GHz. This parameter is typically constrained by frequency crowding considerations, but we shall see later how it affects readout, independently of the other parameters, to derive readout-related constraints on it. This choice for α and Δ leads to $\tilde{\alpha}/2\pi \simeq 450$ MHz. Mimicking the choice from [Walter17], we set $(g/\Delta)_{\text{max}} = 1/8$, which leads to $\chi_{\text{max}}/2\pi \simeq 8$ MHz and $(\chi\tau)_{\text{max}} \simeq 5$ [purple line in Fig. 3.1]. Finally, assuming that, similar to [Walter17], the phase-sensitive detection efficiency is $\eta = 66\%$ and the readout power can be set to $n/n_c = 1/5$ without introducing detrimental effects, the minimum integration times needed to reach 99% SNR-limited fidelity (or equivalently $\text{SNR}_{\text{target}} \simeq 26.5$) is $\tau_{\text{min}} \simeq 43$ ns, which is smaller than the budgeted 50 ns.

The corresponding SNR scaling is $f_{\chi_{\text{max}}}^{\text{opt}}(\tau_{\text{min}}) \simeq 0.4$. We find that $f_{\chi_{\text{max}}}^{\text{opt}}(\tau_{\text{min}})$ varies between 0.4 and 0.8 for typical parameters ($\text{SNR}_{\text{target}} \simeq 26.5$, $n/n_c = 1/5$, $(g/\Delta) = 1/8$, $\tilde{\alpha}/2\pi \simeq \alpha/2\pi \in [150, 450]$ MHz and $\eta \in [0.15, 0.75]$). Therefore τ_{min} can be estimated by

$$\tau_{\text{min}} \sim \frac{\text{SNR}_{\text{target}}}{2.4(n/n_c)\eta\tilde{\alpha}},$$

with $\pm 30\%$ accuracy. The fact that the optimal f is significantly below unity in most cases demonstrates the necessity to account for transient dynamics when optimizing

readout speed.

3.3 Including the Purcell filter in the SNR optimization

For sub-microsecond integration times, Purcell filters are needed to get high enough χ and κ while keeping the Purcell decay rate negligible [Jeffrey14, Walter17, Bronn17, Heinsoo18]. The semi-classical Langevin equation for such a system [Fig. 2.12 (b)] in the frame rotating at the drive frequency ω_d and when the qubit is in state $|k\rangle$ is [Sete14]

$$\begin{aligned}\dot{\alpha}_{k,r} &= -i(\omega_k - \omega_d)\alpha_{k,r} - iJ\alpha_{k,f} \\ \dot{\alpha}_{k,f} &= -i(\omega_p - \omega_d)\alpha_{k,f} - iJ^*\alpha_{k,r} - \frac{\kappa_f}{2}\alpha_{k,f} - i\varepsilon\end{aligned}\quad (3.13)$$

with $\alpha_{k,r}$ and $\alpha_{k,f}$ the coherent state number inside the resonator and Purcell filter mode, ω_k the resonator frequency, ω_p the resonance frequency of the Purcell filter, J the resonator-filter coupling rate, and κ_f the Purcell filter linewidth. Using the same method as for the single resonator case, one can find an analytical solution of the SNR ($= 4\kappa_f \|\beta_f\|_{2,\tau}^2$). We assume without proof that, like in the single-resonator case, the SNR is optimal when $n_g = n_e = n$ and determine the drive frequency so that this condition is fulfilled (see appendix C). Then the SNR can be expressed as in Eq. (3.11), except that the normalized SNR function f is now a function of $\chi\tau$, $J\tau$, $\kappa_f\tau$, and $\delta\tau$. Here $\delta = \omega_p - (\omega_g + \omega_e)/2$ is the detuning between the Purcell filter and the mean frequency of the resonator.

Finite values of δ typically degrade the SNR and therefore targeting $\delta = 0$ is desirable. In practice, because the resonator frequencies are affected by parameters which are sensitive to fabrication or wiring imperfections, such as the output impedance, substrate over-etch or stray capacitances to airbridges, the value of δ obtained experimentally can be significantly inaccurate [Heinsoo18, Kurpiers18, Magnard20]. However, for simplicity, we first consider the ideal case where $\delta = 0$.

Further, by fixing the ratio $r = J/\kappa_f$, the normalized SNR function f can be expressed as a function of $\chi\tau$ and $\kappa\tau$, where we use Eq. (2.54) to define the effective external coupling rate $\kappa = 4r^2\kappa_f$ [Sec. 2.1.6]. Then we can compare the difference of SNR in the the presence and absence of a Purcell filter. For $r = 1/10$, we have $(4J)^2 \ll \kappa^2$, the Purcell filter can be adiabatically eliminated, and the normalized SNR is very similar to that in the non-filtered case [Fig. 3.1 (b)]. However, as discussed in Sec. 2.1.6, larger r are beneficial to further suppress Purcell decay [Eq. (2.56)]. For

higher ratios, *e.g.* $r = 1/3$, f differs from the non-filtered case in the following ways: lower values of χ/κ (small θ) are favoured at low $\tilde{\tau}$, f rises with a delay in $\tilde{\tau}$, and the optimal choice of κ is an even bigger fraction of χ when optimizing under the constraint $\chi\tau < \chi_{\max}\tau$ [Fig. 3.1 (c)].

3.4 SNR reduction due to experimental parameter uncertainty

So far, we considered that the detuning δ between the resonator and the Purcell filter is zero, but its experimental value will be finite because of its sensitivity to fabrication imperfections. Greater magnitudes of δ typically degrade the SNR. One way to qualitatively understand the impact of Purcell filter misalignment is to determine its effect on the effective external coupling rate κ . Noting from Eq. (2.54) that κ reaches a maximum $\kappa_0 = 4J^2/\kappa_f$ at zero detuning, and expressing the Purcell decay rate $\Gamma = (g^2/\Delta^4)J^2\kappa_f = t_c^2J^2\kappa_f$, we can rewrite Eq. (2.54) in terms of κ_0 , Γ and δ by substituting $J^2 = \sqrt{\kappa_0\Gamma}/2t_c$ and $\kappa_f = 2\sqrt{\Gamma/\kappa_0}/t_c$:

$$\kappa = \kappa_0 \frac{1}{1 + \left(\delta t_c \sqrt{\frac{\kappa_0}{\Gamma}}\right)^2}. \quad (3.14)$$

κ depends on δ as a Lorentzian of amplitude κ_0 and bandwidth $2\sqrt{\Gamma/\kappa_0}/t_c$. Because we already fix κ_0 to optimize the SNR, improving the bandwidth of this Lorentzian, and thus the robustness of the SNR on δ , must be achieved at the expense of larger Purcell decay Γ .

Other elements which depend on δ , such as the optimal drive frequency, also affect the SNR. Therefore our analysis based on Eq. (3.14) does not account for these effects, therefore it should be seen as a qualitative description which helps gaining intuition on the problem. To qualitatively assess the dependence of the SNR on δ , we use the SNR derived from Eq. (3.13) for the full system (appendix C). Guided by our qualitative analysis, we first observe the dependence of the SNR on readout parameters for fixed Purcell decay times T_1^p .

For instance, using the parameter values introduced at the end of the previous section, we fix $J^2\kappa_f$ such that $T_1^p = 500\ \mu\text{s}$ and compute the dependence of the SNR on δ for various values of J and corresponding κ_f . Interestingly, for a fixed T_1^p , there is one particular choice of J and corresponding κ_f which yields better SNR than any

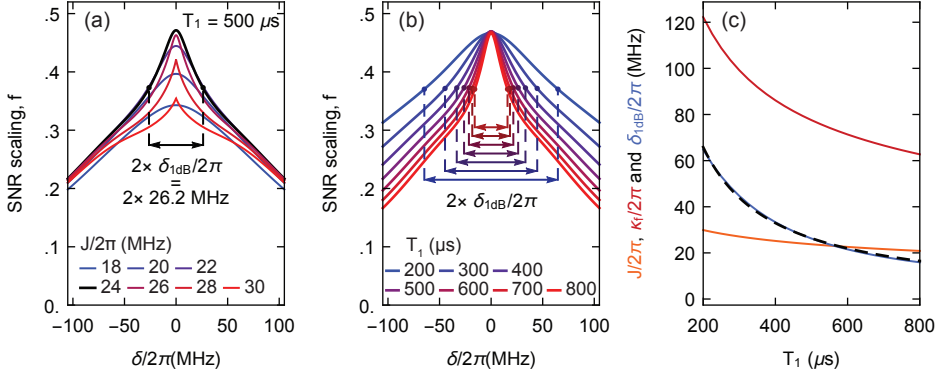


Figure 3.2 (a) SNR scaling factor f vs detuning δ between the readout resonator and its Purcell filter, for fixed $\chi/2\pi = 8$ MHz, $\tau = 50$ ns and $T_1^p = 500 \mu$ s, and for various J (and corresponding κ_f). The thicker black curve corresponds to the optimal choice of J and κ_f , maximizing the SNR over the full range of δ . (b) SNR scaling factor f vs δ for various Purcell decay time T_1^p using the optimal choice of J and κ_f . The arrows in (a,b) indicate the misalignment tolerance bandwidth δ_{1dB} . (c) Optimal values of J (orange) and κ_f (red), and misalignment tolerance bandwidth δ_{1dB} (blue) vs Purcell decay time T_1^p . The black dashed line is a fit of the form $\delta_{1dB} \propto 1/T_1^p$.

other parameter, and for all detuning δ [black curve in Fig. 3.2 (a)], therefore, we can unambiguously define an optimal choice of J and κ_f [Fig. 3.2 (c)]. The comparison of such optimal SNR curves for various T_1^p shows that higher T_1^p leads to a sharper SNR reduction with δ without affecting the peak SNR at $\delta = 0$ [Fig. 3.2 (b)], as expected from our qualitative analysis (Eq. (3.14)).

To quantify the robustness of the SNR on δ , we introduce a new metric, the “misalignment tolerance bandwidth” δ_{1dB} , defined as the misalignment δ at which the SNR is reduced by 1 dB ($\sim 79.8\%$) compared to the peak SNR at $\delta = 0$ [arrows in Fig. 3.2 (a,b)]. To illustrate the physical meaning of this metric: the readout fidelity is equally affected by a misalignment $\delta = \delta_{1dB}$ and by a 1 dB reduction of the detection efficiency (e.g. 1 dB loss before the first amplifier). It is therefore important to ensure that the experimental uncertainty on δ is small compared to δ_{1dB} . From the \sqrt{f} dependence of the bandwidth of κ in Eq. (3.14), we would expect that δ_{1dB} is proportional to $1/\sqrt{T_1^p}$, however, due to the dependence of the SNR on other δ -dependent parameters, we rather observe that $\delta_{1dB} \propto 1/T_1^p$ [black dashed line in Fig. 3.2 (c)]. The Purcell decay / tolerance bandwidth product $\delta_{1dB} \times T_1^p/2\pi \simeq 13000$ is fixed by χ , α and Δ and quantifies the compromise to make between δ_{1dB} and $\times T_1^p$.

3.5 Considering non-linear effects for readout

At low levels of n/n_c , we expect Eq. (3.11) to faithfully predict the SNR [Walter17], and second-order corrections can be applied for better accuracy [Boissonneault09]. We note that those second order correction terms lead to an improved (degraded) SNR when Δ and α have opposite (same) signs, which is another reason to design a readout circuit where $\alpha/\Delta < 0$. However the linear model fails to account for measurement-induced state mixing, which typically limits the readout fidelity in practice [Walter17, Reed10a, Jeffrey14]. We are aware of three mechanisms which can lead to qubit state mixing during readout: (i) the power dependence of the qubit decay and thermal excitation rates of dressed states [Boissonneault10], (ii) dressed-state dephasing [Boissonneault09, Boissonneault10], and (iii) Jaynes-Cumming resonances due to counter-rotating wave coupling terms [Sank16].

Spontaneous qubit decay and thermal excitation

According to Ref. [Boissonneault10], the qubit decay and thermalization rates between dressed states decreases with increasing number of photons in the readout resonator. However higher readout power increase leakage from the dressed state $|e\rangle$ to higher levels. Because leakage from $|e\rangle$ to higher levels impacts QND-ness but not readout fidelity, we do not consider (i) as a critical effect for our application.

Dressed dephasing

Dressed-state dephasing is a phenomenon where the qubit state can flip through a three-wave mixing spontaneous up/down-conversion process involving a resonator photon, a qubit excitation, and a photon which parametrically modulates the qubit frequency at frequency Δ . The state-mixing rate is then proportional to the readout power n/n_c , and the σ_z noise $\nu^2 S_\phi(\Delta)$ on the qubit frequency [Boissonneault09, Boissonneault10], as was demonstrated experimentally in Ref. [Slichter12]. Dressed dephasing can therefore be mitigated by lowering the sensitivity ν of the qubit frequency to flux or charge noise (e.g. parking the qubit at a sweetspot during readout), or by selecting higher values of Δ to reduce the magnitude of the environmental noise at the relevant frequency ($S_\phi(\Delta) \propto \Delta^{-a}$ with $a \sim 0.5 - 1$ [Slichter12, Bialczak07, Bylander11]). The proportionality of dressed dephasing mixing rate with n/n_c illustrates perfectly the compromise one has to do on readout power to maximize the SNR while maintaining low enough state-mixing errors. In practice, the optimal readout power is chosen

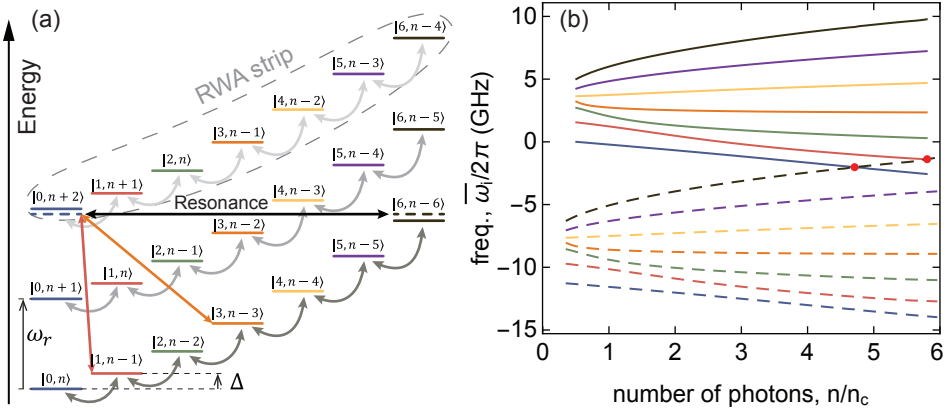


Figure 3.3 (a) Energy level diagram of the Jaynes-Cummings Hamiltonian for $\omega_q/2\pi = 7.2$ GHz, $\omega_r/2\pi = 5.64$ GHz, $\chi/2\pi = -8$ MHz, $\alpha/2\pi = -350$ MHz and $n = 58$. The dashed levels show the energy of the dressed states. The curved grey arrows represent the interaction terms $g_{k,k-1}\sqrt{m}|k-1, m\rangle\langle k, m-1| + h.c$ kept under the RWA, and connect levels belonging to the same RWA strip. Interaction terms dropped under the RWA are shown as colored straight arrows. The black horizontal arrow highlight the resonance between states $|0, n+2\rangle$ and $|6, n-6\rangle$. (b) Renormalized energies $\bar{\omega}_i$ of states $|i, n-i\rangle$ (solid lines) and $|i, n-2-i\rangle$ (dashed lines) vs excitation number n . Red dots indicate resonances between next-nearest-neighboring RWA strips.

experimentally [Walter17].

Level crossings beyond RWA

At high drive power ($n \geq n_c$), the transmon population can leak into highly excited states due to resonances mediated by counter-rotating wave coupling terms [Sank16]. States with the same number of excitation n are coupled in a chain via excitation-number-preserving terms, which are kept under the rotating-wave approximation [RWA, see Fig. 3.3 (a)]. Under the RWA, population can be exchanged only within such an ‘‘RWA strip’’, but counter-rotating wave terms couple states from next-nearest neighbour RWA strips, where n differs by 2 (e.g. $|j, n-j\rangle$ and $|j+1, n+1-j\rangle$, where the first and second number represent the transmon state, and the Fock state of the readout resonator, respectively). Because the coupling between levels within an RWA strips is proportional to \sqrt{n} , the dressed state within an RWA strip repel each other more as n increases. For some values of n , the state $|0, n\rangle$ or $|1, n-1\rangle$ couples resonantly, via multiple intermediate state, with a state from the next-nearest neighbouring RWA strip and exchange population with it [black arrow in Fig. 3.3 (a)]. This is illustrated in Fig. 3.3 (b), where we compute the renormalized energies ($\hbar = 1$) $\bar{\omega}_i(n) = \omega_{i,n} - n\omega_r$,

of the dressed eigenstates $|i, n - i\rangle$ for a given RWA strip, where ω_r is the resonator frequency, using the method described in [Sank16]. As expected, we observe that the RWA strip levels fan out with increasing drive power n (solid lines in Fig. 3.3). The next-nearest neighbouring RWA strip has the same curve with an offset of $2\omega_r$ [dashed line in Fig. 3.3 (b)]. Resonances between these RWA strips happen where lines cross and are indicated by the red dots.

Transitions between nearest-neighboring RWA should in principle be forbidden, due to the symmetry of the transmon potential, but such transitions were nonetheless observed experimentally in [Sank16] and should therefore be considered. The nearest-neighboring RWA strip is only offset by ω_r , therefore it crosses with the main RWA strip at much lower drive powers.

To push the resonances to higher powers, D. Sank et al. [Sank16] recommend to decrease the ratio Δ/ω_r . Indeed, a resonance between (next-)nearest neighbours RWA strips of order k cannot occur if the RWA strip frequency spread $\Delta_{\text{RWA}}^{(k)} = |\bar{\omega}_k - \bar{\omega}_0|$ is smaller than the inter-RWA strip splitting $(2\times)|\omega_r|$. From the approximate formula

$$\Delta_{\text{RWA}}^{(k)} \simeq \left| k\Delta + k(k-1)\frac{\alpha}{2} \right|, \quad (3.15)$$

we see that this condition can be achieved as long as Δ is sufficiently low compared to ω_r . By considering more transmon states in the RWA strip, e.g. from $|0, n\rangle$ to $|k, n - k\rangle$ with a growing k , the RWA strip frequency spread increases. Therefore there is always a value of k for which a resonance between $|0, n\rangle$ and $|k, n + 2 - k\rangle$ happens at low enough power to be bothering. However, the number of intermediate states involved in the resonance increases linearly with k (e.g. $|1, n + 1\rangle, |2, n\rangle \dots |k - 1, n + 1 - k\rangle$), therefore the effective coupling rate should vanish at large k , especially for low n/n_c . Finally, we note that $\Delta_{\text{RWA}}^{(k)}$ is smaller when Δ and α have opposite signs, which is yet another advantage of such a design choice for readout.

3.6 Parameter optimization procedure

From the arguments discussed above, we propose the following procedure to find the optimal readout circuit target parameters:

1. Maximize the anharmonicity α of the transmon, under the constraint that charge dispersion and qubit-qubit cross-talk stay at an acceptable level.
2. Consider opting for a circuit design where Δ and α have opposite signs. It leads

to higher SNR, higher χ_{\max} , favourable second-order corrections to the SNR and smaller RWA strip frequency spread. Such a configuration might be inconvenient for other applications, such as performing gates with flux-tunable qubits, so one should weight pros and cons carefully.

3. Choose Δ , with considerations on frequency crowding, and making a trade-off between Purcell decay, RWA strip crossings and dressed dephasing.
4. Prefer a qubit parking frequency with small Ramsey dephasing rate for readout, to minimize dressed dephasing.
5. Set a short but realistic integration time τ , e.g. such that the expected SNR $\sim 0.6\eta(1/5)\tilde{\alpha}\tau$ is sufficiently high.
6. Maximize χ under the constraint to stay in the dispersive regime. If the optimal normalized SNR $\max_{\kappa} f(\chi\tau, \kappa\tau)$ is too small, come back to step 5 and set a larger τ .
7. Choose T_1^p making a good compromise with δ_{1dB} . If $\delta_{\text{1dB}}T_1^p$ is too small, come back to step 6 and set a smaller χ_{\max} .
8. Choose the optimal J and κ_f for this fixed T_1^p .
9. If the SNR or $\delta_{\text{1dB}}T_1^p$ is larger than necessary, consider choosing a higher χ_{\max} , a smaller integration time τ , and start over from 5.

By applying this optimization procedure under the requirements formulated in Sec. 2.2.4, where one needs to perform high fidelity readout in less than 50 ns to close the locality loophole in a 30 m long Bell test setup, we obtain the parameters listed in table 3.2. We choose a conservative value of $T_1^p = 400 \mu\text{s}$ for several reasons. First, one should consider all Purcell decay channels to evaluate the Purcell limit on T_1 . For the SuperQuNet project, setting $T_1^p = 120 \mu\text{s}$ for the drive line and $T_1^p = 400 \mu\text{s}$ for the transfer resonator leads to a Purcell limit of $75 \mu\text{s}$, which already has noticeable effects on T_1 . Second, the Purcell decay is stronger for the $e - f$ transition, *a fortiori* when Δ and α have opposite signs, leading to an $e - f$ Purcell limit of $28 \mu\text{s}$ only.

name	symbol (unit)	value
integration time*	τ (ns)	50
qubit frequency*	$\omega_q/2\pi$ (GHz)	7.2
anharmonicity*	$\alpha/2\pi$ (MHz)	-350
g-e charge dispersion limit	$T_{2,c}^{ge}$ (μ s)	900
e-f charge dispersion limit	$T_{2,c}^{ef}$ (μ s)	18.6
qubit/res detuning*	$\Delta/2\pi$ (MHz)	1560
readout power*	n/n_c	0.2
res /Purcell filt. detuning*	$ \delta /2\pi$ (MHz)	< 15
res /Purcell filt. coupling*	$J/2\pi$ (MHz)	25.2
Purcell filt. ext. coupling*	$\kappa_f/2\pi$ (MHz)	87
dispersive shift*	$\chi/2\pi$ (MHz)	-8
qubit res. coupling	$g/2\pi$ (MHz)	208
Purcell limit ge	T_1^p (μ s)	400
Purcell limit ef	$T_{1,ef}^p$ (μ s)	72
Misalignment tolerance BW	$\bar{\delta}_{1dB}/2\pi$ (MHz)	33
detection efficiency	η (%)	> 65
readout fidelity	F (%)	> 98

Table 3.2 Readout circuit parameters optimized under the constraints derived in Sec. 2.2.4. The asterisk* marks design parameters which are primarily set, and from which the other parameters are derived.

Chapter 4

Prototyping of a Cryogenic Link Technology

One Kelvin seems cold, but not from the point of view of a microwave photon.
— An altruist high-energy boson

Superconducting circuits are one of the top-contending quantum computing platforms [Blais21, Andersen20a, Arute20, Jurcevic20], but it is rarely considered to realize quantum networks [Kimble08, Duan10, Awschalom21]. This is likely because of the absence of a natural interface between superconducting circuits and optical photons, the workhorse of quantum networks [Pirandola16]. Coherence-preserving microwave-to-optical quantum transducers would realize this interface, but despite great advances, realizing such a device remains elusive [Hease20, Mirhosseini20]. By contrast, itinerant microwave photons can be interfaced with superconducting qubits with near-unit fidelity [Wallraff04, Wenner13, Pechal14, Pfaff17, Ilves20, Besse20b], and therefore constitute an ideal information carrier, enabling deterministic, high-fidelity, bidirectional and error-correctable quantum communication between remote superconducting devices [Kurpiers18, Axline18, Campagne-Ibarcq18, Leung19, Burkhardt21, Zhong21]. However, unlike optical photons in fiber optics, microwave photons must propagate in a cryogenic environment to reduce photon loss [Kurpiers17] and thermal background to acceptable levels [Xiang17]. Therefore, a microwave quantum network must take the form of a cryogenic network.

In this chapter, we present a modular cryogenic link solution to connect super-

conducting circuits via cold and lossless microwave waveguides over tens of meters distance. Thanks to a heat-transfer-optimized design, we realize elementary cryogenic networks as large as 30 m, and anticipate this distance could be extended to 100 m.

4.1 Dilution Refrigerator

Superconducting quantum devices operate at frequencies ω_q in the few GHz regime, which requires temperatures much lower than $\hbar\omega_q/k_b \sim 200$ mK. Such cryogenic environment can be provided for macroscopic systems of a few kilograms by state-of-the-art, commercial dilution refrigerators. In our experiments, we use the cryogen-free dilution refrigerator (BF-LD400 from BlueFors Cryogenics Oy Ltd.), shown in Fig. 4.1 (a), which consists of five gold plated copper plates held at approximate temperatures of 50 K, 4 K, 1 K (still plate), 100 mK (cold plate) and 10 mK (base temperature plate). The system is housed in a vacuum can sealed with rubber o-rings and pumped to high vacuum levels. This suppresses heat transfer through gas, from the lab environment at room temperature, to the refrigerated parts, and between the temperature plates.

The 50K and 4K plates are cooled with a pulse tube cooler (PT-415 from CryoMech Inc). Using a set of heaters and temperature sensors on the 50K and 4K plates, we measure the 50K and 4K plate temperatures vs the heat generated on each plate, to probe how much power the pulse tube can cool for a given plate temperature [Fig. 4.1 (b)]. We measure a cooling power of 20 W at 55 K on the 50K stage, and 1.5 W at 5.5 K to the 4K stage. Interestingly, we observe that the 4K cooling power depends little on the 50K temperature, as witnessed by the flat horizontal lines in Fig. 4.1 (b), whereas the 50K cooling power decreases with increasing 4K temperature, as witnessed by the slanted vertical lines in Fig. 4.1 (b).

To cool the still and base temperature (BT) stages to even lower temperatures, the refrigerator uses a dilution unit which removes heat from the mixing chamber via the dilution of ^3He into a helium mixture phase rich in ^4He [Lounasmaa74]. For each stage, we measure the plate temperature for various values of applied heat. We observe a quadratic increase of the cooling power with temperature, which reaches 20 mW at 1 K for the still stage, and $400 \mu\text{W}$ at 100 mK for the base temperature stage [Fig. 4.1 (c,d)].

The outer surface of the vacuum can is in contact with ambient air. It is therefore at a room temperature of approximately $T_{\text{RT}} \simeq 295$ K. Its inner surface behaves as a gray body: i.e. it absorbs and emit a fraction ε , called the emissivity, of black-body radiation. This corresponds to $\varepsilon\sigma T_{\text{RT}}^4 \sim 20 \text{ W/m}^2$, where σ is the Stefan-Boltzmann constant,

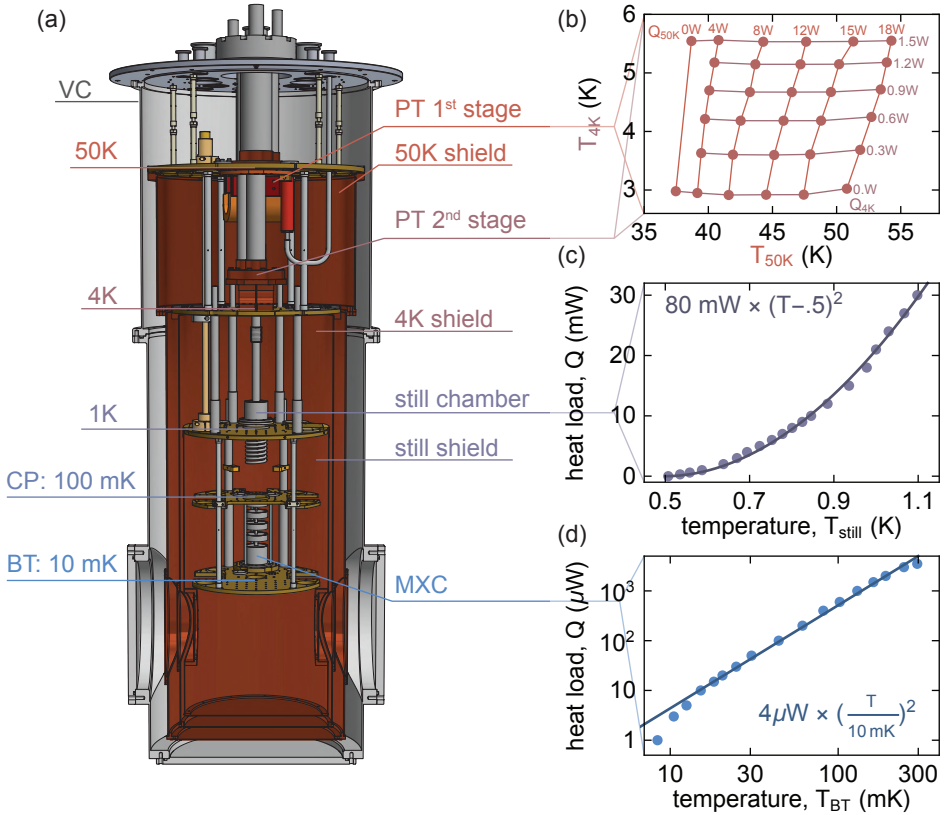


Figure 4.1 (a) Schematic of the the first of the two LD-400 BlueFors dilution refrigerator used in the experiments presented in this thesis. (b) 50K and 4K stage temperature vs heat applied on the 50K (red vertical lines) and the 4K stages (purple horizontal lines). (c) and (d), stage temperature vs heat applied on the still and base temperature stages, respectively. The solid lines are fits to power laws. VC: vacuum can; CP: cold plate; BT: base temperature; MXC: mixing chamber; PT: pulse tube.

and $\varepsilon \sim 0.05$ is the emissivity of roughly polished aluminum [Estalote77, Musilova05, Lienhard20]. The resulting heat load on the 50K stage is lower or comparable to the 50K stage cooling power, but higher than the cooling power of any colder stage. Therefore, a 50K radiation shield prevents room temperature radiation from heating the colder stages. Similarly, radiation shields at the 4K and still stages shield the colder stages from gray-body radiation emitted by the 50K and 4K shields, respectively [see Fig. 4.1 (a)].

4.2 General Design of the Cryogenic Link

The dilution refrigerators constitute the nodes of cryogenic networks. To connect these nodes with a cold microwave link suitable for quantum communication, we design a cryogenic link system consisting of a vacuum can enclosing a set of concentric, octagonal, radiation shields made of copper, which are connected to and cooled by the 50K, 4K, still and BT stages of the node nearby [Fig. 4.2 (a-c)]. A WR90, rectangular, aluminum waveguide, serving as the quantum bus for microwave photons, is hosted inside the BT shield, to which it is thermalized every 25 cm using flexible copper braids.

The cryogenic link is made of 2.5 m long link modules, which can be connected to each other to increase the link length [Fig. 4.2 (a,d)]. In a link module, each shield is supported by two sets of three thin-walled, low-heat-conductance posts [Fig. 4.2 (b,d,e)]. The vertical post carries the weight of the shields, and the side-posts ensure the structure's stability. The posts are fixed to a single shield. This allows the shields to slide freely relative to each other in the longitudinal direction ensuring a stress-free differential thermal contraction of the shields [see blue arrows in Fig. 4.2 (d)]. The waveguide can slide freely along the longitudinal axis of the link over ~ 10 cm in each direction, which is required to cope with its thermal contraction [Fig. 4.2 (d,e)].

To connect two link modules with each other, we first position them to accurately align their vacuum cans. Then we connect the waveguide flanges with four brass screws [Fig. 4.2 (f)]. For each temperature stage, we cover the gap in-between the two modules with a small radiation shield which is mechanically and thermally attached to one of the modules, and can slide over the shield of the other module. The two modules are then thermally connected to each other by a set of flexible, high-conductivity, copper braids. The braids give a ~ 2 cm slack, necessary for the shield of each module to thermally contract without buildup of mechanical strain, see blue arrows in Fig. 4.2 (f). Indeed, each shield shrinks by about 8 mm when cooled from RT to 50K or below. We connect the vacuum cans of the two modules with a sliding vacuum can [see Fig. 4.2 (f)].

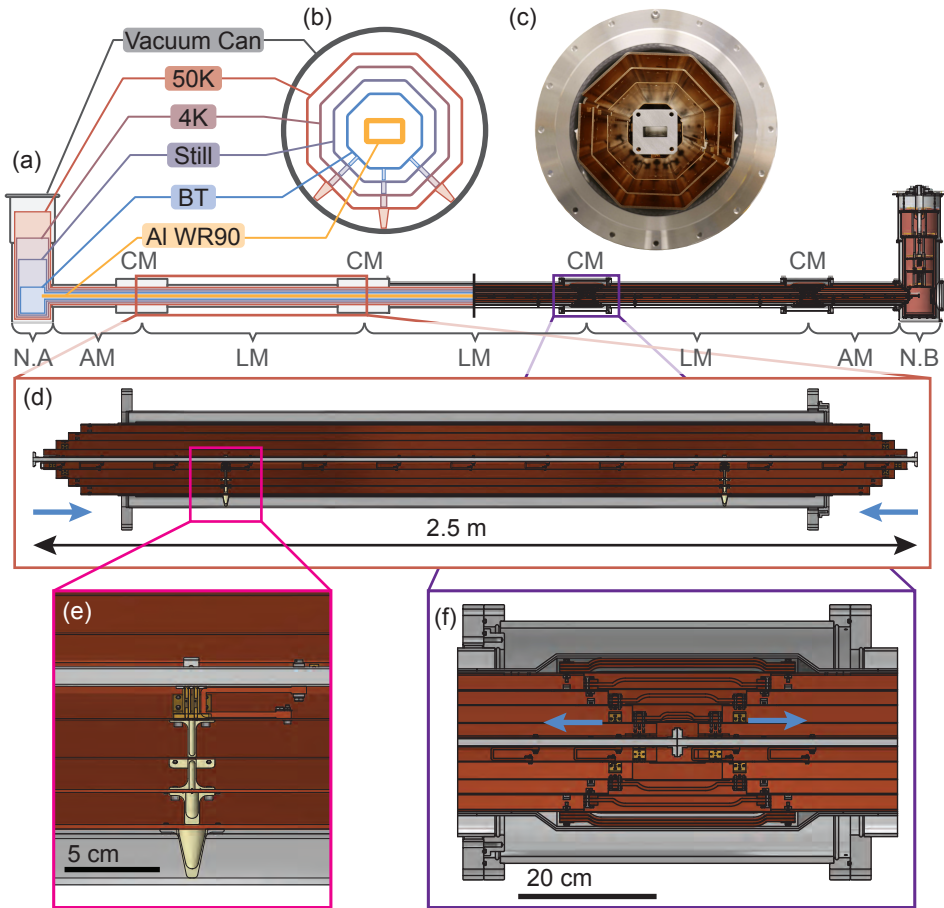


Figure 4.2 (a) Longitudinal cross-section of a schematic representation (left half) and a 3D model (right half) of a cryogenic link system. (b) Schematic representation, and (c) picture of a transverse cross-section of a link element. (d) Longitudinal cross-section of the 3D model of a link module. (e) Enlarged cross-sectional view of the set of posts which mechanically support the shields of the link module. (f) Enlarged cross-sectional view of the set of a connection between two link modules. The blue arrows in (d) and (f) show the direction in which the copper shield ideally move during a cooldown due to thermal contraction. N.A/N: node A/B; AM: adapter module; LM: link module; CM: connection module.

We refer to the set of braids, shields and cans used to connect two link modules as a *connection module*.

The link connects to the side of a dilution refrigerator via an *adapter module*: a 1.25 m long, special type of link module whose shields are rigidly connected to the side-port flanges of the dilution refrigerator [see Fig. 4.1 (a)].

4.3 Heat Transfer

A key aspect in the successful design of the cryogenic link is to understand and optimize its thermal properties. To that end, we developed a simplified model of heat transfer between the different temperature stages of a cryogenic link, and another one describing how the propagating field of the waveguide thermalizes to the base-temperature shield of the link.

4.3.1 Between Radiation Shields

Consider a cryogenic link connecting two nodes at a distance l from each other. We model each temperature stage n of the cryogenic link as a one-dimensional object subject to lateral heat loads, cooled at its ends [Fig. 4.3 (a)]. The heat loads stem exclusively from heat exchanges with the enclosing stage $n+1$, either via gray-body radiation or via thermal conduction through the support posts, as indicated in Fig. 4.3 (b) by the wiggling and straight red arrows, respectively. We neglect heat exchange via residual gas in the vacuum can.

As shown below, the lateral heat leaving stage n to stages $n \pm 1$ is typically proportional to T_n^b , with $1 \leq b \leq 4$. Assuming that $T_n \ll T_{n+1}$, it is therefore much smaller than that entering stage n and can be neglected. Radiative heat loads can be well approximated by that of two concentric cylindrical gray-bodies of emissivity $\varepsilon_n, \varepsilon_{n+1} \ll 1$ [Lienhard20, Parma14, Kurpiers19b]

$$\varphi_{\text{rad}} \simeq \lambda \sigma T_{n+1}^4, \quad (4.1)$$

with the attenuation factor λ defined as

$$\frac{1}{\lambda} \simeq \frac{1}{\varepsilon_n} + \frac{F}{\varepsilon_{n+1}},$$

and with $F = C_n/C_{n+1}$ the form factor, and C_i the circumference of the shield at stage i . Modeling the posts as one-dimensional bars with zero lateral heat flow and integrating

Fourier’s law, we obtain the heat load per post

$$Q_{\text{post}} = \frac{A_p}{l_p} \int_{T_n}^{T_{n+1}} \rho(T) dT \approx \frac{A_p}{l_p} \int_0^{T_{n+1}} \rho(T) dT, \quad (4.2)$$

with l_p the post length, $1/A_p$ the 1D average of its inverse cross-section area, and ρ its thermal conductivity. The approximation holds for $T_n \ll T_{n+1}$. An additional term should be accounted for if the radiation load on the post is comparable to the conductive load. As a result, heat loads on stage n are fully determined by the temperature profile T_{n+1} of stage $n + 1$ and by fixed geometrical and thermal parameters.

Due to symmetry, we can consider only the left half of the link ($x < l/2$). In this half, all heat loads must flow towards the left node and generate a left-flowing heat

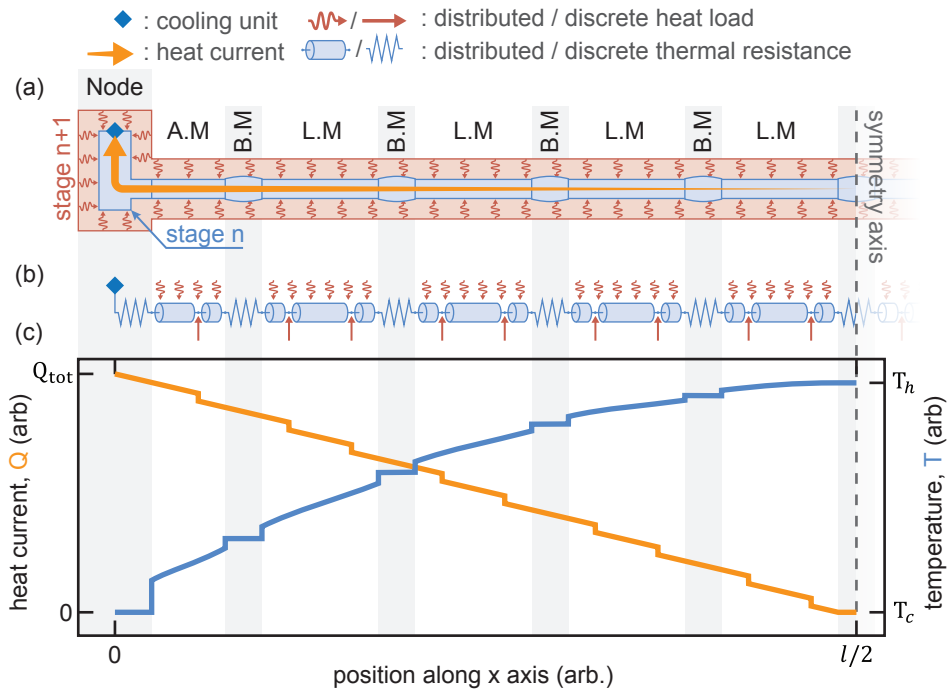


Figure 4.3 (a) Schematic representation of heat transfers from stage $n + 1$ to the next colder stage n . The increasing width of the orange arrow depicts the increasing heat current flowing along the link. (b) Equivalent electrical circuit used to model the heat transfer from stage $n + 1$ to stage n . (c) Representative curves of the heat current (orange) and temperature (blue) profiles along the link. Here, Q_{tot} is the sum of all heat loads on the half section of stage n , T_c is the temperature at the cooling unit, and T_h is the maximum temperature, reached in the middle of the link.

current

$$Q(x) = \int_x^{l/2} \psi_{\text{eff}}(x) dx,$$

which is fully determined by the effective heat load per unit length $\psi_{\text{eff}}(x)$. The current $Q(x)$ increases smoothly as it accumulates distributed heat loads (radiation), and by steps at each point-like heat load (posts), as qualitatively shown by the orange arrow and the orange curve in Fig. 4.3 (a,c).

The total heat load $Q_{\text{tot}} = Q(0)$ received by the cooling node determines the node temperature T_c , according to the capacity curve of the cooling unit [see Fig. 4.1 (b-d)]. Knowing the boundary condition $T_n(0) = T_c$ and the heat current distribution $Q(x)$, one can integrate Fourier's law in one dimension

$$Q(x) = A_n \rho(T_n) \frac{\partial T_n}{\partial x}, \quad (4.3)$$

to determine the temperature profile. Here A_n is the cross-sectional area of the shield of stage n and ρ is its temperature-dependent thermal conductivity. Like the heat current, the temperature gradient is maximal at the node, decreases with x and is zero at the symmetry point of the link [Fig. 4.1 (c)]. Heat current across a contact interface generates a finite temperature drop ΔT which can be characterized with the temperature-dependent *thermal contact resistance* $R := \Delta T/Q$ [Salerno97]. Therefore we model elements containing multiples contact interfaces, such as the node or the connection modules, as thermal resistances [Fig. 4.1 (b)], across which the temperature increase by a step $\Delta T = R(T)Q$ [Fig. 4.1 (c)]. This allows us to accurately model the temperature profile T_n . From this profile, one can iterate the method described above to model the temperature profile T_{n-1} of stage $n-1$, and by recursive iteration of the method, that of all colder stages.

To gain a qualitative understanding of this recursive model of heat transfer, we study a toy-model example in which T_{n+1} is uniform, the thermal conductivity ρ of the shields is independent of temperature, and the capacity curve of stage n is of the form $T_{c,n} = T_{0,n} + \alpha_n \sqrt{Q_{\text{tot},n}}$ [see Fig. 4.1 (b-d)]. The heat load per unit length on stage n is of the form $\psi_{\text{eff}} = \tilde{\psi} T_{n+1}^b$, with $b \in [2, 4]$ (see Sec. 4.8.1), and $\tilde{\psi}$ a scaling factor which depends on the geometry, the material and the emissivity of the shields and posts [see Eqs. (4.1) and (4.2)]. The solution $T_n(x)$ to Eq. (4.3) is a parabolic

curve with a maximum at $x = l/2$ and extremal temperatures

$$T_{c,n} = T_{0,n} + \alpha_n \sqrt{\tilde{\psi} l / 2} T_{n+1}^{b/2}, \quad (4.4)$$

$$T_{h,n} = T_{c,n} + \frac{\tilde{\psi}}{8A_n \rho} l^2 T_{n+1}^b. \quad (4.5)$$

The node temperature, T_c , increases as $\sqrt{l\tilde{\psi}}$, and depends linearly to quadratically on T_{n+1} . By contrast, the maximal link temperature depends linearly on $\tilde{\psi}$, quadratically on l , quadratically to quartically on T_{n+1} (depending on the value of b), and inversely proportionally to the shield conductance $A_n \rho$.

Because T_n is non-uniform, the result is different for stage $n - 1$. Supposing the link is long enough that $T_{h,n}^{b/2} \gg T_{c,n}^{b/2}$, and approximating T_n with $T_{h,n} \sim T_{h,n} - T_{c,n}$, the total heat load on stage $n - 1$ is $l\tilde{\psi} T_{h,n}^b$. Consequently the node temperature

$$T_{c,n-1} \simeq T_{0,n-1} + \frac{\alpha_{n-1}}{\sqrt{2}} \frac{1}{(8A_n \rho)^{b/2}} l^{b+1/2} \tilde{\psi}^{\frac{b+1}{2}} T_{n+1}^{b^2/2},$$

has a high power dependence on the length l , the heat load scaling factor $\tilde{\psi}$, the resistivity per unit length $1/A\rho$ and temperature T_{n+1} . As a result, there is a critical length the value of which increases with decreasing T_{n+1} , $\tilde{\psi}$ and $1/A\rho$, and above which $T_{c,n-1}$ and, by recursion, the temperature of all colder stages increase sharply, leading to a cooldown failure. It is therefore critical to aim at minimizing the temperature profile of all stages, which is achieved by minimizing $\tilde{\psi}$ and $1/A\rho$, to maximize this critical length.

4.3.2 Waveguide Field

To analyze the effective temperature of the microwave field propagating in the waveguide, we model the heat exchange between this field and the bosonic heat bath of the waveguide bulk as an interaction happening in a continuum of infinitesimal beam-splitters of size dx and reflection coefficient αdx [Xiang17], see Fig. 4.4. This yields the differential equation

$$\partial_x n = \alpha(n_{\text{th}} - n), \quad (4.6)$$

on the thermal occupation number n of the propagating field, with

$$n_{\text{th}}(x) = \frac{1}{\exp\left[\frac{h\nu}{k_b T_{\text{BT}}(x)}\right] - 1}$$

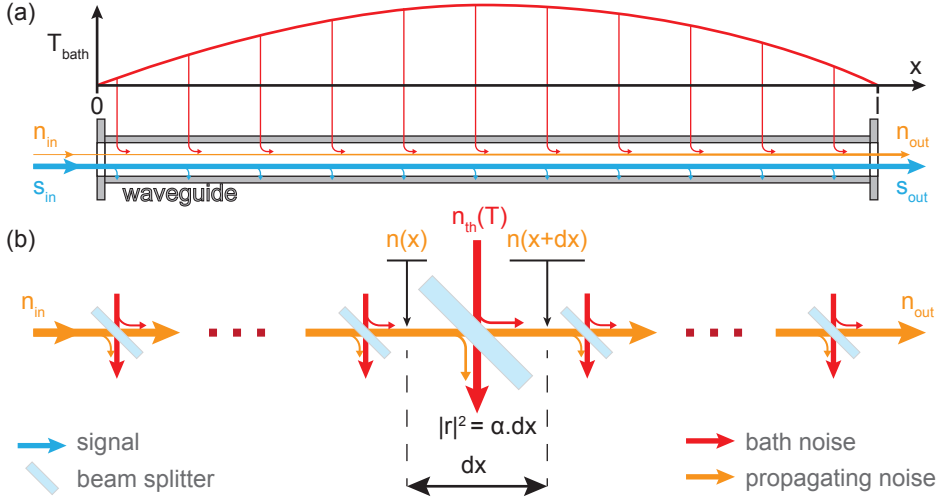


Figure 4.4 (a) Schematic of fields propagating inside the waveguide. The arrows leaving (entering) the waveguide represent signal lost to (noise added from) the waveguide bulk heat bath. The graph on top represents a typical temperature profile of the waveguide heat bath. (b) Infinitesimal beam splitter representation of the thermalization of the right-propagating noise-field of the waveguide with the waveguide heat bath.

the thermal occupation of the bath at the frequency ν of the propagating field, given by the Bose-Einstein distribution. Integrating Eq. (4.6) yields the relation

$$n_{\text{out}} = \eta n_{\text{in}} + \underbrace{\int_0^l \alpha \exp[-\alpha(l-x)] n_{\text{th}}(x) dx}_{n_{\text{added}}}, \quad (4.7)$$

with $1 - \eta = 1 - \exp[-\alpha l]$ the total waveguide loss.

In the low loss limit $\alpha l \ll 1$, the added noise simplifies to $n_{\text{added}} \simeq \alpha l \langle n_{\text{th}} \rangle$, where the average is taken over length. The added noise is directly proportional to the total loss $\alpha l \simeq 1 - \eta$ and the mean occupation number of the bath. Therefore, for a given link length l , the added noise is minimized by decreasing the temperature profile T_{BT} , increasing the photon frequency ν , and minimizing the loss rate α .

If a cold isolator is placed at the input of the waveguide, the the input noise $n_{\text{in}} = n_{\text{th}}(T_{\text{BT}}(0)) \ll 1$ can be neglected and the output noise corresponds to the added noise. In the absence of a circulator, by symmetry $n_{\text{in}} = n_{\text{out}}$, yielding

$$n_{\text{out}} = \frac{n_{\text{added}}}{1 - \eta} \simeq \langle n_{\text{th}} \rangle \frac{\alpha l}{1 - \eta}. \quad (4.8)$$

If the total loss $1 - \eta$ is due uniquely to waveguide loss, then Eq. (4.8) reduces to $n_{\text{out}} = \langle n_{\text{th}} \rangle$. Otherwise, if most of the loss comes from cold components connecting the quantum devices to the waveguide, such as coaxial cables or PCB transmission lines, then the field is mainly thermalized by these cold elements and $n_{\text{out}} \ll \langle n_{\text{th}} \rangle$.

4.4 Design Considerations to Optimize Heat Transfer

Our link design takes particular care to minimize heat loads and the effective resistivity per unit length at every temperature stages.

To mitigate the heat load Q_p carried by the support post, we fabricate them from Accura Bluestone: a vacuum-compatible material with very high ratio σ/ρ_p between compressive strength and thermal conductivity at cryogenic temperatures (see Sec. 4.8.1). In addition, unlike other materials which require mechanical machining, Bluestone is compatible with stereolithography 3D-printing, which enables the fabrication of posts with very thin walls and complex geometries reliably and at low cost. We design a cross-sectional area A_p such that the yield force $A_p\sigma$ is approximately five times the weight the post is designed to carry. The post length $l_p \sim 3$ cm is set as a compromise to minimize $Q_p \propto 1/l_p$ while keeping acceptable mechanical stability and compactness of the link. A detailed characterization of posts thermal and mechanical properties is presented in Sec. 4.8.1.

As depicted in Fig. 4.3 (b), the two elements contributing to the effective resistivity $1/A\rho$ of the link are the thickness and conductivity of the radiation shields, and the thermal resistances of the connection module and the cooling node. The shields are made of oxygen-free high-conductivity copper, with grade C10100, to ensure high thermal conductivity at cryogenic temperatures without the need for annealing. See Sec. 4.8.2 for details on the choice of copper and its material characteristics. The thickness of the shields, 1 mm for the BT and still stages, 2 mm for the 4K stage, and 3 mm for the 50K stage, is chosen as a compromise between their conductance and their weight. At low temperatures, the thermal contact resistances are proportional to T^{-2} , whereas the resistance of bulk copper pieces scales as T^{-1} (see Secs. 4.8.3 and 4.8.4). As a result, contact resistances are negligible on the 50K stage, are significant on the 4K and still stages, and limit the effective conductance of the link at base temperature. Therefore we mitigate contact resistances, by electropolishing the contact surfaces and greasing them with Apiezon N grease, on all stages except the 50K stage [Salerno97]. See Secs. 4.8.3 and 4.8.4 for a detailed characterization of contact resistances in the node shields and in the connection modules.

The largest heat load in the system stems from gray-body radiation emitted from the room-temperature vacuum can. Due to the low emissivity $\varepsilon \simeq 2\%$ of the 50K shield surface, the radiation load on the 50K shield is 7.5 W/m^2 in our system (see subsec-CLProp50KRad). Covering the 50K shields with a custom-designed set of multi-layer insulation (MLI) reduces this heat load further to below 1 W/m^2 , a level comparable to the effective post heat load per unit area. The MLI is therefore a crucial element to increase the critical length of the system. See Sec. 4.8.3 for an experimental characterization of the radiative heat load on the 50K shield with and without MLI. By contrast, because the radiative heat load decreases rapidly with the temperature of the radiating shield ($\propto T^4$), it becomes significant on the 4K stage only for $T_{50\text{K}} \gtrsim 100\text{K}$, and are negligible on the colder temperature stages. However, radiative heat leaks from the vacuum can or the 50K shields to the still and BT shields via cm^2 -sized holes in the shields in between can be significant. Therefore it is important that each temperature stage is assembled to be as radiation tight as possible.

We characterize the thermal parameters relevant for the heat transfer in a set of independent measurements described in Sec. 4.8. The result of this characterization is summarized in table 4.1.

4.5 Cryogenic Link Prototypes

We have assembled and cooled down three cryogenic link prototypes, bridging distances of 5 m, 10 m, and 30 m. See photographs in Fig. 4.5. The 50K and 4K stages of the 30 meter long cryogenic link is cooled by an additional, home-built cooling node in the middle of the link to keep their temperature profiles low enough for a successful link cooldown to mK temperatures across that distance [Fig. 4.5 (c)].

The nodes of the 5 m, 10 m, and 30 m link are cold enough to start condensing the Helium mixture 1.8 days, 3.4 days, and 5.7 days after the beginning of the cooldown, respectively. In all systems, the base temperature at the nodes reached below 20 mK approximately 4 hours after condensation. The cooldown time is mainly limited by heat diffusion in the 50K shield, from the middle of the link to the nodes, which happens with a characteristic diffusion time proportional to l^2 [Lienhard20] with l the distance between two 50K stage coolers.

Several extra days after the systems are condensed, the link temperature profiles reach the steady-state values shown in Fig. 4.6. For all systems, the 50K stage is everywhere below 90K, the 4K stage below 6K, the still stage below 1K and the base temperature below 50mK. As expected, the temperature profiles display minima

	50K	4K	still	BT
T_0	50K	4K	1K	10mK
P_0	$46(\tilde{T} - 3/4)^{0.7} \text{ W}$	$2.5(\tilde{T} - 3/4)^{1.2} \text{ W}$	$80(\tilde{T} - 0.5)^2 \text{ mW}$	$4\tilde{T}^2 \mu\text{W}$
Q_p	0.2 – 0.6W	$10\tilde{T}_h^{1.8} \text{ mW}$	$34\tilde{T}_h^{2.2} \mu\text{W}$	$120\tilde{T}_h^{3.3} \text{ nW}$
φ_{rad}	$\leq 1.1 \text{ W/m}^2$	$4\tilde{T}_h^4 \text{ mW/m}^2$	0	0
φ_{eff}	2.2 W/m^2	$(30\tilde{T}_h^{1.8} + 4\tilde{T}_h^4) \text{ mW/m}^2$	$150\tilde{T}_h^{2.2} \mu\text{W/m}^2$	$1\tilde{T}_h^{3.3} \mu\text{W/m}^2$
ψ_{eff}	1.4 W/m	$(13\tilde{T}_h^{1.8} + 2\tilde{T}_h^4) \text{ mW/m}$	$50\tilde{T}_h^{3.3} \mu\text{W/m}$	$0.2\tilde{T}_h^{3.3} \mu\text{W/m}$
t	3 mm	2 mm	1 mm	1 mm
RRR	230	220	140 – 200	140 – 200
R_n	$\frac{0.5 \text{ K/W}}{\rho_{25}^{\text{Cu}}(T)}$	$2.4\tilde{T}^{-2} \text{ K/W}$	$60\tilde{T}^{-2} \text{ K/W}$	$5\tilde{T}^{-2} \text{ K/mW}$
R_{LM}	$\frac{1 \text{ K/W}}{\rho_{230}^{\text{Cu}}(T)}$	$\frac{1.5 \text{ K/W}}{\rho_{230}^{\text{Cu}}(T)}$	$\frac{20 \text{ K/W}}{\rho_{200}^{\text{Cu}}(T)}$	$\frac{5.4 \text{ K/mW}}{\rho_{140}^{\text{Cu}}(T)}$
R_{CM}	$\frac{0.15 \text{ K/W}}{\rho_{320}^{\text{Cu}}(T)}$	$0.5\tilde{T}^{-2.6} \text{ K/W}$	$10\tilde{T}^{-1.7} \text{ K/W}$	$40\tilde{T}^{-2} \text{ K/mW}$

Table 4.1 Summary of all extracted thermal parameters relevant for modelling heat transfer inside a cryogenic link. Here, T_0 is the reference stage temperature, T is the actual stage temperature, T_h is the temperature of the next hotter stage, and $\rho_{\text{RRR}}^{\text{Cu}}$ is the thermal conductivity of copper with residual resistivity ratio RRR. Each quantity X is expressed with its unitless, renormalized quantity $\tilde{X} := X(T)/X(T_0)$. P_0 : cooling power of cooling unit; Q_p : post heat load; $\varphi_{\text{rad/eff}}$: radiative/effective heat load per unit area; ψ_{eff} : effective heat load per unit length; t : shield thickness; RRR: residual resistivity ratio; $R_{\text{n/LM/CM}}$: thermal resistance of the node / link module / connection module. See Sec. 4.1 for the measurement of P_0 , Secs. 4.8.1 and 4.8.5 for the measurement of heat load parameters Q_p , $\varphi_{\text{rad/eff}}$ and ψ_{eff} , and Secs. 4.8.2, 4.8.3 and 4.8.5 for the measurement of the RRR and thermal resistances.

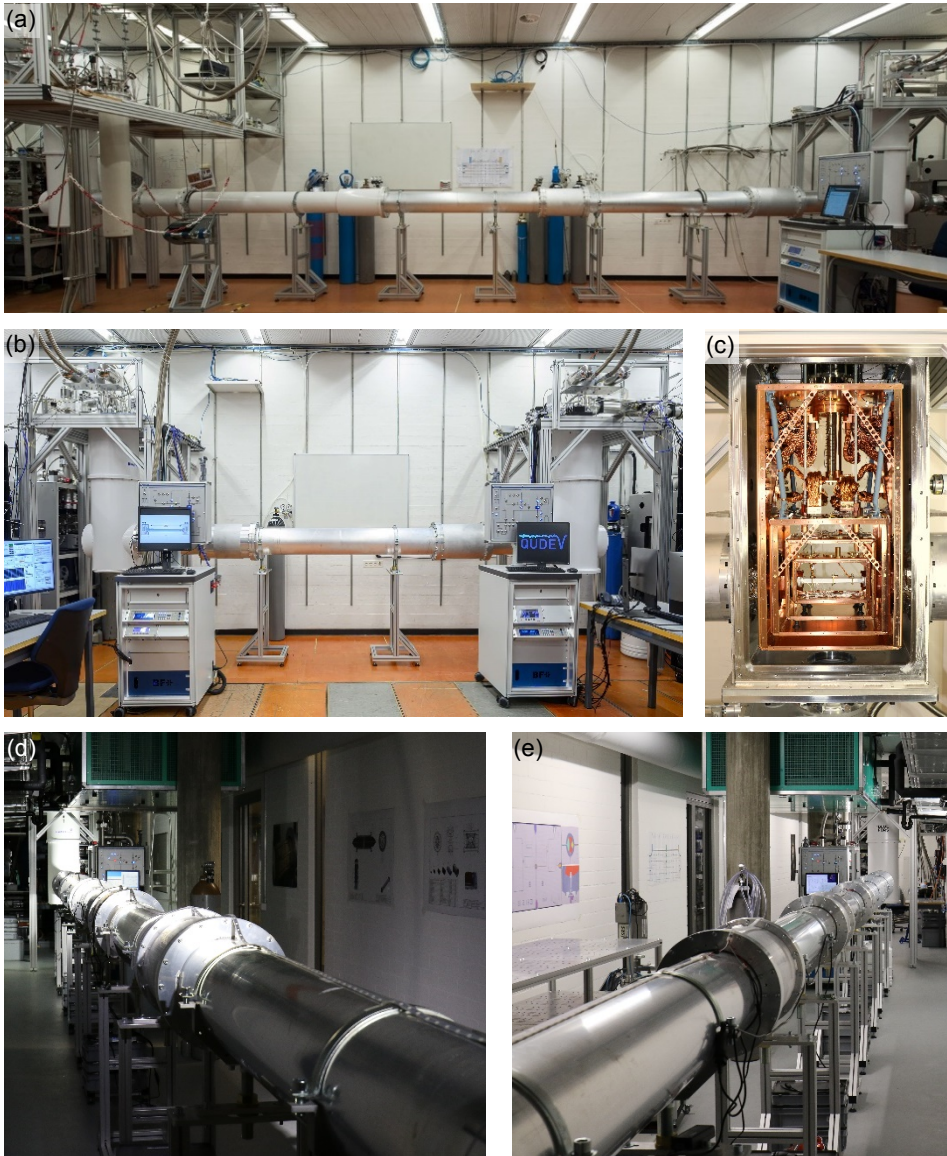


Figure 4.5 Photographs of cryogenic link systems. (a) 10 m link. (b) 5 m link. (c) Intermediate pulse tube cooler used to cool the center of the 30 m link, with side panels of every temperature stages removed. (d) and (e), views towards the opposite ends of the 30 m link.

at the cooling nodes and maxima in the center point between the coolers, with an exception for the still stage of the 5 m system for which we heated the right node to 900 mK to optimize cooling power by increasing the flow of ^3He . Moreover, as expected

from Eqs. (4.4) and (4.5), for all stages we observe that the node temperatures and the temperature drop across the link increase with the distance between two cooling units. Over the course of the cooldown, the temperature in the middle of the 50K shield increase slowly (0.5K a day for the 30 m system). We suspect this is due to gas diffusion through the orings of the vacuum can, which is adsorbed on the surface of the 50K shield leading to an increase in emissivity over time.

From the attenuation factor $\alpha < 1$ dB/km of the waveguide and the measured base temperature distribution, we calculate with Eq. (4.7) that, in the waveguide of the 30 m system, the total loss does not exceed 0.7% and the number of added noise photons is below 10^{-6} . The link waveguide itself should therefore introduce negligible amounts of error in microwave quantum communication protocols [Magnard20, Kurpiers18, Axline18, Campagne-Ibarcq18, Leung19, Zhong19, Chang20, Zhong21, Burkhardt21], below threshold for both entanglement purification [Bennett96a, Nickerson15] and error correction [Fowler10, Xiang17, Vermersch17]. The excellent cryogenic performance of our system on such different length scales demonstrates the robustness, modularity, and high performance of the design.

We simulate the steady-state temperature profiles using the recursive method described in Sec. 4.3, with heat load functions and thermal conductance parameters measured independently (see Sec. 4.8 and table 4.1). The temperatures at the nodes of each stage are set to their measured values. The 50K temperature distribution is simulated with finite-elements on a 3D model of the 50K stage, see Sec. 4.8.5 for more details. The temperature profile on all other stages is calculated from the 1D model depicted in Fig. 4.3 (b). The fitted curves are in excellent agreement with the data (solid lines in Fig. 4.6). Using the cooling power curves P_0 and the temperature T_c at the nodes, we can extract a total heat load $Q_{\text{tot}} = P_0(T_c)$ on each node. This quantity is greater than the heat load on the nodes $Q_{\text{tot}} = Q(x = 0, l)$ calculated from the heat distribution, within 20%. We attribute this discrepancy to heat loads introduced by the cabling at the node, and to the dependence of the cooling power at one stage on the temperature of other stages [Krinner19]. The good agreement between the fitted model and the data is evidence that the extracted thermal parameters are reliable, and that the recursive model captures the complex heat transfers in the system to a good approximation.

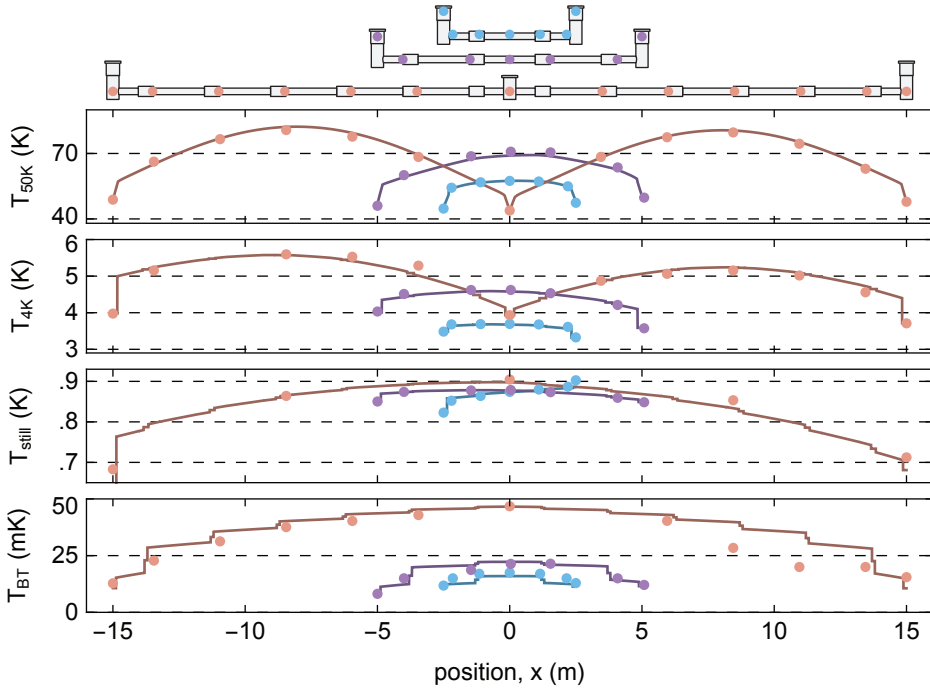


Figure 4.6 Measured steady-state temperature distribution of the 5 m long (blue dots), the 10 m long (purple dots) and the 30 m long (pink dots) cryogenic link prototypes. The pictograms above the panels represent the cryogenic prototypes and their corresponding temperature sensor locations (dots), to scale with the x-axis of the plots below. The solid lines are results of simulations, with the temperature of nodes on the 50K, 4K and still stages as the only fit parameters.

4.6 Achievable lengths for cryogenic links

We use the recursive model described in Sec. 4.3, with the measured experimental parameters compiled in table 4.1, to extrapolate the temperature profile of longer cryogenic links, and quantitatively estimate the link length beyond which the cryogenic link fails to cool down. For this, we define the following criteria for a successful cool down. (i) The 50K plate in each cooling unit should be below 77K to ensure the proper functioning of the internal cold trap located there. (ii) The 4K plate should be below 5.2K: the highest 4K plate temperature at which we successfully condensed the Helium mixture. (iii) The still plate should be below 1.2K otherwise the circulation of ^3He becomes unstable and the base plate warms up. (iv) The base plate should be below 50mK. (v) The thermal occupation n_{added} of the propagating field of the

waveguide should small (*e.g.* $< 1\%$), to be error correctable [Xiang17] and to induce little qubit dephasing [Gambetta06]. Note that the thresholds for criteria (i) to (iii) are strict, whereas those for criteria (iv) and (v) are subjective and could be set to different values depending on the application.

We first simulate the temperature profiles of cryogenic links with length l varying from 2.5 m to 30 m, in the absence of additional cooling elements in the link at any temperature stage [Fig. 4.7 (a)]. The temperatures T_c at the node and T_h in the middle of the link both increase with l [Fig. 4.7]. Beyond a critical length $l = 20$ m, the 4K plate temperature at each node exceeds 5.2 K, violating criterion (ii) [Fig. 4.7 (b)]. Criteria (iii) and (iv) fail at slightly longer lengths, as expected from the rapid temperature rise of all stages beyond the critical length, which we described at the end of Sec. 4.3.1.

Bridging larger distances therefore requires to actively cool the link at intermediate locations between the nodes and at a selected set of temperature stages. If the 50K

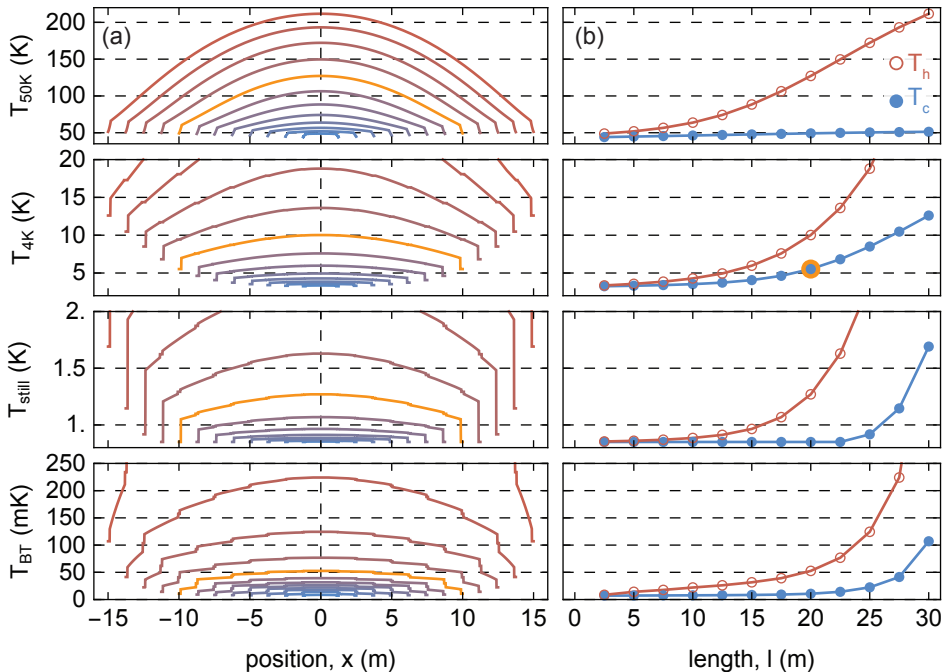


Figure 4.7 (a) Simulated temperature distribution of cryogenic links of various length, from the hottest (top) to the coldest (bottom) temperature stage, assuming there is no cooling element in between the nodes. (b) Corresponding coldest (filled blue) and hottest (open red) temperature in the link vs cryogenic link length. For a 20 m long cryogenic link [orange curves in (a)], the 4K plate temperature exceeds 5 K [orange dot in (b)], beyond which a successful condensation is uncertain.

stage is uniformly cooled to 70 K, our simulation suggests that the 4K temperature at the node [filled red dots in Fig. 4.8 (a)] stays below 5.2K until the link length reaches 50 m, beyond which criterion (ii) fails. As before, the other criteria fail at slightly longer lengths [see filled red dots in Fig. 4.8 (b-d)]. Assuming that the 4K stage is uniformly cooled to 4.2K (purples dots in Fig. 4.8), or that the 50K and 4K stages are periodically cooled by a pulse tube unit every 15 m (blue dots in Fig. 4.8), lead to similar results for all link lengths. Criterion (v) is the first one to fail [orange highlight in Fig. 4.8 (d)], as the thermal occupation of the waveguide exceeds 1% beyond a link length of approximately 120 m in both cases, when no intermediate dilution units are used to cool the waveguide further.

In conclusion, with the current link design, a cryogenic network would need active cooling elements every 15 m on the 50K and 4K stages and a dilution refrigerator every 100 m, approximately. These critical lengths could be further increased with attempts at reducing the heat loads, the effective resistivity of the shields, and the waveguide loss rate. Such attempts could include: using Kevlar strings to support the shields, suppressing electrical and thermal contact resistances by soldering or welding the contacts, improving the shield conductivity with oxygen annealing [Fickett82, Rosenblum77], or using seamless MLI on both the 50K and 4K stages.

4.7 Discussion and outlook

This realization of cryogenic links suitable for microwave quantum communication, covering distances of up to 30 m relies on a few key insights. First the design is modular, providing simple means to scale up the system to larger distances. Second, the design makes use of flexible elements, such as copper braids and sliding parts, to be resilient to thermal contraction. Third, we attempt to minimize heat loads by covering the 50K stage with MLI, by using high-yield-strength, low-thermal-conductivity, non-brittle support posts, and by ensuring the shields are installed in a radiation tight fashion. Fourth we maximize the thermal conductance of the link by using high-conductivity copper shields and braids, and by mitigating contact resistances at interfaces. Fifth and last, we use a low-loss waveguide to minimize the temperature of the waveguide field.

The cryogenic link design presented here consists of a non-flexible link which can be connected to cryogenic nodes only if the the two nodes are warm and vented. Future versions of the cryogenic link could have fully flexible sections. This would ease the requirement to precisely align the vacuum cans of all modules and greatly simplify

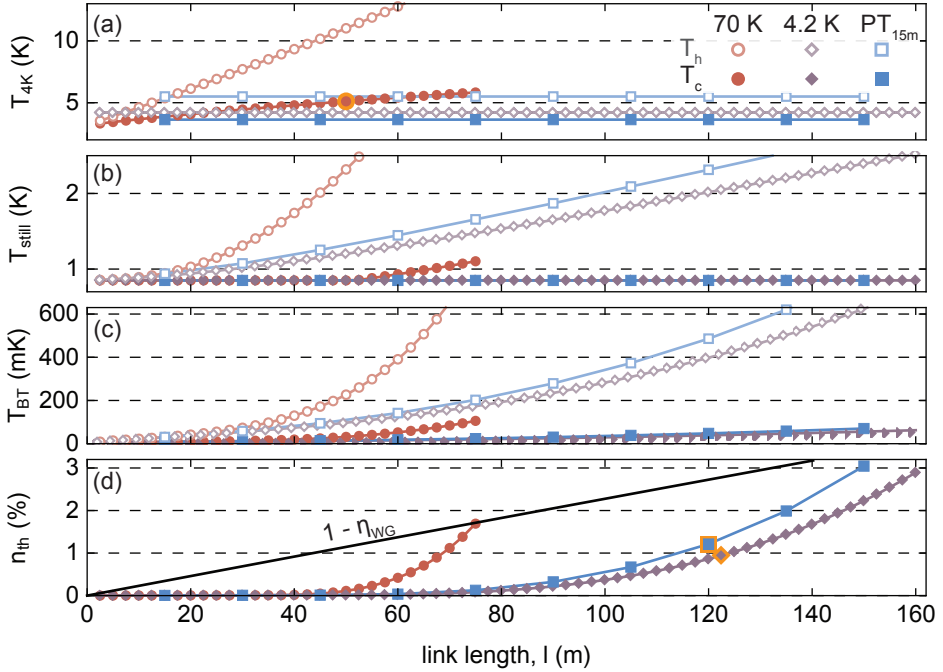


Figure 4.8 Simulated temperature at the coldest (filled points) and hottest (open points) location of, (a) the 4K stage, (b) the still stage, and (c) the BT stage of the cryogenic link, vs link length. The simulation assumes either that the 50K stage is uniformly cooled to 70 K (red dots), or that the 4K stage is uniformly cooled to 4.2 K (purple diamonds), or that the 50K and 4K stages are cooled by a pulse tube unit every 15 m (blue squares). (d) Corresponding number of thermal photons, n_{th} , injected per travel in the waveguide at 9.5 GHz (dots) and photon loss in the waveguide (solid black line), vs length of the cryogenic link. The orange dots in (a) and (d) highlight the maximum link length before degrading the performance of the link (see main text).

the installation of the link. Another interesting feature would be to design a system to connect a cryogenic link to a running dilution refrigerator, without warming up or venting the system. With such a cryogenic link plug, one could change the topology of a cryogenic network, for instance adding or removing nodes and links, while keeping the network cold and running, and essential capability for a practical quantum network.

As we discuss in chapter 6, this system can be used to perform basic quantum communication operations between superconducting qubits housed in separate dilution refrigerators, like deterministically transferring qubit states, preparing entangled states on-demand and violating Bell's inequality with high repetition rates. The 30 m length scale which we demonstrated here brings several applications within reach, such as performing a loophole-free Bell test, using the waveguide as a high density storage mode [Chakram20], exploring new regimes of non-Markovian waveguide QED [Dinc20, Calajó19, Kim21], or generating high-dimensional cluster states [Besse20b, Pichler17, Wan20]. Simulations suggest that campus-scale cryogenic networks of a few 100 m could be realized with the current design, and that intra-city km-scale networks could be realized with further improvements, which highlights the practical relevance of microwave cryogenic links for local area quantum networks.

4.8 Characterizing the properties of individual parts

As discussed in Sec. 4.4, we have conducted a series of experiments to extract the thermal parameters, listed in table 4.1, describing heat transfers in our cryogenic link design. In this section we present these different experiments.

4.8.1 Mechanical and thermal properties of the mechanical support posts

The posts used to support the different stages of the link module, shown in Fig. 4.9, consist of thin-walled, hollow tubes or cones which are stereolithographically 3D printed with Accura BlueStone.

We test the mechanical properties of these posts with a compression-testing machine, schematically shown in Fig. 4.10 (a), which measures the strain l obtained when applying a varying vertical force F . The posts contract proportionally to F at low forces due to elastic deformation, and experience a plastic deformation, and then a mechanical rupture as the force increases [Fig. 4.10 (b)]. The 0.2% offset yield strength ($R_{p0.2}$), defined as the amount of stress resulting in a plastic strain of 0.2%, is a widely used

metric to characterize the effective compressive strength of a material [Beer12]. We calculate it by normalizing the force resulting in 0.2% plastic strain [Fig. 4.10 (b)] with the mean cross-section of the posts. We find that $R_{p0.2}$ varies between 100 MPa and 130 MPa [Fig. 4.10 (c)]. We performed the same test on posts made of glass-, and carbon-fiber-reinforced polyamid (Nylon), and PEEK, which showed comparable yield strengths (see table 4.2).

To determine the thermal properties of a post at cryogenic temperatures, we prepare the measurement setup shown in Fig. 4.10 (d): the foot of the post is clamped to the base temperature plate of a dilution refrigerator, and its top is glued to a copper block to which a heater and a temperature sensor (RX-102B from Lakeshore Cryotronics, Inc.) are thermalized. The dilution refrigerator is pumped to high vacuum and cooled down to a base temperature of 10 mK, which is monitored by a second sensor on the base plate. The leads of the heater and of the temperature sensors are made of superconducting NbTi embedded in a low-conductivity CuNi matrix, to ensure that their thermal conductance is much smaller than that of the post. This way, one can neglect heat flow through the leads and the heat Q dissipated at the heater must flow almost entirely through the post.

For heat current Q ranging from $0.1 \mu\text{W}$ to $10 \mu\text{W}$, the base plate temperature T_c varies only from 10 mK to 20 mK [Fig. 4.1 (d)], whereas we measure temperatures T_h at the top of the post ranging from 600 mK to 4 K [Fig. 4.1 (e)]. For a given $T_h < 2 \text{ K}$, the

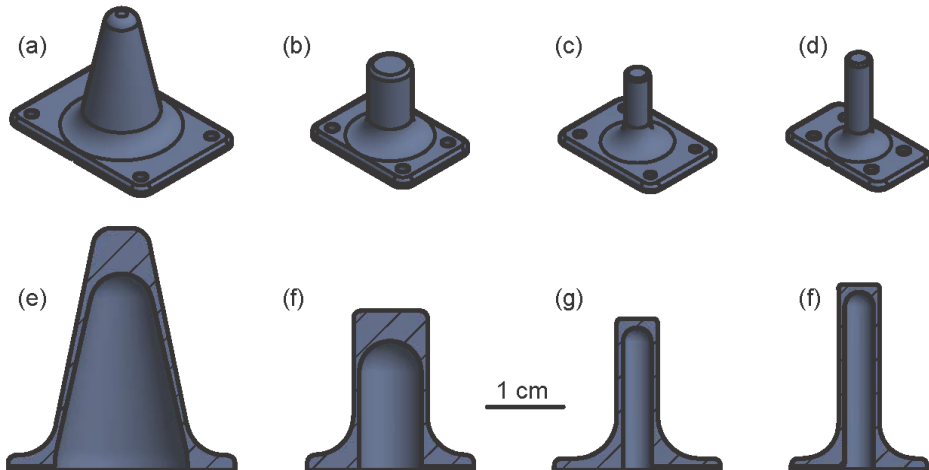


Figure 4.9 (a) to (d), perspective view, and (e) to (h), cross-section of CAD representations of the 3D printed posts used to support the 50K, 4K, still, and base temperature shields of the link elements, respectively. Panels (e - h) are to scale, unlike panels (a - d).

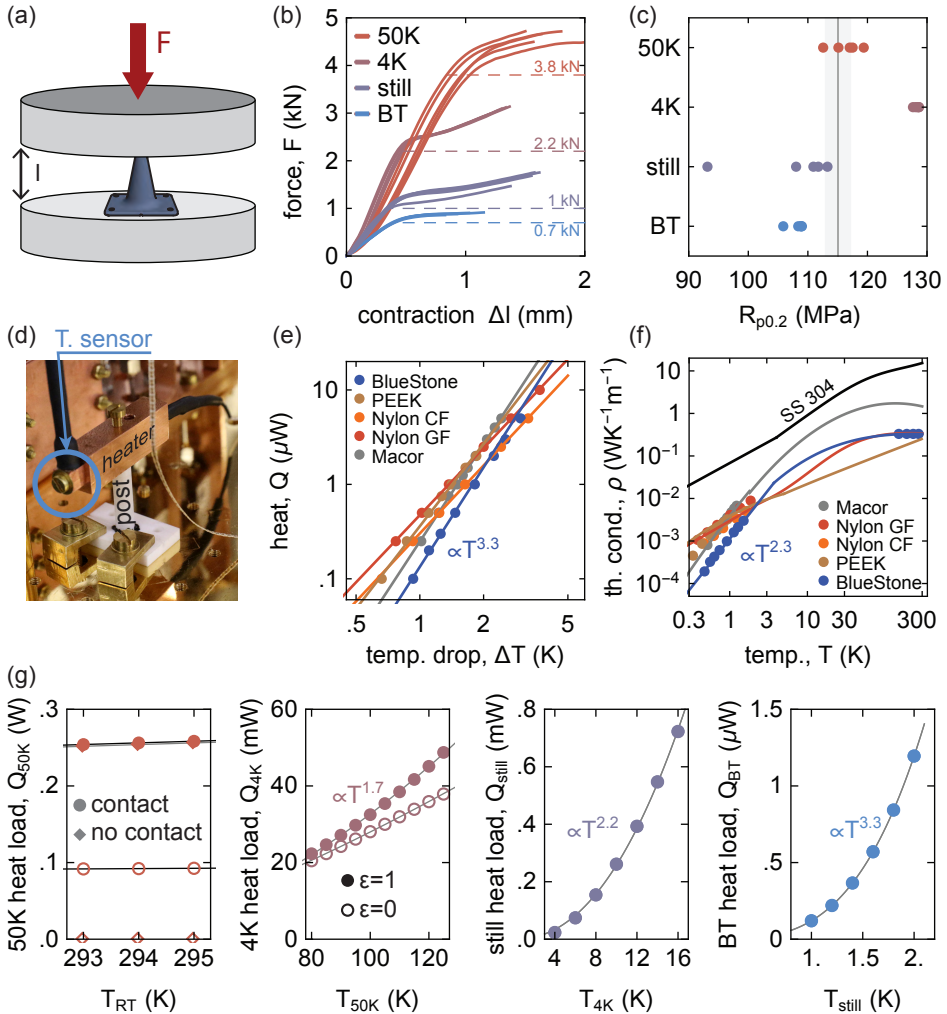


Figure 4.10 (a) Schematic representation of the compression test machine used to characterize the compressive yield force of the posts. (b) Force applied on the post vs post length contraction for several copies of each type of post. The dashed line indicate the mean elastic limit after which permanent deformation occurs. (c) Estimate of the offset yield pressure point at 0.2% plastic strain, $R_{p0.2}$ for each BlueStone post tested. The average offset yield pressure for BlueStone 115 ± 2 MPa is represented by the grey vertical line (region). (d) Photograph of a typical experimental setup used to characterize the thermal conductance of posts made of different materials (here, macor). (e) Dissipated heat vs measured temperature drop across BT posts, anchored to the BT plate of the refrigerator, and fabricated from the specified materials. The solid lines are power law fits. (f) Thermal conductivity extracted from (e). The solid line for BlueStone is obtained as a piecewise function which fits the data at different temperature scales. The other solid lines are obtained from [Marquardt02, Woodcraft09]. (g) Heat load of a post on stage n vs temperature of stage $n + 1$, simulated with a finite elements method. The solid lines are power law fits.

corresponding heat current Q flowing through BlueStone posts is approximately two times smaller than for any other material tested [Fig. 4.1 (e)]. Noticing that $T_c \ll T_h$, Eq. (4.2) rewrites

$$\int_0^{T_h} \rho dT = \frac{Ql_p}{A_p},$$

with l_p the length of the post, and $1/A_p$ is the average over length of the inverse cross-section area, we first fit $Q(T_h)$ with a power law of the form $a T_h^b$, which we then differentiate to obtain the thermal conductivity $\rho(T_h) = l_p a b T_h^{b-1}/A_p$. We find that the thermal conductivity of BlueStone below 2K scales as $T^{2.3}$ and is the lowest of all tested materials [Fig. 4.1 (e)]. We also measure the thermal conductivity of BlueStone at temperatures ranging from 50K to 300K with a similar procedure, by applying heat on a post thermalized to the 50K plate of the dilution refrigerator. In this measurement however, we parametrize the thermal conductivity as a sum of a constant and a linear term. We also need to account for radiation from the post to the 50K stage, which we do with a 3D gray-body simulation of the experiment. We interpolate the thermal conductivity between 4.2K and 50K with a function of the form $\rho(T) = a + bT^c$.

The ratio between yield strength σ and thermal conductivity $\rho(T_0)$ at T_0 dictates how much force can a post withstand per unit of thermal conductance at temperature T_0 , for a fixed length. Therefore this ratio is a metric of the performance of a material for heat insulating support structures. We find that, of all materials considered, Bluestone has the highest σ/ρ ratio at 1 K. In addition, it is 3D printable, robust to shocks (not brittle), cheap to produce and compatible with high vacuum. This combination of advantages is unequalled by any other material we have considered (see table 4.2). This lead us to choose BlueStone as the material for posts.

Material	SS	M	PEEK	PA	BS
$\rho(1\text{ K}) (\text{mWK}^{-1}\text{m}^{-1})$	70	5	5	3	1
Yield strength σ (MPa)	550	350	120	120	120
Ratio σ/ρ (GNK/Wm)	8	70	20	40	120
3D printable?	no	no	no	yes	yes
Brittle?	no	yes	no	no	no
Cost	\$\$	\$\$\$	\$\$	\$	\$
Vacuum compatibility	UHV	UHV	HV	no	HV

Table 4.2 Comparison of the properties of different materials which are relevant for post fabrication and performance. SS: stainless steel; M: Macor; PA: Polyamid (Nylon); BS: Bluestone; HV: high vacuum; UHV: ultra high vacuum.

For simulation purpose, it is convenient to have an estimate of the heat load of each

post as a function of the temperature at the hotter stage. To that end, we simulate the heat current Q which flows through the BlueStone post supporting the 50K (resp. 4K, still and BT) shield when it's top is at a given temperature T and it's outer surface is exposed to a black-body radiation bath of temperature T using the thermal conductivity curve shown in Fig. 4.10 (f). Note a big interpolation gap between 2 K and 100 K, for which the simulations might be less accurate.

For the 50K post, we swept T from 293 K to 295 K, representative of room temperatures measured in our lab. Interestingly, the simulation suggests that if the post is a black-body absorber ($\epsilon = 1$), then the heat load induced by the post is 0.26 W whether the post is in contact or not with the vacuum can [Fig. 4.10 (g)]. If the surface of the post is fully reflective ($\epsilon = 0$), then the post heat load reduces to 0.09 W. For the 4K post, the absorption of black body radiation by the post has a much smaller effect on the post heat load, and the heat load is well approximated by a power law proportional to $T_{50K}^{1.7}$. For the still and BT posts, black-body radiation is negligible for the considered ranges of T , and the heat load is well approximated by a power law proportional to $T_{4K}^{2.2}$ and $T_{still}^{3.3}$, respectively [Fig. 4.10 (g)].

4.8.2 Thermal conductivity of copper

High purity copper, together with silver, is the best thermal conductor at cryogenic temperatures and is therefore the material of choice to manufacture high conductivity radiation shields [Pobell06, Woodcraft05, D'Addabbo18]. For such applications, one typically use a class of high purity copper called oxygen-free high conductivity (OFHC) copper, which exist in three industrial grades. Electrolytic-tough-pitch (ETP) copper, also known as C11000, is a high conductivity copper containing at least 99.9% copper content, or purity, and 200 ppm to 400 ppm oxygen content, and is the cheapest and most commonly used type of high conductivity copper. Oxygen-free (OF) copper, also known as C10200, is more than 99.95% pure, and has an oxygen content below 10 ppm. Finally, oxygen-free electronic (OFE) copper, also known as C10100, is the purest and most expensive grade of copper. It is 99.99% pure and contains less than 5 ppm oxygen content.

To choose a copper grade and a copper manufacturer for our radiation shields, we measure the thermal conductivity of test pieces at cryogenic temperatures using the dipstick shown in Fig. 4.11 (a,b). The test piece is a copper strip with a standard size of 12 mm \times 150 mm, cut from the 1, 2, or 3 mm thick copper sheet produced by the manufacturer. One end of the copper strip is mechanically and thermally anchored to

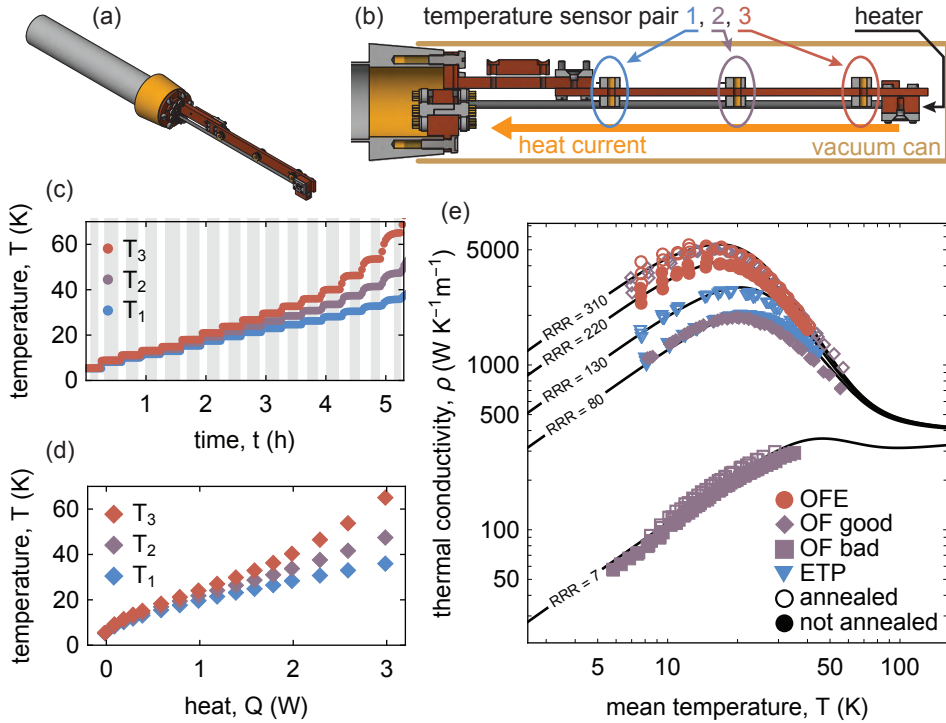


Figure 4.11 (a) Perspective view, and (b), cross-section of a CAD representation of the dipstick test setup used to characterize the thermal conductivity of copper strips. (c) Mean temperature of each temperature sensor pair vs time for the non-annealed “good OF” copper test sample. Each plateau corresponds to a different source heat applied to the sample. (d) Temperature vs dissipated heat for the non-annealed “good OF” copper test sample. The temperature is obtained from averaging in the steady-state of each heat setting, illustrated by the grey regions in (c). (e) Thermal conductivity vs mean temperature for selected copper samples before and after annealing. The black lines are theoretical curves of the thermal conductivity of copper for various RRRs.

a thermalizing block acting as a heat sink, at the end of the dipstick. We attach a 25 Ω cryogenic heater with 100 W heating power to the other end of the strip which stands freely. In between the heater and the heat sink, we place three pairs of temperature sensors (CX1010 from LakeShore Cryotronics, Inc.) spaced 51 mm away from each other, which we label 1, 2 and 3 from the pair closest to, to farthest away from the heat sink [Fig. 4.11 (b)]. The end of the dipstick is covered with a brass vacuum can and is pumped to high vacuum ($< 10^{-4}$ mbar at room temperature), to ensure that all the heat dissipated at the heater flows through the copper strip down to the heat sink [Fig. 4.11 (b)].

The dipstick is then immersed in liquid helium stored in a dewar, to cool it to 4.2K. Once the dipstick reached equilibrium, we dissipated heat Q at the heater and wait 20 minutes before increasing Q to another value. At each change of the heat setting, the temperatures increase and reach a new steady-state after 2 to 10 minutes [Fig. 4.11 (c)]. The temperature indicated by two sensors of the same pair never differ by more than 50 mK, thereby confirming that the sensors stay calibrated. For each heat setting, we take the average temperature of each sensor over the steady-state plateaus indicated by the grey shaded regions in Fig. 4.11 (c), to obtain the steady-state temperature distributions shown in Fig. 4.11 (d). Because of the finite thermal resistivity R between the position of sensor pair 1, and the liquid helium surrounding the dipstick, we observe that $T_1 = 4.2\text{K} + RQ$ increases significantly with Q . Similarly, integrating Fourier's law in-between sensor pairs i and j leads to

$$l_{ij}Q = A \int_{T_i}^{T_j} \rho(T')dT', \quad (4.9)$$

with l_{ij} the distance between the two sensor pairs, A the cross-section area of the copper strip, and $\rho(T)$ its temperature-dependent thermal conductivity. Therefore, the temperature differences $\Delta T_{ij} := T_j - T_i$ increase with Q [Fig. 4.11 (d)]. Expanding ρ to first order around its mean temperature $T := (T_i + T_j)/2$ over the interval $[T_i, T_j]$, Eq. (4.9) rewrites

$$\rho(T) \simeq \frac{l_{ij}Q}{A\Delta T_{ij}}, \quad (4.10)$$

with $\Delta T_{ij} = T_j - T_i$, which gives a mean to estimate the thermal conductivity of the material.

We measured more than 60 copper strips of all grades and from various manufacturers, some of which were measured before, and after annealing them in vacuum at approximately 450°C for 2 hours, and of which we plot a selection in Fig. 4.11 (e).

The thermal conductivity of copper is uniquely determined by the RRR [Simon92]. It increases monotonously with the RRR, and depends linearly on it in the low temperature regime where ρ is proportional to temperature [Fig. 4.11 (e)]. Therefore, the RRR is a good metric of the thermal conductivity, particularly significant for low temperatures. Note the maximum of the thermal conductivity in the 10K to 50K range, which increases with RRR, and is 10 times larger than at room temperature for RRR > 300. We fit the model given in [Simon92] to each thermal conductivity curve, with the residual resistivity ratio (RRR) as a free parameter.

ETP copper displays RRR ranging from 80 to 150. The RRR typically increases to 100 to 200 after annealing, but the effect is not systematically significant [Fig. 4.11 (e)]. OF copper usually is usually delivered with RRR values around 80 to 150, similar to ETP. Annealing typically increases the RRR to values as high as 300, even though not systematically. However, some OF copper strips display prohibitively low RRR, below 7, and do not improve after annealing, which can be due to the trace presence of magnetic impurities [Woodcraft05, Fickett82, Rosenblum77]. Performing mass spectrometry revealed that the atomic composition of the low RRR samples differed from that of the high RRR ones only by the fraction of Phosphorus impurities, which went from less than 5 ppm to 15 ppm. We therefore suspect that Phosphorus impurity levels which can be found in some OF copper can severely degrade the RRR. Finally OFE copper systematically has RRR in excess of 140 upon receipt, and can reach up to 350 after vacuum annealing.

We decided to use OFE copper to manufacture the radiation shield, to obtain high RRR values reliably without the need for annealing. We note that annealing copper in a low-pressure oxygen atmosphere has been demonstrated to efficiently increase the RRR of ETP, OF and OFE copper above 1000 by introducing oxygen atoms which selectively oxidize the magnetic impurities inside the copper, but not the copper itself [Fickett82, Rosenblum77]. In addition, unlike vacuum annealing, oxygen annealing hardens copper, which is a desirable property for our radiation shields. We did not try oxygen annealing because we could not find a commercial offer for this service, which is typically done in laboratory conditions [Woodcraft05]. Developing an oxygen annealing furnace could constitute a valuable next step to improve the radiation shields.

4.8.3 Thermal resistance of the nodes

In each temperature stage of the dilution refrigerators, the radiation shield consists of distinct sections which are screwed to each other [Fig. 4.12 (a)]. A vertical cylindrical section, referred to as the “tube”, which constitutes the largest part of the node shield, is screwed to the bottom of the temperature stage plate. The tube is closed at its bottom by a bottom blind. Finally on each side of the tube is a flange, meant to be connected to the link, but which is closed by a side-blind in the experiment presented in this subsection. The heat current coming from the link will therefore flow through several contact interfaces, highlighted in Fig. 4.12 (a), between: the side-blind and the side-flange (SF-SB, light green), the side-flange and the tube (T-SF, light blue), and the

tube and the temperature plate (TP-T, dark blue). The thermal resistance of each of these bulk and interface elements contributes to the temperature drop between the top plate and the beginning of the link.

To characterize the thermal resistance of the node 50K, 4K and still shields, we mounted temperature sensors on the top plate, along the tube, on the bottom blind, on four locations of the side-flange, and on the side-blind, as indicated by the purple dots in Fig. 4.12 (a) for the 4K shield. We also placed one heater at the center of the side-blind, and one at the center of the bottom blind [orange diamonds in Fig. 4.12 (a)]. We used CX1010 sensors from LakeShore Cryotronics, Inc. on the still and 4K stages, and CX1080 sensors on the 50K stage.

To determine the thermal conductivity of the tube, we generate the heat Q at the bottom-blind heater, wait for steady-state, and record the temperature of the sensors placed on the tube, *i.e.* those labelled from 2 to 6 in Fig. 4.12 (a). We repeat this procedure for different applied values of Q . As expected from Fourier's law, the temperature increases with the distance from the cooling unit, and with Q [Fig. 4.12 (b)]. To extract the RRR of the tube, we simulate the process with a finite element method in a 3D model of the shield at a given temperature stage. For each value of Q , we set as a boundary condition that the temperature of the tube is T_2 everywhere above the position of sensor 2. We fit the results of this simulation to the data with the copper RRR and the radiative heat load φ_{rad} on the shield as free parameters, and find an excellent agreement of the fit to the data [see solid lines and shaded region in Fig. 4.12 (b)].

For the still and 4K stages, we find an RRR of approximately 82 and cannot resolve the radiative load φ_{rad} . This is expected because the radiation load φ_{rad} calculated from Eq. (4.1) is supposed to be in the few tens of μW range, and in the few mW range for the still and 4K stages, respectively, which is far below the minimum heat Q necessary to resolve a temperature drop between sensors [Fig. 4.12 (b)]. For the 50K stage, we obtain $\varphi_{\text{rad}} = 14\text{W}/\text{m}^2$, but cannot resolve the RRR, because the thermal conductivity of copper varies little with the RRR, for temperatures above 40K and RRRs above 40 [see Fig. 4.11 (e)]. Therefore, for the rest of the simulations of the 50K stage, we set the RRR to 82, the value measured on the other stages.

To extract the thermal contact resistance of the interfaces, we apply the heat Q using the side-blind heater, and compare the temperature distribution measured in steady-state with that of a finite element simulation in which contact resistances are set to 0 [Fig. 4.12 (c)]. For each value of Q , we set the temperature at the plate in the simulation to that measured by sensor 1. For each sensor, the discrepancy T_{diff} between the measured and simulated temperature stems from the temperature drops

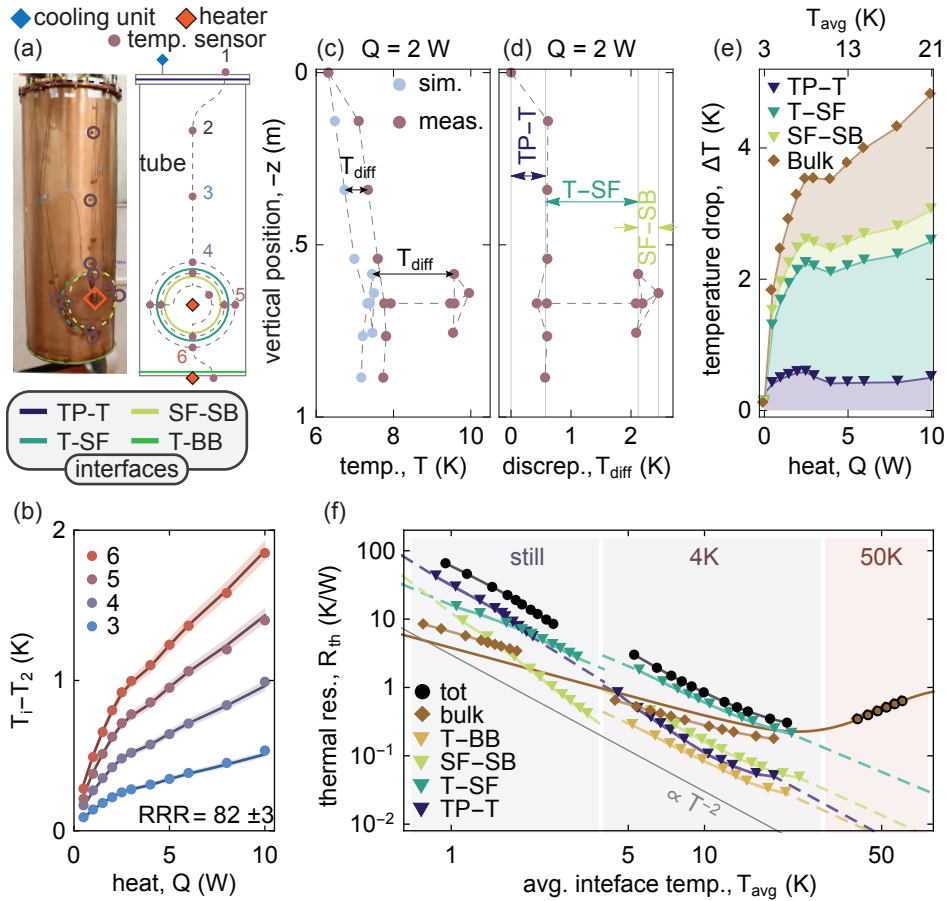


Figure 4.12 (a) Photograph (left) and schematic (right) of the 4K radiation shield of one of the dilution refrigerators and its temperature sensor layout used to characterize its thermal properties. (b) Temperature difference of sensors 3 to 6 relative to sensor 2 vs heat applied at the bottom blind of the 4K shield. Solid lines are results of a finite element simulation with the indicated RRR. The shaded regions corresponds to the RRR uncertainty. (c) Measured (purple) and simulated (blue) temperature distribution for 2W heat dissipated at the 4K SB heater. The simulation assumes no interface resistance. (d) Difference T_{diff} between measured and simulated temperature distribution. The vertical gray lines are the mean T_{diff} of each copper piece (from left to right: plate, tube, side-flange and side-blind). The colored arrows highlight the contribution of each interface. In (c) and (d), the location of the sensors can be identified by their position on the vertical axis (y-axis) and their “thermal connectivity” (gray dashed lines), which are the same as in (a). (e) Total temperature drop between the plate and the side-blind (diamond) vs heat generated at the SB heater. The filling shows the contributions of interfaces (triangles) and finite bulk conductivity to ΔT . (f) Thermal resistance of interfaces (triangles), finite bulk conductivity (diamonds) and their sum (round) vs temperature as measured for the still, 4K and 50K shields (shaded regions). The dashed lines are extrapolation of interface resistances from power law fits. The brown and gray solid lines are a fit of the form $\propto 1/\rho_{RRR=75}^{Cu}(T)$ to the 50K resistance, and an illustrative $R \propto T^{-2}$ curve, respectively. TP: temperature plate; T: tube; SF: side-flange; SB: side-blind; BB: bottom blind.

at the interfaces between the sensor and the top plate. Sensors placed on the tube display the same discrepancy $T_{\text{diff}} = \Delta T_{\text{TP-T}}$, stemming from the contact resistance of the interface between the plate and the tube (TP-T). For those on the side-flange, $T_{\text{diff}} = \Delta T_{\text{TP-T}} + \Delta T_{\text{T-SF}}$ due to the contact resistance of the TP-T and the T-SF (tube / side-flange) interfaces. And for that on the side-blind, $T_{\text{diff}} = \Delta T_{\text{TP-T}} + \Delta T_{\text{T-SF}} + \Delta T_{\text{SF-SB}}$ due to the contact resistance of the TP-T, T-SF and SF-SB (side-flange / side-blind) interfaces [Fig. 4.12 (d)].

For the 4K stage, interfaces contribute to the majority of the temperature drop independent of the applied heat [Fig. 4.12 (e)]. This is even more pronounced on the still stage. On the 50K stage however, we were not able to resolve any discrepancy T_{diff} , suggesting that contact resistances are negligible in this temperature range.

For each value of applied heat Q and interface i , we extract the temperature-dependent contact resistance

$$R_{\text{th},i}(T_i) = \Delta T_i / Q,$$

with T_i the mean of the temperatures measured just across interface i [Fig. 4.12 (f)], and observe that they vary approximately as $\propto T^{-2}$, as expected for contact resistances [Salerno97]. The bulk resistance, which we calculate from the simulated plate-to-side-blind temperature drops, is inversely proportional to $\rho_{\text{RR}=82}^{\text{Cu}}(T)$ with a proportionality constant given by the geometry of the shield. As a result, it is proportional to T^{-1} at low temperatures and starts increasing again above ~ 30 K, as shown by the solid brown line extrapolating the 50K bulk thermal resistance in Fig. 4.12 (f). This different temperature scaling explains why the bulk resistance dominates above ~ 30 K while interface resistances dominate below ~ 10 K.

Our measurements highlight the importance of contact resistances at low temperature. The node shields, which were provided by BlueFors, have 2 to 3 times lower RRR than the link module shield, and display significant thermal contact resistances at interfaces at 4K and below. This explains why we observe large temperature drops across the nodes in the still and 4K stages of the cryogenic link realizations (Fig. 4.6). The performance of the cryogenic link could therefore be significantly improved by optimizing the thermal conductance of the shield elements at each node. The design of the intermediate pulse tube cooler addresses these issues presented in Sec. 4.5 addresses these issues.

4.8.4 Thermal resistance of link and braid modules

To extract the conductance along the cryogenic link, we assembled a cryogenic prototype consisting of a single cryogenic node connected to 4 m of cryogenic link consisting of one adapter module and one link module [see Fig. 4.13 (a)]. The radiation shields at the open end of the link were closed with radiation-tight caps. On each temperature stage, we mounted temperature sensors at the positions indicated by the purple dots in Fig. 4.13 (a), and a heater at the end of the cryogenic arm. Similar to what we described in Sec. 4.8.2, the temperatures measured in steady state increase with the distance from the cooling unit, and with the heat Q generated at the heater [Fig. 4.13 (a)].

The sensors labelled 3 and 4 in Fig. 4.13 (a) are mounted at opposite ends of the link module. Approximating the heat transfer between these sensors as a one-dimensional

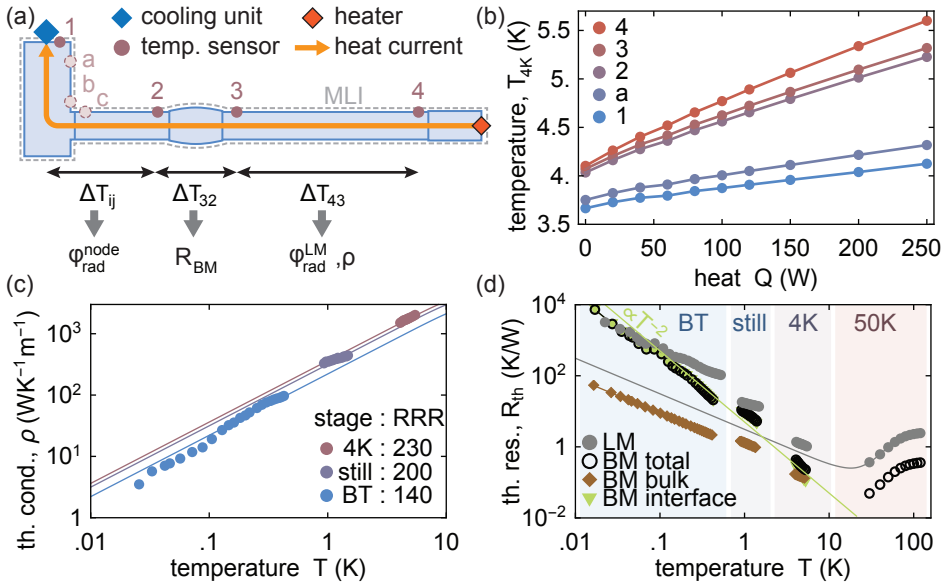


Figure 4.13 (a) Schematic of the experimental setup used to characterize heat transfer in the link and braid modules. (b) 4K stage temperature distribution vs heat applied at the end of the link. (c) Temperature dependence of thermal conductivity of the BT, still and 4K shields of the link module (LM), extracted from the temperature drops ΔT_{43} . Solid line lines are fit with the RRR as a free parameter [Simon92]. (d) Temperature dependence of the thermal resistances of the braid module (BM) and its contributions from bulk conductivity and interfaces, and of the link module. The green line is a guide-to-the-eye highlighting the approximate T^{-2} dependence of interface resistances. The solid gray line is an extrapolation of the form $\propto 1/\rho_{230}^{Cu}(T)$ of the 50K link module resistance.

problem, Fourier's law writes

$$Q + Q_0(x) = A\rho(T(x))\partial_x T, \quad (4.11)$$

with $Q_0(x)$ the sum of all heat loads applied to the system between position x and the end of the link, A the cross-sectional area of the radiation shield of the link module, and ρ its thermal conductivity. Integrating Equation (4.11) between sensors 3 and 4, and expanding ρ to first order around the mean temperature $T := (T_3 + T_4)/2$, we obtain

$$\rho(T) = \frac{Q + \bar{Q}_{34}}{\Delta T_{43}} \frac{\Delta x}{A}, \quad (4.12)$$

with \bar{Q}_{34} the mean value of $Q_0(x)$ between sensors 3 and 4, and Δx and ΔT_{43} the distance and temperature difference between sensors 3 and 4, respectively. We estimate \bar{Q}_{34} and the RRR of the radiation shield by minimizing the quadratic error between a fit function $\rho_{\text{RRR}}^{\text{Cu}}(T)$ parametrized by the RRR [Simon92] and the values obtained with Eq. (4.12) [Fig. 4.13 (c)]. The obtained RRR values are similar to those extracted using dipstick measurement of test samples, cut from the sheets used to fabricate the radiation shields (see Sec. 4.8.2). For the 4K, still and base temperature shields, the values of \bar{Q}_{34} are within the error bars of what is expected from conduction through the posts (see Sec. 4.8.1). We use a different analysis method, presented in Sec. 4.8.5, for the 50K stage.

According to Eq. (4.12), the link module thermal resistance $R_{\text{th}}^{\text{LM}}(T) := \Delta T_{43}/(Q + \bar{Q}_{34})$ is inversely proportional to $\rho_{\text{RRR}}^{\text{Cu}}(T)$. It is therefore inversely proportional to T at low temperatures but rises again after ~ 30 K [see gray dots and gray line in Fig. 4.13 (d)] Similarly, we can estimate the thermal resistance $R_{\text{th}}^{\text{BM}}(T) := \Delta T_{32}/(Q + \bar{Q}_{23})$ of the set of braids connecting the two modules, where we extrapolate the mean heat current \bar{Q}_{23} between sensors 2 and 3 when $Q = 0$ from \bar{Q}_{34} . The resistance $R_{\text{th}}^{\text{BM}}$ is the sum of two terms: the bulk resistance $R_{\text{bulk}}^{\text{BM}}$ of the copper braids, and the contact resistance R_c^{BM} at the interface between the braid and the radiation shields. We calculate the bulk resistance term from the geometry of the braids and their RRR, which we extracted in independent thermal measurements similar to those described in Sec. 4.8.2. From this, we extract R_c^{BM} and fit it with power law which reveals a T^{-2} dependence [Fig. 4.13 (d)], characteristic of contact resistances [Salerno97]. Therefore, we expect R_c/R_{bulk} to be large at low temperatures ($\propto T^{-1}$) and negligible at high temperatures ($\propto T^{-2}$).

Indeed, contact resistances [green data points in Fig. 4.13 (d)] are negligible on

the 50K stage, but they contribute to more than half of braid resistance $R_{\text{bulk}}^{\text{BM}}$ on the 4K stage, and dominate on the still and base temperature stages. On the still and base temperature stages, the contact resistance of the braids is even comparable to the total resistance $R_{\text{th}}^{\text{BM}} + R_{\text{th}}^{\text{LM}}$ of the link module in series with a connection module [green vs black and gray data points in Fig. 4.13 (d)]. For that reason, it is crucial to mitigate contact resistances, which we do by electropolishing the contact surfaces, and greasing them with Apiezon N grease just before fastening the braids to the shields with as much force as possible [Salerno97].

The temperature drops between sensors 1 and 2 arise from the thermal resistance of the adapter module in series with the node shields [Fig. 4.13 (a)], and is consistent with independent estimates of these two contributions (see Sec. 4.8.3).

4.8.5 Radiative heat load on the 50K stage

Unlike on the other temperature stages, on the 50K stage, radiation is the main source of heat load, thermal contact resistance are negligible (see Secs. 4.8.3 and 4.8.4) and the thermal conductivity of copper varies only weakly with the RRR [see Fig. 4.11 (a)]. Therefore we analyze heat transfers on the 50K stage differently, using a finite element method on a 3D model of the 50K stage. We make a thin-shell approximation, in which the temperature is approximated to be uniform across the thickness of the shields, to reduce simulation times by modelling the shields as two-dimensional surfaces. We assume radiative heat loads of the form $\phi_{\text{rad}} = \lambda \sigma (T_{\text{RT}}^4 - T^4)$ on the surface of the 50K stage, with $T_{\text{RT}} = 295\text{K}$, where σ is the Stefan-Boltzmann constant, and the attenuation factor $\lambda \in [0, 1]$ comes from geometric factors and non-unit emissivity of the surfaces [see Eq. (4.1)]. Note that Eq. (4.11) is not correct any more because of the temperature-dependence of the heat load, which is the main motivation to model the 50K stage heat transfer with a finite-element simulation.

We report on two cooldowns of the setup described in Sec. 4.8.4 and schematized in Fig. 4.13 (a). In the cooldown which we refer to as “cooldown 1”, the outer surface of 50K shields was directly exposed to the room temperature radiation of the vacuum can. In the other cooldown, “cooldown 2”, we covered the 50K stage with MLI.

To analyze cooldown 1, we simulate the steady-state temperature profile sweeping the attenuation factor λ . The best agreement between the simulated and the measured temperatures is obtained for $\lambda = 2 \pm 0.1\%$ which corresponds to a mean heat load per unit area $\varphi_{\text{eff}} = 8.5 \pm 0.4\text{W/m}^2$, see empty circles in Fig. 4.14 (a).

For cooldown 2, we mounted three additional temperature sensors on the nodes

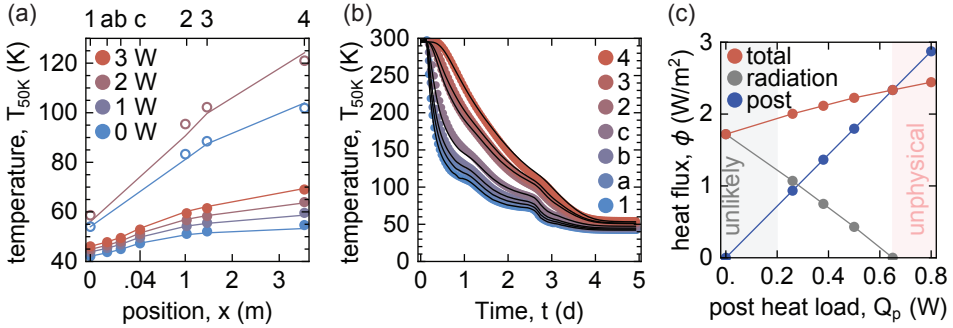


Figure 4.14 (a) 50K steady-state temperature distribution in the presence (filled circles) or absence (empty circles) of multilayer insulation, for the indicated heat applied at the end of the link. The x-axis is non-linear from 0 to 40 cm, to differentiate sensors 1, a, b and c, which have similar x-coordinates. The solid lines are results of finite elements simulation, with the heat flux as a free parameter. (b) 50K temperature vs time after beginning of the cooldown. Solid lines are results from a finite elements simulation whose parameters are extracted from the steady-state temperatures [see panel (e)]. (c) Heat fluxes on the 50K link element shield vs assumed heat load per post. The gray region corresponds to post heat loads which are smaller than expected from independent measurements. The red shaded region corresponds to negative radiative heat flux.

at positions labelled a, b, and c in Fig. 4.13 (a), which allowed us to better resolve the spatial distribution of heat load at the node. As we discuss in more detail in the next paragraph, the MLI is not installed with the same performance standard everywhere on the system due to design constraints imposed by the geometry of the system. We account for this by dividing the 50K stage into three absorption regions covering the node, the side-flange and the link, parametrized with attenuation factors λ_n , λ_{sf} and λ_l , respectively. Due to manufacturing problem of the node shield, in the real system, the side-port flange is fixed to the vertical cylinder of the radiation shield using a press contact fastened with screws realizing only a small fraction of the designed contact area, on the sides of the flange. The absence of a physical contact between the vertical cylinder and the top part of the side-flange increases the length of the path taken by the heat current. To account for the extra thermal resistance this reduced contact induces in the CAD model, we make the thickness t_{sf} of the side-port flange a free parameter, which can be arbitrary low. We obtain the best fit for $t_{sf} = 0.18$ mm, $\lambda_n = 2.4\%$, $\lambda_{sf} = 48\%$ and $\lambda_l = 0.4\%$. The presence of MLI reduces the 50K heat load by a factor of five, down to $1.7 W/m^2$, which results in a significant reduction of the 50K temperatures along the link, see Fig. 4.14 (a).

We note that the MLI is ineffective on the node ($\lambda_n = 2.4\%$). Also, the value

extracted on the side-flange ($\lambda_{\text{sf}} = 48\%$) is close to the black-body radiation limit, corresponding to a heat leak of 3.6W. We suspect that the poor performance of the MLI at the node and its side-flange is caused by MLI design flaws. For instance, the MLI piece covering the top plate has to be compressed to avoid a thermal short with the vacuum can, and has many cuts to let space for the cooler, the support posts and the cabling. In addition, the MLI piece covering the side-flange has open-ended edges, which effectively behave as black-body absorbers. Such design imperfections are known sources of heat leaks [Parma14, Marlow11], but could not be avoided in our design due to constraints imposed by the geometry of the dilution refrigerator. For that reason, in all two-node cryogenic link systems, we decided to cover the link elements with MLI, but not the nodes. In a next generation system, we could increase the spacing between the 50K shield and the vacuum can at the node, to enable a high-performance installation of the MLI.

As a sanity check, we perform a simulation of the cooldown dynamics of the 50K stage, using the fitted thermal parameters, and fixing the plate temperature to its measured value at all times. Here again, the simulation is in very good agreement with the data, as can be seen for cooldown 2 in Fig. 4.14 (b).

From the characterization described in Sec. 4.8.1, we expect that each post will introduce a point-like heat load Q_p ranging from 0.2W to 0.8W, which leads to an effective heat load per unit area ranging from 0.7W/m^2 to 2.9W/m^2 . The lower bound is obtained by assuming that the emissivity of the post is $\varepsilon = 0.8$ and that its foot base is covered by MLI, while the upper bound is obtained assuming that $\varepsilon = 1$ and that the foot base is fully exposed to radiation. In any case, when MLI is used, post heat loads contribute to a significant fraction of the effective heat flux $\varphi_{\text{eff}} := \varphi_{\text{rad}} + n_p Q_p$, where φ_{rad} is the radiative heat flux and $n_p \simeq 3.6\text{m}^{-2}$ is the mean number of post per unit shield area in the link. To analyze the contribution of posts heat loads and radiative heat loads, we fit λ_l to the steady-state temperature profile of cooldown 2, for a fixed heat load per post Q_p which we sweep. The extracted value of λ_l is anticorrelated with the value fixed for Q_p , because the resulting effective heat flux φ_{eff} varies little [Fig. 4.14 (c)]. This reflects the fact that Q_p and λ_l cannot be resolved from the steady-state temperature. The extracted φ_{rad} becomes negative for $Q_p > 0.65\text{W}$, which is not physical and therefore sets a stricter upper bound for Q_p . For a realistic post heat loads $0.2\text{W} < Q_p < 0.8\text{W}$, we find that $0 < \varphi_{\text{rad}} < 1.2\text{W/m}^2$ and $2\text{W/m}^2 < \varphi_{\text{eff}} < 2.3\text{W/m}^2$ [Fig. 4.14 (c)].

This suggests that the MLI leads to a five- to ten-fold reduction of φ_{rad} , and that the post contribution to the total heat flux φ_{eff} is significant or even dominant. The

total heat flux φ_{eff} could therefore be further reduced by improving the 50K posts design. For instance, surrounding the posts with a highly reflective metal shell, or electroplating it with a $1\ \mu\text{m}$ thick copper or tin layer [Le Sage21] would effectively null the emissivity of the post without significantly increasing its thermal conductance, leading to a $\sim 70\%$ reduction of its heat load [Fig. 4.10 (g)].

4.8.6 Waveguide attenuation constant

This subsection is adapted from [Magnard20].

To estimate the loss in the rectangular waveguide housed within the base temperature shield of the link, we measure its attenuation constant using the resonant cavity technique described in Ref. [Kurpiers17]. The device under test consists of two pieces of rectangular waveguide of the WR90 type, made of AL6061 aluminum without any surface treatment. The two pieces, of $12''$ (304.8 mm) and 2.5 m, respectively, are joined in a flange-to-flange flat connection and held below 20 mK inside the single-node prototype [Fig. 4.15 (a)]. Both ends of the waveguide are closed with aluminum plates with an aperture hole, to form a multi-mode 3D cavity displaying an inter-mode frequency spacing ranging from 30 MHz to 45 MHz through the X band. The dimensions of the aperture holes are chosen such that the cavity modes are undercoupled.

Using a vector network analyzer (VNA), we measure selected resonance peaks between 7.5 GHz and 11 GHz in transmission, and fit them to a Lorentzian curve to extract their loaded quality factor Q [Fig. 4.15 (b,c)]. The loaded quality factor being a lower bound to the internal quality factor Q_i , we determine an upper-bound to the attenuation constant [Pozar12, Kurpiers17]

$$\alpha(\nu) = \frac{1}{Q(\nu)} \frac{2\pi\nu}{c\sqrt{1 - \left(\frac{c}{2a\nu}\right)^2}},$$

where ν is the resonance frequency, c is the speed of light in vacuum and $a = 22.86\ \text{mm}$ is the width of the waveguide. The attenuation constant is found to be below 1 dB/km for all measured data points [Fig. 4.15 (d)].

We suspect that the attenuation constant is currently limited by seam loss, which could be reduced using choke flanges or by welding the waveguide pieces to each other. Quality factors as high as 10^8 can be obtained in seamless cavities made of high purity aluminum with the proper annealing and surface etch treatment [Reagor13, Reagor16, Chakram20]. Therefore, waveguide losses as low as 0.01 dB/km may be achievable.

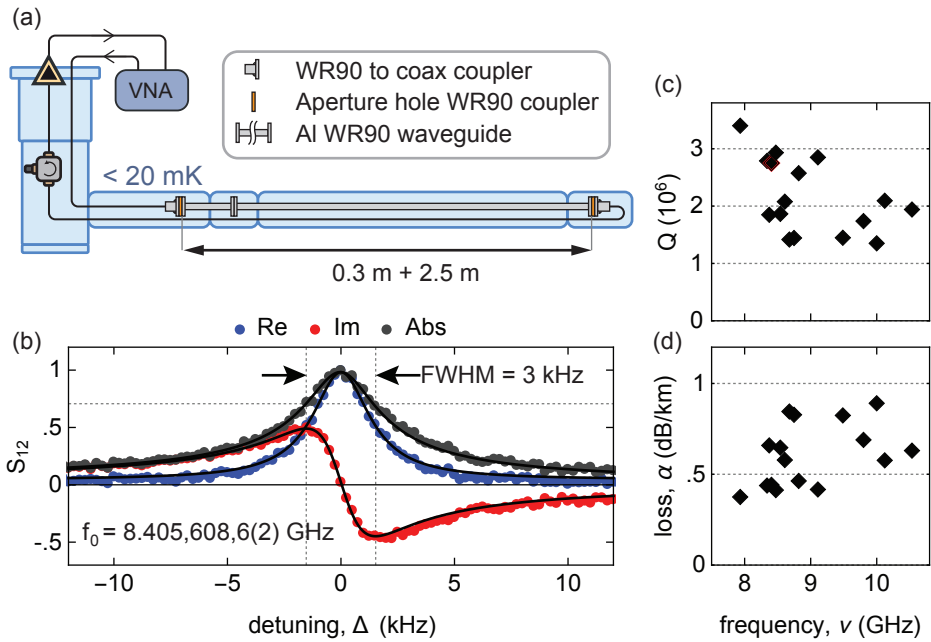


Figure 4.15 (a) Schematic diagram of the waveguide loss characterization experiment. (b) Real part (blue), imaginary part (red) and absolute value (black) of the transmission spectrum S_{12} around a waveguide cavity mode resonance at $f_0 = 8.405,608,6(2)$ GHz [indicated with a red edge in panel (c)]. (c) Loaded quality factor Q , and (d), loss rate α vs resonance frequency ν for selected waveguide cavity mode resonances.

Chapter 5

Unconditional, All-Microwave Reset

*If you call it Fast All-microwave Reset of a
Transmon qubit, you might be remembered as the
FART guy.*

— Andreas Wallraff

The efficient initialization of a set of qubits into their ground state is one of the DiVincenzo criteria for quantum information processing [DiVincenzo00]. Initialization is also critical for the implementation of error correction codes [Schindler11, Reed12, Chiaverini04] to reset ancilla qubits on demand to a fiducial state in short time and with high fidelity. Indeed, reset times as short as a few hundreds of nanoseconds leads to a non-negligible contribution to the physical errors in quantum error correction codes [Chen21b]. For this reason, qubit reset procedures have been implemented for a wide range of physical quantum computation platforms [Monroe95b, Jelezko04, Elzerman04, Dutt07, Rogers14], including superconducting qubits [Valenzuela06, Reed10b, Mariantoni11b, Johnson12, Ristè12b, Ristè12a, Campagne-Ibarcq13, Salathé18, Geerlings13, Magnard18, Egger18, McEwen21, Zhou21]. In this chapter, we will give an overview of the different types of reset protocols used for superconducting qubits, and present our approach: an all-microwave reset protocol achieving high speed and fidelity, putting little constraint on hardware or design, and actively resetting higher energy levels of the transmon qubit.

5.1 Literature Overview

Reset protocols for superconducting qubits can be categorized in two approaches. A common approach is to use the outcome of a strong projective measurement to either herald the ground state [Johnson12] or deterministically prepare it using feedback [Ristè12b, Ristè12a, Campagne-Ibarcq13, Salathé18, Córcoles21]. Measurement-induced state mixing limits the achievable single-shot readout fidelity and the performance of this approach [Campagne-Ibarcq13, Boissonneault09, Slichter12]. The fidelity of such reset-by-measurement protocols can be improved by using low-power qubit readout and repeating the reset-protocol multiple-times until success, at the cost of a slower total reset duration [Córcoles21, Elder20]. In addition, measurement-induced mixing constrains the quantum-non-demolition nature of dispersive readout giving rise to leakage out of the qubit subspace [Campagne-Ibarcq13, Sank16], which is particularly detrimental to quantum error correction [Fowler13, Chen21b].

Alternatively, qubit reset can be achieved by coupling the qubit excited state to a cold and rapidly decaying quantum system. Such driven reset schemes [Valenzuela06, Grajcar08, Reed10b, Geerlings13, Egger18, McEwen21, Zhou21, Magnard18] make use of ideas related to dissipation engineering [Murch12, Premaratne17, Tan17a, Liu16]. In one variant of this approach [Reed10b], the qubit is quickly tuned into resonance with a Purcell filtered, large-bandwidth, resonator using magnetic flux. The qubit then quickly thermalizes to its ground state due to Purcell decay, the rate of which can be adjusted, on-demand, by three orders of magnitude. By tuning the qubit frequency down adiabatically through that of the resonator, one can also reset higher transmon levels [McEwen21]. The DC flux pulses employed in these schemes require careful calibration, they may affect subsequent gates by bleedthrough and neighboring qubits through cross-talk [Kelly14]. To bypass these inconvenients, another scheme induces a qubit-resonator coupling by modulating the qubit frequency with an AC flux pulse [Zhou21]. However, the need for AC or fast DC flux pulses renders these schemes incompatible with fixed frequency qubit architectures [Jurcevic20], or 3D qubits housed inside a superconducting cavity [Wang16, Campagne-Ibarcq18].

An all-microwave reset protocol utilizing the qubit-state-dependent response of a resonator [Geerlings13] avoids the use of flux tuning and its potentially detrimental effects. This protocol [Geerlings13] has minimal hardware requirements, only a single resonator, but requires a cavity linewidth κ smaller than the dispersive interaction strength χ limiting both the speed of the reset process and the readout if the same resonator is used [Gambetta07, Walter17].

In this chapter, we demonstrate an alternative all-microwave reset protocol of a three-level transmon coupled to a resonator with no constraint on κ . Driving the transmon simultaneously with two coherent tones forms a Λ system in the Jaynes-Cummings ladder [Pechal14] and unconditionally transfers any excitation in the two lowest excited states of the transmon to a single-photon emitted to the environment, thus resetting the transmon qutrit on-demand. This protocol outperforms prior measurement-based and all-microwave driven reset schemes in speed and fidelity Fig. 5.1, populates the resonator with one photon at most, resets population leaked to the second excited state of the qubit, and can be extended to other types of superconducting qubits. In addition, this protocol is of practical interest as it is optimized when the resonator is designed for rapid and high-fidelity transmon readout [Walter17]. A pulsed approach using the same transitions as ours was demonstrated shortly afterwards [Egger18].

We compare experimental implementations of superconducting qubit reset proto-

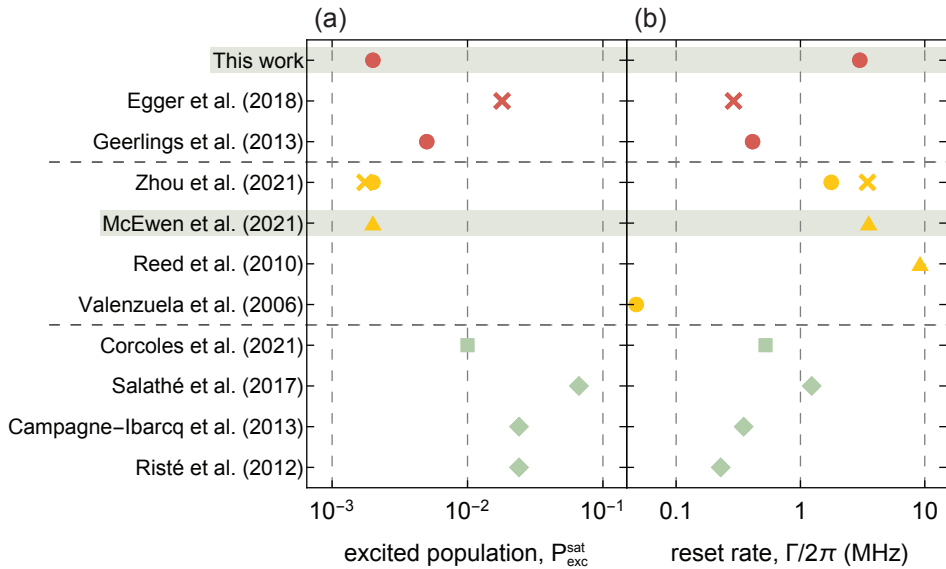


Figure 5.1 Experimentally achieved residual excited state populations P_{exc}^{sat} (a) and reset rates Γ (b) of selected implementations of superconducting qubit reset protocols group by three categories. Green: single (diamonds) and repeated (square) qubit measurement and feedback control [Risté12b, Campagne-Ibarcq13, Salathé18, Córcoles21]. Yellow: qubit frequency tuning via flux pulses [Valenzuela06, Reed10b, McEwen21, Zhou21]. Red: all-microwave drive-induced dissipation [Geerlings13, Magnard18]. For flux and microwave driven reset schemes, we distinguished those based on DC pulses (triangles), AC pulses (rounds), and time-resolved π pulses (crosses). Schemes which also reset higher energy levels are shaded in light gray.

cols by two performance metrics, the reset rate Γ and the residual excited state population $P_{\text{exc}}^{\text{sat}}$ (Fig. 5.1). $P_{\text{exc}}^{\text{sat}}$ is obtained at the end of the reset procedure (measurement-based and π -pulse-based reset) or at steady-state (microwave and flux driven reset), corresponding in all cases to the lowest residual excitation reached. For driven reset protocols, Γ is defined as the rate at which the qubit approaches the ground state. For measurement and π -pulse based protocols, Γ satisfies $P_{\text{exc}}^{\text{sat}} = e^{-\Gamma t_p}$, where t_p is the total protocol duration. Overall, schemes based on flux pulses perform slightly better than those using microwave drives which in turn outperform than those based on measurement and feedback. Our all-microwave implementation performs as well as the best flux based schemes.

5.2 Experimental setup and concept

The device used in our experiment and schematically illustrated in Fig. 5.2 (a), uses a transmon qubit [Koch07, Schreier08] (orange), with transition frequency $\omega_q/2\pi = 6.343$ GHz, anharmonicity $\alpha/2\pi = -265$ MHz and energy relaxation time $T_1 = 5.5 \mu\text{s}$. We control the qubit state with microwave pulses up-converted from an arbitrary waveform generator (AWG), applied to the transmon through a dedicated drive line. To perform the reset, the transmon is capacitively coupled with rate $g_r/2\pi = 335$ MHz to a resonator of frequency $\omega_r/2\pi = 8.400$ GHz, resulting in a dispersive interaction with rate $\chi_r/2\pi = -6.3$ MHz (light blue). The reset resonator is connected through a Purcell-filter resonator to cold 50Ω loads with an effective coupling $\kappa/2\pi = 9$ MHz. This resonator can, in principle, be used for transmon readout. However, in the present work, to decouple the reset from its characterization process, we read out the transmon with a dedicated, Purcell-filtered resonator (light green). The parameters of the qubit are extracted using the methods presented in Sec. 2.1.4 and are listed in table 5.1. The parameters of the readout and reset circuits are obtained from fits to the transmission spectrum of the respective Purcell filter using the technique and model discussed in Ref. [Walter17].

We read out the transmon state using a gated drive applied to the input port of the readout resonator at a frequency optimized for qutrit readout [Bianchetti10]. The signal scattered off the readout resonator is amplified at $T_{\text{BT}} = 10$ mK by a Josephson parametric amplifier [Yurke96, Eichler14b]. The signal is then amplified at 4 K with high electron mobility transistors, down-converted using an I-Q mixer, digitized using an analog-to-digital converter, digitally down-converted and processed using a field programmable gate array.

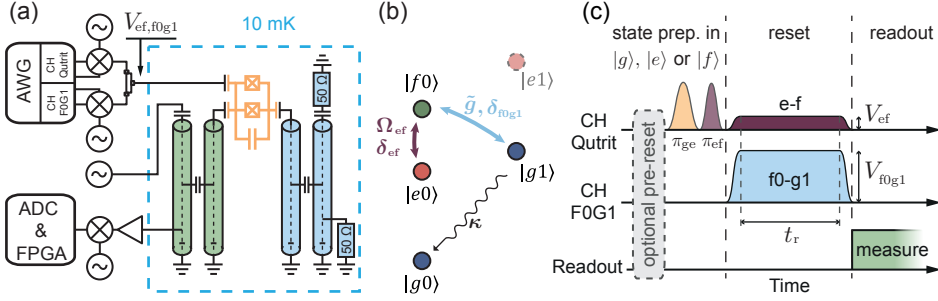


Figure 5.2 (a) Simplified schematic of the experimental setup. A transmon (orange) is coupled to two Purcell filtered resonators. The readout resonator (green) is connected to room temperature electronics (description in the main text), while the reset resonator (blue) is connected to two 50Ω ports thermalized at base temperature. (b) Jaynes-Cummings ladder diagram of the transmon/reset resonator energy levels. The purple and light blue arrows represent the e-f and f0-g1 pulsed coherent drives, respectively, and the black arrow labelled κ illustrates the resonator decay process. (c) Illustration of the pulse schemes used to test the reset protocol. We initialize the qutrit to its ground state passively or optionally with an unconditional reset, then prepare the desired state $|g\rangle$, $|e\rangle$ or $|f\rangle$ with control pulses (labelled π_{ge} and π_{ef}). We reset the qutrit by simultaneously applying flat-top e-f (purple) and f0-g1 (light blue) pulses for a reset time t_r . The resulting qutrit state is then measured by applying a microwave tone to the readout resonator (green).

$\omega_q/2\pi$	6.343 GHz		
$\alpha/2\pi$	-265 MHz		
n_{th}	17 %		
T_1^{ge}	5.5 μs	T_1^{ef}	2.1 μs
T_2^{ge}	7.6 μs	T_2^{ef}	4.2 μs
T_2^{*ge}	3.5 μs	T_2^{*ef}	2.0 μs
$\chi_m/2\pi$	-5.8 MHz	$\chi_r/2\pi$	-6.3 MHz
$g_m/2\pi$	210 MHz	$g_r/2\pi$	335 MHz
$\omega_m/2\pi$	4.787 GHz	$\omega_r/2\pi$	8.400 GHz
$\omega_{PFm}/2\pi$	4.778 GHz	$\omega_{PFr}/2\pi$	8.443 GHz
Q_{PFm}	91	Q_{PFr}	60
$J_m/2\pi$	13.6 MHz	$J_r/2\pi$	20.9 MHz
$\kappa_m/2\pi$	12.6 MHz	$\kappa/2\pi$	9.0 MHz

Table 5.1 Sample parameters: From time resolved Ramsey measurements we extract the ge transition frequency $\omega_q/2\pi$, and the anharmonicity $\alpha/2\pi$. From resonator transmission spectroscopy we obtain the frequencies, quality factors and couplings of the measurement (m) and reset (r) resonators: Purcell filter frequency $\omega_{PFm,r}/2\pi$, resonator frequency $\omega_{m,r}/2\pi$, quality factor of the Purcell filter $Q_{PFm,r}$ and the coupling rate of the resonator to Purcell filter $J_{m,r}/2\pi$. We obtain the dispersive shifts $\chi_{m,r}/2\pi$ by performing resonator spectroscopy with the qutrit initially prepared in $|g\rangle$, $|e\rangle$ and $|f\rangle$. The coherence times of the qutrit are extracted from time resolved measurements as described in Sec. 2.1.4.

The reset concept, illustrated in Fig. 5.2 (b), is based on a cavity-assisted Raman transition between $|f, 0\rangle$ and $|g, 1\rangle$ which we described in details in Sec. 2.1.7 [Pechal14, Zeytinoglu15, Gasparinetti16]. Here, $|s, n\rangle$ denotes the tensor product of the transmon in state $|s\rangle$, with its three lowest energy eigenstates $|g\rangle$, $|e\rangle$ and $|f\rangle$, and the reset resonator in the n photon Fock state $|n\rangle$. By simultaneously driving the $|f, 0\rangle \leftrightarrow |g, 1\rangle$ (f0-g1) transition and the $|e, 0\rangle \leftrightarrow |f, 0\rangle$ (e-f) transition, the population is transferred from the qutrit excited states, $|e, 0\rangle$ and $|f, 0\rangle$, to the state $|g, 1\rangle$. The system then rapidly decays to the target dark state $|g, 0\rangle$ by photon emission at rate κ , effectively resetting the qutrit to its ground state.

We model the dynamics of the reset by the non-Hermitian Hamiltonian

$$H/\hbar = \begin{bmatrix} -\delta_{ef} & \Omega_{ef} & 0 \\ \Omega_{ef}^* & 0 & \tilde{g} \\ 0 & \tilde{g}^* & -\delta_{f0g1} - i\kappa/2 \end{bmatrix}, \quad (5.1)$$

acting on the states $|e, 0\rangle$, $|f, 0\rangle$ and $|g, 1\rangle$. Here, the non-Hermitian term $-i\kappa/2$ accounts for the photon emission process, and Ω_{ef} and \tilde{g} are the e-f and f0-g1 drive-induced Rabi rates, respectively. Because the f0-g1 drive acts on a second order-transition, it requires a high amplitude V_{f0g1} and induces significant ac Stark shifts $\bar{\Delta}_{ef}$ and $\bar{\Delta}_{f0g1}$ of the e-f and f0-g1 transitions, see Sec. 2.1.7 and [Zeytinoglu15]. In Hamiltonian (5.1), δ_{ef} and δ_{f0g1} denote the detuning of the drives from their respective ac Stark shifted transitions. Therefore, gaining experimental control over the reset drive parameters requires to characterize the dependence of $\bar{\Delta}_{ef}$ and $\bar{\Delta}_{f0g1}$ on V_{f0g1} as well as the relation between the drive amplitudes and their corresponding Rabi rates.

5.3 Calibration

First, we determine the ac Stark shift $\bar{\Delta}_{f0g1}$. We initialize the transmon in $|g\rangle$, then apply a sequence of two π -pulses (π_{ge} , π_{ef}) to prepare the system in $|f, 0\rangle$ [Fig. 5.2 (c)]. We apply a flat top f0-g1 pulse of carrier frequency ν_{f0g1} , amplitude V_{f0g1} and duration t_r and read out the resulting transmon state populations. Here and in all calibration measurements, the populations $P_{g,e,f}$ of the transmon qutrit are extracted by comparing the averaged signal transmitted through the readout resonator to reference traces [Bianchetti10, Kurpiers19b]. We repeat the process varying ν_{f0g1} and V_{f0g1} , while keeping $V_{f0g1} t_r$ fixed to obtain comparable Rabi angles for the rotations induced by the f0-g1 drive. For a given value of V_{f0g1} , we fit the dependence of P_g on ν_{f0g1}

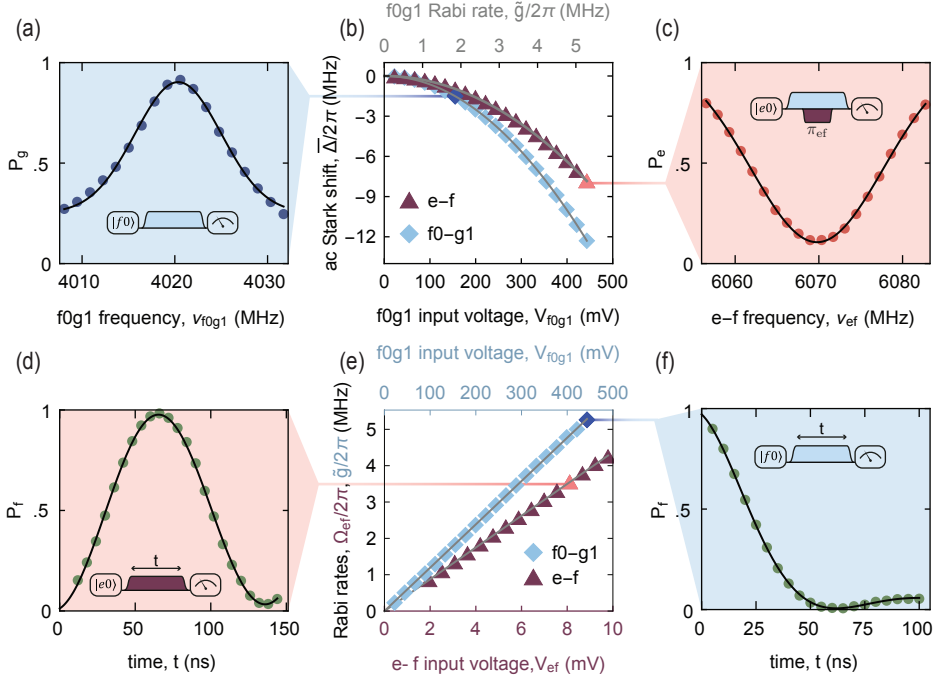


Figure 5.3 (a) Population P_g vs the frequency ν_{f0g1} of a flat-top $f0-g1$ pulse, of input voltage amplitude V_{f0g1} , applied to the qutrit initially prepared in $|f, 0\rangle$. (b) Measured ac Stark shifts $\bar{\Delta}_{f0g1}$ and Δ_{ef} of the $f0-g1$ (blue diamonds) and $e-f$ (purple triangles) transitions, vs. amplitude V_{f0g1} of the $f0-g1$ drive. The solid lines are quadratic fits to the data. (c) Population P_e vs frequency ν_{ef} of a flat-top $e-f$ π -pulse applied on the qutrit, initially prepared in state $|e, 0\rangle$, in the presence of a continuous $f0-g1$ drive of amplitude V_{f0g1} . (d) Population P_f vs duration t of a resonant flat-top $e-f$ pulse, of amplitude $V_{ef} = 8$ mV. (e) Extracted Rabi rates Ω_{ef} and \tilde{g} , of the $e-f$ (purple triangles) and $f0-g1$ (blue diamonds) drives versus their amplitude, V_{ef} and V_{f0g1} . The solid lines are linear fits. (f) Population P_f vs the duration t of a resonant square $f0-g1$ pulse, of amplitude V_{f0g1} . The pulse schemes used to acquire the data shown in panels (a), (c), (d) and (f) are shown as insets, with the $f0-g1$ and $e-f$ pulse envelopes represented in blue and purple, respectively. The solid lines in (a) and (c) are fits to Gaussians. The solid lines in (c) and (f) are fits to Rabi oscillation models described in <INSERT SECTION OR EQ.>.

to a Gaussian whose center yields the ac Stark shifted frequency, at which the population transfer from $|f, 0\rangle$ to $|g, 1\rangle$ is maximized [Fig. 5.3 (a)]. The ac Stark shift $\bar{\Delta}_{f0g1}$ extracted in this way shows a quadratic dependence on V_{f0g1} [blue diamonds in Fig. 5.3 (b)].

To determine $\bar{\Delta}_{ef}$, we prepare the system in $|e, 0\rangle$ and apply a short square $e-f$ π -pulse of frequency ν_{ef} in the presence of a continuous, resonant $f0-g1$ drive of amplitude V_{f0g1} . For each V_{f0g1} , we extract the ac Stark shifted frequency of the $e-f$ transition by

finding the minimum of P_e vs. ν_{ef} with a fit to a Gaussian [Fig. 5.3 (c)]. As before, we observe a quadratic dependence of $\bar{\Delta}_{ef}$ on V_{f0g1} [purple triangles in Fig. 5.3 (b)].

Finally, we perform resonant Rabi oscillation measurements on the e-f and f0-g1 transitions to extract the linear relation between the drive amplitudes V_{ef} and V_{f0g1} , and their corresponding Rabi rates [Fig. 5.3 (d-f)]. For the e-f Rabi oscillation measurement, we fit the time-dependence of the population P_e displayed in Fig. 5.3 (d) with the function

$$f_{\Omega_{ef}}(t) = \frac{1}{2} e^{-\gamma_a t^*} \left(1 - e^{-\gamma_b t^*} \cos\left(\frac{\Omega_{ef} t^*}{2}\right) \right), \quad (5.2)$$

where $t^* = t - t_0$ offsets the time t by t_0 to account for the fact that the rising and falling edges of the e-f pulse drive the e-f transition for a finite time. The fit parameters γ_a and γ_b account for transmon relaxation to $|g\rangle$ and decoherence in the $\{|e\rangle, |f\rangle\}$ subspace, respectively. We verified numerically that Eq. (5.2) is a good approximation of the time dependence of P_e during e-f Rabi oscillations and that it yields an unbiased estimate of Ω_{ef} , by comparing it to the result of a master equation simulation. To reduce the number of free parameters, we fit all data sets simultaneously and constrain t_0 , γ_a and γ_b to be the same for all sets as these parameters are expected to be independent of Ω_{ef} .

To model the f0-g1 damped oscillations displayed in Fig. 5.3 (f), we use a two-level model with loss described by the non-Hermitian Hamiltonian

$$H_{f0g1} = \begin{bmatrix} i\gamma/2 & \tilde{g} \\ \tilde{g}^* & i\kappa/2 \end{bmatrix},$$

which acts on states $|f, 0\rangle$ and $|g, 1\rangle$, analyzed in a rotating frame. The non-Hermitian terms $i\kappa/2$ and $i\gamma/2$ account for photon emission and transmon decay from $|f\rangle$ to $|e\rangle$, which bring the system to the dark states $|g, 0\rangle$ and $|e, 0\rangle$, respectively. Based on this model we derive an analytical expression for the $|f\rangle$ state population as a function of time

$$P_f(t) = e^{-\frac{(\kappa+\gamma)}{2}t} \left| \cosh\left(\frac{\Omega t}{2}\right) + \frac{\kappa - \gamma}{2\Omega} \sinh\left(\frac{\Omega t}{2}\right) \right|^2,$$

where $\Omega = \sqrt{-(2\tilde{g})^2 + (\kappa - \gamma)^2}/4$ is real positive or imaginary depending on the drive rate \tilde{g} . Using $P_f(t)$ we obtain the fit function

$$f_{\tilde{g}}(t) = \lambda P_f(t - t_0) + \mu, \quad (5.3)$$

where the parameters λ and μ account for potential state preparation and measurement

(SPAM) errors and the parameter t_0 accounts for the fact that the gaussian rising and falling edges of the flat top f0-g1 pulse drive the f0-g1 transition for a finite time. For each drive amplitude V_{f0g1} , we obtain Rabi oscillation data which we fit with Eq. (5.3). Similarly to the e-f Rabi rate calibration, we fit all data sets simultaneously and constrain λ , μ , t_0 and κ to be the the same for all sets.

5.4 Reset operating regimes

In all following experiments, we adjust the drive frequencies such that $\delta_{ef} = \delta_{f0g1} = 0$ to reset the transmon, leaving only \tilde{g} and Ω_{ef} as tunable parameters. From Eq. (5.1), we derive the time-dependence of the population

$$P_{s|s_0}^H(t) = \left| \sum_k \langle s | \hat{A}_k | s_0 \rangle e^{-i\lambda_k t} \right|^2 \quad (5.4)$$

of state $|s\rangle \in \{|e, 0\rangle, |f, 0\rangle, |g, 1\rangle\}$ during the reset. Here, $|s_0\rangle$ is the initial state of the system, λ_k are the eigenvalues of Hamiltonian (5.1) and \hat{A}_k are operators that depend only on Hamiltonian (5.1). These populations oscillate at rates $2\text{Re}(\lambda_k)$ and decay exponentially at rates $2|\text{Im}(\lambda_k)|$. As the smallest decay rate dominates at long reset times, we define the reset rate as $\Gamma \equiv \min[2|\text{Im}(\lambda_k)|]$. The reset can be operated in two regimes. In the low drive-power region hatched in Fig. 5.4 (a), the eigenvalues λ_k are purely imaginary: the reset is in an over-damped regime where the qutrit excited populations decay with no oscillation. When crossing the critical damping boundary, two eigenvalues abruptly display a finite real part and the reset enters an under-damped, oscillatory regime. The reset rate Γ is bounded by its maximum value $\kappa/3$ which it reaches on a line in parameter space, defining an optimal branch (solid red line in Fig. 5.4). The optimal branch intersects the critical-damping boundary at an exceptional point (black cross in Fig. 5.4) where all three eigenvalues are identical [Heiss04]. At this point, the reset has maximum rate and displays no oscillations. For a given \tilde{g} , there is a unique value of Ω_{ef} maximizing the reset rate to $\Gamma_{\max}(\tilde{g})$. The parameter configuration then lies on the critical-damping boundary if \tilde{g} is below its value at the exceptional point $\tilde{g}_{\text{ep}} = \sqrt{2/27}\kappa$ (red dashed line in Fig. 5.4), and on the optimal branch otherwise. As \tilde{g} goes below \tilde{g}_{ep} , $\Gamma_{\max}(\tilde{g})$ abruptly drops [Fig. 5.4 (b)]. Therefore, the ability to drive the f0-g1 transition with $\tilde{g} > \tilde{g}_{\text{ep}}$ is crucial to achieve fast reset.

We give a detailed thorough derivation of Eq. (5.4) and analysis of the different

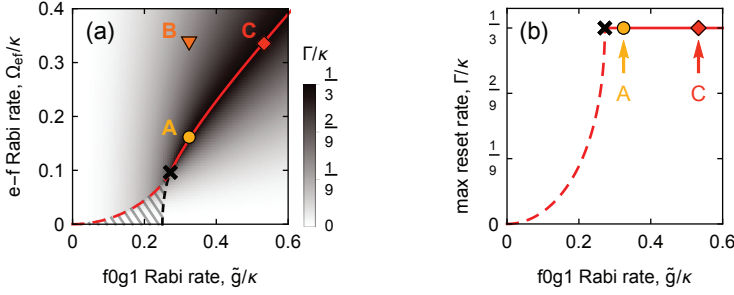


Figure 5.4 (a) Calculated reset rate Γ/κ , vs Rabi rates \tilde{g}/κ and Ω_{ef}/κ . The over-damped parameter region is hatched. The red line shows the values of Ω_{ef} maximizing Γ as a function of \tilde{g} , and corresponds to the optimal branch where it is solid. (b) Maximized reset rate Γ_{\max}/κ vs \tilde{g}/κ (we follow the red line from (a)). In (a) and (b), the parameter configurations A, B and C at which the reset dynamic was probed (see main text and Fig. 5.5) are indicated with colored symbols and the exceptional point is represented by a black cross.

reset operation regimes in appendix D.

5.5 Experimental results

We probed the reset dynamics at the three parameter configurations labelled A, B and C in Fig. 5.4 (a). We initialize the transmon in $|e, 0\rangle$ or $|f, 0\rangle$, apply the reset drive pulses for a time t_r , and then readout the transmon with single-shot measurements, as illustrated in Fig. 5.2 (c). Utilizing the single-shot statistics, we correct for the qutrit state assignment errors, to determine the population of the qutrit with systematic errors below 0.3%, as we discuss in greater detail later in Sec. 5.6. We first probed the reset in configuration A ($\Omega_{ef}/2\pi = 1.5$ MHz, $\tilde{g}/2\pi = 2.9$ MHz), which is on the optimal branch and is the closest to the exceptional point. During the reset, the transmon state oscillates between $|g\rangle$, $|e\rangle$ and $|f\rangle$ while rapidly decaying to $|g\rangle$ on a time scale of 300 ns, independent of the initial state [Fig. 5.5 (a,b)]. The excited population $P_{\text{exc}} = P_e + P_f$ drops to below 1% without displaying any oscillations [Fig. 5.5 (c)]. The reset dynamics calculated from Eq. (5.4) is in excellent agreement with the data, as shown by the solid lines in Fig. 5.5 (a,b). When increasing the e-f drive to $\Omega_{ef}/2\pi = 3$ MHz (B), the decaying state $|g, 1\rangle$ is populated earlier. As a result, we observe that P_{exc} drops faster initially but at a slower rate at longer times since configuration B is not on the optimal branch [Fig. 5.5 (c)]. Because this parameter set realizes the under-damped regime, P_{exc} displays oscillatory features. Configuration C ($\Omega_{ef}/2\pi = 3$ MHz, $\tilde{g}/2\pi = 4.8$ MHz) is on the optimal branch and has higher drive rates than configuration A. Therefore, P_{exc}

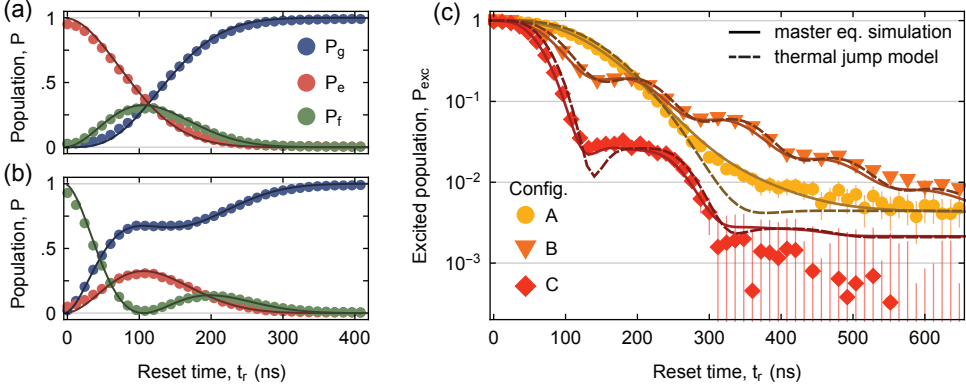


Figure 5.5 Qutrit populations $P_{g,e,f}$ vs reset time t_r with reset parameters in configuration A (see main text), and system initialized in $|e, 0\rangle$ (a) or $|f, 0\rangle$ (b). The solid lines in (a) and (b) are calculated from Eq. (5.4). (c) Excited population P_{exc} as a function of reset time t_r , when the qutrit is initialized in $|e, 0\rangle$, shown for reset parameter configurations A, B and C. The solid and dashed lines are calculated from a master equation simulation, and from Eq. (5.5), respectively.

drops faster initially, and with the same long-time rate, leading to a more efficient reset. In this configuration, P_{exc} drops below 1% in only 280 ns, and below measurement errors ($\sim 0.3\%$) in steady-state [Fig. 5.5 (c)], outperforming all existing measurement-based and microwave-driven reset schemes by an order of magnitude (Fig. 5.1).

At long reset times, P_{exc} saturates to a non-zero steady-state value $P_{\text{exc}}^{\text{sat}}$ which is determined by three effects: transmon rethermalization, finite temperature of the reset resonator, and off-resonant driving of the g-e transition with the e-f drive.

The effective temperatures of superconducting qubits are typically higher than the base temperature of the dilution refrigerator T_{BT} , which implies that the thermal excitation rate k_{\uparrow} of the qubit is higher than expected from T_{BT} [Jin15]. At equilibrium, thermalization competes against decay and the qubit has an equilibrium excited population $n_{\text{th}} \simeq k_{\uparrow} T_1$ (in the limit where $n_{\text{th}} \ll 1$). Similarly, for the unconditional reset protocol, the competition between thermalization and reset rate should yield the steady-state excitation population $P_{\text{exc}}^{\text{sat}} = k_{\uparrow} T_{\text{rst}}$, with T_{rst} a characteristic time of the reset. We model thermal excitations as quantum jumps to derive an analytical expression for $P_{\text{exc}}^{\text{sat}}$. At any time τ , the probability of a transmon rethermalization event (jump from $|g\rangle$ to $|e\rangle$) in a time window of width $d\tau$ is

$$(1 - P_{\text{exc}}(\tau))k_{\uparrow}d\tau.$$

If such an event happens at time τ , the excited population a time $t \geq \tau$ is $P_{\text{exc}}(t - \tau)$ as defined from Eq. (5.4). Integrating over all possible rethermalization jump times, we obtain

$$\begin{aligned} P_{\text{exc}}(t) &= P_{\text{exc}}^{\text{H}}(t) + \int_0^t P_{\text{exc}}(t - \tau)[1 - P_{\text{exc}}(\tau)]k_{\uparrow}d\tau \\ &= P_{\text{exc}}^{\text{H}}(t) + k_{\uparrow}(1 - P_{\text{exc}}) * P_{\text{exc}} \\ &\simeq P_{\text{exc}}^{\text{H}}(t) + k_{\uparrow}(1 - P_{\text{exc}}^{\text{H}}) * P_{\text{exc}}^{\text{H}}, \end{aligned} \quad (5.5)$$

where $P_{\text{exc}}^{\text{H}}$ is the population dynamics given by Eq. (5.4) in the absence of competing thermalization, $*$ is the symbol for convolution, and the third line is obtained by approximating P_{exc} with $P_{\text{exc}}^{\text{H}}$. In steady-state, $P_{\text{exc}}^{\text{H}} = 0$, which yields a simple expression of the saturation excited population

$$\begin{aligned} P_{\text{exc}}^{\text{sat}} &= k_{\uparrow} T_{\text{rst}} \\ \text{with } T_{\text{rst}} &:= \int_0^{+\infty} P_{\text{exc}} d\tau, \end{aligned} \quad (5.6)$$

which tends towards k_{\uparrow}/Γ for large drive rates. Faster drops of P_{exc} , obtained by increasing the drive rates along the optimal branch, lead to a smaller T_{rst} , which results in lower steady-state excited populations [Fig. 5.5 (c)]. Indeed, we calculate $P_{\text{exc}}^{\text{sat}} = 0.26\%$, 0.46% and 0.34% for configuration A, B and C, respectively, in good agreement with the data [see dashed lines in Fig. 5.5 (c)].

In the level diagram of Fig. 5.2 (b), the black arrow labelled κ , connecting $|g, 1\rangle$ to $|g, 0\rangle$ represents the decay of the reset resonator. A finite temperature T_{rr} of the reset resonator can be accounted for by a transition in the opposite direction with rate $\kappa \cdot \exp[-\hbar\omega_{\text{r}}/k_{\text{b}}T_{\text{rr}}]$. If the unconditional reset is dominated by this rate, the entropy of the transmon and of the resonator equalize and the temperature of the transmon would reach $T_{\text{rr}}\omega_{\text{ge}}/\omega_{\text{r}}$ in steady-state. Driving the e-f transition during unconditional reset broadens also the g-e transition. The e-f drive, being detuned from the g-e transition by approximately the anharmonicity α of the transmon, also drives the g-e transition which leads to e-f drive induced thermalization. A trade-off between speed and reset fidelity has to be made when this effect is limiting.

We account for all effects and qubit decoherence with a master equation simulation of the process, which is described in details in appendix E.1. The numerical simulations obtained with independently measured parameters (table 5.1) and a resonator temperature set to zero, are in excellent agreement with the data and Eq. (5.5) for all

probed reset parameter configurations [solid lines in Fig. 5.5 (c)]. This suggests that the $P_{\text{exc}}^{\text{sat}}$ achievable in our experiment is limited by transmon rethermalization, and that other limitations are negligible for the presented parameters.

5.6 Qubit measurement and population extraction

To study the reset dynamics (Fig. 5.5), we pre-reset the transmon with an unconditional reset, and prepare it in state $|e, 0\rangle$ or $|f, 0\rangle$ with a sequence of π -pulses [Fig. 5.6 (a)]. Next, we apply the reset pulses for a duration t_r and apply a microwave tone at the readout resonator to readout the transmon. We record the I and Q quadratures of the readout signal for a duration of $t_m = 120$ ns starting at the rising edge of the readout tone. We refer to each recorded readout signal as a single-shot trace S .

To define an assignment rule which discriminates the transmon state based on a single-shot trace, we collect reference sets of 40000 single-shot traces obtained with the transmon initialized in states $|g\rangle$, $|e\rangle$ or $|f\rangle$. State initialization is performed using a pre-selection readout pulse that heralds the transmon in its ground state (details discussed later in this section) followed by control π -pulses to prepare states $|e\rangle$ and $|f\rangle$ [Fig. 5.6 (b)]. We integrate each reference single-shot trace with weight functions w_1 and w_2 , to calculate the integrated quadratures $u = \int_0^{t_m} S(t)w_1(t)dt$ and $v = \int_0^{t_m} S(t)w_2(t)dt$, in post-processing. We choose w_1 and w_2 such that they maximize the distinguishability between the three qutrit states (see Sec. 3.1). For each prepared state $|k\rangle$, the set of integrated traces $\vec{x} = (u, v)$ forms three clusters in the u - v plane [Fig. 5.6 (c)] following a trimodal Gaussian distribution of mixture density

$$f_k(\vec{x}) = \sum_s \frac{A_{s,k}}{2\pi\sqrt{|\Sigma|}} e^{-\frac{1}{2}(\vec{x}-\mu_s)^\top \cdot \Sigma^{-1} \cdot (\vec{x}-\mu_s)}.$$

We extract the parameters $A_{s,k}$, Σ and μ_s with maximum likelihood estimation. Based on these parameters, we define regions in the u - v plane used to assign the result of the readout trace: if an integrated trace \vec{x}_i is in the region labeled m , we assign it state m [Fig. 5.6 (c)]. By counting the number of traces assigned the value m when the qutrit was prepared in state $|s\rangle$, we estimate the elements $R_{m,s} = p(m|s)$ of the reference assignment probability matrix R (see table 5.2).

To extract the qutrit state populations $P = (P_g, P_e, P_f)$ after a reset of duration t_r , we also repeat the scheme illustrated in [Fig. 5.6 (a)] 40000 times, and record single-shot traces for each run. As for the reference sets, the assignment probability M_m is

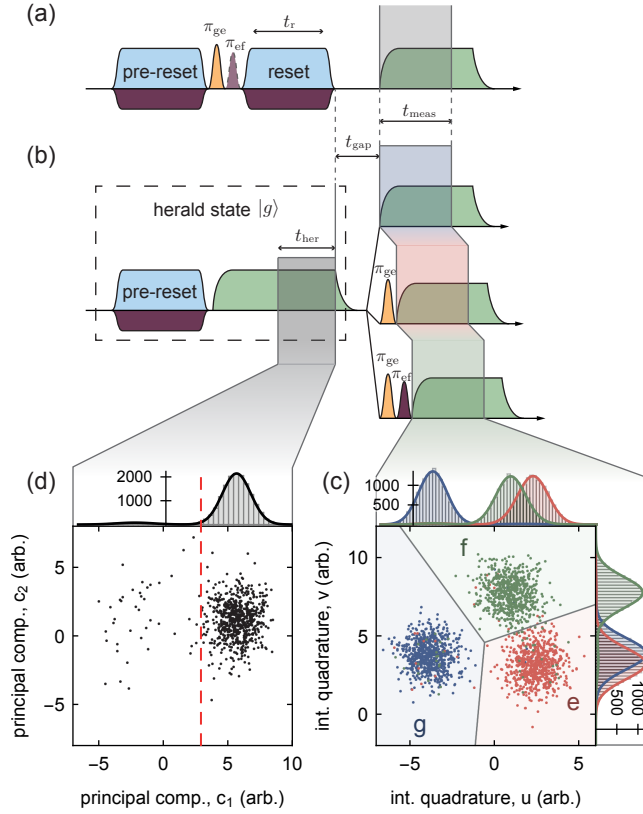


Figure 5.6 (a) Schematic of the pulse scheme used to test the unconditional reset protocol. (b) Schematic of the pulse scheme used to record reference single-shot counts. (c) Subset of 500 reference traces displayed in the u - v plane, when the qutrit is prepared in state $|g\rangle$ (blue dots), $|e\rangle$ (red dots) or $|f\rangle$ (green dots). The assignment regions labeled g , e and f are shaded in blue, red and green, respectively, and are separated by a gray line at their boundaries. (d) Sub-sample of 1000 traces acquired during the pre-selection pulse, projected in the principal component plane c_1 - c_2 . Here c_1 and c_2 are the two first principal components of the set of traces. The red dashed line indicates the threshold for selection/rejection of traces. The plots on the top or right axes of (c) and (d) show histogram counts of the traces. The solid lines in these plots correspond to the density of the marginal probability distributions of the traces, scaled to match the histograms.

	$ g\rangle$	$ e\rangle$	$ f\rangle$
g	98.2	2.5	2.4
e	0.9	95.7	4.6
f	0.9	1.8	93.0

Table 5.2 Reference assignment probability matrix of identifying prepared states (columns) as the measured states (rows). The diagonal elements show correct identification, the off-diagonal elements misidentifications.

estimated by counting the number of traces assigned the value m and follows

$$M_m = p(m|P) = \sum_s R_{m,s} \cdot P_s, \quad (5.7)$$

which can be expressed as $M = R \cdot P$. A simple approach to estimate the population P of the qutrit is to set $P = M$. This approach is, however, sensitive to assignment errors due to readout imperfections: $P = M$ holds true only if $R_{m,s} = \delta_{m,s}$. To account for readout errors, we invert Eq. (5.7) and set $P = R^{-1} \cdot M$. However, this procedure relies on the accurate characterization of R , which is sensitive to errors in state-preparation for the reference trace sets. The qutrit therefore needs to be initialized in $|g\rangle$ before applying the reference readout tone, with a residual excitation that can be bounded, and that is ideally smaller than that of the unconditional reset protocol presented in this manuscript. As mentioned earlier in this section, to do so, we pre-reset the transmon with our protocol, then herald the ground state of the transmon qubit with a pre-selection readout pulse [Fig. 5.6 (b)]. We record single-shot traces during the last 72 ns of the pre-selection pulse t_{her} . The pre-selection traces form two clusters, corresponding to ground and excited traces, that are maximally separated along their first principal component axis [Fig. 5.6 (d)]. We model the distribution of the first principal component c_1 of the traces with a bimodal Gaussian distribution and extract its parameters with maximum-likelihood estimation. Based on this model, we calculate a threshold value c_{thr} such that $p(c_1 > c_{\text{thr}}|\text{exc}) = 10^{-5}$. Selecting only traces with $c_1 > c_{\text{thr}}$ heralds the ground state of the transmon. On the set of selected traces, the residual excitation of the transmon qubit at the rising edge of the reference readout tone is therefore dominated by transmon thermalization, which occurs at rate $k_{\uparrow}/2\pi = 5$ kHz in our sample. We use the same waiting time t_{gap} between initialization and readout to characterize the unconditional reset dynamics [Fig. 5.6 (a)] and the reference trace set [Fig. 5.6 (b)]. As a result, thermalization occurring during this time can be seen as a source of readout error, which is compensated for. State preparation errors are then mostly explained by transmon thermalization occurring during the pre-selection, which we can bound by $k_{\uparrow}t_{\text{her}} \simeq 0.25\%$.

In conclusion, the corrected single-shot readout method we developed suffers from state preparation error resulting in a systematic under-estimation of the extracted populations, bounded by 0.25%. This residual error is small compared to the populations extracted during the unconditional reset for most measured points [Fig. 5.5 (c)]; this readout method is therefore suitable for the analysis presented here.

5.7 Discussion and outlook

High transmon anharmonicity α combined with large transmon-resonator coupling g allows for reaching larger Ω_{ef} and \tilde{g} without driving unwanted transitions [Zeytinoğlu15]. Driving the reset at higher Rabi rates, we can reach the optimal branch, where $\Gamma = \kappa/3$, for larger values of κ . As a result, increasing g , α and κ maximizes Γ and optimizes the reset. Coincidentally, as showed in chapter 3, increasing these parameters also optimizes speed and fidelity of qubit readout without degrading the coherence and thermalization of the qubit, if Purcell filters are used [Walter17]. Therefore, our reset protocol performs best if the reset resonator is designed for optimal readout. As an illustration, using the results of the present work, we calculate that implementing this reset protocol with the readout resonator of Ref. [Walter17] would reset the qutrit below $P_{\text{exc}} = 0.1\%$ in 83 ns, and to a steady-state value $P_{\text{exc}}^{\text{sat}} = 1.6 \times 10^{-4}$ in 200 ns, provided that the f0-g1 Rabi rate exceeds $\sqrt{2/27}\kappa \simeq 2\pi \times 10$ MHz.

We would also like to stress that parameters we chose to optimize the reset are not the cause for the relatively large rethermalization rate $k_{\uparrow}/2\pi \simeq 5$ kHz measured in our sample ($n_{\text{th}} = 17\%$ and $T_1 = 5.5 \mu\text{s}$). Indeed, plugging the parameters of table 5.1 in Eq. (2.54), we estimate the Purcell decay through both resonators to limit the relaxation times to $370 \mu\text{s}$. In addition, we observed thermal excitation levels as low as $n_{\text{th}} = 0.3\%$ in a sample with similar design and parameters in previous work [Walter17]. Therefore, with improved fabrication processes we expect to be able to decrease the rethermalization rate down to $k_{\uparrow}/2\pi \simeq 0.2$ kHz ($n_{\text{th}} < 5\%$ and $T_1 \sim 30 \mu\text{s}$). With such a rate, transmon rethermalization would not limit the reset any more and we expect to reach saturation levels as low as $P_{\text{exc}}^{\text{sat}} = 2 \times 10^{-4}$ with the current sample parameters.

Interestingly our scheme can be adapted for other purposes. For instance, F. Battistel *et al.* proposed to use the f0-g1 transition alone, to suppress leakage errors in data qubits used in a surface code computation [Battistel21]. In a second variation, H. Zhang *et al.* demonstrated the active initialization a low frequency fluxonium qubit ($\hbar\omega_q \ll k_B T$) by simultaneously driving a transmon transition and a cavity-assisted Raman sideband transition, which are the equivalent to the e-f and f0-g1 transitions in our work, to transfer the qubit excitation to a fast decaying photon in the readout resonator [Zhang21].

In a multi-qubit system, the protocol's need for high f0-g1 drive power increases the sensitivity to cross-talk and can cause spurious driving of two-qubit transitions. Addressing these concerns in scaled up circuits will require improved shielding of drive

lines, and careful selection of resonator and qubit frequencies, but we do not foresee fundamental obstacles beyond these. We later demonstrated our f_0 - g_1 reset scheme works equally well when simultaneously applied to two qubits [Krinner20]. We envision our scheme to scale up to larger systems similar to two-qubit gates activated with strong tones, such as the cross resonant gate [Sheldon16, Jurcevic20], or parametric gates [Hong20, Otterbach17]. We did not observe any degradation of qubit coherence and operation fidelity in the presence of the reset drive tones [Kurpiers18, Krinner20], but a systematic study of these effects constitutes valuable future work.

Chapter 6

Inter-Cryogenic Microwave Quantum Communication

*It's hard to think when someone Hadamards your
brain*

— Scott Aaronson

Superconducting circuits are an appealing platform to execute quantum information processing algorithms on noisy-intermediate-scale or error-correctable quantum hardware [Preskill18, Arute19, Kandala19, Ofek16, Andersen20b], and, also, to study fundamental quantum phenomena [vanLoo13, Hacothen-Gourgy16, Cottet17, Mineev19]. Today's state-of-the-art superconducting quantum processors contain a few dozen qubits on a single chip, held at cryogenic temperatures in individual dilution refrigerators. Efforts in qubit integration and packaging [Béjanin16, Das18, Foxen18, Lei20] will likely extend the scale of these processors to thousands of qubits in the foreseeable future. However, limitations such as available wafer size, refrigerated space and cooling power may arise beyond that scale [Krinner19]. Therefore, major innovations in both device integration and cryogenics are required to realize error-corrected quantum computers able to tackle interesting problems intractable on high-performance computing (HPC) systems, likely requiring millions of qubits [Reiher17, Babbush18a]. Networking quantum processors housed in different cryogenic nodes may provide a modular solution to scale up quantum computers beyond these limitations [Nickerson14, Brecht16]. The capabilities of quantum computers may be extended by forming clusters of networked processors housed in individual cryogenic modules, similar to the clusters of processing units used in HPC

systems.

One approach to realize such networks is to use microwave-to-optical quantum transducers [Fan18, Higginbotham18, Forsch19, Mirhosseini20, Hease20], with which superconducting circuits may be entangled with optical photons to communicate over long distances in a fashion similar to single atoms [Moehring07], trapped ions [Hofmann12], or defects in diamond [Bernien13]. However, despite the constant improvement of microwave-to-optical transducers, bringing their conversion efficiency, bandwidth, added noise, laser-induced quasiparticle poisoning and heat loads to practical levels on a single device remains a challenge.

A complementary approach is to connect dilution-refrigerator based cryogenic systems with cold, superconducting waveguides [Xiang17]. This approach could prove advantageous to distribute quantum computing tasks in local cryogenic quantum networks, as it would benefit from readily available, fast, deterministic, error-correctable and high-fidelity, chip-to-chip quantum communication schemes with microwave photons [Xiang17, Vermersch17, Kurpiers18, Campagne-Ibarcq18, Axline18, Zhong19, Leung19, Chang20, Burkhardt21, Zhong21]. In this chapter, which is based on [Magnard20], we report the realization of such a cryogenic quantum microwave channel between superconducting qubits located in two distinct dilution refrigerator units, based on the cryogenic link technology detailed in chapter 4. Using the photon shaping technique we demonstrated in [Kurpiers18] to transfer excitations deterministically [Cirac97], we transfer qubit states and generate entanglement on-demand between the distant qubits. We also report the violation of the CHSH inequality in this system, when performing a Bell test with pre-determined measurement bases.

6.1 Connecting superconducting circuits located in different cryogenic systems with a cold waveguide

Our experimental setup consists of two cryogen-free, dilution refrigerators, each of which houses a superconducting circuit with a single qubit cooled to below 20 mK temperature, and separated by 5 m (Figs. 6.1 and 6.2). The two identically designed circuits have a frequency-tunable transmon qubit, each with relaxation and coherence times $T_1 \simeq 12 \mu\text{s}$ and $T_2^e \simeq 6 \mu\text{s}$, coupled dispersively to two Purcell filtered resonators: one for readout, and one for excitation transfer, shown in green and yellow, respectively, in Fig. 6.1 (b). The $|g\rangle$ to $|e\rangle$ transition frequencies of transmon qubits labeled A and B are tuned to $\omega_{q,A}/2\pi = 6.457 \text{ GHz}$ and $\omega_{q,B}/2\pi = 6.074 \text{ GHz}$, respectively, by applying

6.1 Connecting superconducting circuits located in different cryogenic systems with a cold waveguide 145

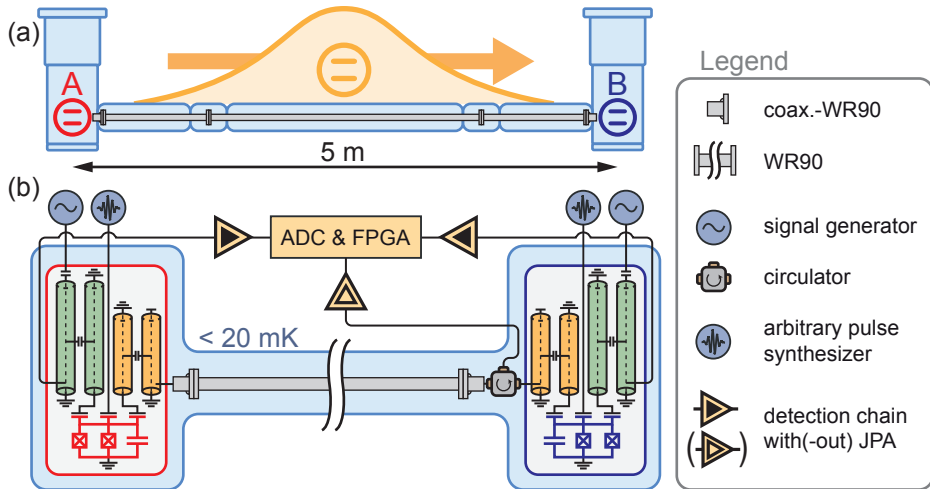


Figure 6.1 (a) Schematic representation, and (b), simplified circuit diagram of the experimental setup. Each transmon qubit, at node A (red) and B (blue), is connected to two Purcell filtered $\lambda/4$ resonators: one for readout (green) and one for excitation transfer by emission of a shaped photon (yellow). The light blue background illustrates the refrigerated space.



Figure 6.2 Photograph of the experimental setup during operation. The dilution refrigerator units, whose vacuum cans appear as white vertical cylinders, are connected to each other by the cryogenic link (long horizontal aluminum cylinder). The superconducting qubits and the cold waveguide are housed inside the dilution refrigerator units and the cryogenic link, respectively. The electronic instruments are stored in two black racks seen on the far sides of the picture.

a magnetic field to their SQUID loops. This adjusts the dispersive shift on each transfer resonator such that their frequencies $\omega_t/2\pi = 8.406$ GHz are matched [Kurpiers18].

We connect the transfer resonators to each other through a 4.9 m long, superconducting, rectangular aluminum WR90 waveguide, in series with two flexible, coaxial copper cables of 0.4 m length each and a circulator. As shown in Sec. 4.8.6, at millikelvin temperatures, the waveguide exhibits attenuation below 1 dB/km over the X band (8–12 GHz), which amounts to a total loss below 10^{-3} over 4.9 m of waveguide.

We cool the waveguide to temperatures below 20 mK by mounting it in a 5 m long version of the custom-made modular cryogenic link system described in chapter 4,

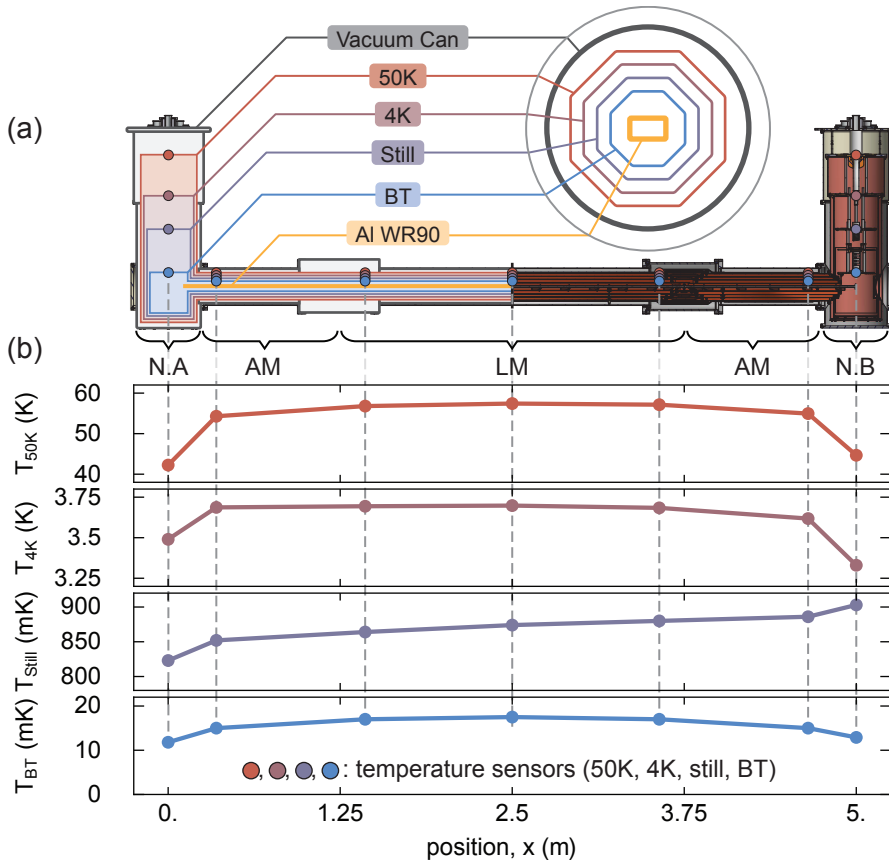


Figure 6.3 (a) Longitudinal cross-section of a schematic representation (left half) and a 3D model (right half) of the cryogenic system. The inset on the top right shows a transverse cross-section of the link. (b) Measured temperature in steady-state vs sensor position x on the axis along the link for all four temperature stages. Node A/B: N.A/B, adapter module: AM, link module: LM.

which consists of concentric, octagonal, radiation shields held at temperatures of approximately 50 K, 4 K, 850 mK (still), and 15 mK (base temperature), installed in an o-ring sealed vacuum can [Fig. 6.3 (a)]. The waveguide is thermalized to the base temperature shield every 0.25 m using flexible copper braids, and the radiation shields are cooled to their equilibrium temperatures using the dilution refrigerators at each end of the system. To compensate for thermal contraction during cool-down, we use flexible coaxial cables to connect the samples to the waveguide.

To monitor the temperature profile of the link, we installed temperature sensors at the positions indicated in Fig. 6.3 (a). Three days after commencing cool-down, the system reaches the steady-state temperature distribution shown in [Fig. 6.3 (b)], demonstrating excellent performance of the system. As expected, on each stage, the temperature is lowest at the nodes and the highest in the middle of the link, with an exception for the still stage where we heated node B to 900 mK to optimize cooling power by increasing the flow of ^3He .

6.2 Experimental cQED setup

We fabricated the two samples on $4.3\text{ mm} \times 7\text{ mm}$ silicon substrates (Fig. 6.4). We patterned the qubit pad and the coplanar waveguide (CPW) structures in a 150 nm

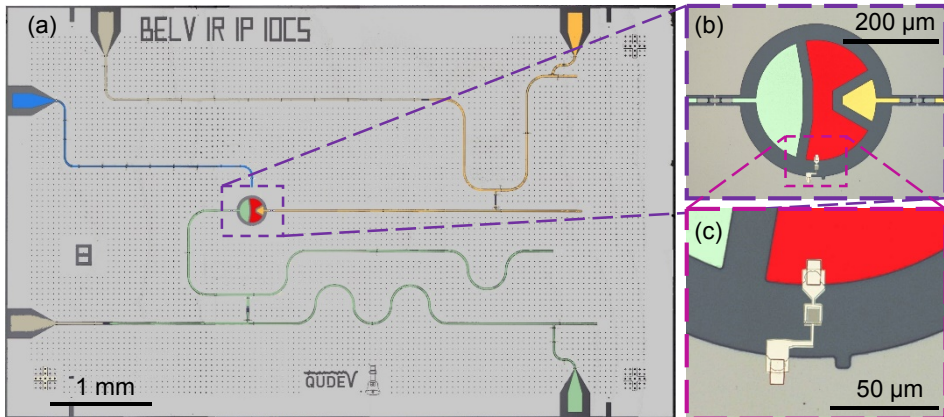


Figure 6.4 (a) False color photograph of a chip similar to those used in the experiment, before deposition of the Josephson junctions, showing the transmon island (red), the drive line (blue), the readout circuitry (green) and the transfer circuitry (yellow). (b) Microscope image of the transmon qubit, after deposition of the Josephson junctions. (c) Enlarged view of the Josephson junctions, see scale bars.

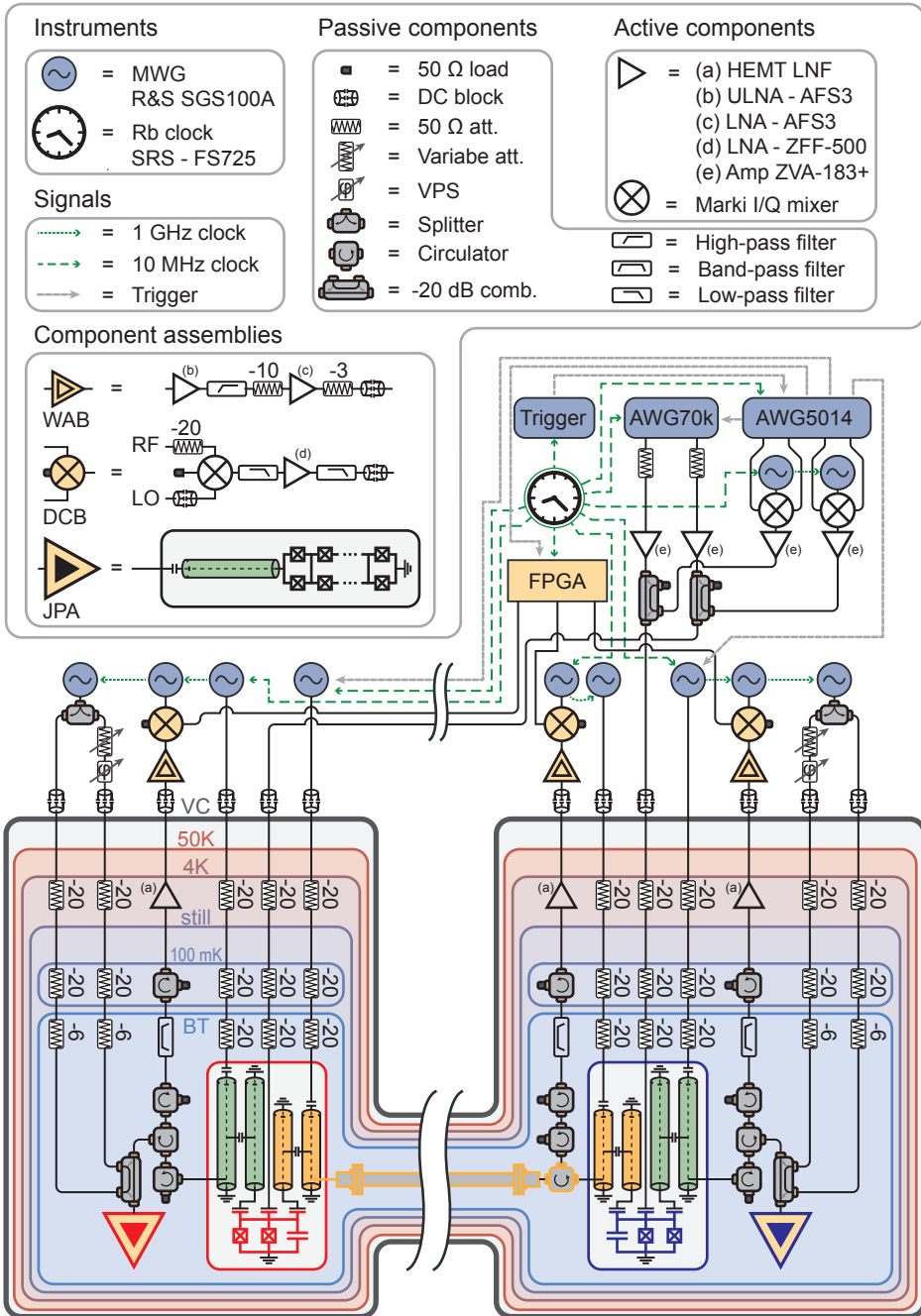


Figure 6.5 Schematic diagram of the experimental setup. WAB: warm amplifier board; DCB: down-conversion board; JPA: Josephson parametric amplifier; MWG: microwave generator; VPS: variable phase shifter.

thick niobium film sputtered on the substrate with reactive ion etching in a photolithographic process. In a second photolithographic step, we deposited Al/Ti/Al airbridges to connect the ground plane at selected places across the CPWs. We fabricated the Al/AlOx/Al Josephson junctions in a third step with electron-beam lithography and double-angle shadow evaporation. Each sample was then mounted, glued and wire-bonded to a copper PCB, which was packaged in a copper sample holder. We mounted each sample holder to the base plate of the corresponding dilution refrigerator and wired the devices to the instruments as documented in the wiring diagram Fig. 6.5. Note that the cryogenic system is connected only via one transmission line to the ground of the instrument setup. All other lines have inner/outer DC-blocks to avoid ground loops, which could introduce detrimental noise to the setup.

For each chip, we characterized the parameters of the readout and transfer resonator and Purcell filter circuitry, including resonant frequencies, coupling rates and dispersive shifts, from the transmission spectra through their respective Purcell filtering resonator with the transmon initialized in state $|g\rangle$ or $|e\rangle$, using methods and models similar to those described in Ref. [Walter17]. Using Ramsey-type experiments, we extracted the transition frequencies and coherence times of the three-level transmon qubits. Both chips have similar parameters (table 6.1). However, because we tuned qubit A and B to different operating frequencies, qubit frequency dependent parameters such as the qubit/resonator dispersive shifts and the $|f0\rangle \leftrightarrow |g1\rangle$ transition frequencies are different at node A and B. The transfer Purcell filter bandwidth differs significantly between the samples, which we suspect to be due to the sensitivity of this parameter to the output impedance.

Using the procedure described in Ref. [Geerlings13], we measured a transmon thermal population at equilibrium of approximately 16% for each qubit. We suspect that the absence of infra-red filters in the cables connecting to the samples, and of radiation tight base temperature shields at the node cryostats, leading to poor infra-red shielding, causes this high effective transmon temperature [Serniak18].

To perform single-qubit gates, we apply microwave pulses created by arbitrary waveform generators to each qubit through dedicated drive lines. We use DRAG pulses [Motzoi09], with 28 and 24 ns duration, resonant with the $g-e$ and $e-f$ transitions, respectively, to drive transitions between the three lowest energy states of the transmon qubits.

To emit photons and reset the qubits, we apply microwave drives to the transmon qubit at the f_0-g_1 frequency, following the methods described in Sec. 2.1.7 and chapter 5, to convert transmon excitations into a single photon in the transfer resonator,

quantity,	symbol	Node A	Node B	unit
qubit transition frequency	$\omega_q/2\pi$	6.457	6.074	GHz
transmon anharmonicity	$\alpha/2\pi$	-262	-262	MHz
energy relaxation time on ge	T_{1ge}	12.2	11.7	μs
energy relaxation time on ef	T_{1ef}	4.9	5.0	μs
coherence time on ge	T_{2ge}^e	7.6	5.0	μs
coherence time on ef	T_{2ef}^e	7.1	5.0	μs
thermal excitation at equilibrium	n_{th}	16.2	16.8	%
$ f, 0\rangle \leftrightarrow g, 1\rangle$ transition frequency	ν_{f0g1}	4.022	3.485	GHz
readout resonator frequency	$\omega_r/2\pi$	4.698	4.701	GHz
readout Purcell filter frequency	$\omega_{pr}/2\pi$	4.704	4.723	GHz
readout resonator/qubit coupling	$g_r/2\pi$	202	214	MHz
readout circuit dispersive shift	$\chi_r/2\pi$	-4.1	-7.9	MHz
readout resonator/filter coupling	$J_r/2\pi$	19.9	20.0	MHz
readout Purcell filter bandwidth	$\kappa_{pr}/2\pi$	71	67	MHz
readout resonator eff. bandwidth	$\kappa_r/2\pi$	21.7	16.8	MHz
transfer resonator frequency	$\omega_t/2\pi$	8.406	8.406	GHz
transfer Purcell filter frequency	$\omega_{pt}/2\pi$	8.444	8.470	GHz
transfer resonator/qubit coupling	$g_t/2\pi$	307	306	MHz
transfer circuit dispersive shift	$\chi_t/2\pi$	-5.75	-4.0	MHz
transfer resonator/filter coupling	$J_t/2\pi$	20	20.8	MHz
transfer Purcell filter bandwidth	$\kappa_{pt}/2\pi$	110	155	MHz
transfer resonator eff. bandwidth	$\kappa/2\pi$	8.6	6.25	MHz

Table 6.1 Device parameters for chips A and B.

which couple to the bus waveguide. We apply a microwave tone at frequency 4.249 GHz (3.482 GHz) with amplitude A to transmon A (B) to induce the effective drive rate \tilde{g} between states $|f0\rangle$ and $|g1\rangle$. The $|f0\rangle \leftrightarrow |g1\rangle$ drives are directly synthesized by a separate AWG, then are amplified and combined with the DRAG pulse AWG channel to the drive line of the transmon (Fig. 6.5).

Using the procedure described in chapter 5, we extract the drive rate \tilde{g} and the ac-stark shift Δ_{f0g1} vs drive amplitude A , and fit each of them with a polynomial function to get a continuous relation between \tilde{g} , Δ_{f0g1} and A (Fig. 5.3). This calibration procedure assumes that the transfer resonator decays into a Markovian environment. To realize this condition, we mount a circulator at the far end of the waveguide.

To perform our protocol with high fidelity despite a significant initial thermal population, we reset both transmon qubits at the beginning of each experiment cycle using the method presented in chapter 5. We simultaneously drive the e - f and $|f0\rangle \leftrightarrow |g1\rangle$ transitions with two resonant, flat-top pulses to couple the states $|e0\rangle$ and $|f0\rangle$ to state $|g1\rangle$, which decays to $|g0\rangle$ at a high rate κ into a cold, $50\ \Omega$ environment (the photon detection line in this case).

To measure transmon A (B), we apply a 4.692 GHz (4.680 GHz), gated microwave tone to the input port of the readout Purcell filter. Due to the qubit state dependent dispersive shift $\chi_r/2\pi = -4.1$ MHz (-7.9 MHz) of the readout resonator, the complex amplitude of the transmitted signal carries information about the transmon state, which results in a quantum non-demolition measurement of the transmon, see chapter 3 and [Walter17].

For qutrit state detection, we amplify the signal using a near quantum-limited reflective Josephson parametric amplifier (JPA) with 23.6 dB gain (21.3 dB) and 14 MHz bandwidth (47 MHz), pumped at 4.689 GHz (4.668 GHz). We cancel the JPA pump interferometrically at base temperature to avoid pump-induced qubit dephasing and saturation of subsequent amplifiers. We further amplify the signal at the 4K plate with high-electron-mobility transistors (HEMT), then at room temperature with (ultra-)low-noise amplifiers. The signal is then down-converted to 250 MHz, digitized at 1 Gs/s, and digitally down-converted to complex DC values by an FPGA using custom firmware (Fig. 6.5).

Over an acquisition window of duration $\tau = 248$ ns, the FPGA integrates the signal with two sets of weights to reduce the signal to two real-valued components u and v . The integration weights are chosen to maximize contrast in the $\{u, v\}$ plane between measurement traces obtained with the qubit initialized in either one of the states $|g\rangle$, $|e\rangle$ or $|f\rangle$. Similar to what we described in Sec. 5.6, the integrated traces follow a

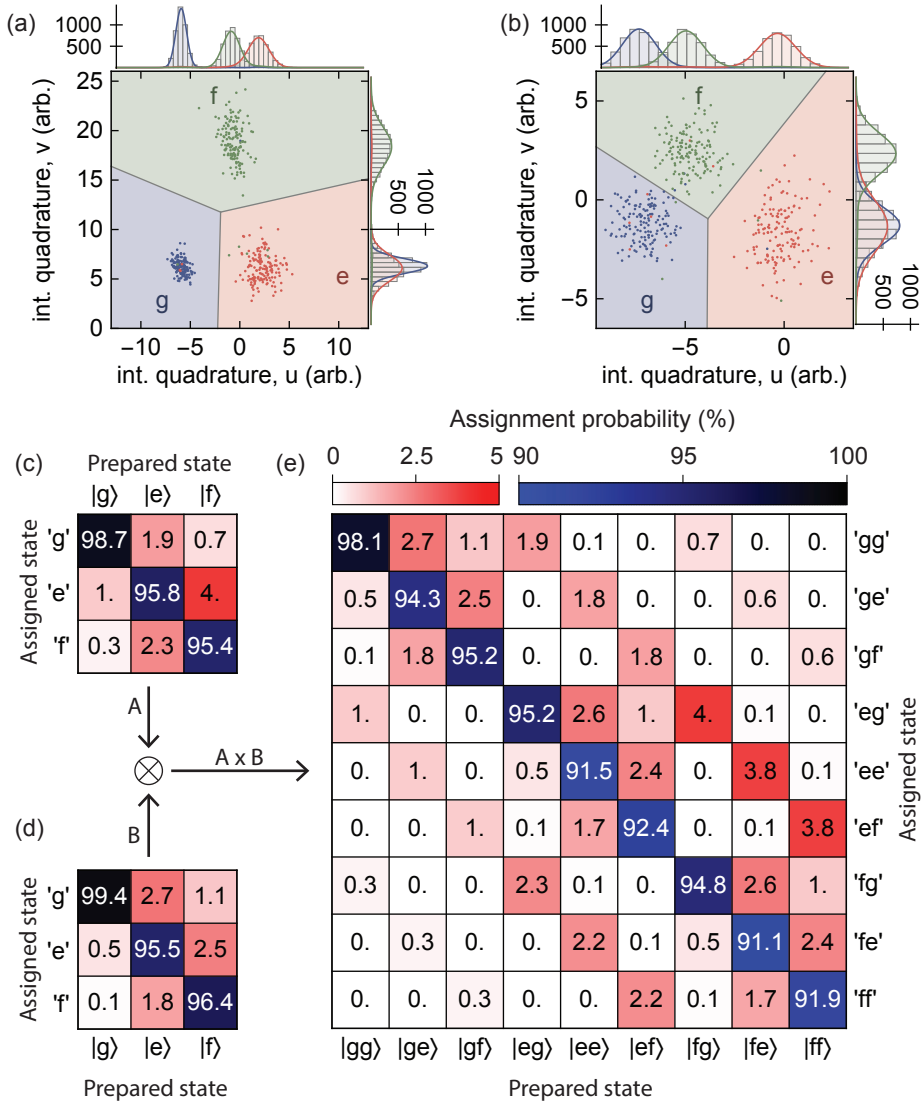


Figure 6.6 (a) and (b) Scatter plot of the readout traces, integrated for 248 ns with optimal weights, with the qubit prepared in state $|g\rangle$ (blue dots), $|e\rangle$ (red dots) and $|f\rangle$ (green dots), for transmon A and B, respectively. The marginal histogram along the integration quadrature u and v is shown for each preparation state on the top and right axes, respectively. Solid-lines are density functions of the marginal three-modal, gaussian distribution estimated from the integrated traces, and scaled to fit the histograms. The $|g\rangle$, $|e\rangle$ and $|f\rangle$ assignment regions are shaded in blue, red and green, respectively. (c) [resp. (d)] Three-state assignment probability matrix R_A (resp. R_B) extracted from the readout traces and the assignment region displayed in (a) [resp. (b)], for qubit A (resp. B). (e) Two-qutrit assignment matrix R_{AB} calculated as the outer product of the single-qutrit assignment matrices.

tri-modal gaussian distribution, the parameters of which we estimate with a maximum likelihood approach. Each gaussian mode corresponds to the probability distribution of a measurement trace in the $\{u, v\}$ plane conditioned on the qubit being in a given state during the measurement. The FPGA then assigns the measurement trace to that state with mode center closest in the $\{u, v\}$ plane [see assignment regions in Fig. 6.6 (a,b)].

We calibrate the integration weights and mode centers used in the FPGA-based state assignment process, and determine the readout assignment probability matrix R of each transmon qubit [Fig. 6.6 (a,b)] following the procedure detailed in Sec. 5.6. We determine an average readout error probability of 3.4% (2.9%) from R_A (R_B), and of 6.2% from the joint system assignment probability matrix $R_A \otimes R_B$ [Fig. 6.6 (e)].

6.3 Emission and absorption of shaped photons

To characterize the excitation transfer through the link, we first reset the transmon qubits and apply two consecutive π -pulses to prepare the qubit/resonator system at node A in the state $|f0\rangle$ [Fig. 6.7 (a)], where $|q\rangle$ and $|n\rangle$ in $|qn\rangle$ denote the transmon state and the transfer resonator Fock state, respectively. We then drive qubit A on the $|f0\rangle \leftrightarrow |g1\rangle$ sideband transition to populate the transfer resonator with one photon. This photon couples into the waveguide at rate $\kappa_A/2\pi = 8.9$ MHz and propagates to node B in 28 ns, as estimated from the waveguide length and the relevant group velocities. We shape the $|f0\rangle \leftrightarrow |g1\rangle$ pulse appropriately to emit the photon with a time-symmetric envelope $\phi(t) \propto \text{sech}(\Gamma t/2)$, where the photon bandwidth Γ can be adjusted up to a maximum value of $\min[\kappa_A, \kappa_B]$ (see appendix B.2). Here we choose $\Gamma/2\pi = \kappa_B/2\pi \simeq 6.2$ MHz to minimize the duration of the protocol. To absorb the photon at node B, we then drive qubit B with an $|f0\rangle \leftrightarrow |g1\rangle$ pulse whose time-reverse would emit a photon indistinguishable from the incoming one (see Sec. 2.1.8 and [Cirac97]). Finally, we apply an e - f π -pulse on qubit B to map the excitation back to the g - e manifold, and then perform single-shot read out on both qutrits. For these parameters, the excitation transfer sequence, consisting of the $|f0\rangle \leftrightarrow |g1\rangle$ pulses and the final e - f π -pulse, completes in 311 ns.

Here and in following experiments, we present data which is corrected for readout errors by multiplying the vector of single-shot assignment frequency associated with each sequence with the inverse of the assignment matrix R_{AB} . Because phase drifts of readout instruments lead to an increase in readout assignment error probability, each experiment contains measurements of reference states to estimate R_{AB} at the time of the experiment. We observe an increase of average readout errors to $\sim 5\%$ and $\sim 10\%$

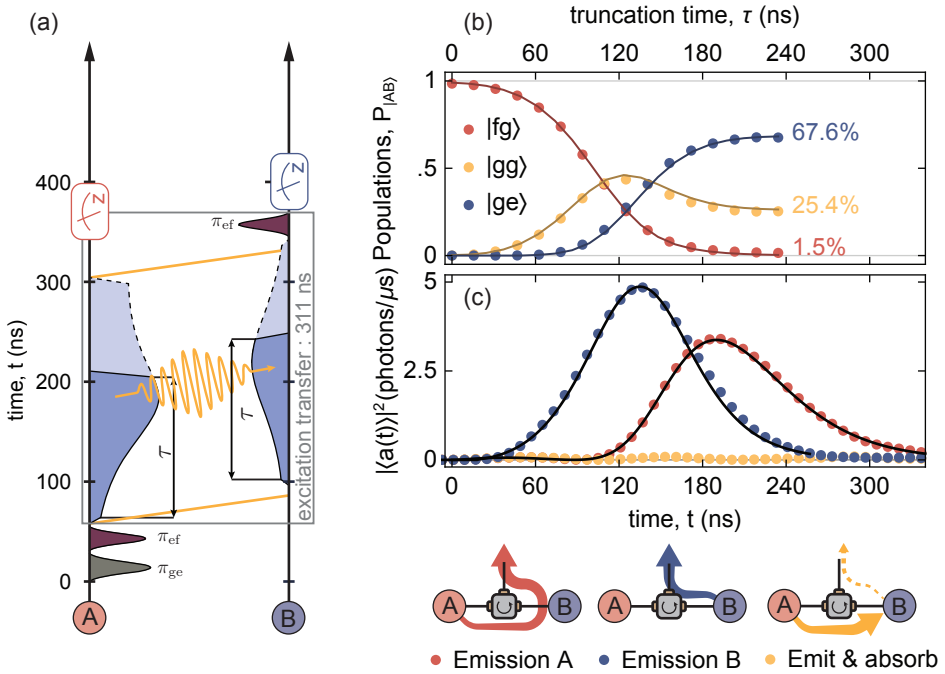


Figure 6.7 (a) Pulse scheme used to characterize the excitation transfer dynamics. The $|f0\rangle \rightarrow |g1\rangle$ drives and the g - e and e - f π pulses are represented in blue, grey and bordeaux, respectively. We use solid and dashed lines for the time-truncated ($\tau = 140$ ns) and the full excitation transfer sequence, respectively. The straight yellow lines illustrate the propagation path of the rising and falling edges of the photon in space-time. The subsequence defining the excitation transfer is enclosed in a grey box. (b) Population P in selected two-transmon states $|AB\rangle$ vs $|f0\rangle \leftrightarrow |g1\rangle$ pulse truncation time τ . Solid lines are results of master equation simulations. (c) Average electric field amplitude squared $\langle |a_{out}(t)|^2 \rangle$ vs time of photons emitted from node B (blue), or emitted from node A and reflected from node B in presence (yellow) or absence (red) of an absorption pulse. The y-axis is normalized to obtain a unit integrated power for photons emitted from B. The solid lines are results of master equation simulations, with an offset in time to obtain the best agreement with the measurement.

for single and two qutrit readout, respectively.

Truncating the $|f0\rangle \leftrightarrow |g1\rangle$ pulses prematurely at time τ , we characterize the time dependence of the state population of the two transmon qubits throughout the transfer pulse [Fig. 6.7 (a,b)]. As the excitation transfers from node A to node B via the photonic modes (the waveguide and both transfer resonators), the population swaps from the state $|fg\rangle$ of the two spatially separated qubits $|AB\rangle$ to $|ge\rangle$ via the intermediate state $|gg\rangle$. The final two-transmon state populations highlight the different sources of errors in the excitation transfer. The $\sim 3\%$ residual population measured in both $|gf\rangle$ and $|ge\rangle$ (not shown) is due to e - f decay. In case of photon loss or failed absorption during the transfer process, the system ends up in the state $|gg\rangle$, which happens with 25.4% probability. Finally, the transfer efficiency is characterized by the 67.5% final population in $|ge\rangle$. Simulations of the transfer dynamics, using the master equation model detailed in [Kurpiers18] and appendix E.2, and independently measured parameters, are in good agreement with the data [solid lines in Fig. 6.7 (b)].

To assess the quality of the photon emission and absorption processes, we measure the mean photon field in the photon detection chain after emitting a photon from A, emitting a photon from B, or emitting a photon from A which we absorb at B, as illustrated by the pictograms in Fig. 6.7 (c). In each case, we prepare the emitter qubit in $(|g\rangle + |f\rangle)/\sqrt{2}$ and apply an $|f0\rangle \leftrightarrow |g1\rangle$ pulse to emit symmetric-shape photons of state $(|0\rangle + |1\rangle)/\sqrt{2}$, with a non-zero average electric field $\langle a_{\text{out}} \rangle(t)$ proportional to the photon envelope $\phi(t)$.

We observe that photons emitted from B have the expected shape and bandwidth, as shown by the close match between the data points and results from master equation simulations using only an offset in time as a fit parameter [solid line in Fig. 6.7 (c)]. Photons emitted from A have a shape corresponding to the convolution of a hyperbolic secant shaped envelope with the time-response function of a reflection from resonator B. This has the effect of distorting the photon shape and delaying its peak power by approximately 60 ns. Here again, simulations agree well with the data. Photons emitted from A have a 22.3% lower integrated power $\int |\langle a_{\text{out}}(t) \rangle|^2 dt$ compared to those emitted from B, which corresponds to the probability $1 - \eta_{AB}$ of losing a photon as it travels from A to B. We use this measured value of η_{AB} as a fixed parameter in master equation simulations of the experiment. From the integrated power ratio of the photon field emitted from node A and reflected from node B in presence (yellow), or absence (red) of an absorption pulse at node B, we measure that 95.8% of the incoming photon is absorbed by node B. The combination of photon loss and absorption inefficiency

leads to a 25.6% probability of qubit B not absorbing a photon¹, in good agreement with the 25.4% probability of finding the two-qubit system in state $|gg\rangle$ at the end of the transfer protocol [Fig. 6.7 (b)].

The time between the applications of the emission and absorption pulses is set to experimentally maximize the transfer efficiency. The offsets in time fitted to the photon emitted from A and B differ by 10 ns. From this we infer that the emission pulse is applied $\Delta\tau_{AB} + 10$ ns before the absorption pulse, where $\Delta\tau_{AB} \simeq 28$ ns is the time it takes the photon to travel from node A to B, according to the length and group velocities of each section of the transfer line. Simulations of excitation transfer with different delays between the emission and absorption pulse also predict that this optimal delay is 10 ns, in excellent agreement with the data.

6.4 Qubit State Transfer from one cryostat to another

To probe the quantum nature of the excitation transfer, we characterize the qubit state transfer protocol with quantum process tomography. To do so, we reset the qubits to their ground states, prepare A in one of the six mutually-unbiased qubit states $|g\rangle$, $|e\rangle$, $(|g\rangle + |e\rangle)/\sqrt{2}$, $(|g\rangle + i|e\rangle)/\sqrt{2}$, $(|g\rangle - |e\rangle)/\sqrt{2}$ or $(|g\rangle - i|e\rangle)/\sqrt{2}$ [vanEnk07], apply an e - f π -pulse on qubit A, then apply an excitation transfer pulse sequence [Fig. 6.7 (a)]. For each input state $\rho_{i,s}$, we measure the three-level population of qubit B with single-shot readout after applying a tomography gate G selected from the rotation set: $\mathcal{S} = \{\mathbb{1}, {}^{ge}R_x^{\pi/2}, {}^{ge}R_y^{\pi/2}, {}^{ge}R_x^{\pi}, {}^{ef}R_x^{\pi/2}, {}^{ef}R_y^{\pi/2}, ({}^{ef}R_x^{\pi/2} \cdot {}^{ge}R_x^{\pi}), ({}^{ef}R_y^{\pi/2} \cdot {}^{ge}R_x^{\pi}), ({}^{ef}R_x^{\pi} \cdot {}^{ge}R_x^{\pi})\}$, where t denotes the qutrit transition, θ the rotation angle, and n the rotation axis. We reconstruct the three-level density matrix out the final state $\rho_{f,s}$ of transmon B [Fig. 6.8 (b)] from this set of measured populations with a maximum likelihood method, assuming ideal tomography gates. From this we determine an average state fidelity $\mathcal{F}_s = \frac{1}{6} \sum_s \mathcal{F}(\rho_{i,s}, \rho_{f,s}) = 82.4 \pm 0.06\%$. When correcting for readout errors, the average state fidelity reaches $85.8 \pm 0.06\%$. Here and in all following tomography reconstruction, the error bars are obtained from a bootstrapping method. We perform simple random sampling from the set of qutrit single-shot assignments to generate 20 sets the same size as the original one. The standard deviation of the fidelity (or any other metric) calculated from each set defines the estimation error.

To rigorously characterize the state transfer process, we define the transfer process matrix χ as the representation of a completely positive trace-preserving map Λ which

¹ $1 - 0.958 \times (1 - 0.223) \simeq 1 - 0.744 = 0.256$.

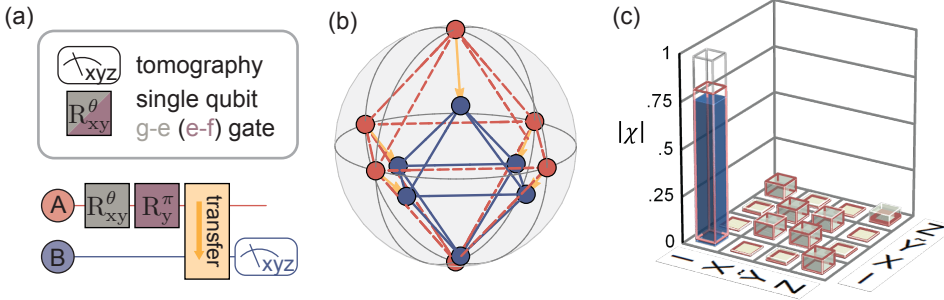


Figure 6.8 (a) Quantum circuit used to perform and characterize the qubit state transfer. (b) Bloch sphere representation of the state transfer. Each input states on qubit A (red) is linked via a gold arrow to its corresponding output states reconstructed on qubit B (blue). (c) Absolute value of the qubit state transfer matrix $|\chi|$, in the Pauli basis $\{\mathbb{1}, X = \hat{\sigma}_x, \tilde{Y} = i\hat{\sigma}_y, Z = \hat{\sigma}_z\}$, where solid blue bars, red wireframes and gray wireframes are the measured, simulated and target quantities, respectively.

maps the input state ρ_{in} of qubit A to the output state ρ_{out} of qubit B through the relation $\rho_{\text{out}} = \Lambda(\rho_{\text{in}}) = \sum_{i,j} \chi_{ij} P_i \rho_{\text{in}} P_j$, in which the operators P_i are in the set of modified Pauli matrices $\{\mathbb{1}, X = \hat{\sigma}_x, \tilde{Y} = i\hat{\sigma}_y, Z = \hat{\sigma}_z\}$ [Chuang97]. Considering only the components of the output density matrices spanned by states $|g\rangle$ and $|e\rangle$, we reconstruct the likelihood-maximizing, two-level process matrix χ shown in Fig. 6.8 (c), from which we determine a process fidelity $\mathcal{F}_p = \text{Tr}(\chi_{\text{ideal}}\chi) = 79.5 \pm 0.1\%$ ($75.3 \pm 0.1\%$) relative to the ideal qubit state transfer process, with (without) correction for readout errors. Simulations of the process are in good agreement with the measurement results, as quantified by the small trace distance $\sqrt{\text{Tr}(|\chi - \chi_{\text{sim}}|^2)} = 0.09$ between the reconstructed and simulated transfer process matrices [red wireframes in Fig. 6.8 (c)].

On average, the input states have equal population in $|g\rangle$ and $|e\rangle$, which are transferred in vacuum states, insensitive to loss, with close-to-unit fidelity, and single-photon Fock states, suffering from loss, with a fidelity of 67.5% corresponding to the transfer efficiency. Therefore the state transfer fidelities \mathcal{F}_s and \mathcal{F}_p can be larger than the photon transfer efficiency, if the phase coherence of the process is sufficiently large.

6.5 Bell state generation

To generate entanglement across the link, we prepare qubit A in $(|e\rangle + |f\rangle)/\sqrt{2}$, qubit B in $|g\rangle$, and apply the excitation transfer pulses [Fig. 6.9 (a)]. Using quantum state tomography, we reconstruct the two-qutrit density matrix $\rho_{3\otimes 3}$ of qubits A

parameter	reconstructed state, ρ	simulated state, ρ_{sim}
ν	$.9684 \pm 0.0005$.984
\mathcal{V}	$.929 \pm 0.003$.948
η_A	$.7035 \pm 0.0005$.696
η_B	1.0126 ± 0.0004	.999
trace distance	0.01	10^{-10}

Table 6.2 Results of a fit of the parametrized density matrix ρ_{AB} to the reconstructed and simulated density matrices. The last column displays the trace distance $\sqrt{\text{Tr}(|\rho - \rho_{AB}|^2)}$.

and B [Fig. 6.9 (b-d)] from single-shot measurements of their population performed after applying a pair of local gates $G_A \otimes G_B$ from the 81-gate set $\mathcal{S} \otimes \mathcal{S}$. To quantify the entanglement with standard metrics, we consider the density matrix ρ , consisting of the two-qubit elements of $\rho_{3 \otimes 3}$ [Fig. 6.9 (e-g)]. This reduction method leads to states with non-unit trace, but it preserves the state fidelity, and gives a conservative estimate to the concurrence and the expected CHSH value compared to a projection of $\rho_{3 \otimes 3}$ on the set of physical two-qubit density matrices. We determine the fidelity $\langle \psi^+ | \rho | \psi^+ \rangle = 79.5 \pm 0.1\%$ ($71.9 \pm 0.1\%$) with respect to the ideal Bell state $|\psi^+\rangle = (|ge\rangle + |eg\rangle)/\sqrt{2}$, and evaluate a concurrence of $\mathcal{C}(\rho) = 0.746 \pm 0.003$ (0.588 ± 0.002), with (without) correction for readout errors. Simulations of the entanglement generation sequences are in good agreement with the measurement results, as quantified by the small trace distances $\sqrt{\text{Tr}(|\rho - \rho_{\text{sim}}|^2)} = 0.023$ between the reconstructed and simulated entangled state.

To understand the different error channels in the entanglement generation process, we fit the reconstructed and simulated states with the state parametrization (2.59)

$$\rho_{AB} = \frac{\nu}{2} \begin{pmatrix} 2 - (\eta_A + \eta_B) & 0 & 0 & 0 \\ 0 & \eta_A & \mathcal{V}\sqrt{\eta_A\eta_B} & 0 \\ 0 & \mathcal{V}\sqrt{\eta_A\eta_B} & \eta_B & 0 \\ 0 & 0 & 0 & 0 \end{pmatrix},$$

given in Sec. 2.1.8, where η_A differs from unity because of photon loss and emission and absorption imperfections, η_B results from decay of qubit B after the final e-f pulse, $\mathcal{V} < 1$ results from dephasing, and $\nu < 1$ is the fraction of the population in the two-qubit subspace. The fitted density matrix, whose parameters are shown in table 6.2, reproduces the data very closely (see trace distances in table 6.2) and suggest that the main error mechanism stem from photon loss and Bell state dephasing. Notably, the simulations lead to a leakage error $1 - \nu$ and a dephasing error $1 - \mathcal{V}$ twice and

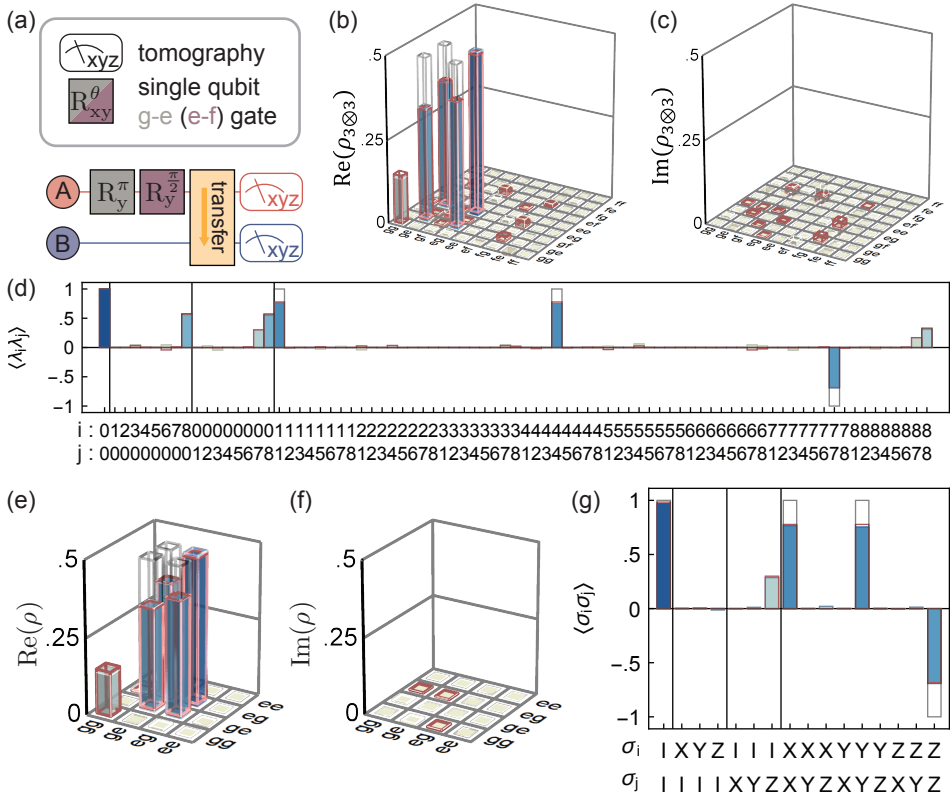


Figure 6.9 (a) Quantum circuit used to deterministically generate and characterize the Bell state $|\psi^+\rangle$. (b) Real part, (c) imaginary part, and (d) expectation value $\langle \lambda_i \lambda_j \rangle$ of the two-qutrit Gell-Mann operators of the density matrix $\rho_{3\otimes 3}$ of reconstructed Bell states. (e) Real part, (f) imaginary part, and (g) expectation value $\langle \sigma_i \sigma_j \rangle$ of the two-qubit Pauli operators of the density matrix ρ of reconstructed Bell states. In panels (b) to (g), solid blue bars, red wireframes and gray wireframes are the measured, simulated and target quantities, respectively.

30% smaller than observed, respectively. The former discrepancy could arise from drifts in the calibration of the emission pulse, and the latter one from low frequency relative phase noise between the different instrument channels used to manipulate the two-qubit state. We also note that the concurrence of the fitted matrix $\mathcal{C}(\rho_{AB}) = \nu\sqrt{\eta_A\eta_B} = 75.9 \pm 0.2\%$ is slightly higher than that calculated directly from ρ .

6.6 Bell test

Considering the g-e single-shot readout fidelities $\mathcal{F}_{r,A} = 96.8\%$, and $\mathcal{F}_{r,B} = 96.7\%$, obtained by attributing 'f' assignments to 'e' from the assignment probability matrices shown in Fig. 6.6, we expect from Eq. (2.87) to be able to obtain a maximum CHSH value $\mathcal{F}_{r,B}\mathcal{F}_{r,A}\mathcal{C}(\rho_{AB})2\sqrt{2} \simeq 2.01$, just above the threshold to violate Bell's inequality.

To test Bell's inequality, we generate the entangled state shown in Fig. 6.9. We reset both qubits, prepare qubit A in the superposition state $(|e\rangle + |f\rangle)/\sqrt{2}$ and apply the transfer pulse sequence [Fig. 6.10 (a)]. According to Eq. (2.84), the CHSH value should be maximized when measuring the two qubits along axes belonging to the x-y equatorial plane. We set the two measurement axes on qubit A to be $A_0 = \vec{x} := (1, 0, 0)$ and $A_1 = \vec{y} := (0, 1, 0)$ in the Bloch sphere, and the two measurement axes of qubit B to be $B_0 = \cos(\varphi_B)\vec{x} + \sin(\varphi_B)\vec{y}$ and $B_1 = -\sin(\varphi_B)\vec{x} + \cos(\varphi_B)\vec{y}$ [Fig. 6.10 (b)]. For each measurement setting, defined by a choice of the relative angle φ_B , and of the inputs $x, y \in \{0, 1\}$, we collect $2^{16} = 65536$ single-shot measurements for each qubit, which we assign to output $a, b = -1$ if the qubit is measured as a ground state, and to output $a, b = +1$ if the qubit is measured in state $|e\rangle$ or $|f\rangle$. This way, every measurement run ends in a binary output, thereby closing the detection loophole (see Sec. 2.2.2 and [Larsson14]). Note, however, that the measurement settings are predetermined, leaving the freedom-of-choice and locality loopholes open.

From these single-shot statistics, we estimate the correlation terms $\langle ab \rangle_{xy} := \langle A_x B_y \rangle$ and observe their sinusoidal dependence on φ_B , as predicted by quantum mechanics and the master equation simulation of the process [Fig. 6.10 (c)]. The amplitude of these oscillations is less than unity due to the imperfections in the prepared state and the qubit state readout. The CHSH value

$$S_{\text{CHSH}} := \langle ab \rangle_{10} + \langle ab \rangle_{01} + \langle ab \rangle_{10} - \langle ab \rangle_{11},$$

is a sinusoidal function of φ_B , with extrema at $\varphi_B = 3\pi/8 \pmod{\pi}$ [Fig. 6.10 (d)]. In particular, for $\varphi_B = 3\pi/8$, we obtain the counts shown in table 6.3, from which

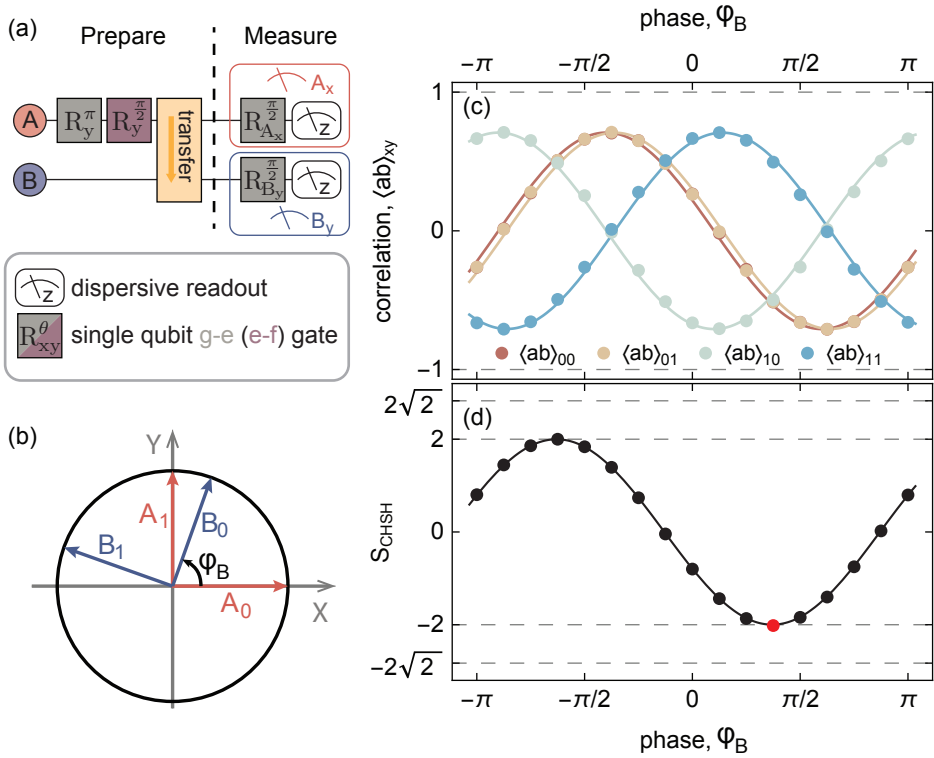


Figure 6.10 (a) Quantum circuit used to perform a Bell test with a deterministic measurement basis choice. (b) Illustration, in the equatorial plane of the Bloch sphere, of the effective measurement axes chosen to perform the Bell test. The measurement axes $A_{0/1}$ ($B_{0/1}$) of qubit A (B) are shown in red (blue). (c) Correlations $\langle ab \rangle_{xy}$ obtained when measuring qubit A and B along axes A_x and B_y , respectively, vs the relative phase φ_B between axes A_0 and B_0 [see panel (b)]. (d) CHSH value $\langle ab \rangle_{00} + \langle ab \rangle_{01} + \langle ab \rangle_{10} - \langle ab \rangle_{11}$ vs φ_B . The red dot shows the setting which violates Bell inequality (see main text).

a, b \ x, y	0, 0	0, 1	1, 0	1, 1
-1, -1	7811	7778	8238	24179
-1, +1	24400	24569	24136	8055
+1, -1	25209	24970	24919	8483
+1, +1	8115	8219	8243	24819
$\langle ab \rangle_{xy}$	-0.514	-0.512	-0.497	-0.495
$\Delta \langle ab \rangle_{xy}$	0.0034	0.0034	0.0034	0.0034

Table 6.3 Number of runs which were assigned to the output pair a, b for input pair x, y , for $\varphi_B = 3\pi/8$. The last two rows show the values of the estimator of the correlations and their uncertainty.

we calculate $S_{\text{CHSH}} = -2.0181 \pm 0.067$, corresponding to a violation of the CHSH Bell inequality by more than 2.6 standard deviations [red dot in Fig. 6.10 (d)]. The confidence with which we can reject local hidden variable (LHV) models is quantified by the P -value of 0.01 associated with the null hypothesis of LHV models, in which we account for all possible memory effects [Elkouss16].

6.7 Random basis choice

We plan to select the measurement basis randomly and rapidly using the scheme illustrated in Fig. 6.11 (a). In this scheme, we generate a $\pi/2$ pulse to rotate the qubit just before it is dispersively read out. The pulse first goes through a microwave switch whose state depends on the output of a quantum random number generator (QRNG). If the QRNG outputs $x = 1$, the pulse goes through and the qubit is effectively measured along an axis in the XY plane of the Bloch sphere. If instead $x = 0$, the switch is switched off, the pulse is blocked, and the qubit is measured along the z-axis.

The QRNG, a QuFresh model from QuSide Inc. shown in Fig. 6.11 (b), is an adaptation of the QRNG described in [Abellán15] and used in the first three loophole-free Bell tests [Hensen15, Giustina15, Shalm15]. The quantum entropy source (QES) consists of a laser cavity driven at a 400 MHz rate in and out of its lasing mode to emit a 1 ns long laser pulse with a random phase every 2.5 ns. An unbalanced Mach-Zender interferometer (UMZI) converts the train of phase-random pulses into power-random pulses. The pulse power signal is measured with a photodetector (PD) and digitized with a 1-bit digitizer whose threshold is constantly adjusted to have equal probabilities of outputting 0 or 1.

Due to a finite amount of predictable noise stemming from the photodetector, the

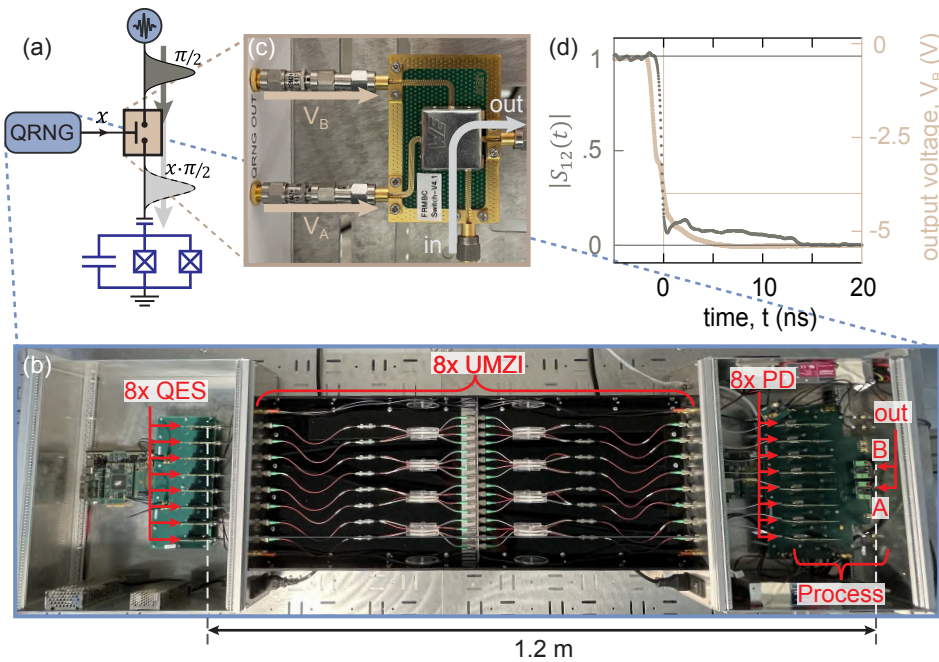


Figure 6.11 (a) Conceptual diagram of the random measurement basis selection scheme. (b) Top-view photograph of the QRNG, with all top covers open. (c) Top-view photograph of the microwave switch PCB, with control ports A and B connected to the corresponding outputs of the QRNG. (d) Oscilloscope measurement of the transmission coefficient $|S_{12}|$ through the switch of a 6 GHz continuous wave, and voltage applied to control the A port, vs time. The origin of time is defined as the moment the control A voltages goes below -3.5V .

1-bit digitizer, and from delayed contributions of previous pulses, the random bits generated by a single QES have a large excess predictability $\varepsilon_{\text{QES}} \sim 0.2$. To reduce the predictability of the output bit, the QRNG makes use of eight QES, generating high-excess-predictability bits in parallel, and computes the parity of these eight bits in real-time with a set of XOR gates to extract the parity bit d with excess predictability $\varepsilon = \varepsilon_{\text{QES}}^8$. In the most paranoid scenario, $\varepsilon = 4.23 \times 10^{-6}$ and a LHV model can reach CHSH values up to $S = 2.015$ [Eq. (2.74)]. This sets the threshold to be violated to reject local realism.

The value of d , which randomly flips every 2.5 ns, is latched to the output bit x by an external latching trigger. By default, in the absence of a trigger, $x = 1$, and if a trigger rising edge is received at time t , then $x = d(t)$ for the duration of the trigger. Once the trigger stops, x is set back to 1. The output bit voltage is offset and amplified to yield voltages $V_A = -5\text{V}$ and $V_B = 0\text{V}$ for $x = 1$, and $V_A = 0\text{V}$ and $V_B = -5\text{V}$ for $x = 0$, at the output ports A and B , to control the state of the microwave switch.

The switch is a single-pole double throw microwave switch with 2 ns specified switching time, working from DC to 18 GHz (CMD193C3 from Custom MMIC), and which we use as a single-pole single-throw switch by terminating one of the output ports [Fig. 6.11 (c)]. The signal is routed to the output port when $V_A = -5\text{V}$ and $V_B = 0\text{V}$ and towards the terminated port when $V_A = 0\text{V}$ and $V_B = -5\text{V}$. Consequently, the state of the switch is given by the values of the QRNG output bit x . By default, when the QRNG is not triggered, $x = 1$ and the switch is on. When the QRNG is triggered, either $x = d = 1$ and the switch stays on, or $x = 0$ and the switch switches off in approximately 1 ns after V_B starts to drop and stays off for the duration of the QRNG trigger [Fig. 6.11 (d)].

The freshness time of the QRNG is defined as the interval between the earliest spontaneous-emission event used to generate the output bit x , and the moment the switch is switched off (for $x = 0$, corresponding to $V_B < -3.5\text{V}$). Measurements performed by QUSIDE specify a freshness time below 17 ns, consisting of 6 ns propagation delay of the laser pulses in the short optical path of the UMZIs, 3 ns to convert the output x to the control voltages $V_{A/B}$, and 8 ns from the rest of the elements: laser pulse rise time, 1-bit digitizer, synchronizing flip-flops, real time parity extraction of the 8 parallel random bits, rise time of the random bits, and propagation time of the signals through the tracks of the device. The fiber optics length of the UMZI could not be reduced for manufacturing reasons. The QRNG design makes use of the long UMZI length to physically separate the QES and the QRNG output by 1.2 m [Fig. 6.11 (d)]. This 1.2 m increase of the distance between remote parties gives an extra 4 ns measurement time

to the close the locality loophole in a Bell test.

To test how this setup implements a random measurement basis scheme, we modify the measurement setup of qubit B as follows: we use a 25 Gs/s AWG (70002A by Tektronix) to directly synthesize the qubit pulses with high bandwidth and route the pulses through the QRNG-controlled switch [Fig. 6.12 (a)]. We prepare qubit B in one of the cardinal states $|s\rangle \in \{|g\rangle, |e\rangle, |+i\rangle, |-i\rangle, |+\rangle, |-\rangle\}$, rotate it with a $\pi/2$ pulse of duration $t_g = 12$ ns and measure the qubit state dispersively. The QRNG is triggered to switch off the switch at a time $t = 0$ and the rotation pulse starts at a time τ [Fig. 6.12 (b)]. For $\tau > 0$, the rotation pulse is blocked, and we measure $\langle\sigma_z\rangle = 2P_g - 1 = \pm 1$ when $|s\rangle = |g/e\rangle$, and $\langle\sigma_z\rangle = 0$ when preparing an equal superposition state, as expected from a measurement of the σ_z observable [Fig. 6.12 (c)]. For $\tau < -t_g = -12$ ns, the rotation pulse passes entirely and maps states $|\pm i\rangle$ to $|g/e\rangle$, implementing an effective measurement of the σ_y observable. At intermediate values of τ , the pulse is partially blocked and realizes a rotation by an angle

$$\theta = \int_{-\infty}^{+\infty} \Omega_{\text{DRAG}}(t - \tau - t_g/2) |S_{12}(t)| dt, \quad (6.1)$$

ranging between $\pi/2$ and 0. Here $\Omega_{\text{DRAG}}(t)$ is the drive rate the rotation pulse would induce if the switch would stay on [given by Eq. (2.32)], and $|S_{12}(t)|$ is the time-dependent transmission coefficient of the switch. This leads to an effective measurement of the observable

$$R_x^{-\theta} \cdot \sigma_z \cdot R_x^\theta = \cos \theta \sigma_z + \sin \theta \sigma_y.$$

For each τ , we reconstruct the axis $\vec{n} = (n_x, n_y, n_z)$ of the effective measurement $\vec{n} \cdot \vec{\sigma}$ by minimizing

$$\sum_s |\langle s | \vec{n} \cdot \vec{\sigma} | s \rangle - \langle \sigma_z \rangle_s|^2,$$

where $\langle \sigma_z \rangle_s$ is the measured $\langle \sigma_z \rangle$ when the qubit is initialized in $|s\rangle$. As expected from Eq. (6.1), the reconstructed measurement axis angle θ varies from $\pi/2$ to 0 as τ increases from -12 ns to 0 ns [Fig. 6.12 (d)]. Fitting Eq. (6.1) with an offset in time as the only free parameter yields excellent agreement to the data [see solid lines in Fig. 6.12 (c,d)], and calibrates the relative timing between the switch and the drive pulse.

At a time $\tau = 1$ ns, the pulse is fully blocked when the QRNG outputs $x = 0$. Therefore, the measurement axes $\vec{n}_{x=0}$ and $\vec{n}_{x=1}$ are orthogonal, which leads to optimal

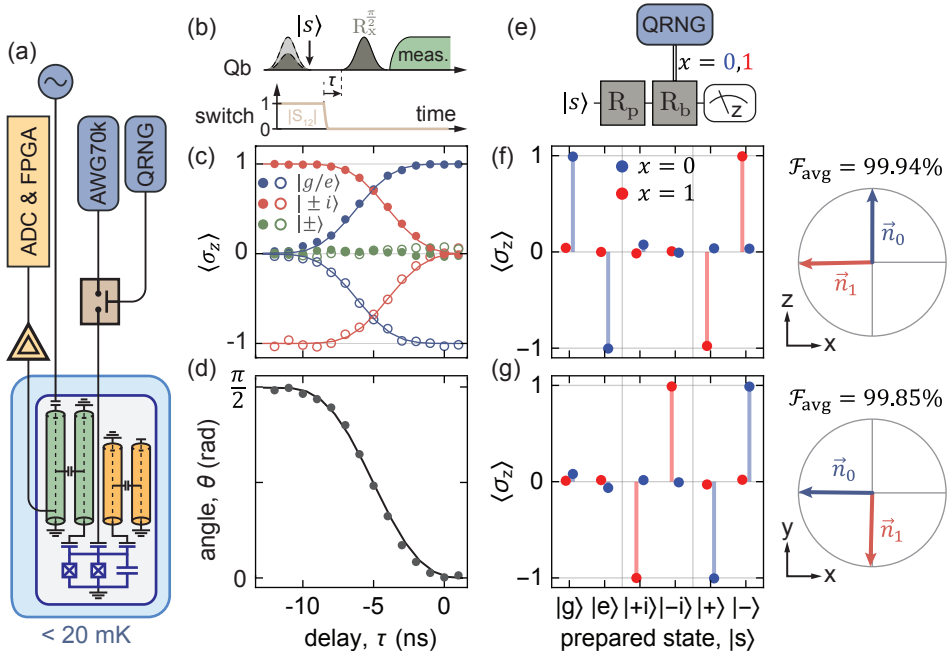


Figure 6.12 (a) Simplified electrical diagram of the setup used to implement and characterize the random measurement basis choice on qubit B. (b) Pulse scheme to calibrate timing between the qubit pulses (gray) and the switch, whose transmission, shown in beige, ranges from 1 to 0. (c) Expectation value $\langle \sigma_z \rangle$ versus delay τ between the beginning of the switch-off and that of the $R_x^{\pi/2}$ rotation pulse, when the qubit is initialized in any of the six cardinal states $|s\rangle \in \{|g\rangle, |e\rangle, |+i\rangle, |-i\rangle, |+\rangle, |-\rangle\}$. (d) Angle θ between the z-axis and the effective measurement axis vs delay τ . The solid lines in (c,d) are fit to equation 6.1 with an offset in time as the only free parameter. (e) Quantum circuit diagram to implement and characterize a random choice between two arbitrary measurement axes. The rotation R_b is conditioned on the QRNG outputting a 1. (f,g) Expectation value $\langle \sigma_z \rangle$ measured when implementing the quantum circuit (e) with the qubit initialized in any of the cardinal states $|s\rangle$, conditioned on the QRNG output x for a delay $\tau = 1 \text{ ns}$ (left), and their corresponding effective measurement axis \vec{n}_x represented in a plane cut of the Bloch sphere (right), with (f), $R_p = \text{Id}$ and $R_b = R_y^{\pi/2}$, and (g), $R_p = R_y^{\pi/2}$ and $R_b = R_x^{\pi/2}$.

violation of Bell's inequality, see Sec. 2.2.3 and [Brunner14]. In fact, it is possible to implement a random selection between any arbitrary pair of measurement axes $\vec{n}_{0/1}$ by first applying a rotation R_p which maps $\vec{n}_{0/1} \cdot \vec{\sigma}$ to $|g/s\rangle$, with $|s\rangle$ and arbitrary qubit state, followed by a conditional rotation R_b mapping $|s\rangle$ to $|g\rangle$ [Fig. 6.12 (e)].

For instance, to select between a z-axis and an x-axis measurement, we prepare the qubit in one of the cardinal states $|s\rangle$, apply the rotation $R_p = \text{Id}$, send a rotation pulse $R_b = R_y^{\pi/2}$ conditioned on the QRNG outcome and record single-shot measurements of the qubit and the QRNG output x . The expectation value $\langle \sigma_z \rangle$ conditioned on the random output x is consistent with a measurement of the observable σ_z for $x = 0$ and $-\sigma_x$ for $x = 1$, as quantified by the average overlap $\mathcal{F}_{\text{avg}} = (\vec{n}_0 \cdot \vec{z} - \vec{n}_1 \cdot \vec{x})/2 = 99.94\%$ between the reconstructed and target measurement axes [Fig. 6.12 (f)]. Repeating this experiment with $R_p = R_y^{\pi/2}$ and $R_b = R_x^{\pi/2}$, we select between an x-axis and a y-axis measurement [Fig. 6.12 (e)], which optimizes the CHSH violation in a Bell test using the type of entangled state we generate (see Secs. 2.2.3 and 6.5). In this case, we determine an average overlap $\mathcal{F}_{\text{avg}} = -(\vec{n}_0 \cdot \vec{x} + \vec{n}_1 \cdot \vec{y}) = 99.85\%$ between the reconstructed and target measurement axes [Fig. 6.12 (e)].

In principle, the conditional rotation pulse can be as short to $2 \times 2\pi/\alpha \simeq 7$ ns while retaining high fidelity and low $|f\rangle$ -level leakage [Motzoi09, Gambetta11a]. To confirm this, we repeat the X/Y measurement basis choice experiment with rotation pulse duration varying from 12 ns to 4 ns. For a pulse duration of 6 ns or more, we observe less than 1% leakage to the $|f\rangle$, and near-unit overlap with the target measurement axes.

6.8 Closing the locality loophole

6.8.1 Experimental setup

To close the locality loophole, we improve on the experimental setup described in Sec. 6.1 to Sec. 6.6. We cool the transmon qubits in the opposite nodes of the 30 m long cryogenic link described in chapter 4 [Fig. 6.13 (a)]. As before, we connect the transfer resonators of the circuits to each other through the 29.95 m long WR90 waveguide housed inside the base temperature shield of the cryogenic link, in series with two flexible coaxial copper cables of 0.4 m length each, and a circulator located at node A. The transmon circuits are cooled to below 20 mK and the waveguide is entirely below 50 mK (Fig. 4.6).

The room temperature electronics used to control and measure the qubits are split

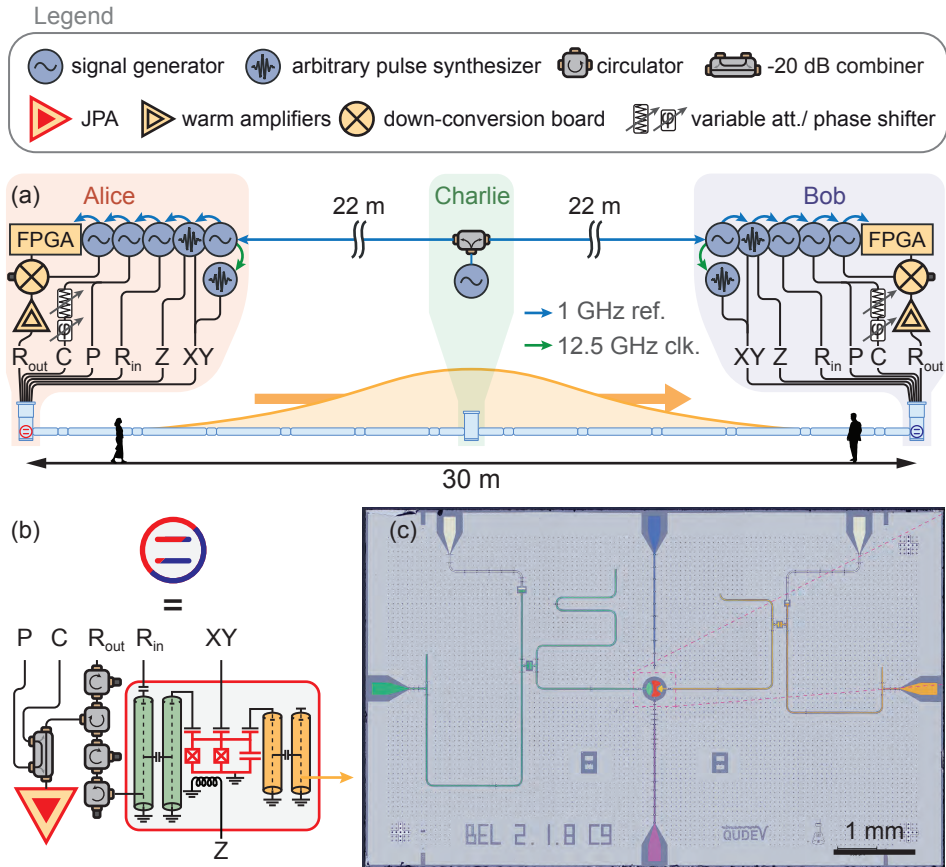


Figure 6.13 (a) Schematic representation of the 30 m long experimental setup and the signals used to phase-lock the room temperature electronics. The silhouettes are to scale with the cryogenic system. In this scale, the length of the wavepacket in yellow corresponds to a photon bandwidth $\Gamma/2\pi \sim 10$ MHz. (b) Simplified circuit diagram of the qubit chips and their Josephson parametric amplifier chain, with port labels. The port labels are abbreviations for: R_{out}: readout output; R_{in}: readout input; P: JPA pump; C: pump cancellation; Z: flux line (Z-control); XY: drive line (XY-control). (c) False color photograph of a chip similar to those used in the 30 m experiment. The legend and color codes are consistent with those given in Figs. 6.1, 6.4 and 6.5.

into two setups, one at node A (Alice), and one at node B (Bob), see Fig. 6.13 (a). They are phase synchronized by a common 1 GHz phase reference signal generated by a reference oscillator in the middle of the link at point C (Charlie). The reference signal is distributed to Alice and Bob through two cables of equal length (22 m) to ensure that the relative phase of the reference signal at A and B is insensitive to uniform temperature changes in the laboratory environment. At each setup, the phase reference is distributed in a daisy-chain of 1 GHz reference signals between the microwave generators (SGS100A from Rhode & Schwarz), to minimize phase drifts between elements of the setup [Rhode&Schwarz16]. In each setup, the f_0 - g_1 transition drive is generated by a 25 Gs/s AWG (AWG70002 from Tektronix), which is clocked externally at 12.5 GHz by the first microwave generator of the reference-signal daisy-chain to minimize phase noise and phase drifts of this instrument with the rest of the setup [Fig. 6.13 (a)]. See [Copetudo21] for a detailed characterization of the phase stability of this setup.

The cabling inside and outside the cryogenic system is optimized to reduce propagation delay of signals which are time-critical for a Bell test. In each node, the drive line [XY, in Fig. 6.13 (a,b)], which carries the conditional rotation pulse to implement the random measurement basis choice, and the readout output line [R_{out} , in Fig. 6.13 (a,b)] are fed through the side port of the dilution refrigerator, described in Sec. 4.1 [Fig. 4.1 (a)], to minimize their lengths. Characterizing the signal propagation delays through each of the elements of the drive line and of the readout output line with an oscilloscope, we determine the total propagation delay in the drive and output lines to be below 18 ns.

In addition, the line-of-sight geometry of the cabling through the side-port, of the room temperature detection chain, and of the QRNG, increases the spatial separation between the QRNG lasers on one side, and the ADC on the other side to 33 m. This leaves approximately 110 ns Bell-test-run measurement time to close the locality loophole (see Sec. 2.2.2). Of that time budget, 17 ns is taken by the QRNG freshness time, 18 ns is taken by signal propagation delay in cables and components, and up to 12 ns is needed by the conditional, measurement-basis-choice, rotation pulse. There remains 63 ns to integrate the readout signal.

The qubit chips used in this setup, illustrated in Fig. 6.13 (b,c), improve on the design presented in Sec. 6.2 to optimize readout speed. To that end we target a high bare qubit anharmonicity $\alpha/2\pi \simeq -350$ MHz, or dressed anharmonicity $\alpha/2\pi \simeq -320$ MHz. To ensure that the e-f coherence is not limited by charge dispersion (see Sec. 2.1.3), we design the qubit to target a frequency $\omega_q^{\text{RO}}/2\pi \geq 7.2$ GHz for readout

and $\omega_q/2\pi = 7.7$ GHz at the sweet spot, at which we intend to manipulate them. The qubit couples dispersively to two Purcell filtered resonators: one for readout (green) of frequency $\omega_r/2\pi \simeq 5.64$ GHz, whose parameters are optimized as described in chapter 3, and one of frequency $\omega_t/2\pi \simeq 9.5$ GHz for photon transfer (yellow).

The qubits have frequencies $\omega_q^A/2\pi = 7.811$ GHz and $\omega_q^B/2\pi = 7.875$ GHz at their sweetspot, for which the transfer resonators have a matched frequency $\omega_t/2\pi = 9.49$ GHz and the qubits have the highest coherence times $T_1 \simeq 18 \mu\text{s}$, $T_2^* \simeq 10 \mu\text{s}$, and $T_2^e \simeq 30 \mu\text{s}$. All target and measured sample parameters are listed in table 6.4. A dedicated flux line inductively coupled to each qubit's SQUID loop is used to rapidly change the qubit frequency between its parking and readout values.

The sweetspot frequency increase relative to its designed value is unfortunate, because it brings the qubits (qubit A in particular) closer to a critical frequency $\omega_{f \rightarrow g}/2\pi = (\omega_r + \omega_t - \alpha)/4\pi \simeq 7.73$ GHz at which states $|f00\rangle$ and $|g11\rangle$ are resonant. Labels k , n , and m in $|k, n, m\rangle$ denote the number of excitations in the qubit, the readout resonator, and the transfer resonator, respectively. This leads to an effective $|f\rangle \rightarrow |g\rangle$ Purcell decay channel, which limits the $|f\rangle$ -level lifetime of qubit A. The negative AC Stark shift induced by the f0-g1 drive brings the qubit closer to $\omega_{f \rightarrow g}/2\pi$, which limits the maximum f0-g1 drive rate to $2\tilde{g}_{\text{max}}/2\pi \simeq 25$ MHz before $|f\rangle \rightarrow |g\rangle$ decay limit the photon emission fidelity. In addition, the coupling J_t between the transfer resonator and its Purcell filter is significantly higher than expected, leading to an effective transfer resonator external coupling rate $\kappa_t/2\pi \simeq 32$ MHz larger than the maximum f0-g1 drive rate $2\tilde{g}_{\text{max}}$. Therefore, as discussed in detail in appendix B.3, the f0-g1 drive rate limits the speed of the photon emission.

6.8.2 Rapid Single-Shot Readout

To test the readout performance of qubit A (B), we initialize it in state $|g\rangle$ or $|e\rangle$ with a reset pulse and an optional π pulse, then apply a flux pulse to rapidly tune the qubit frequency from the upper sweetspot to $\omega_{q,\text{RO}}/2\pi = 7.2$ GHz (7.55 GHz) and apply a 5.622 GHz (5.636 GHz), gated microwave tone to the input port of the readout Purcell filter [Fig. 6.14 (a)]. The readout tone frequency and power are chosen after a sweep to maximize readout fidelity. Bob's qubit couples strongly to a defect at ~ 7.5 GHz, which causes $\sim 10\%$ population decay when Bob's frequency is rapidly tuned from above to below the defect frequency. Therefore, we set $\omega_{q,\text{RO}}^B = 7.55$ GHz, for which the dispersive shift $\chi_r/2\pi = -5.4$ is suboptimal, to avoid crossing this defect. We define the measurement start time $t = 0$ as the end of the excitation π pulse. The

quantity,	symbol	target	Node A	Node B	unit
qubit upper sweetspot frequency	$\omega_q/2\pi$	7.7	7.811	7.875	GHz
transmon anharmonicity	$\alpha/2\pi$	-320	-299	-307	MHz
energy relaxation time on ge	T_{1ge}	-	20	15	μs
energy relaxation time on ef	T_{1ef}	-	3.4	7	μs
coherence time on ge	T_{2ge}^e	-	28	18	μs
coherence time on ef	T_{2ef}^e	-	10	9	μs
thermal excitation at equilibrium	n_{th}	0	3.3	3	%
$ f, 0\rangle \leftrightarrow g, 1\rangle$ transition frequency	ν_{f0g1}	5.58	5.797	5.927	GHz
qubit frequency for readout	$\omega_q^{RO}/2\pi$	7.2	7.22	7.55	GHz
readout resonator frequency	$\omega_r/2\pi$	5.648	5.634	5.637	GHz
readout Purcell filter frequency	$\omega_{pr}/2\pi$	5.64	5.623	5.611	GHz
readout resonator/qubit coupling	$g_r/2\pi$	210	215	218	MHz
readout circuit dispersive shift	$\chi_r/2\pi$	-8	-8.15	-5.4	MHz
readout resonator/filter coupling	$J_r/2\pi$	25	26.2	26.2	MHz
readout Purcell filter bandwidth	$\kappa_{pr}/2\pi$	87	89	92	MHz
readout resonator eff. bandwidth	$\kappa_r/2\pi$	31.4	38.3	24	MHz
transfer resonator frequency	$\omega_t/2\pi$	9.5	9.490	9.491	GHz
transfer Purcell filter frequency	$\omega_{pt}/2\pi$	9.5	9.489	9.477	GHz
transfer resonator/qubit coupling	$g_t/2\pi$	350	320	324	MHz
transfer resonator/filter coupling	$J_t/2\pi$	25	36.2	36.4	MHz
transfer Purcell filter bandwidth	$\kappa_{pt}/2\pi$	130	163.9	146	MHz
transfer resonator eff. bandwidth	$\kappa_t/2\pi$	23.5	~ 30	~ 35	MHz

Table 6.4 Device parameters for chips A and B used in the 30 m long setup.

timing of the flux pulse and the readout drive are calibrated in such a way that they start as early as possible, without degrading the fidelity of a qubit pulse ending at $t = 0$. Because of a ring-up time $t_d \sim 5$ ns of the readout resonator, the rising edge of the readout pulse arrives at a negative time $-t_d$ [Fig. 6.14 (a)].

We amplify the information-rich quadrature Q of the readout signal using a near

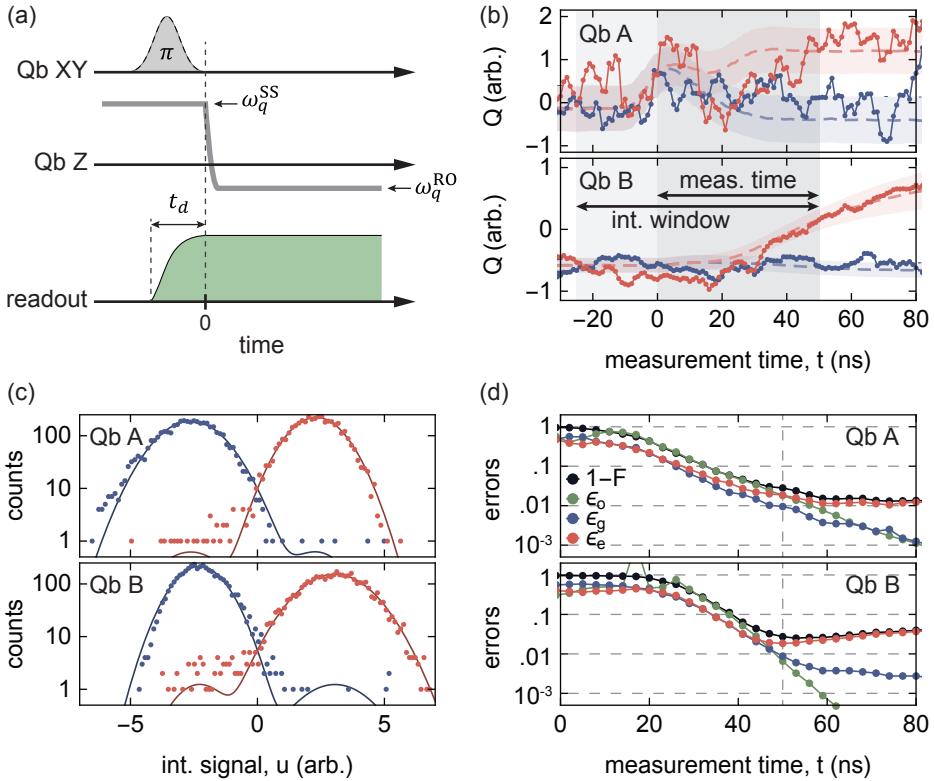


Figure 6.14 (a) Pulse scheme to perform and characterize single-shot readout of the transmon qubits. The flux pulse starts at time $t = 0$ and rapidly sets the qubit frequency from its sweetspot ω_q^{SS} to the readout value ω_q^{RO} . (b) Information-rich quadrature Q of single-shot readout traces vs time t when the qubit is prepared in state $|g\rangle$ (blue) and $|e\rangle$ (red). The dashed lines are the average traces and the shaded region around them correspond to one standard deviation of the signal. The grey rectangles indicate the integration window, and the corresponding measurement time. (c) Histograms of single-shot traces integrated with optimal weights for 50 ns measurement time (75 ns integration time). The solid lines are bi-modal Gaussian fits. The x-axis is offset such that the red and blue lines cross at $u = 0$, which defines the discrimination threshold. (d) Measurement infidelity $1 - \mathcal{F}_r$, its contribution from overlap error ε_o , and its decomposition into ground and excited state errors ε_g and ε_e , as functions of the measurement time.

quantum-limited reflective Josephson parametric amplifier (JPA) [Eichler11, Walter17] with 31 dB phase-sensitive gain (30.7 dB) and 14 MHz bandwidth (7 MHz), pumped at 5.622 GHz (5.636 GHz). We further amplify the signal at the 4K plate with high-electron-mobility transistors (HEMT), then at room temperature with (ultra-)low-noise amplifiers. The signal is then down-converted to 250 MHz, digitized at 1 Gs/s, and digitally down-converted to complex DC values by the FPGA.

We collect 2000 single-shot traces for each qubit preparation state. The ground and excited-state readout signal can be clearly distinguished in a single-shot measurement after just a few tens of ns [Fig. 6.14 (b)]. For a given measurement time t , we integrate the readout signal in the interval $[-t_r, t]$ with weights chosen to maximize the contrast between the ground and excited state traces, accounting for the finite bandwidth of the JPA, as described in Sec. 3.1. Here $t_r = 25$ ns is chosen to be larger than the characteristic response time of the detection chain (Sec. 3.1).

The integrated signal $u(t)$ follows a bi-modal Gaussian distribution, whose modes correspond to the ground and excited state responses [Fig. 6.14 (c)]. The width of the two Gaussian modes are different because of the strong readout tone, which drives the resonator into a qubit-state-dependent, non-linear regime. We fit the ground and excited-state histograms of u each with a bi-modal Gaussian curve. We define the assignment threshold q at the intersection between the two fitted curves. A single shot trace is assigned to outcome g if $u < q$ and to e otherwise. We estimate the probability $P(i|j)$ to assign a measurement trace to outcome i when the qubit was prepared in state j from the fraction of the integrated traces u assigned to i . At early measurement times, $t < 40$ ns, the readout fidelity

$$\mathcal{F}_r = 1 - P(e|g) - P(g|e)$$

is limited by the low signal-to-noise ratio (SNR) between the main modes of the ground and excited traces. The SNR increases with measurement time resulting in lower overlap errors $\varepsilon_o = \text{erfc}[\sqrt{\text{SNR}/8}]$ and higher readout fidelity [Fig. 6.14 (d)]. At $t \sim 50 - 80$ ns, qubit decay starts to limit the excited state errors $P(g|e)$. The readout fidelity reaches its maximum value $\mathcal{F}_{r,A} = 99\%$ at $t = 60$ ns, and $\mathcal{F}_{r,B} = 97.5\%$ at $t = 55$ ns, beyond which it decreases as qubit decay events become more probable over longer measurement times.

In particular, the qubits can be read out with high fidelity ($\mathcal{F}_{r,A} = 98\%$ and $\mathcal{F}_{r,B} = 97.2\%$) in 50 ns measurement time, which should allow to violate CHSH inequalities while closing the locality loophole with 13 ns margin. Bob's readout fidelity could

further increase in the absence of the 7.5 GHz defect. Indeed, in a previous cooldown of the same chip, in which the defect was absent, we could readout Bob's state with $\mathcal{F}_{r,B} = 99.4\%$ fidelity in 50 ns by tuning its frequency to $\omega_{q,RO} = 7.2$ GHz during readout.

6.8.3 Quantum communication over 30 meters

We repeat the protocol described in Sec. 6.3 to emit single photons with approximate shape $\phi(t) = \text{sech}(\Gamma t/2)$ from qubit A and absorb them with qubit B using the f0-g1 transitions. The photons propagate from Alice to Bob in $\tau_d = 142$ ns, as estimated from the lengths and group velocity of each section of the waveguide. The photon bandwidth, $\Gamma/2\pi = 20$ MHz, is limited by the f0-g1 drive power which the device at Alice can tolerate. Nonetheless, the photon is emitted in 60 ns, which is a factor of three faster than in the previous experiment (Sec. 6.3), and is also more than twice shorter than the group delay τ_d of the waveguide. The transfer efficiency, defined as the excited population at Bob at the end of the photon transfer protocol, is 70%, limited by photon loss in the circulator and the lossy coaxial cables at each end of the waveguide, and by qubit relaxation. The transfer efficiency is 3 percentage points higher than in the previous experiment because the benefits of improved qubit relaxation time and shorter photon emission duration outweighs the $\sim 0.5\%$ increase of photon loss due to the longer waveguide (see Secs. 4.5 and 4.8.6).

Using this photon transfer protocol, we transfer qubit states from Alice to Bob in the fashion described in Sec. 6.4. We reset both qubits to their ground state, prepare Alice in one of the cardinal states $|s\rangle \in \{|g\rangle, |e\rangle, |+i\rangle, |-i\rangle, |+\rangle, |-\rangle\}$, apply an e-f π pulse on Alice, transfer the f level excitation to Bob with f0-g1 emission and absorption pulses, and apply a final e-f pulse on Bob [Fig. 6.15 (a)]. We perform a qutrit state tomography on Bob to reconstruct the transferred state $\rho_{f,s}$ for each initial state $|s\rangle$, from which we determine an average state fidelity of the transferred states $\mathcal{F}_s = 85.5\%$. We reconstruct the most likely transfer process matrix χ from the set of final states and determine a process fidelity $\mathcal{F}_p = 80.2\%$ to the ideal process, correcting for readout errors [Fig. 6.15 (a)].

We generate and characterize an entangled state using the pulse scheme described in Sec. 6.5 and illustrated in Fig. 6.15 (b). We reconstruct the entangled state ρ with two-qutrit state tomography, correcting for readout errors [Kurpiers18]. We determine a fidelity $\langle \Psi^+ | \rho | \Psi^+ \rangle = 78.8\%$ with respect to the ideal Bell state $|\Psi^+\rangle$ and a concurrence $\mathcal{C}(\rho) = 0.722$, which are similar to the values obtained in the 5 m experiment (Sec. 6.5).

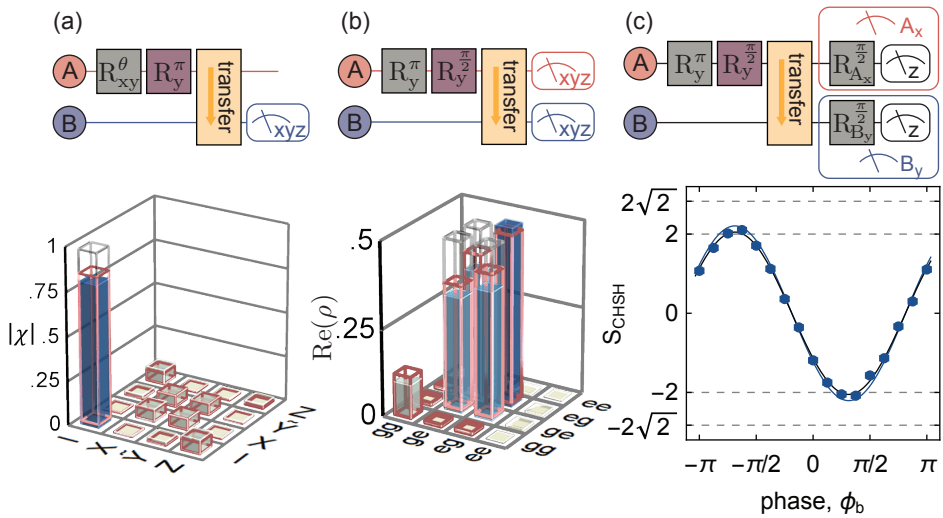


Figure 6.15 (a) Absolute value of the transfer process matrix χ , characterized with the quantum circuit shown at the top. (b) Real part of the density matrix ρ of the Bell state, generated and reconstructed with the quantum circuit shown at the top. (c) CHSH value $\langle ab \rangle_{00} + \langle ab \rangle_{01} + \langle ab \rangle_{10} - \langle ab \rangle_{11}$ vs phase offset ϕ_B of the measurement axes of qubit B. The blue and black lines are simulated and fitted curves, respectively. In (a,b), the solid blue bars, red wireframes and gray wireframes are the reconstructed, simulated, and target quantities, respectively.

parameter	reconstructed state, ρ	simulated state, ρ_{sim}
Population in two first levels, ν	.938	.996
Bell state coherence, \mathcal{V}	.897	.985
Transfer efficiency, η_A	.70	.748
Qubit A decay, η_B	1.09	.1.006
Trace distance	.017	.015

Table 6.5 Results of a fit of the parametrized density matrix ρ_{AB} to the reconstructed and simulated density matrices. The last column displays the trace distance $\sqrt{\text{Tr}(|\rho - \rho_{AB}|^2)}$.

However, unlike in Sec. 6.5, simulations of the process using parameters extracted from independent measurement lead to a fidelity $\langle \Psi^+ | \rho_s | \Psi^+ \rangle = 86.2\%$ and concurrence $\mathcal{C}(\rho_s) = 0.85$ clearly higher than what is measured, see red wireframes in Fig. 6.15 (b), as one would expect from the improved coherence times and photon bandwidth.

To understand this discrepancy, we fit the the reconstructed and simulated states ρ and ρ_s with the state parametrization (2.59) given in Secs. 2.1.8 and 6.5. The fitted density matrices, whose parameters are shown in table 6.5, reproduces ρ and ρ_s very closely (see trace distances in table 6.5).

We note three significant differences between ρ and ρ_s . First, the population $1 - \nu$ leaked outside the two-qubit subspace is large compared to simulation ($\simeq 6\%$ vs 0.4%). The population leaks mostly in state $|gf\rangle$ (2%) and $|fg\rangle$ (3.4%), which can be due to emission inefficiencies, e-f decay of qubit B just before the final e-f π pulse, or poor calibration of the e-f single qubit pulses, which are used both in the state generation protocol and in the tomography. Second, the Bell state coherence \mathcal{V} is significantly smaller than expected from simulation. This extra dephasing could come from relative phase noise between the electronics setups of Alice and Bob, to dephasing induced by the amplitude noise of the AC Stark-shift-inducing f0-g1 drive [Wei21, Caldwell18, Valery21], or to the incoherent emission process happening when state $|f00\rangle_A$ couples to $|g11\rangle_A$. The second possibility could be tested with Ramsey measurements in the presence of a f0-g1 drive, and mitigated using emission methods inducing small amounts of AC Stark shift [Besse20b], or engineering dynamical sweetspots with extra drive tones [Valery21, Huang21b]. Third, the transfer efficiency η_A should in principle be larger by 5 percentage points, which could come from imperfections in the absorption pulse, or impedance mismatches in the waveguide. Characterizing and understanding these potential error sources would constitute valuable work to further increase the fidelity of the generated entangled state.

We repeat the procedure described in Sec. 6.6 to perform a Bell test with predetermined measurement bases. We generate the entangled state and measure Alice along

$a, b \backslash x, y$	0,0	0,1	1,0	1,1
-1,-1	416	427	368	145
-1,+1	86	102	133	377
+1,-1	100	98	144	337
+1,+1	398	373	355	141
$\langle ab \rangle_{xy}$	0.628	0.6	0.446	-0.428
$\Delta \langle ab \rangle_{xy}$	0.024	0.025	0.028	0.029

Table 6.6 Number of runs which were assigned to the output pair a, b for input pair x, y , for $\varphi_B = -5\pi/8$. The last two rows show the values of the estimator of the correlations and their uncertainty.

the x-axis or y-axis, and Bob along one of two orthogonal axes in the x-y plane, in single-shots with a single-shot readout fidelities $\mathcal{F}_{r,A} = 98\%$ and $\mathcal{F}_{r,B} = 96.4\%$ [Fig. 6.15 (c)]. For each qubit and each measurement setting, we collect 1000 single-shot traces each of which is assigned to output -1 or $+1$ by the FPGAs, thereby closing the detection loophole.

The CHSH value oscillates with the angle φ_B between Bob's measurement axis B_0 and the x-axis, with a fitted amplitude of 2.05 and extrema at $\varphi_B = 3\pi/8 \pmod{\pi}$ [Fig. 6.15 (c)]. For $\varphi_B = -5\pi/8$, we obtain the counts shown in table 6.6, from which we calculate $S_{\text{CHSH}} = -2.102 \pm 0.054$. This corresponds to a violation of the CHSH Bell inequality by more than 1.9 standard deviations, and a P -value of 0.028 to reject local hidden variable models assuming no memory effects. As expected from previous discussions, simulations of the process predict a higher maximum CHSH value $S = 2.207$ with our experimental readout fidelities. Understanding and correcting the origins of the discrepancy between the experiment and the simulation would lead to a larger violation of Bell's inequality.

6.9 Conclusion

Conducting simulations in which all error sources but one are set to zero, we identify that photon loss and qubit decoherence are the dominant sources of errors in transferring qubit states and generating entanglement. In the 5 m long setup, these sources of errors contribute to 11.8% and $\sim 6\%$ infidelity, respectively. In the 30 m long setup, photon loss causes the same amount of errors, but the decoherence-induced errors reduce to $\sim 2\%$ thanks to the improved photon bandwidth and qubit coherence times. The additional error channels observed in the 30 m setup and discussed at the end of

the previous section are not captured by the simulation and contribute to $\sim 8\%$ error.

To improve the fidelity, the first step would be to understand and correct these additional error channels. As a next step, one could tackle other sources of errors. For instance, the photon loss may be reduced to 5% by removing the circulator [Zhong19, Leung19, Chang20, Burkhardt21], by using a printed circuit board (PCB) metallized with a superconductor, and by using low-loss coaxial cables between the device and the waveguide. Simulations of the protocols with 5% photon loss indicate that Bell state fidelities and state transfer process fidelities as high as 96% may be achievable, which may enable distributed surface-code computation [Nickerson14] and communication [Fowler10] between distant cryogenic nodes. Such simulations also indicate that CHSH values exceeding $S_{\text{CHSH}} = 2.6$ could be obtained, putting yet-unachieved device-independent tasks within experimental reach [Barrett05, Murta19, Tan20]. Further improvement may be obtainable using protocols requiring less time compared to the coherence of the circuit elements [Zhong19], or ones which are resilient to photon loss [Kurpiers19b, Bergmann19, Chang20, Burkhardt21] and thermal excitation [Xiang17, Vermersch17].

This realization of milli-Kelvin temperature, microwave-frequency coherent quantum links and their use for quantum state transfer, entanglement generation and Bell's inequality violation constitutes the very first demonstrations of meter-scale superconducting quantum networks. As a next step, we envisage to integrate the random-measurement-basis-choice setup characterized in Sec. 6.7 with the 30 m long setup presented in Sec. 6.8 to reject local realism with a loophole-free Bell test. Such a realization with superconducting circuits would open a number of directions for future research which we detail in the outlook given in the next chapter.

Chapter 7

Outlook

*Et qui m'empêchera de mettre en notre étable,
Vu le prix dont il est, une vache et son veau,
Que je verrai sauter au milieu du troupeau ?
Perrette là-dessus saute aussi, transportée.
Le lait tombe : adieu veau, vache, cochon, couvée.*
— Jean de la Fontaine

All the work presented in this thesis has been motivated by the goal of conducting a loophole-free Bell test using superconducting qubits. To that end, we developed a protocol to entangle qubits fabricated on different chips connected by a microwave link [Kurpiers18] and realized a cryogenic link technology to increase the distance between connected qubits to tens of meters (chapters 4 and 6 and [Magnard20]). We pushed transmon qubit dispersive readout to its speed limit to minimize the link distance needed to close the locality loophole (chapter 3 and [Walter17]), and we developed a microwave reset scheme to generate highly entangled states despite the significant effective temperature of our transmon qubits (chapter 5 and [Magnard18]). Assembling all these elements together, we were able to realize prototypes of a microwave quantum network, covering distances up to 30 m, and successfully benchmarked the network by deterministically transferring qubit states, generating highly entangled states on-demand and violating Bell's inequality. The very next step will be to choose the Bell test measurement bases from the output of the quantum random number generator to close the remaining loopholes as much as can be.

Local realism has already been rejected experimentally since a long time [Freedman72, Aspect82a, Aspect82b, Weihs98, Rowe01], and more recently in loophole-free set-

tings [Hensen15, Giustina15, Shalm15, Rosenfeld17, Kenny21]. However, the loophole-free demonstrations have either suffered from low acquisition rates (sub-Hertz), when using atomic or solid-state bits, or from small Bell violation, when using pairs of entangled photons. By contrast, we expect our setup to combine the benefits of both platforms: high CHSH violations and tens of kHz repetition rates. This would put yet unachieved tasks beyond Bell tests, such as device-independent randomness amplification [Colbeck12, Kessler17, Ramanathan18] or quantum key distribution [Barrett05, Murta19, Tan20], within experimental reach. It would also be possible to reject local realism to a greater extent than in standard Bell test scenarios by testing chained Bell inequalities [Pearle70, Tan17b].

The versatility of circuit QED systems opens a number of other interesting possibilities. One could probe the interplay between local weak measurements and non-locality and reject local-macrorealism by testing the hybrid Bell-Leggett-Garg inequality [Dressel14, White16]. Extending on [Katz08], one could reverse the effect of space-like separated weak measurements on a pair of remote entangled qubits. Using a pair of cavities at each node, with photon emission capabilities [Pfaff17, Axline18], and tunable beam-splitter interaction [Gao18, Gao19], one could test the interplay between bosonic indistinguishability and non-contextuality, in a non-local fashion [Asadian21]. Finally, one could demonstrate probabilistic supraluminal teleportation of a randomly chosen wavefunction by embedding quantum state teleportation [Steffen13] in the Bell test framework.

Another interesting research direction is to investigate the distribution of quantum information processing tasks between quantum nodes hosting multiple qubits using a coherent cryogenic network, an essential part of a modular quantum computer architecture [Cirac99, Monroe14]. On a practical level, one could develop tools to improve the efficiency of microwave networks. For instance, one could increase the communication bandwidth of the link by developing methods to multiplex in frequency the emission and absorption of itinerant microwave photons, and developing rapid and lossless multi-pole, multi-throw switches [Pechal16b] to reconfigure the graph topology of the quantum network *in situ* would render the network considerably more flexible. Using linear quantum emitters, one could study the robustness of bosonic encoded wavepacket transfer against loss and thermal noise in the waveguide, to relax thermal constraints on the cryogenic link, and thus its cost [Xiang17, Vermersch17]. On a higher level, teleporting quantum state [Steffen13] and quantum gates [Chou18] would demonstrate the possibility to perform universal computation across the network. Remote entangled state purification [Bennett96a] would demonstrate the possibility

to perform error-corrected quantum computation [Nickerson13, Nickerson14]. Finally, one could stabilize a Bell state between remote data qubits with repeated parity measurements using entangled ancillae [Andersen19, Negnevitsky18], to demonstrate the building block for distributed surface code error correction [Fowler10].

Another remarkable property of our setup is that photons are fully emitted from one node before their wavefronts reach the other node. In this regime, one can remove the circulator without affecting the photon emission calibration procedure, and obtain a low-loss, bidirectional long link. Many new experiments can be performed in this bidirectional long-link setting. For instance, similar to the on-chip experiments presented in [Zhong19, Bienfait19], one could perform a two-qubit SWAP gate between the remote qubits via a simultaneous qubit state transfer, in which the emitted photons are criss-crossing in the waveguide. Emitting a photon from node A, letting it perform a controlled phase gate with qubit B as it reflects off node B [Duan04, Reiserer14, Kono18, Besse18], and absorbing it back at node A would effectively implement a direct and deterministic two-qubit controlled-phase gate, which could be benchmarked against gate teleportation [Chou18]. The significant propagation delay introduced by the waveguide could also be used in combination with sequential emission of entangled photonic states [Besse20b] and photon-photon gates [Reuer21] to generate two-dimensional graph states of propagating microwave photon with a single-emitter [Pichler17]. Finally, one could test measurement collapse models via delayed entanglement and disentanglement of an emitter qubit with a propagating measurement field.

In addition, the long waveguide setting offers a playground to investigate the physics of qubits coupled to non-Markovian, open, waveguide fields. One could investigate the non-exponential decay of a qubit in front of a remote mirror [Ferreira20], collective emission effects beyond super-radiance [Dinc19], or the so called *bound states in the continuum*, which are quantum states of light trapped in between two remote qubit-mirrors [Calajó19, Mirhosseini19]. The natural cutoff frequency of the waveguide enables to generate qubit-photon bound states [Sundaresan19, Kim21], which can interact with tunable strength from remote locations. Such effects can also be studied in metamaterial transmission lines [Mirhosseini18, Sundaresan19, Kim21], which offers similar group delays on a single chip. However the three-dimensional geometry of the waveguide offers some advantages: losses are small [Reagor13, Kurpiers17, Chakram20], qubits can be mounted and unmounted modularly to the waveguide [Burkhart21, Rosario Hamann18], magnetic elements can be placed in the waveguide far away from any qubits to introduce nonreciprocity [Owens18, Pozar12], the waveguide dispersion

relation is simple and leads to small wavepacket distortion, and finally light can be polarized using other waveguide modes [Pozar12]. These properties offer countless possibilities to explore uncharted territories in open-waveguide microwave photonics.

In a decade or two, cryogenic quantum links might even represent a commercial interest. Indeed, first error-corrected quantum computers will consist of more qubits than a single cryostat, be it large, can handle [Reiher17, Babbush18b, Krinner19]. Therefore, inter-cryogenic quantum interconnects will play a vital role in scaling up superconducting quantum computers. Most of current research on realizing such interconnects focuses on realizing microwave-to-optics quantum transducers [Andrews14, Balram16, Fan18, Higginbotham18, Hease20, McKenna20, Jiang20, Mirhosseini20, Chu20, Lambert20, Lauk20] to distribute quantum information with optical photons [Kimble08, Duan11, Awschalom21]. Apart from the transducers, the hardware needed to implement such an optical-frequency quantum network would consist of optical fibers at room temperature. Cryogenic links would be costly and impractical in comparison. However, a multi-cryogenic-node quantum computing cluster would already look like a giant cryogenic factory, and the inter-cryogenic distances would be on the meter scale. Cryogenic links would therefore represent a small fraction of the cost and time spent to install the cryogenics facility. Moreover, our demonstration is only the first prototype. We anticipate that engineering and industrialization efforts would enable future cryogenic links to be 10 times cheaper than this prototype (approximately 15 M€/km), to be mechanically flexible, to host multiple microwave buses and switching elements, and to have the possibility to be plugged in-and-out of running cryogenic networks. Finally, such cryogenic links enable microwave-based quantum communication protocols, which will likely keep higher fidelity and bit rate than optical-transducer-based protocols, thanks to their deterministic and low-noise features [Kurpiers18]. Cryogenic links might therefore be the technology of choice for quantum intranets, the size of a building or even of a campus. Microwave-to-optics transducers would then play a complementary role: bridging larger distance and connect cryogenic microwave LANs to the quantum internet [Kimble08].

Appendix A

External Coupling

Inspiring citation
— Someone influential

When designing the physical layout of a superconducting quantum chip, it is extremely important to relate physical parameters, such as inductances, capacitances and lengths of distributed elements, to Hamiltonian parameters. During my thesis, I could not find a reference which would present a large set of general formulae to calculate the external coupling rate of microwave resonators coupled to output lines. Instead, I had often to derive these formulae myself using methods introduced in [Pozar12]. In this chapter, I derive the formulae giving the frequency shift and the external coupling of lumped and distributed resonators, coupled capacitively or galvanically to an output line.

A.1 LC-Resonator

We start with the circuit shown in Fig. A.1 (a), of a LC resonator coupled with capacitance C_g to an output line of impedance Z_0 . The output line can be equivalently represented by a resistance Z_0 . The output admittance seen by the qubit is that of the coupling capacitor and the output resistance in series

$$\begin{aligned} Y_{\text{out}}(\omega) &= \frac{1}{Z_0 + \frac{1}{iC_g\omega}} \\ &= \frac{1}{Z_0} \frac{b^2 + ib}{1 + b^2} \end{aligned}$$

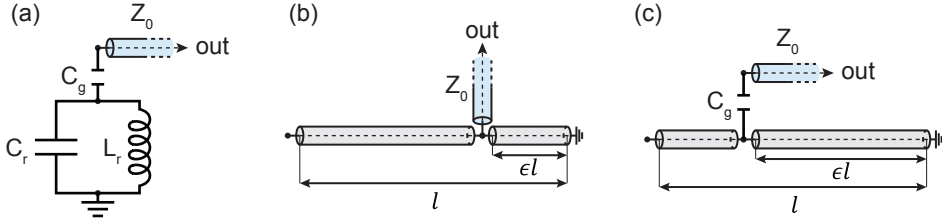


Figure A.1 Electrical circuit diagram of, (a) an LC-circuit capacitively coupled to an output port, (b) a $\lambda/4$ resonator galvanically coupled to an output port, and (c) a $\lambda/4$ resonator capacitively coupled to an output port. The output port transmission line is in blue.

where $b := C_g Z_0 \omega$. The admittance of the full circuit is

$$\begin{aligned}
 Y(\omega) &= iC\omega + \frac{1}{iL\omega} + \frac{1}{Z_0} \frac{ib}{1+b^2} + \frac{1}{Z_0} \frac{b^2}{1+b^2} \\
 &\simeq i \underbrace{(C + C_g)}_{C_\Sigma} \omega + \frac{1}{iL\omega} + \frac{1}{Z_0} b^2
 \end{aligned} \tag{A.1}$$

where we assumed $b \ll 1$ and expanded Y_{out} to first order in b to get to the second line. From standard microwave resonator theory [Poza12], we see that the admittance (A.1) corresponds to that of an LC-circuit with frequency $\omega_r = 1/\sqrt{LC_\Sigma}$, impedance $Z_r = \sqrt{L/C_\Sigma}$ and quality factor $Q = 1/Z_r \text{Im}[Y(\omega_q)]$. Therefore external coupling of the resonator is

$$\kappa_{\text{ext}} = \frac{\omega_r}{Q} \simeq Z_r \frac{b^2}{Z_0} \omega_r = C_g^2 Z_r Z_0 \omega_r^3. \tag{A.2}$$

A.2 CPW $\lambda/4$ resonator

We will now consider different cases of a $\lambda/4$ resonator coupled capacitively or galvanically to an output port. A convenient method to calculate the resonance frequency and the external quality factor of such an output-coupled distributed element circuit consists in computing the normalized input admittance $y_{\text{in}} = Z_0 Y_{\text{in}}$ or the normalized input impedance $z_{\text{in}} = Z_{\text{in}}/Z_0$ seen from the coupling port. For a lossless parallel(series)-LC-type resonance, the normalized input admittance (impedance) zeros at the resonance frequency ω_r . The quality factor is then given by

$$Q = \frac{1}{2i} \left. \frac{dx_{\text{in}}}{d\left(\frac{\omega}{\omega_r}\right)} \right|_{\omega=\omega_r}, \tag{A.3}$$

where x_{in} is either the admittance or the impedance [Pozar12].

The formulae below can be easily extended to the case of $\lambda/2$.

A.2.1 Galvanic coupling

Targeting low quality factors with a capacitive coupling scheme requires large C_g . In practice this regime can be difficult to reach without introducing parasitic effects due to the size of the capacitor, like stray inductance. As an alternative, one can couple a

Consider a $\lambda/4$ resonator of length l , impedance Z_0 , and phase velocity v_p , galvanically connected via a tee-junction to the output port. The tee-junction separates the $\lambda/4$ resonator into a shorted section of length ϵl and an open-ended section of length $(1 - \epsilon)l$ [see Fig. A.1 (b)]. Introducing the variable $\theta = \omega l/v_p$, it can be easily shown that the normalized input admittance

$$y_{\text{in}} = -i [\cot(\epsilon\theta) - \tan((1 - \epsilon)\theta)],$$

is zero when $\theta = \pi/2$. Therefore the presence of the coupler does not disturb the resonance frequency $\omega_r = \omega_0$. The derivative of the admittance at resonance is

$$\begin{aligned} \left. \frac{dy_{\text{in}}}{d\theta} \right|_{\theta=\pi/2} &= -i [-\epsilon(1 + \cot^2(\epsilon\theta)) - (1 - \epsilon)(1 + \tan^2((1 - \epsilon)\theta))] \\ &= i [\epsilon(1 + \cot^2(\epsilon\theta)) + (1 - \epsilon)(1 + \cot^2(\epsilon\theta))] \\ &= i (1 + \cot^2(\epsilon\theta)) \\ &= \frac{i}{\sin^2(\epsilon \frac{\pi}{2})}. \end{aligned}$$

Using Eq. (A.3), we obtain the external quality factor and corresponding coupling rate of the galvanic port

$$\begin{aligned} Q_{\text{ext}} &= \frac{\pi}{4 \sin^2(\epsilon \frac{\pi}{2})} \simeq \frac{1}{\pi \epsilon^2} \\ \kappa_{\text{ext}} &= \frac{4 \sin^2(\epsilon \frac{\pi}{2})}{\pi} \omega_0 \simeq \pi \epsilon^2 \omega_0 \end{aligned}$$

where the approximation is valid up to third order in ϵ .

A.2.2 Capacitive coupling

Let's consider a $\lambda/4$ resonator of length l , characteristic impedance Z_0 and propagation velocity v_p , capacitively coupled with capacitance C_g to the output. The coupling capacitor is located at a distance ϵl from the shorted end [Fig. A.1 (c)]. For simplicity, we first consider $\epsilon = 1$, *i.e.* the coupling capacitor is at the open end of the resonator.

Because the input capacitor acts as an impedance inverter, the circuit should behave as a series LC resonator near resonance [Pozar12]. The normalized input impedance seen from the output port is

$$z_{\text{in}} = \frac{Z_{\text{in}}}{Z_0} = \frac{1}{iZ_0C_g\omega} + i \tan\left(\frac{\omega l}{v_p}\right).$$

The calculation simplifies when introducing the variables $\theta = \omega l/v_p$ and $\eta = Z_0C_gv_p/l = C_g/C = C_g/2C_r$, where $C = c_x l$ is the total capacitance of the resonator, and C_r is the capacitance of the LC circuit equivalent to the uncoupled $\lambda/4$ resonator (Eq. (2.7)). The input impedance is then

$$z_{\text{in}} = -i \left(\frac{\cot \theta - \eta \theta}{\eta \theta \cot \theta} \right).$$

A resonance occurs at the angle θ_r such that $\cot \theta_r = \eta \theta_r$. Assuming that $\eta \ll 1$, or equivalently that $C_g \ll C$, we see that θ_r is close to, but slightly below $\pi/2$. Writing $\theta = \pi/2 + \delta\theta$ and expanding up to second order in $\delta\theta$, we obtain the resonance condition

$$\begin{aligned} z_{\text{in}} = 0 &\iff \cot \theta_r - \eta \theta_r = 0 \\ &\iff -\tan(\delta\theta_r) - \eta(\pi/2 + \delta\theta_r) = 0 \\ &\iff -\delta\theta_r - \eta(\pi/2 + \delta\theta_r) = 0 \\ &\iff \delta\theta_r = -\frac{\pi}{2} \frac{\eta}{1 + \eta} \\ &\iff \theta_r = \frac{\pi}{2} \frac{1}{1 + \eta} \\ &\iff \omega_r = \frac{\omega_0}{1 + \eta}, \end{aligned} \tag{A.4}$$

where $\omega_0 = \pi v_p/2l$ is the resonance frequency of the uncoupled $\lambda/4$ resonator.

To obtain the external quality factor associated with the coupling port, we use the

fact that $\cot \theta_r = \eta \theta_r$ at resonance and calculate

$$\left. \frac{dz_{\text{in}}}{d\theta} \right|_{\theta=\theta_r} = i \frac{1 + \eta + (\eta \theta_r)^2}{(\eta \theta_r)^2} \simeq \frac{i}{(\eta \theta_r)^2},$$

from which we get the external quality factor and corresponding output coupling rate

$$Q_{\text{ext}} = \frac{\pi}{(2\eta \theta_r)^2} = \frac{\pi}{4Z_0^2 \omega_r^2 C_g^2} \quad (\text{A.5})$$

$$\kappa_{\text{ext}} = \frac{\omega_r}{Q_{\text{ext}}} = C_g^2 \frac{4Z_0^2}{\pi} \omega_r^3 \quad (\text{A.6})$$

Interestingly, the same results can be obtained by first representing the uncoupled $\lambda/4$ resonator as it's equivalent parallel LC-circuit, then applying the method used in appendix A.1. The coupled circuit then reduces to that of Fig. A.1 (a), with $Z_r = 4Z_0/\pi$ [see Eq. (2.7)]. Using this in Eq. (A.2) we find that same output coupling rate as in Eq. (A.6). Also, we had seen that the resonance frequency is shifted by the coupling capacitor to

$$\begin{aligned} \omega_r &\simeq \frac{1}{\sqrt{L_r(C_r + C_g)}} \\ &= \frac{1}{\sqrt{L_r C_r}} \frac{1}{\sqrt{1 + C_g/C_r}} \\ &= \omega_0 \frac{1}{\sqrt{1 + 2\eta}} \\ &\simeq \frac{\omega_0}{1 + \eta} \end{aligned}$$

which is the result obtained in Eq. (A.4).

Combining the method used in appendix A.2.1 and this subsection, one can calculate the resonance frequency and the external coupling of the resonator for any $\epsilon \in [0, 1]$. However, the derivation is cumbersome and does not give new insight, so we skip it and directly give the formulae

$$\begin{aligned} \kappa_{\text{ext}} = \kappa_{\text{ext}} &\simeq \sin^2\left(\epsilon \frac{\pi}{2}\right) C_g^2 Z_r Z_0 \omega_r^3, \\ \omega_r &= \frac{\omega_0}{1 + \eta \sin^2\left(\epsilon \frac{\pi}{2}\right)}. \end{aligned}$$

A.3 Practical considerations for capacitive external coupling

In practice, to estimate the coupling capacitance, one performs a capacitance matrix simulation on a finite section of length ϵl at the coupled end of the resonator to obtain the coupling capacitance C_g , and a shunt capacitance to ground $C_{\text{gnd}} = \epsilon C + C_0$, which can be divided in a contribution C_0 from the coupler, and a contribution ϵl from the core of the transmission line. This end section is therefore treated as lumped element, and its distributed inductance is neglected. To estimate the error which is made with this approximation, we shall look at how the resonance frequency varies with the fraction ϵ of the transmission line which is considered as a lumped element.

Defining $\omega'_0 = \omega_0/(1-\epsilon)$ as the resonance frequency of the $(1-\epsilon)l$ long, uncoupled $\lambda/4$ resonator, and $\eta' = (C_g + C_0 + \epsilon C)/(1-\epsilon)C$, the reasoning used in Eq. (A.4) leads to

$$\begin{aligned}
 \omega'_r &= \omega'_0 \frac{1}{(1 + \eta')} \\
 &= \frac{\omega_0}{1 - \epsilon} \frac{1}{1 + \frac{\eta + \epsilon}{1 - \epsilon}} \\
 &= \frac{\omega_0}{1 - \epsilon} \frac{1 - \epsilon}{1 - \epsilon + \eta + \epsilon} \\
 &= \frac{\omega_0}{1 + \eta} \\
 &= \omega_r,
 \end{aligned} \tag{A.7}$$

where we defined $\eta = \eta'(\epsilon = 0) = (C_g + C_0)/C$. Because the equations used to derive Eq. (A.7) make use of a second order expansion in η and $\eta' \simeq \eta + \epsilon$, the error in estimating the resonance frequency with Eq. (A.4) is bounded as $O((\epsilon + \eta)^3)$. For realistic values of $\epsilon, \eta < 5\%$, the error is on the level of hundred parts per millions, corresponding to sub-MHz precision for a 5 GHz resonator.

A corollary is that, the imaginary line dividing the distributed part of a resonator, and the lumped-element part close to its coupling capacitor can be chosen arbitrarily, as long as $\epsilon \ll 1$. This result is useful to estimate the coupling rates and frequency of a capacitively coupled resonator from a physical layout.

Appendix B

Photon shaping

Inspiring citation
— Someone influential

B.1 Emitting photons of arbitrary shapes

We consider a two-level system with eigenstates $|0\rangle$ and $|1\rangle$ driven with detuning δ at a time-dependent complex rate $\tilde{g} e^{-i\phi}$. We also consider that population leaks from state $|1\rangle$ to a dark state $|D\rangle$, by the emission of a propagating photon at a constant rate κ . States $|0\rangle$, $|1\rangle$ and $|D\rangle$ would correspond to states $|f0\rangle$, $|g1\rangle$ and $|g0\rangle$ in the photon shaping scheme described in Sec. 2.1.8, and the drive term is induced by the second order f0-g1 transition described in Sec. 2.1.7.

This system can be solved using a wavefunction framework by considering the manifold spanned by $|0\rangle$ and $|1\rangle$ and describing loss outside of this manifold with a non-Hermitian term. In a frame rotating at the drive carrier frequency, the non-Hermitian Hamiltonian is

$$H/\hbar = (\delta - i\kappa/2)|1\rangle\langle 1| + \tilde{g} e^{-i\phi} |1\rangle\langle 0| + \tilde{g} e^{+i\phi} |1\rangle\langle 0| \quad (\text{B.1})$$

Let $|\psi\rangle$ be the wavefunction obeying Hamiltonian (B.1). The photon emitted in the process will have a real envelope

$$f(t) = \sqrt{\kappa} \langle 1|\psi\rangle, \quad (\text{B.2})$$

and a carrier frequency detuned by δ from the $|1\rangle \rightarrow |D\rangle$ transition. Our goal is to determine what shall the drive amplitude \tilde{g} and phase ϕ be to emit a photon of target shape f and carrier frequency detuning δ , when the system is initialized in state $|\psi\rangle_{t=-\infty} = |0\rangle$.

Due to the non-Hermiticity of Hamiltonian (B.1), the norm of the wavefunction decays as

$$\partial_t \langle \psi | \psi \rangle = -\kappa \langle 1 | \psi \rangle^2 = -f^2(t),$$

which we integrate to obtain

$$\langle \psi | \psi \rangle (t) = 1 - \int_{-\infty}^t f^2(t) dt = 1 - F_2. \quad (\text{B.3})$$

Here, $F_2(t)$ is the primitive of the photon power $f^2(t)$. It corresponds to the fraction of a photon which has been emitted at time t . To solve the problem, we introduce the normalized wavefunction

$$|\bar{\psi}\rangle := \frac{|\psi\rangle}{\sqrt{\langle \psi | \psi \rangle}} := e^{-i\alpha} \cos\left(\frac{\theta}{2}\right) |0\rangle + \sin\left(\frac{\theta}{2}\right) |1\rangle,$$

which can be written as a function of the mixing angle $\theta(t)$ and the state phase α .

Using Eqs. (B.2) and (B.3), we obtain the following simple relations between the photon shape and θ

$$\sin\left(\frac{\theta}{2}\right) = \langle 1 | \bar{\psi} \rangle = \frac{f}{\sqrt{\kappa(1-F_2)}}, \quad (\text{B.4})$$

$$\cos\left(\frac{\theta}{2}\right) = \sqrt{1 - \sin^2\left(\frac{\theta}{2}\right)} = \sqrt{\frac{\kappa(1-F_2) - f^2}{\kappa(1-F_2)}}, \quad (\text{B.5})$$

$$\tan\left(\frac{\theta}{2}\right) = \frac{\sin(\theta/2)}{\cos(\theta/2)} = \frac{f}{\sqrt{\kappa(1-F_2) - f^2}}. \quad (\text{B.6})$$

Now, let's express the time derivative of $|\bar{\psi}\rangle$ with respect to α and θ :

$$|\dot{\bar{\psi}}\rangle = e^{i\alpha} \left[i\dot{\alpha} \cos\left(\frac{\theta}{2}\right) - \frac{\dot{\theta}}{2} \sin\left(\frac{\theta}{2}\right) \right] |0\rangle + \frac{\dot{\theta}}{2} \cos\left(\frac{\theta}{2}\right) |1\rangle \quad (\text{B.7})$$

Using the Schrödinger equation $i\hbar|\dot{\bar{\psi}}\rangle = H|\bar{\psi}\rangle$, we can also express $|\dot{\bar{\psi}}\rangle$ as a

function of the Hamiltonian parameters

$$\begin{aligned}
 |\dot{\psi}\rangle &= -i \left[H/\hbar + i \frac{\kappa}{2} \sin^2 \left(\frac{\theta}{2} \right) \right] |\bar{\psi}\rangle \\
 &= \left[-i \tilde{g} e^{-i\phi} \sin \left(\frac{\theta}{2} \right) + \frac{\kappa}{2} \cos \left(\frac{\theta}{2} \right) \sin^2 \left(\frac{\theta}{2} \right) e^{i\alpha} \right] |0\rangle \\
 &\quad + \left[-i \tilde{g} e^{i(\phi+\alpha)} \cos \left(\frac{\theta}{2} \right) + \frac{\kappa}{2} \sin^3 - i \left(\delta - i \frac{\kappa}{2} \right) \sin \left(\frac{\theta}{2} \right) \right] |1\rangle.
 \end{aligned} \tag{B.8}$$

Identifying the real and imaginary parts of the eigenstate coefficients of $|\dot{\psi}\rangle$ given by Eqs. (B.7) and (B.8), we obtain the system of equations

$$\dot{\alpha} = -g \tan \left(\frac{\theta}{2} \right) \cos(\phi - \alpha), \tag{B.9}$$

$$\tilde{g} \cos(\phi - \alpha) = -\delta \tan \left(\frac{\theta}{2} \right), \tag{B.10}$$

$$\tilde{g} \sin(\phi - \alpha) = -\frac{1}{2} \left[\dot{\theta} + \kappa \sin \left(\frac{\theta}{2} \right) \cos \left(\frac{\theta}{2} \right) \right]. \tag{B.11}$$

Inverting the relation $\partial_t [\sin(\theta/2)] = \dot{\theta} \cos(\theta/2)/2$, whose left-hand-side can be calculated from Eq. (B.4), we obtain

$$\dot{\theta} = \frac{1}{\sqrt{\kappa(1-F_2)-f^2}} \left(2\dot{f} + \frac{f^3}{1-F_2} \right).$$

Inserting this result in Eq. (B.11), we compute (B.10)²+(B.11)² to obtain the the drive amplitude as a function of time

$$\tilde{g} = \sqrt{\frac{(\dot{f} + \frac{\kappa}{2}f)^2 + (\delta f)^2}{\sqrt{\kappa(1-F_2)-f^2}}}. \tag{B.12}$$

Inserting Eq. (B.12) in Eq. (B.10) leads, after a lengthy calculation which we skip for conciseness, to an analytical expression of the instantaneous drive frequency offset

$$\dot{\phi} = \frac{\delta}{\kappa(1-F_2)-f^2} \left(f^2 + \frac{f\ddot{f}-\dot{f}^2}{\tilde{g}^2} \right). \tag{B.13}$$

Note, that the instantaneous frequency is constant ($\dot{\phi} = 0$) when $\delta = 0$.

Equations (B.12) and (B.13) constitute the main result of this section. They give the drive amplitude and phase required to emit a photon with arbitrary real envelope

and detuning from the emitter mode, under the constraint that \tilde{g} does not diverge. This condition is valid as long as the denominator of the right-hand-side of Eq. (B.12) is not 0, or equivalently $\kappa(1 - F_2) = \kappa \langle \psi | \psi \rangle \geq f^2$. In words, the emitted power f^2 cannot be larger than the emission rate κ times the population $\langle \psi | \psi \rangle$ left in the manifold.

This result is also valid for a time-dependent photon detuning $\delta(t)$ as long as δ/\tilde{g} varies slowly compared to the transition frequencies of the system. To extend this result to photons with fast frequency chirps, one would need to repeat the demonstration allowing the envelope f to take complex values, and encode the target frequency chirp in the argument of f .

B.2 Optimal photon shape

During the photon emission and absorption pulse, the qubit is subject to decoherence. The resulting errors can be reduced by minimizing the emission time. In the following, we will present some considerations to optimize the photon emission rate.

First, what is the shortest photon shape which one can emit? The mathematical phrasing of this question takes the form of the following constrained optimization: one needs to find a photon shape f of unit norm $\int f^2 dt = 1$, such that at any time t , the emitted photon fraction $F_2(t)$ is larger than for any other shape, under the physicality constraint $\kappa(1 - F_2) \geq f^2$. To have a well-posed problem, we restrict it to shapes which are zero at negative times: *i.e.* the emission starts at $t = 0$ at earliest.

A simple way to maximize F_2 is to maximize its derivative, the photon power f^2 . Which leads to the equation $f^2 = \kappa(1 - F_2)$, which can be written as $F_2' = \kappa(1 - F_2)$. This equation accepts a simple exponential solution of the form $F_2 = 1 - e^{-\kappa t}$, with the exponential photon amplitude $f_{\text{fastest}} = \sqrt{\kappa} e^{-\kappa t/2}$. The shortest photon shape which can be emitted is a single-sided decaying exponential with rate κ limited by the emission coupling rate. Such a photon can be emitted by applying an instantaneous π pulse mapping state $|0\rangle$ to $|1\rangle$, and let the state decay to $|D\rangle$ at a rate $|D\rangle$.

However, the time-reversed of this photon shape clearly violates the emissibility constraint $\kappa(1 - F_2) \geq f^2$. Therefore, such a photon shape cannot be absorbed with unit fidelity. To enable perfect absorption, the rising edge of the photon should not increase with a rate higher than κ . The shortest photon shape which can be both emitted and absorbed is therefore a double-sided exponential of the form (symmetrized around $t = 0$)

$$f^2 = \frac{\kappa}{2} e^{-\kappa|t|}.$$

Note that this shape has an infinite support. This means that perfect photon transfer in finite time is impossible. In practice, the photon shape must be truncated. Thanks to the exponential shape of the photons truncation errors tend exponentially towards zero with the truncation interval. So near-perfect photon transfer can be achieved in a finite transfer time of several $1/\kappa$.

If nodes A and B have different emission rates $\kappa_A \neq \kappa_B$, the optimal shape is an asymmetric double-sided exponential

$$f^2 = \mathcal{N}(\Theta(t)e^{-\kappa_A t} + \Theta(-t)e^{-\kappa_B t}), \quad (\text{B.14})$$

with Θ the Heavyside function and \mathcal{N} a normalization constant.

These double-sided exponential shapes lead to a divergence of the required drive rate \tilde{g} at time $t = 0$, where the derivative of the photon power f^2 suddenly changes. Photon with such shapes can be transferred in theory, but not in practice. To avoid this divergence, we shall emit photons with a smooth shape. A near-optimal photon shape is given by

$$f = \frac{\mathcal{N}}{e^{\kappa_A t/2} + e^{-\kappa_B t/2}}. \quad (\text{B.15})$$

Indeed, it is asymptotically equal to shape (B.14), and tends exponentially towards this asymptotic curve away from $t = 0$. In the symmetric case where $\kappa_A = \kappa_B = \kappa$, this shape becomes

$$f = \frac{\sqrt{\kappa}}{2} \text{sech}(-\kappa t/2). \quad (\text{B.16})$$

This is why, in this thesis, we emit photon shapes of the form $\Gamma \text{sech}(-\kappa t/2)/2$, with the physicality constraint $\Gamma \leq \kappa$. In any case, the maximum emission rate is physically limited by κ .

Both shapes symmetric and asymmetric sech shapes lead to analytical solutions of the drive rate \tilde{g} using Eq. (B.12). In the simple case $\delta = 0$ and $\Gamma \text{sech}(-\kappa t/2)/2$ with $\Gamma \leq \kappa$, the drive rate obtained from Eq. (B.12) is real and takes the form [Kurpiers18, Pechal16a, Kurpiers19a]

B.3 Design considerations

We have seen that the photon bandwidth Γ is ultimately limited by the external coupling rate κ . However, if κ is much larger than the maximum drive rate \tilde{g}_{max} the that can experimentally be applied, then drive power will limit the maximum photon bandwidth. In this section, we discuss how to choose κ to maximize the photon bandwidth Γ , taking

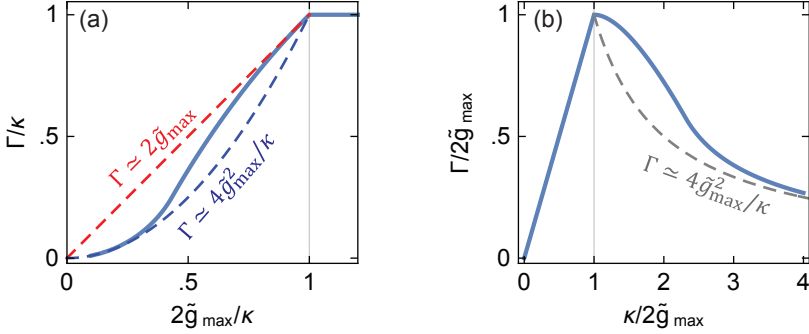


Figure B.1 (a) Photon bandwidth vs drive amplitude, both normalized by the external coupling rate. The blue and red dashed lines are asymptotes at $2\tilde{g}_{\max} \lesssim \kappa$ and $2\tilde{g}_{\max} \ll \kappa$, respectively. (b) Photon bandwidth vs external coupling rate, both normalized by the maximum drive amplitude $2\tilde{g}_{\max}$. The gray dashed line is an asymptote for $\kappa \gg 2\tilde{g}_{\max}$

into account this drive power limitation.

We restrict ourselves to the simple case where $\delta = 0$ and $\Gamma \operatorname{sech}(-\kappa t/2)/2$ with $\Gamma \leq \kappa$. Using Eq. (B.12), we find that the drive rate to obtain this photon shape is real and takes the form [Kurpiers18, Pechal16a, Kurpiers19a]

$$\tilde{g} = \frac{\Gamma}{4} \operatorname{sech}\left(\frac{\Gamma t}{2}\right) \frac{(1 - e^{\Gamma t}) + \frac{\kappa}{\Gamma}(1 + e^{\Gamma t})}{\sqrt{\frac{\kappa}{\Gamma}(1 + e^{\Gamma t}) - e^{\Gamma t}}}.$$

For photons with maximal bandwidth $\Gamma = \kappa$, the drive amplitude simplifies further to

$$\tilde{g} = \frac{\Gamma}{4} \operatorname{sech}\left(\frac{\Gamma t}{2}\right).$$

From this last equation, it is obvious that the maximum drive amplitude needed to emit this shape is $2\tilde{g} = \Gamma = \kappa$. If $2\tilde{g}_{\max} = \kappa$, then the photon bandwidth is limited by the external coupling and $\Gamma = \kappa$. Otherwise, if the maximum drive amplitude is smaller than external coupling rate, we have $\Gamma < 2\tilde{g}_{\max} < \kappa$: the photon transfer speed is limited by drive power [Fig. B.1 (a)]. In this drive-power limited regime, we distinguish to asymptotic cases: if $2\tilde{g} \sim \kappa$ then $\Gamma \sim 2\tilde{g}_{\max}$, else if $2\tilde{g}_{\max} \ll \kappa$, then $\Gamma \sim 4\tilde{g}_{\max}^2/\kappa \ll 2\tilde{g}_{\max}$ [see dashed lines in Fig. B.1 (a)].

In practice, to chose design parameters which maximize the photon bandwidth, one should first seek to maximize the available drive amplitude \tilde{g}_{\max} . Taking the exmple of the f0-g1 transition, we have seen in Sec. 2.1.7 that the f0-g1 drive rate

is [Zeytinoğlu15, Pechal16a]

$$\tilde{g} = \Omega \frac{g\alpha}{\sqrt{2}\Delta(\Delta + \alpha)},$$

where α is the transmon anharmonicity, $\Delta = \omega_q - \omega_r$ is the detuning between the qubit and resonator frequencies, and Ω is the qubit drive rate. To maximize \tilde{g}_{\max} , one should therefore maximize α , g/Δ and Ω/Δ , under the typical circuit QED design constraints, like staying in the transmon regime ($\alpha \ll \omega_q$), staying in the dispersive regime ($g \ll \Delta$), staying in the adiabatic Raman regime ($\Omega \ll \Delta$) and limiting Purcell decay.

Once the target parameters maximize \tilde{g}_{\max} , one should find the optimal κ given this value of \tilde{g}_{\max} . For a fixed \tilde{g}_{\max} , if $\kappa < 2\tilde{g}_{\max}$, then the photon transfer speed is limited by the external coupling and $\Gamma = \kappa$ [Fig. B.1 (b)]. For $\kappa \geq 2\tilde{g}_{\max}$, the photon bandwidth is power limited. For $\kappa \gtrsim 2\tilde{g}_{\max}$, the photon bandwidth is close to its maximum value \tilde{g}_{\max} , but if κ is much larger than $2\tilde{g}_{\max}$ then the photon bandwidth tends towards $4\tilde{g}_{\max}^2/\kappa \ll 2\tilde{g}_{\max}$ [see dashed line in Fig. B.1 (b)]. To maximize the photon bandwidth, one should therefore target a value $\kappa \gtrsim 2\tilde{g}_{\max}$.

in a matrix form

$$\dot{\vec{\alpha}} = -i(\mathcal{H} \cdot \vec{\alpha} + \mathcal{D}), \quad (\text{C.1})$$

with $\vec{\alpha} = (\alpha_1, \dots, \alpha_m)$ the vector of field amplitudes, \mathcal{D} the vector of drive rates and \mathcal{H} the classical, non-Hermitian Hamiltonian of the resonator system. Equation (C.1) can account for more complex loss channels in the non-Hermitian Hamiltonian and multiple-port simultaneous drive. Assuming that the resonators are initially in their vacuum state ($\vec{\alpha} = 0$) and that the drive is constant, the solution to Eq. (C.1) takes the general form

$$\begin{aligned} \vec{\alpha}(t) &= -(\mathbb{1} - e^{-i\mathcal{H}t}) \cdot \vec{\alpha}_{+\infty} \\ &= -(\mathbb{1} - P e^{-iD(\Lambda)t} P^{-1}) \cdot \vec{\alpha}_{+\infty} \\ &= -(\mathbb{1} - P D(e^{-i\Lambda t}) P^{-1}) \vec{\alpha}_{+\infty}, \end{aligned}$$

where $\Lambda = (\lambda_1, \dots, \lambda_m)$ is the vector of eigenvalues of \mathcal{H} , P is the matrix form of the eigenvectors of \mathcal{H} , $D(\vec{x})$ is a diagonal matrix filled with the elements of \vec{x} , and $\vec{\alpha}_{+\infty} = -\mathcal{H}\mathcal{D}$ is the field amplitudes in steady-state. The field amplitude of each resonator can thus be written as a simple sum of exponentially decaying terms

$$\begin{aligned} \alpha_i(t) &= \alpha_{i,+\infty} - \sum_{j=1}^m A_{i,j} e^{-i\lambda_j t} \\ &= -\sum_{j=0}^m A_{i,j} e^{-i\lambda_j t}, \end{aligned} \quad (\text{C.2})$$

where the coefficients $A_{i,j} = P_{i,j}(P^{-1} \cdot \vec{\alpha}_{+\infty})_j$, sum up to $\alpha_{i,+\infty}$, and where we introduced the notations $A_{i,0} = -\alpha_{i,+\infty}$ and $\lambda_0 = 0$ for convenience. The SNR can then

take the analytical form

$$\begin{aligned}
\text{SNR}(\tau) &= 2\kappa \int_0^\tau |\alpha_1^+ - \alpha_1^-|^2 dt \\
&= 2\kappa \int_0^\tau \left| \sum_{j=0}^m (A_{i,m}^+ e^{-i\lambda_j^+ t} - A_{i,m}^- e^{-i\lambda_j^- t}) \right|^2 dt \\
&= 2\kappa \int_0^\tau \left| B_0 + \sum_{j=1}^{2m} B_j e^{-i\lambda_j t} \right|^2 dt \\
&= 2\kappa \int_0^\tau \left[|B_0|^2 + \sum_{\substack{j,k=0 \\ \{j,k\} \neq \{0,0\}}}^{2m} B_j B_k^* e^{-i(\lambda_j - \lambda_k^*)t} \right] dt,
\end{aligned} \tag{C.3}$$

where we introduced the notations $B_0 = A_{0,m}^+ - A_{0,m}^-$, $B_j = A_{j,m}^+$, $B_{j+m} = -A_{j,m}^-$, $\lambda_j = \lambda_j^+$ and $\lambda_{j+m} = \lambda_j^-$. The integrand can then be resolved, yielding

$$\text{SNR}(\tau) = 2\kappa \left[|B_0|^2 \tau + \sum_{\substack{j,k=0 \\ \{j,k\} \neq \{0,0\}}}^{2m} \frac{B_j^* B_k}{i(\lambda_j - \lambda_k^*)} (1 - e^{-i(\lambda_j - \lambda_k^*)\tau}) \right] \tag{C.4}$$

In this last step, we have assumed that all bare modes have a coupling path to the output mode m , which leads to all the eigenvalues λ_j having a strictly negative imaginary part, and thus $\lambda_j - \lambda_k \neq 0$ when $j \neq 0$ and $k \neq 0$. This assumption can be done without loss of generality because modes which do not have a coupling path to the output can be omitted from the Hamiltonian.

To calculate the SNR as a function of time for an optimal drive frequency, we made a program which goes through the following steps:

1. Set the drive frequency such that $n_g = |\alpha_{1,g,+ \infty}|^2 = |\alpha_{1,e,+ \infty}|^2 = n_e$.
2. Diagonalize the non-Hermitian Hamiltonians for each qubit state: find P_\pm and Λ^\pm such that $\mathcal{H} = P_\pm D(\Lambda^\pm) P_\pm^{-1}$.
3. Compute the coefficients $A_{j,m}^\pm$ [Eq. (C.2)], then the coefficients B_j [Eq. (C.3)].
4. Compute Eq. (C.4).

We performed two sanity checks on the protocol described above and its implementation as a Mathematica function. First we verified that it leads to Eq. (3.10) for

a single resonator. Second, as discussed in Sec. 3.3, we verified that the SNR for a resonator coupled to a Purcell filter in the adiabatic elimination regime is the same as that of the corresponding single, effective resonator.

Appendix D

Derivation of Reset Operating Regimes

Inspiring citation
— Someone influential

The discussion about the reset operating regimes in Sec. 5.4 is based on Eq. (5.4). To derive this equation, we start with the expression for the population

$$P_{s|s_0}^H(t) = |\langle s | e^{-iHt} |s_0\rangle|^2,$$

of state $|s\rangle \in \{|e, 0\rangle, |f, 0\rangle, |g, 1\rangle\}$, where s_0 is the initial state. We introduce the diagonalization matrix

$$T = \sum_k |\lambda_k\rangle \langle k|,$$

where $|\lambda_k\rangle$ are the eigenvectors of H and the vectors $|k\rangle$ form an orthonormal basis in which $D = T^{-1} \cdot H \cdot T$ is diagonal. Note that, since H is non-Hermitian, its eigenvectors $|\lambda_k\rangle$ are not orthogonal and T is not unitary. We then obtain

$$\begin{aligned} P_{s|s_0}^H(t) &= |\langle s | T e^{-iDt} T^{-1} |s_0\rangle|^2 \\ &= \left| \sum_{jklm} \langle s | T_{jk} |j\rangle \langle k | e^{-iDt} T_{lm}^{-1} |l\rangle \langle m | s_0 \right|^2 \\ &= \left| \sum_k \langle s | \left(\sum_{jm} T_{jk} T_{km}^{-1} |j\rangle \langle m| \right) |s_0\rangle e^{-i\lambda_k t} \right|^2. \end{aligned}$$

We recover Eq. (5.4) by defining

$$\hat{A}_k = \sum_{jm} T_{jk} T_{km}^{-1} |j\rangle \langle m|.$$

As discussed in the main text, we can define operating regimes of the reset by studying the eigenvalues λ_k of Hamiltonian (5.1). We set $\delta_{\text{ef}} = \delta_{\text{f0g1}} = 0$, both to simplify the analysis and to ensure that the full three-level transmon is reset. To reduce the notations, we tackle an equivalent problem and solve for the eigenvalues $\Lambda_k = i2\lambda_k/\kappa$ of the renormalized Hamiltonian

$$\tilde{H} = \begin{bmatrix} 0 & \sqrt{\Omega} & 0 \\ -\sqrt{\Omega} & 0 & \sqrt{G} \\ 0 & -\sqrt{G} & -1 \end{bmatrix}, \quad (\text{D.1})$$

where the dimensionless drive powers $\Omega = (2\Omega_{\text{ef}}/\kappa)^2$ and $G = (2\tilde{g}/\kappa)^2$ are real and positive. Hamiltonian (D.1) has the characteristic polynomial

$$P_{\tilde{H}}(X) = X^3 + X^2 + (G + \Omega)X + \Omega,$$

whose roots are the eigenvalues Λ_k . The discriminants of this cubic equation are

$$\Delta_0 = 1 - 3(G + \Omega), \quad (\text{D.2})$$

$$\Delta_1 = 2 - 9(G - 2\Omega). \quad (\text{D.3})$$

Note that Δ_0 is a linear function of $G + \Omega$, so $(-\Delta_0)$ indicates the amount of total drive power. Conversely, Δ_1 indicates the level of asymmetry between the power of the two drives. Defining the sub-roots

$$C^\pm = \sqrt[3]{\frac{\Delta_1 \pm \sqrt{\Delta_1^2 - 4\Delta_0^3}}{2}},$$

we find the expression for the eigenvalues

$$\Lambda_k = -\frac{1}{3} \left(1 + \xi^k C^+ + \xi^{-k} C^- \right), \quad (\text{D.4})$$

where $k \in \{-1, 0, 1\}$, and $\xi^k = \exp[i2\pi k/3]$ are the cubic roots of unity. A consequence of Eq. (D.4) is that the reset rate is bounded by $\Gamma/\kappa \equiv \min |\text{Re}(\Lambda_k)| \leq 1/3$. We

can distinguish three cases based on the sign of $\Delta_1^2 - 4\Delta_0^3$.

Under-damped regime: $\Delta_1^2 > 4\Delta_0^3$. In this case, the sub-roots C^+ and C^- are real and distinct from each other. Therefore, the eigenvalues Λ_k are complex, with a non-zero imaginary part: the populations display oscillations during the reset. Depending on the sign of Δ_1 , we have

$$\Gamma/\kappa = \begin{cases} \frac{1}{3} \left[1 - \frac{1}{2} (C^+ + C^-) \right] < \frac{1}{3} & , \text{ if } \Delta_1 > 0 \\ \frac{1}{3} \left[1 + (C^+ + C^-) \right] < \frac{1}{3} & , \text{ if } \Delta_1 < 0 \\ \frac{1}{3} & , \text{ if } \Delta_1 = 0. \end{cases} \quad (\text{D.5})$$

The reset rate is thus maximized ($\Gamma = \kappa/3$) only when the drives are strong enough ($\Delta_0 \leq 0$) and well balanced ($\Delta_1 = 0$). The conditions $\Delta_0 \leq 0$ and $\Delta_1 = 0$ define the optimal branch (solid red line in Fig. 3a).

Over-damped regime: $\Delta_1^2 < 4\Delta_0^3$. In this low power regime (Δ_0 has to be positive), C^+ and C^- are complex conjugates of each other. As a result, all eigenvalues Λ_k are purely real and the qutrit populations show no oscillatory features during the reset. In this regime, the reset rate can be expressed as

$$\Gamma/\kappa = \frac{1}{3} \left[1 - \sqrt{\Delta_0} \left(\cos \frac{\theta}{3} + \sqrt{3} \sin \frac{\theta}{3} \right) \right],$$

where $\theta = \arccos(\Delta_1/2\Delta_0^{3/2})$ is the argument of $(C^+)^3$, and ranges from 0 to π . Because $\Delta_0 > 0$, we have the strict inequality $\Gamma < \kappa/3$, which means that the optimal branch does not cross the over-damped region.

Critical-damping: $\Delta_1^2 = 4\Delta_0^3$. When this equality holds, we have $C^+ = C^- = \sqrt[3]{\Delta_1/2} = \sqrt{\Delta_0}$, and the eigenvalues are real. We parametrize the critical damping equality by introducing the variable $\beta = \sqrt[3]{\Delta_1/2}$. We then have $\Delta_0 = \beta^2$ and $C^\pm = \beta$, which leads to

$$\Gamma/\kappa = \begin{cases} \frac{1}{3} (1 - \beta) & , \text{ if } \beta \geq 0 \\ \frac{1}{3} (1 + 2\beta) & , \text{ otherwise.} \end{cases}$$

Inverting Eqs. (D.2) and (D.3) we obtain a parametrization of the critical damping boundary region

$$G(\beta) = \frac{8}{27} \left(1 - \frac{3}{4} \beta^2 - \frac{1}{4} \beta^3 \right),$$

$$\Omega(\beta) = \frac{1}{27} (1 - 3\beta^2 + 2\beta^3),$$

where β ranges from $-1/2$ to 1 , to keep Γ , G and Ω positive.

For $\beta = 0$, we have $\Gamma = \kappa/3$. This point is an exceptional point, where all eigenvalues are identical [Eq. (D.4) with $C^\pm = 0$] and the eigenvectors coalesce [Heiss04]. This point ($G = 8/27$ and $\Omega = 1/27$, or equivalently, $\tilde{g} = \tilde{g}_{\text{ep}} = \sqrt{2/27}\kappa$ and $\Omega_{\text{ef}} = \Omega_{\text{ef,ep}} = \sqrt{1/108}\kappa$) is the only one that maximizes Γ without displaying oscillatory features of the populations.

For a given value of G , there is a unique Ω^{opt} that maximizes the reset rate to $\Gamma_{\text{max}}(G)$. For $G \geq 8/27$, according to Eq. (D.5), the reset rate is maximized by choosing Ω such that $\Delta_1 = 0$. Using Eq. (D.3), we find that $\Omega_{\text{opt}}(G) = G/2 - 1/9$. The parameters are then on the optimal branch and $\Gamma_{\text{max}}(G) = \kappa/3$. For $G < 8/27$, the reset rate is maximized by choosing Ω such that $\Delta_1^2 = 4\Delta_0^3$ (critical damping) and $\Delta_1 > 0$ (upper branch). This can be proven by showing that $\partial_\Omega \Gamma \geq 0$ in the over-damped region, and that $\partial_\Omega \Gamma$ and Δ_1 have opposite signs in the under-damped region. Using these results, we obtain

$$\Gamma_{\text{max}}(G) = \frac{2}{3} \left[1 - \cos \left(\frac{1}{3} \arccos \left(1 - \frac{27G}{4} \right) \right) \right].$$

The derivative of Γ_{max} diverges as $G \rightarrow 8/27$ from the left side (Fig. 3b). If one cannot drive the f0-g1 transition with enough power to get $G > 8/27$, or equivalently $\tilde{g} > \sqrt{2/27}\kappa$, Γ_{max} is abruptly reduced. To obtain a fast reset, one should therefore target a value of κ that is as high as possible within the limit that $\kappa < \tilde{g}_{\text{max}} \sqrt{27/2} \simeq 3.67 \tilde{g}_{\text{max}}$, where \tilde{g}_{max} is the maximum f0-g1 drive rate experimentally achievable, without driving unwanted transitions [Zeytinoglu15]. This ensures that the maximum reset rate $\Gamma = \kappa/3$ is high and always attainable.

Appendix E

Master Equation Simulations

Inspiring citation
— Someone influential

E.1 Reset

To model the transmon qutrit reset process numerically, we model the transmon qubit as an anharmonic oscillator with annihilation (creation) operator \hat{b} (\hat{b}^\dagger) [Koch07], which we truncate at the second excited state $|f\rangle$ and denote the annihilation and creation operators of the reset resonator \hat{a} and \hat{a}^\dagger , respectively. Setting $\hbar = 1$, the driven Jaynes-Cummings Hamiltonian is given by

$$\begin{aligned} \hat{H} = & \omega_r \hat{a}^\dagger \hat{a} + \omega_{ge} \hat{b}^\dagger \hat{b} + \Omega(t)(\hat{b} + \hat{b}^\dagger) \\ & + g_r(\hat{a}^\dagger \hat{b} + \hat{a} \hat{b}^\dagger) - \frac{E_C}{2} \hat{b}^\dagger \hat{b}^\dagger \hat{b} \hat{b}, \end{aligned} \tag{E.1}$$

where g_r denotes the coupling between the transmon and the reset resonator, E_C the charging energy of the transmon qubit and $\Omega(t) = \Omega \cos[\omega_d^i t + \varphi^i(t)]$ is the amplitude of the microwave drive inducing the desired coupling $\tilde{g}(t)$. Since the readout resonator does not play a role in the reset dynamics, it is omitted from the Hamiltonian and the static Lamb shift it induces is implicitly included in the parameters.

In order to make the effective coupling $\tilde{g}(t)$ between the $|f, 0\rangle$ and $|g, 1\rangle$ states apparent and to simplify the simulations, we perform a series of unitary transformations on Equation (E.1). We first move to a frame rotating at the drive frequency ω_d , and then perform a displacement transformation $\hat{b} \rightarrow \hat{b} - \beta, \hat{a} \rightarrow \hat{a} - \gamma$ and choose β, γ

such that the amplitude of the linear drive terms is set to zero. Next, we perform a Bogoliubov transformation $\hat{b} \rightarrow \cos(\Lambda)\hat{b} - \sin(\Lambda)\hat{a}$, $\hat{a} \rightarrow \cos(\Lambda)\hat{a} + \sin(\Lambda)\hat{b}$, where $\tan(2\Lambda) = -2g_r/(\omega_r - \omega_{ge} + 2E_C|\beta|)$ and, neglecting small off-resonant terms, obtain the resulting effective Hamiltonian

$$\begin{aligned} \hat{H}_{\tilde{g}} = & \Delta_r \hat{a}^\dagger \hat{a} + \Delta_{ge} \hat{b}^\dagger \hat{b} + \frac{\alpha}{2} \hat{b}^\dagger \hat{b}^\dagger \hat{b} \hat{b} + \frac{K}{2} \hat{a}^\dagger \hat{a}^\dagger \hat{a} \hat{a} \\ & + 2\chi_r \hat{a}^\dagger \hat{a} \hat{b}^\dagger \hat{b} + \frac{1}{\sqrt{2}} (\tilde{g} \hat{b}^\dagger \hat{b}^\dagger \hat{a} + \tilde{g}^* \hat{a}^\dagger \hat{b} \hat{b}), \end{aligned} \quad (\text{E.2})$$

where $\alpha = -E_C \cos^4 \Lambda$ is the transmon anharmonicity, $K = -E_C \sin^4 \Lambda$ is the qubit-induced resonator anharmonicity, $\chi_r = -E_C \cos^2 \Lambda \sin^2 \Lambda$ is the dispersive shift, $\Delta_r = \omega_r \cos^2 \Lambda + (\omega_{ge} - 2E_C|\beta|^2) \sin^2 \Lambda - g_r \sin 2\Lambda - \omega_d$ is the resonator-drive detuning and $\Delta_{ge} = (\omega_{ge} - 2E_C|\beta|^2) \cos^2 \Lambda + \omega_r \sin^2 \Lambda + g_r \sin 2\Lambda - \omega_d$ is the qubit-drive detuning. In Equation (E.2), the desired effective coupling $\tilde{g} = -E_C \beta \sqrt{2} \cos^2 \Lambda \sin \Lambda$ between the $|f, 0\rangle$ and $|g, 1\rangle$ states is now made explicit.

Adding the Rabi drive between the $|e\rangle, |f\rangle$ states of the transmon qubit required for the unconditional reset protocol, the transmon-resonator system in a frame rotating at Δ_r for the resonator and $\Delta_{ge} + \alpha/2$ for the transmon qubit is described by the Hamiltonian

$$\begin{aligned} \hat{H} = & -\frac{\alpha}{2} \hat{b}^\dagger \hat{b} + \frac{\alpha}{2} \hat{b}^\dagger \hat{b}^\dagger \hat{b} \hat{b} + 2\chi_r \hat{a}^\dagger \hat{a} \hat{b}^\dagger \hat{b} + \frac{K}{2} \hat{a}^\dagger \hat{a}^\dagger \hat{a} \hat{a} \\ & + \frac{\tilde{g}}{\sqrt{2}} (\hat{b}^\dagger \hat{b}^\dagger \hat{a} + \hat{a}^\dagger \hat{b} \hat{b}) + \frac{\Omega_{ef}}{\sqrt{2}} (\hat{b} e^{iat/2} + \hat{b}^\dagger e^{-iat/2}), \end{aligned} \quad (\text{E.3})$$

where Ω_{ef} is the Rabi rate between the $|e\rangle, |f\rangle$ states of the transmon qubit.

Numerical results are obtained by initializing the system in the $|e, 0\rangle$ state and integrating the master equation

$$\begin{aligned} \dot{\rho} = & -i[\hat{H}, \rho] \\ & + \kappa \mathcal{D}[\hat{a}] \rho + \kappa_{\text{int}} \mathcal{D}[\hat{a}] \rho \\ & + \gamma_{1ge} (1 + n_{\text{th}}) \mathcal{D}[|g\rangle \langle e|] \rho + \gamma_{1ge} n_{\text{th}} \mathcal{D}[|e\rangle \langle g|] \rho \\ & + \gamma_{1ef} (1 + n_{\text{th}}) \mathcal{D}[|e\rangle \langle f|] \rho + \gamma_{1ef} n_{\text{th}} \mathcal{D}[|f\rangle \langle e|] \rho \\ & + \frac{\gamma_{\phi_{ge}}}{2} \mathcal{D}[|e\rangle \langle e| - |g\rangle \langle g|] \rho \\ & + \frac{\gamma_{\phi_{ef}}}{2} \mathcal{D}[|f\rangle \langle f| - |e\rangle \langle e|] \rho, \end{aligned} \quad (\text{E.4})$$

where $\mathcal{D}[\hat{O}]\bullet = \hat{O}\bullet\hat{O}^\dagger - \{\hat{O}^\dagger\hat{O}, \bullet\}/2$ denotes the dissipation super-operator, κ_{int} the internal decay rate of the resonator, $\gamma_{1nm} = 1/T_{1nm}$ the decay rates of the transmon qubit between the $|n\rangle, |m\rangle$ states, $\gamma_{\phi nm} = 1/2T_1^{nm} - 1/T_2^{nm}$ the dephasing rates between the $|n\rangle, |m\rangle$ states of the transmon qubit and n_{th} the thermal population of the transmon qubit in steady state.

E.2 Quantum Communication

To model photon transfer process numerically, we start by modelling each sample with the driven Jaynes-Cumming Hamiltonian (E.1). Applying the same displacement and Bogoliubov transformations as in appendix E.1, each sample can be modelled by a dispersive Hamiltonian similar to Hamiltonian (E.2). Using the same notation as in appendix E.1, introducing the subscript $i = A, B$ to denote the emitter and receiver samples, and setting $\hbar = 1$, in a frame rotating at Δ_T^i for the transfer resonator and $\Delta_{\text{ge}}^i + \alpha^i/2$ for the transmon qubit, the driven Hamiltonian for sample i is given by

$$\begin{aligned} \hat{H}^i = & -\frac{\alpha^i}{2}\hat{b}_i^\dagger\hat{b}_i + \frac{\alpha^i}{2}\hat{b}_i^\dagger\hat{b}_i^\dagger\hat{b}_i\hat{b}_i + \frac{K^i}{2}\hat{a}_i^\dagger\hat{a}_i^\dagger\hat{a}_i\hat{a}_i \\ & + 2\chi_T^i\hat{a}_i^\dagger\hat{a}_i\hat{b}_i^\dagger\hat{b}_i + \frac{1}{\sqrt{2}}[\tilde{g}^i(t)\hat{b}_i^\dagger\hat{b}_i^\dagger\hat{a}_i + \tilde{g}^i(t)^*\hat{a}_i^\dagger\hat{b}_i\hat{b}_i]. \end{aligned} \quad (\text{E.5})$$

The combined effective Hamiltonian of the two samples can be written as

$$\hat{H}_{\text{eff}} = \hat{H}^A + \hat{H}^B - i\frac{\sqrt{\kappa_T^A\kappa_T^B}\eta_c}{2}(\hat{a}_A\hat{a}_B^\dagger - \hat{a}_A^\dagger\hat{a}_B),$$

where η_c is the photon loss probability of the circulator between the two samples, and κ_T^i is the external coupling rate of the transfer resonator of sample i . Using this effective

Hamiltonian, numerical results are obtained by integrating the master equation

$$\begin{aligned}
\dot{\rho} = & -i[\hat{H}_{\text{eff}}, \rho] \\
& + \kappa_T^A(1 - \eta_c)\mathcal{D}[\hat{a}_A]\rho + \mathcal{D}[\sqrt{\kappa_T^A}\eta_c\hat{a}_A + \sqrt{\kappa_T^B}\hat{a}_B]\rho \\
& + \sum_{i=A,B} \left\{ \kappa_{\text{int}}^i \mathcal{D}[\hat{a}_i]\rho + \gamma_{1ge}^i \mathcal{D}[|g\rangle\langle e|_i]\rho \right. \\
& \quad \left. + \gamma_{1ef}^i \mathcal{D}[|e\rangle\langle f|_i]\rho \right\} \\
& + \sum_{i=A,B} \left\{ \gamma_{\phi ge}^i \mathcal{D}[|e\rangle\langle e|_i - |g\rangle\langle g|_i]\rho \right. \\
& \quad \left. + \gamma_{\phi ef}^i \mathcal{D}[|f\rangle\langle f|_i - |e\rangle\langle e|_i]\rho \right\},
\end{aligned} \tag{E.6}$$

where $\mathcal{D}[\hat{O}]\bullet = \hat{O}\bullet\hat{O}^\dagger - \{\hat{O}^\dagger\hat{O}, \bullet\}/2$ denotes the dissipation super-operator, κ_{int}^i the internal decay rates of the resonators, $\gamma_{1nm}^i = 1/T_{1nm}^i$ the decay rates of the transmon qubits between the $|n\rangle_i, |m\rangle_i$ states and $\gamma_{\phi nm}^i = 1/2T_{1nm}^i - 1/T_{2nm}^i$ the dephasing rates between the $|n\rangle_i, |m\rangle_i$ states of the transmon qubits. The last term in \hat{H}_{eff} combined with the resonator dissipators in the second line of the master equation (E.6), assure that the output of the emitter A is cascaded to the input of the receiver B [Gardiner93, Carmichael93] through a circulator with photon loss η_c .

Bibliography

- [Abellán15] C. Abellán, W. Amaya, D. Mitrani, V. Pruneri, and M. W. Mitchell. “Generation of fresh and pure random numbers for loophole-free bell tests.” *Phys. Rev. Lett.*, **115**, 250403 (2015). Cited on pages 58, 65, 66 and 162.
- [Alexanian95] M. Alexanian and S. K. Bose. “Unitary transformation and the dynamics of a three-level atom interacting with two quantized field modes.” *Phys. Rev. A*, **52**, 2218–2224 (1995). Cited on pages 41 and 42.
- [Ambegaokar63a] V. Ambegaokar and A. Baratoff. “Erratum: Tunneling between superconductors.” *Phys. Rev. Lett.*, **11**, 104–104 (1963). Cited on page 211.
- [Ambegaokar63b] V. Ambegaokar and A. Baratoff. “Tunneling between superconductors.” *Phys. Rev. Lett.*, **10**, 486 (1963). Erratum-ibid. [Ambegaokar63a]. Cited on page 15.
- [Andersen19] C. K. Andersen, A. Remm, S. Lazar, S. Krinner, J. Heinsoo, J.-C. Besse, M. Gabureac, A. Wallraff, and C. Eichler. “Entanglement stabilization using ancilla-based parity detection and real-time feedback in superconducting circuits.” *npj Quantum Information*, **5**, 69 (2019). Cited on page 181.
- [Andersen20a] C. K. Andersen, A. Kamal, N. A. Masluk, I. M. Pop, A. Blais, and M. H. Devoret. “Quantum versus classical switching dynamics of driven dissipative kerr resonators.” *Phys. Rev. Applied*, **13**, 044017 (2020). Cited on pages 4 and 87.
- [Andersen20b] C. K. Andersen, A. Remm, S. Lazar, S. Krinner, N. Lacroix, G. J. Norris, M. Gabureac, C. Eichler, and A. Wallraff. “Repeated quantum error detection in a surface code.” *Nature Physics*, **16**, 875–880 (2020). Cited on pages 69 and 143.
- [Andrews14] R. W. Andrews, R. W. Peterson, T. P. Purdy, K. Cicak, R. W. Simmonds, C. A. Regal, and K. W. Lehnert. “Bidirectional and efficient conversion

- between microwave and optical light.” *Nat. Phys.*, **10**, 321–326 (2014). Cited on page 182.
- [Ansmann09] M. Ansmann, H. Wang, R. C. Bialczak, M. Hofheinz, E. Lucero, M. Neeley, A. D. O’Connell, D. Sank, M. Weides, J. Wenner, A. N. Cleland, and J. M. Martinis. “Violation of Bell’s inequality in Josephson phase qubits.” *Nature*, **461**, 504–506 (2009). Cited on page 65.
- [Arnon-Friedman18] R. Arnon-Friedman, F. Dupuis, O. Fawzi, R. Renner, and T. Vidick. “Practical device-independent quantum cryptography via entropy accumulation.” *Nature Communications*, **9**, 459 (2018). Cited on pages 3 and 55.
- [Arnon-Friedman19] R. Arnon-Friedman and J.-D. Bancal. “Device-independent certification of one-shot distillable entanglement.” *New J. Phys.*, **21**, 033010 (2019). Cited on pages 3 and 55.
- [Arute19] F. Arute, K. Arya, R. Babbush, D. Bacon, J. C. Bardin, R. Barends, R. Biswas, S. Boixo, F. G. S. L. Brandao, D. A. Buell, B. Burkett, Y. Chen, Z. Chen, B. Chiaro, R. Collins, W. Courtney, A. Dunsworth, E. Farhi, B. Foxen, A. Fowler, C. Gidney, M. Giustina, R. Graff, K. Guerin, S. Habegger, M. P. Harrigan, M. J. Hartmann, A. Ho, M. Hoffmann, T. Huang, T. S. Humble, S. V. Isakov, E. Jeffrey, Z. Jiang, D. Kafri, K. Kechedzhi, J. Kelly, P. V. Klimov, S. Knysh, A. Korotkov, F. Kostritsa, D. Landhuis, M. Lindmark, E. Lucero, D. Lyakh, S. Mandrà, J. R. McClean, M. McEwen, A. Megrant, X. Mi, K. Michielsen, M. Mohseni, J. Mutus, O. Naaman, M. Neeley, C. Neill, M. Y. Niu, E. Ostby, A. Petukhov, J. C. Platt, C. Quintana, E. G. Rieffel, P. Roushan, N. C. Rubin, D. Sank, K. J. Satzinger, V. Smelyanskiy, K. J. Sung, M. D. Trevithick, A. Vainsencher, B. Villalonga, T. White, Z. J. Yao, P. Yeh, A. Zalcman, H. Neven, and J. M. Martinis. “Quantum supremacy using a programmable superconducting processor.” *Nature*, **574**, 505–510 (2019). Cited on pages 4 and 143.
- [Arute20] F. Arute, K. Arya, R. Babbush, D. Bacon, J. C. Bardin, R. Barends, S. Boixo, M. Broughton, B. B. Buckley, D. A. Buell, B. Burkett, N. Bushnell, Y. Chen, Z. Chen, B. Chiaro, R. Collins, W. Courtney, S. Demura, A. Dunsworth, E. Farhi, A. Fowler, B. Foxen, C. Gidney, M. Giustina, R. Graff, S. Habegger, M. P. Harrigan, A. Ho, S. Hong, T. Huang, W. J. Huggins, L. Ioffe, S. V. Isakov, E. Jeffrey, Z. Jiang, C. Jones, D. Kafri, K. Kechedzhi, J. Kelly, S. Kim, P. V. Klimov, A. Korotkov, F. Kostritsa, D. Landhuis, P. Laptev, M. Lindmark, E. Lucero, O. Martin, J. M. Martinis, J. R. McClean, M. McEwen, A. Megrant, X. Mi, M. Mohseni, W. Mruczkiewicz, J. Mutus, O. Naaman, M. Neeley, C. Neill, H. Neven, M. Y. Niu, T. E. O’Brien,

- E. Ostby, A. Petukhov, H. Putterman, C. Quintana, P. Roushan, N. C. Rubin, D. Sank, K. J. Satzinger, V. Smelyanskiy, D. Strain, K. J. Sung, M. Sza-lay, T. Y. Takeshita, A. Vainsencher, T. White, N. Wiebe, Z. J. Yao, P. Yeh, and A. Zalcman. “Hartree-fock on a superconducting qubit quantum computer.” *arXiv:2004.04174* (2020). Cited on page 87.
- [Asadian21] A. Asadian and A. Cabello. “Bosonic indistinguishability-dependent contextual-ity.” *arXiv:2102.00746* (2021). Cited on page 180.
- [Aspect82a] A. Aspect, J. Dalibard, and G. Roger. “Experimental test of bell’s inequal-ities using time- varying analyzers.” *Phys. Rev. Lett.*, **49**, 1804–1807 (1982). Cited on pages 3, 69 and 179.
- [Aspect82b] A. Aspect, P. Grangier, and G. Roger. “Experimental realization of einstein-podolsky-rosen-bohm gedankenexperiment: A new violation of bell’s in-equalities.” *Phys. Rev. Lett.*, **49**, 91–94 (1982). Cited on pages 3 and 179.
- [Awschalom21] D. Awschalom, K. K. Berggren, H. Bernien, S. Bhave, L. D. Carr, P. Davids, S. E. Economou, D. Englund, A. Faraon, M. Fejer, S. Guha, M. V. Gustaf-son, E. Hu, L. Jiang, J. Kim, B. Korzh, P. Kumar, P. G. Kwiat, M. Lončar, M. D. Lukin, D. A. Miller, C. Monroe, S. W. Nam, P. Narang, J. S. Orcutt, M. G. Raymer, A. H. Safavi-Naeini, M. Spiropulu, K. Srinivasan, S. Sun, J. Vučković, E. Waks, R. Walsworth, A. M. Weiner, and Z. Zhang. “Devel-opment of quantum interconnects (quics) for next-generation information technologies.” *PRX Quantum*, **2**, 017002 (2021). Cited on pages 4, 87 and 182.
- [Axline18] C. Axline, L. Burkhardt, W. Pfaff, M. Zhang, K. Chou, P. Campagne-Ibarcq, P. Reinhold, L. Frunzio, S. M. Girvin, L. Jiang, M. H. Devoret, and R. J. Schoelkopf. “On-demand quantum state transfer and entanglement be-tween remote microwave cavity memories.” *Nature Physics*, **14**, 705–710 (2018). Cited on pages 44, 47, 48, 87, 101, 144 and 180.
- [Babbush18a] R. Babbush, C. Gidney, D. W. Berry, N. Wiebe, J. McClean, A. Paler, A. Fowler, and H. Neven. “Encoding electronic spectra in quantum cir-cuits with linear t complexity.” *Phys. Rev. X*, **8**, 041015 (2018). Cited on pages 1, 4 and 143.
- [Babbush18b] R. Babbush, N. Wiebe, J. McClean, J. McClain, H. Neven, and G. K.-L. Chan. “Low-depth quantum simulation of materials.” *Phys. Rev. X*, **8**, 011044 (2018). Cited on page 182.

- [Balram16] K. C. Balram, M. Davanco, J. D. Song, and K. Srinivasan. “Coherent coupling between radiofrequency, optical, and acoustic waves in piezomechanical circuits.” *Nat. Photon.* (2016). Cited on page 182.
- [Barends16] R. Barends, A. Shabani, L. Lamata, J. Kelly, A. Mezzacapo, U. L. Heras, R. Babbush, A. G. Fowler, B. Campbell, Y. Chen, Z. Chen, B. Chiaro, A. Dunsworth, E. Jeffrey, E. Lucero, A. Megrant, J. Y. Mutus, M. Neeley, C. Neill, P. J. J. O’Malley, C. Quintana, P. Roushan, D. Sank, A. Vainsencher, J. Wenner, T. C. White, E. Solano, H. Neven, and J. M. Martinis. “Digitized adiabatic quantum computing with a superconducting circuit.” *Nature*, **534**, 222–226 (2016). Cited on page 4.
- [Barrett02] J. Barrett, D. Collins, L. Hardy, A. Kent, and S. Popescu. “Quantum nonlocality, bell inequalities, and the memory loophole.” *Phys. Rev. A*, **66**, 042111 (2002). Cited on pages 61 and 62.
- [Barrett05] J. Barrett, L. Hardy, and A. Kent. “No signaling and quantum key distribution.” *Phys. Rev. Lett.*, **95**, 010503 (2005). Cited on pages 3, 55, 178 and 180.
- [Battistel21] F. Battistel, B. Varbanov, and B. Terhal. “Hardware-efficient leakage-reduction scheme for quantum error correction with superconducting transmon qubits.” *PRX Quantum*, **2**, 030314 (2021). Cited on page 140.
- [BBT18] The BIG Bell Test Collaboration. “Challenging local realism with human choices.” *Nature*, **557**, 212–216 (2018). Cited on page 57.
- [Beer12] F. P. Beer, E. R. J. Johnston, J. T. DeWolf, and D. F. Mazurek. *Mechanics of Materials*. McGraw-Hill, 1221 Avenue of the Americas, New York, NY 10020, 6th edition (2012). Cited on page 107.
- [Béjanin16] J. H. Béjanin, T. G. McConkey, J. R. Rinehart, C. T. Earnest, C. R. H. McRae, D. Shiri, J. D. Bateman, Y. Rohanizadegan, B. Penava, P. Breul, S. Royak, M. Zapatka, A. G. Fowler, and M. Mariantoni. “Three-dimensional wiring for extensible quantum computing: The quantum socket.” *Phys. Rev. Applied*, **6**, 044010 (2016). Cited on pages 4 and 143.
- [Bell64] J. S. Bell. “On the Einstein Podolsky Rosen paradox.” *Physics (N. Y.)*, **1**, 195 (1964). Cited on pages 3 and 49.
- [Bell85] J. Bell. “An exchange on local beables.” *Dialectica*, **39**, 85–96 (1985). Cited on page 57.

- [Bell04] J. S. Bell and A. Aspect. *Speakable and Unspeakable in Quantum Mechanics: Collected Papers on Quantum Philosophy*. Cambridge University Press, 2nd edition (2004). Cited on page 57.
- [Bennett92] C. H. Bennett and S. J. Wiesner. “Communication via one- and two-particle operators on einstein-podolsky-rosen states.” *Phys. Rev. Lett.*, **69**, 2881–2884 (1992). Cited on page 2.
- [Bennett93] C. H. Bennett, G. Brassard, C. Crépeau, R. Jozsa, A. Peres, and W. K. Wootters. “Teleporting an unknown quantum state via dual classical and Einstein-Podolsky-Rosen channels.” *Phys. Rev. Lett.*, **70**, 1895–1899 (1993). Cited on pages 2 and 69.
- [Bennett96a] C. H. Bennett, G. Brassard, S. Popescu, B. Schumacher, J. A. Smolin, and W. K. Wootters. “Purification of noisy entanglement and faithful teleportation via noisy channels.” *Phys. Rev. Lett.*, **76**, 722–725 (1996). Cited on pages 69, 101 and 180.
- [Bennett96b] C. H. Bennett, D. P. DiVincenzo, J. A. Smolin, and W. K. Wootters. “Mixed-state entanglement and quantum error correction.” *Phys. Rev. A*, **54**, 3824–3851 (1996). Cited on pages 2 and 47.
- [Bentkus04] V. Bentkus. “On hoeffding’s inequalities.” *Ann. Probab.*, **32**, 1650–1673 (2004). Cited on page 61.
- [Bergmann19] K. Bergmann, H.-C. Nagerl, C. Panda, G. Gabrielse, E. Miloglyadov, M. Quack, G. Seyfang, G. Wichmann, S. Ospelkaus, A. Kuhn, S. Longhi, A. Szameit, P. Pirro, B. Hillebrands, X.-F. Zhu, J. Zhu, M. Drewsen, W. K. Hensinger, S. Weidt, T. Halfmann, H.-L. Wang, G. S. Paraoanu, N. V. Vitanov, J. Mompart, T. Busch, T. J. Barnum, D. D. Grimes, R. W. Field, M. G. Raizen, E. Narevicius, M. Auzinsh, D. Budker, A. Palfy, and C. H. Keitel. “Roadmap on STIRAP applications.” *Journal of Physics B: Atomic, Molecular and Optical Physics*, **52**, 202001 (2019). Cited on page 178.
- [Bernien13] H. Bernien, B. Hensen, W. Pfaff, G. Koolstra, M. S. Blok, L. Robledo, T. H. Taminiau, M. Markham, D. J. Twitchen, L. Childress, and R. Hanson. “Heralded entanglement between solid-state qubits separated by three metres.” *Nature*, **497**, 86–90 (2013). Cited on pages 5 and 144.
- [Bernstein93] E. Bernstein and U. Vazirani. “Quantum complexity theory.” In “Proceedings of the Twenty-Fifth Annual ACM Symposium on Theory of Computing,” STOC ’93, 11–20. Association for Computing Machinery, New York, NY, USA (1993). Cited on page 1.

- [Bernstein09] D. J. Bernstein. *Introduction to post-quantum cryptography*. Springer Berlin Heidelberg, Berlin, Heidelberg (2009). Cited on page 1.
- [Besse18] J.-C. Besse, S. Gasparinetti, M. C. Collodo, T. Walter, P. Kurpiers, M. Pechal, C. Eichler, and A. Wallraff. “Single-shot quantum non-demolition detection of individual itinerant microwave photons.” *Phys. Rev. X*, **8**, 021003 (2018). Cited on pages 39 and 181.
- [Besse20a] J.-C. Besse, S. Gasparinetti, M. C. Collodo, T. Walter, A. Remm, J. Krause, C. Eichler, and A. Wallraff. “Parity detection of propagating microwave fields.” *Phys. Rev. X*, **10**, 011046 (2020). Cited on page 40.
- [Besse20b] J.-C. Besse, K. Reuer, M. C. Collodo, A. Wulff, L. Wernli, A. Copetudo, D. Malz, P. Magnard, A. Akin, M. Gabureac, G. J. Norris, J. I. Cirac, A. Wallraff, and C. Eichler. “Realizing a deterministic source of multipartite-entangled photonic qubits.” *Nat. Commun.*, **11**, 4877 (2020). Cited on pages 87, 106, 176 and 181.
- [Bialczak07] R. Bialczak, C. McDermott, M. Ansmann, M. Hofheinz, N. Katz, E. Lucero, M. Neeley, A. O’Connell, H. Wang, A. Cleland, and J. Martinis. “ $1/f$ flux noise in josephson phase qubits.” *Phys. Rev. Lett.*, **99**, 187006 (2007). Cited on page 82.
- [Bianchetti10] R. Bianchetti, S. Filipp, M. Baur, J. M. Fink, C. Lang, L. Steffen, M. Boissonneault, A. Blais, and A. Wallraff. “Control and tomography of a three level superconducting artificial atom.” *Phys. Rev. Lett.*, **105**, 223601 (2010). Cited on pages 27, 128 and 130.
- [Bienfait19] A. Bienfait, K. J. Satzinger, Y. P. Zhong, H.-S. Chang, M.-H. Chou, C. R. Conner, É. Dumur, J. Grebel, G. A. Peairs, R. G. Povey, and A. N. Cleland. “Phonon-mediated quantum state transfer and remote qubit entanglement.” *Science*, **364**, 368–371 (2019). Cited on page 181.
- [Blais04] A. Blais, R.-S. Huang, A. Wallraff, S. M. Girvin, and R. J. Schoelkopf. “Cavity quantum electrodynamics for superconducting electrical circuits: An architecture for quantum computation.” *Phys. Rev. A*, **69**, 062320 (2004). Cited on pages 4, 33, 34, 35, 38, 69, 70 and 74.
- [Blais20] A. Blais, S. M. Girvin, and W. D. Oliver. “Quantum information processing and quantum optics with circuit quantum electrodynamics.” *Nature Physics* (2020). Cited on page 34.

- [Blais21] A. Blais, A. L. Grimsmo, S. M. Girvin, and A. Wallraff. “Circuit quantum electrodynamics.” *Rev. Mod. Phys.*, **93**, 025005 (2021). Cited on pages 4 and 87.
- [Blok21] M. S. Blok, V. V. Ramasesh, T. Schuster, K. O’Brien, J. M. Kreikebaum, D. Dahlen, A. Morvan, B. Yoshida, N. Y. Yao, and I. Siddiqi. “Quantum information scrambling on a superconducting qutrit processor.” *Phys. Rev. X*, **11**, 021010 (2021). Cited on page 4.
- [Boissonneault09] M. Boissonneault, J. M. Gambetta, and A. Blais. “Dispersive regime of circuit QED: Photon-dependent qubit dephasing and relaxation rates.” *Phys. Rev. A*, **79**, 013819 (2009). Cited on pages 74, 82 and 126.
- [Boissonneault10] M. Boissonneault, J. M. Gambetta, and A. Blais. “Improved superconducting qubit readout by qubit-induced nonlinearities.” *Phys. Rev. Lett.*, **105**, 100504–4 (2010). Cited on pages 74 and 82.
- [Bouchiat98] V. Bouchiat, D. Vion, P. Joyez, D. Esteve, and M. H. Devoret. “Quantum coherence with a single Cooper pair.” *Phys. Scr.*, **T76**, 165–170 (1998). Cited on page 17.
- [Bouwmeester97] D. Bouwmeester, J. W. Pan, K. Mattle, M. Eibl, H. Weinfurter, and A. Zeilinger. “Experimental quantum teleportation.” *Nature*, **390**, 575–579 (1997). Cited on page 2.
- [Bowles18] J. Bowles, I. Šupić, D. Cavalcanti, and A. Acín. “Device-independent entanglement certification of all entangled states.” *Phys. Rev. Lett.*, **121**, 180503 (2018). Cited on pages 3 and 55.
- [Boyd04] S. Boyd and L. Vandenberghe. *Convex Optimization*. Cambridge University Press, USA (2004). Cited on page 52.
- [Brans88] C. H. Brans. “Bell’s theorem does not eliminate fully causal hidden variables.” *International Journal of Theoretical Physics*, **27**, 219–226 (1988). Cited on page 57.
- [Brassard02] G. Brassard, P. Høyer, M. Mosca, and A. Tapp. *Quantum amplitude amplification and estimation*, volume 305 of *Contemp. Math.* Amer. Math. Soc., Providence, RI (2002). Cited on page 2.
- [Bravyi05] S. Bravyi and A. Kitaev. “Universal quantum computation with ideal clifford gates and noisy ancillas.” *Phys. Rev. A*, **71**, 022316 (2005). Cited on page 69.

- [Brecht16] T. Brecht, W. Pfaff, C. Wang, Y. Chu, L. Frunzio, M. H. Devoret, and R. J. Schoelkopf. “Multilayer microwave integrated quantum circuits for scalable quantum computing.” *npj Quantum Information*, **2**, 16002 (2016). Cited on page 143.
- [Bronn15a] N. T. Bronn, Y. Liu, J. B. Hertzberg, A. D. Córcoles, A. A. Houck, J. M. Gambetta, and J. M. Chow. “Broadband filters for abatement of spontaneous emission in circuit quantum electrodynamics.” *Applied Physics Letters*, **107**, 172601 (2015). Cited on page 40.
- [Bronn15b] N. T. Bronn, E. Magesan, N. A. Masluk, J. M. Chow, J. M. Gambetta, and M. Steffen. “Reducing spontaneous emission in circuit quantum electrodynamics by a combined readout/filter technique.” *IEEE Transactions on Applied Superconductivity*, **25**, 1–10 (2015). Cited on page 40.
- [Bronn17] N. T. Bronn, B. Abdo, K. Inoue, S. Lekuch, A. D. Córcoles, J. B. Hertzberg, M. Takita, L. S. Bishop, J. M. Gambetta, and J. M. Chow. “Fast, high-fidelity readout of multiple qubits.” *Journal of Physics: Conference Series*, **834**, 012003 (2017). Cited on page 79.
- [Brunner14] N. Brunner, D. Cavalcanti, S. Pironio, V. Scarani, and S. Wehner. “Bell nonlocality.” *Rev. Mod. Phys.*, **86**, 419–478 (2014). Cited on pages 3, 49, 51, 53, 63 and 167.
- [Burkhart21] L. D. Burkhardt, J. D. Teoh, Y. Zhang, C. J. Axline, L. Frunzio, M. Devoret, L. Jiang, S. Girvin, and R. Schoelkopf. “Error-detected state transfer and entanglement in a superconducting quantum network.” *PRX Quantum*, **2**, 030321 (2021). Cited on pages 48, 87, 101, 144, 178 and 181.
- [Bylander11] J. Bylander, S. Gustavsson, F. Yan, F. Yoshihara, K. Harrabi, G. Fitch, D. G. Cory, Y. Nakamura, J.-S. Tsai, and O. W. D. “Noise spectroscopy through dynamical decoupling with a superconducting flux qubit.” *Nat. Phys.*, **7**, 565–570 (2011). Cited on pages 29 and 82.
- [Calajó19] G. Calajó, Y.-L. L. Fang, H. U. Baranger, and F. Ciccarello. “Exciting a bound state in the continuum through multiphoton scattering plus delayed quantum feedback.” *Phys. Rev. Lett.*, **122**, 073601 (2019). Cited on pages 106 and 181.
- [Caldwell18] S. A. Caldwell, N. Didier, C. A. Ryan, E. A. Sete, A. Hudson, P. Karalekas, R. Manenti, M. P. da Silva, R. Sinclair, E. Acala, N. Alidoust, J. Angeles, A. Bestwick, M. Block, B. Bloom, A. Bradley, C. Bui, L. Capelluto, R. Chilcott, J. Cordova, G. Crossman, M. Curtis, S. Deshpande, T. E.

- Bouayadi, D. Girshovich, S. Hong, K. Kuang, M. Lenihan, T. Manning, A. Marchenkov, J. Marshall, R. Maydra, Y. Mohan, W. O'Brien, C. Osborn, J. Otterbach, A. Papageorge, J.-P. Paquette, M. Pelstring, A. Polloreno, G. Prawiroatmodjo, V. Rawat, M. Reagor, R. Renzas, N. Rubin, D. Russell, M. Rust, D. Scarabelli, M. Scheer, M. Selvanayagam, R. Smith, A. Staley, M. Suska, N. Tezak, D. C. Thompson, T.-W. To, M. Vahidpour, N. Vodrahalli, T. Whyland, K. Yadav, W. Zeng, and C. Rigetti. "Parametrically activated entangling gates using transmon qubits." *Phys. Rev. Applied*, **10**, 034050 (2018). Cited on page 176.
- [Campagne-Ibarcq13] P. Campagne-Ibarcq, E. Flurin, N. Roch, D. Darson, P. Morfin, M. Mirrahimi, M. H. Devoret, F. Mallet, and B. Huard. "Persistent control of a superconducting qubit by stroboscopic measurement feedback." *Phys. Rev. X*, **3**, 021008 (2013). Cited on pages 69, 125, 126 and 127.
- [Campagne-Ibarcq18] P. Campagne-Ibarcq, E. Zalys-Geller, A. Narla, S. Shankar, P. Reinhold, L. Burkhardt, C. Axline, W. Pfaff, L. Frunzio, R. J. Schoelkopf, and M. H. Devoret. "Deterministic remote entanglement of superconducting circuits through microwave two-photon transitions." *Phys. Rev. Lett.*, **120**, 200501 (2018). Cited on pages 44, 47, 87, 101, 126 and 144.
- [Campagne-Ibarcq20] P. Campagne-Ibarcq, A. Eickbusch, S. Touzard, E. Zalys-Geller, N. E. Fratini, V. V. Sivak, P. Reinhold, S. Puri, S. Shankar, R. J. Schoelkopf, L. Frunzio, M. Mirrahimi, and M. H. Devoret. "Quantum error correction of a qubit encoded in grid states of an oscillator." *Nature*, **584**, 368–372 (2020). Cited on page 4.
- [Carmichael93] H. J. Carmichael. "Quantum trajectory theory for cascaded open systems." *Physical Review Letters*, **70**, 2273–2276 (1993). Cited on page 208.
- [Casares21] P. A. M. Casares, R. Campos, and M. A. Martin-Delgado. "Qfold: Quantum walks and deep learning to solve protein folding." *arXiv:2101.10279* (2021). Cited on page 1.
- [Castellanos-Beltran08] M. A. Castellanos-Beltran, K. D. Irwin, G. C. Hilton, L. R. Vale, and K. W. Lehnert. "Amplification and squeezing of quantum noise with a tunable josephson metamaterial." *Nat. Phys.*, **4**, 929–931 (2008). Cited on page 73.
- [Caves82] C. M. Caves. "Quantum limits on noise in linear amplifiers." *Phys. Rev. D*, **26**, 1817–1839 (1982). Cited on pages 73 and 74.

- [Chakram20] S. Chakram, A. E. Oriani, R. K. Naik, A. V. Dixit, K. He, A. Agrawal, H. Kwon, and D. I. Schuster. “Seamless high-q microwave cavities for multimode circuit qed.” *arXiv:2010.16382* (2020). Cited on pages 106, 122 and 181.
- [Chamberland20] C. Chamberland, K. Noh, P Arrangoiz-Arriola, E. T. Campbell, C. T. Hann, J. Iverson, H. Putterman, T. C. Bohdanowicz, S. T. Flammia, A. Keller, G. Refael, J. Preskill, L. Jiang, A. H. Safavi-Naeini, O. Painter, and F. G. S. L. Brandão. “Building a fault-tolerant quantum computer using concatenated cat codes.” *arXiv:2012.04108* (2020). Cited on page 40.
- [Chang20] H.-S. Chang, Y. P. Zhong, A. Bienfait, M.-H. Chou, C. R. Conner, E. Dumur, J. Grebel, G. A. Peairs, R. G. Povey, K. J. Satzinger, and A. N. Cleland. “Remote entanglement via adiabatic passage using a tunably dissipative quantum communication system.” *Phys. Rev. Lett.*, **124**, 240502 (2020). Cited on pages 48, 101, 144 and 178.
- [Chen16] Z. Chen, J. Kelly, C. Quintana, R. Barends, B. Campbell, Y. Chen, B. Chiaro, A. Dunsworth, A. G. Fowler, E. Lucero, E. Jeffrey, A. Megrant, J. Mutus, M. Neeley, C. Neill, P. J. J. O’Malley, P Roushan, D. Sank, A. Vainsencher, J. Wenner, T. C. White, A. N. Korotkov, and J. M. Martinis. “Measuring and suppressing quantum state leakage in a superconducting qubit.” *Phys. Rev. Lett.*, **116**, 020501 (2016). Cited on page 25.
- [Chen21a] S.-L. Chen, N. Miklin, C. Budroni, and Y.-N. Chen. “Device-independent quantification of measurement incompatibility.” *Phys. Rev. Research*, **3**, 023143 (2021). Cited on page 3.
- [Chen21b] Z. Chen, K. J. Satzinger, J. Atalaya, A. N. Korotkov, A. Dunsworth, D. Sank, C. Quintana, M. McEwen, R. Barends, P. V. Klimov, S. Hong, C. Jones, A. Petukhov, D. Kafri, S. Demura, B. Burkett, C. Gidney, A. G. Fowler, A. Paler, H. Putterman, I. Aleiner, F. Arute, K. Arya, R. Babbush, J. C. Bardin, A. Bengtsson, A. Bourassa, M. Broughton, B. B. Buckley, D. A. Buell, N. Bushnell, B. Chiaro, R. Collins, W. Courtney, A. R. Derk, D. Eppens, C. Erickson, E. Farhi, B. Foxen, M. Giustina, A. Greene, J. A. Gross, M. P. Harrigan, S. D. Harrington, J. Hilton, A. Ho, T. Huang, W. J. Huggins, L. B. Ioffe, S. V. Isakov, E. Jeffrey, Z. Jiang, K. Kechedzhi, S. Kim, A. Kitaev, F. Kostritsa, D. Landhuis, P. Laptev, E. Lucero, O. Martin, J. R. McClean, T. McCourt, X. Mi, K. C. Miao, M. Mohseni, S. Montazeri, W. Mruczkiewicz, J. Mutus, O. Naaman, M. Neeley, C. Neill, M. Newman, M. Y. Niu, T. E. O’Brien, A. Opremcak, E. Ostby, B. Pató, N. Redd, P Roushan, N. C. Rubin, V. Shvarts, D. Strain, M. Szalay, M. D. Trevithick, B. Villalonga, T. White,

- Z. J. Yao, P. Yeh, J. Yoo, A. Zalcman, H. Neven, S. Boixo, V. Smelyanskiy, Y. Chen, A. Megrant, J. Kelly, and A. I. Google Quantum. “Exponential suppression of bit or phase errors with cyclic error correction.” *Nature*, **595**, 383–387 (2021). Cited on pages 4, 69, 125 and 126.
- [Chiaverini04] J. Chiaverini, D. Leibfried, T. Schaetz, M. D. Barrett, R. B. Blakestad, J. Britton, W. M. Itano, J. D. Jost, E. Knill, C. Langer, R. Ozeri, and D. J. Wineland. “Realization of quantum error correction.” *Nature*, **432**, 602–605 (2004). Cited on page 125.
- [Chou18] K. S. Chou, J. Z. Blumoff, C. S. Wang, P. C. Reinhold, C. J. Axline, Y. Y. Gao, L. Frunzio, M. H. Devoret, L. Jiang, and R. J. Schoelkopf. “Deterministic teleportation of a quantum gate between two logical qubits.” *Nature*, **561**, 368 (2018). Cited on pages 2, 69, 180 and 181.
- [Chow10] J. M. Chow, L. DiCarlo, J. M. Gambetta, F. Motzoi, L. Frunzio, S. M. Girvin, and R. J. Schoelkopf. “Optimized driving of superconducting artificial atoms for improved single-qubit gates.” *Phys. Rev. A*, **82**, 040305 (2010). Cited on page 25.
- [Chu20] Y. Chu and S. Groblacher. “A perspective on hybrid quantum opto- and electromechanical systems.” *arXiv:2007.03360* (2020). Cited on page 182.
- [Chuang97] I. L. Chuang and M. A. Nielsen. “Prescription for experimental determination of the dynamics of a quantum black box.” *J. Mod. Opt.*, **44**, 2455–2467 (1997). Cited on page 157.
- [Cirac95] J. I. Cirac and P. Zoller. “Quantum computations with cold trapped ions.” *Phys. Rev. Lett.*, **74**, 4091–4094 (1995). Cited on page 4.
- [Cirac97] J. I. Cirac, P. Zoller, H. J. Kimble, and H. Mabuchi. “Quantum state transfer and entanglement distribution among distant nodes in a quantum network.” *Phys. Rev. Lett.*, **78**, 3221–3224 (1997). Cited on pages 44, 144 and 153.
- [Cirac99] J. I. Cirac, A. K. Ekert, S. F. Huelga, and C. Macchiavello. “Distributed quantum computation over noisy channels.” *Phys. Rev. A*, **59**, 4249–4254 (1999). Cited on page 180.
- [Cirel’son80] B. S. Cirel’son. “Quantum generalizations of bell’s inequality.” *Letters in Mathematical Physics*, **4**, 93–100 (1980). Cited on page 55.

- [Clader13] B. D. Clader, B. C. Jacobs, and C. R. Sprouse. “Preconditioned quantum linear system algorithm.” *Phys. Rev. Lett.*, **110**, 250504 (2013). Cited on page 2.
- [Clauser69] J. F. Clauser, M. A. Horne, A. Shimony, and R. A. Holt. “Proposed experiment to test local hidden-variable theories.” *Phys. Rev. Lett.*, **23**, 880–884 (1969). Cited on pages 49 and 54.
- [Clauser78] J. F. Clauser and A. Shimony. “Bell’s theorem. experimental tests and implications.” *Reports on Progress in Physics*, **41**, 1881–1927 (1978). Cited on page 3.
- [Cleland19] A. Y. Cleland, M. Pechal, P. C. Stas, C. J. Sarabalis, and A. H. Safavi-Naeini. “Mechanical purcell filters for microwave quantum machines.” *Applied Physics Letters*, **115**, 263504 (2019). Cited on page 40.
- [Clerk10] A. A. Clerk, M. H. Devoret, S. M. Girvin, F. Marquardt, and R. J. Schoelkopf. “Introduction to quantum noise, measurement, and amplification.” *Rev. Mod. Phys.*, **82**, 1155–1208 (2010). Cited on pages 73 and 74.
- [Colbeck09] R. Colbeck. *Quantum And Relativistic Protocols For Secure Multi-Party Computation*. Ph.D. thesis, University of Cambridge (2009). Cited on page 3.
- [Colbeck12] R. Colbeck and R. Renner. “Free randomness can be amplified.” *Nat. Phys.*, **8**, 450–454 (2012). Cited on pages 3, 55 and 180.
- [Copetudo21] A. Copetudo. *Setup Synchronization For A Loophole-Free Bell Test*. mathe-sis, ETH Zurich (2021). Cited on page 169.
- [Córcoles21] A. D. Córcoles, M. Takita, K. Inoue, S. Lekuch, Z. K. Mineev, J. M. Chow, and J. M. Gambetta. “Exploiting dynamic quantum circuits in a quantum algorithm with superconducting qubits.” *Phys. Rev. Lett.*, **127**, 100501 (2021). Cited on pages 69, 126 and 127.
- [Cottet17] N. Cottet, S. Jezouin, L. Bretheau, P. Campagne-Ibarcq, Q. Ficheux, J. Anders, A. Auffèves, R. Azouit, P. Rouchon, and B. Huard. “Observing a quantum maxwell demon at work.” *Proceedings of the National Academy of Sciences*, **114**, 7561–7564 (2017). Cited on page 143.
- [D’Addabbo18] A. D’Addabbo, C. Alduino, A. Bersani, M. Biassoni, C. Bucci, A. Caminata, L. Canonica, L. Cappelli, G. Ceruti, N. Chott, S. Copello, O. Cremonesi, J. S.

- Cushman, D. D'Aguzzano, C. J. Davis, S. Dell'Oro, S. Di Domizio, A. Drobizhev, M. Faverzani, E. Ferri, M. A. Franceschi, L. Gladstone, P. Gorla, C. Ligi, L. Marini, T. Napolitano, A. Nucciotti, I. Nutini, J. L. Ouellet, C. E. Pagliarone, L. Pattavina, C. Rusconi, D. Santone, B. Schmidt, V. Singh, D. Speller, L. Taffarello, F. Terranova, J. Wallig, B. Welliver, and T. Wise. "The cuore cryostat." *Journal of Low Temperature Physics*, **193**, 867–875 (2018). Cited on page 110.
- [Das18] R. N. Das, J. L. Yoder, D. Rosenberg, D. K. Kim, D. Yost, J. Mallek, D. Hover, V. Bolkhovskiy, A. J. Kerman, and W. D. Oliver. "Cryogenic qubit integration for quantum computing." In "2018 IEEE 68th Electronic Components and Technology Conference (ECTC)," 504–514 (2018). Cited on pages 4 and 143.
- [Deutsch85] D. Deutsch. "Quantum theory, the Church-Turing principle and the universal quantum computer." *Proceedings of the Royal Society of London. Series A, Mathematical and Physical Sciences*, **400**, 97–117 (1985). Cited on page 1.
- [Deutsch89] D. Deutsch. "Quantum computational networks." *Proceedings of the Royal Society of London A: Mathematical, Physical and Engineering Sciences*, **425**, 73–90 (1989). Cited on page 1.
- [Dial15] O. Dial, D. T. McClure, S. Poletto, J. M. Gambetta, D. W. Abraham, J. M. Chow, and M. Steffen. "Bulk and surface loss in superconducting transmon qubits." *Superconductor Science and Technology*, **29**, 044001 (2015). Cited on page 27.
- [DiCarlo09] L. DiCarlo, J. M. Chow, J. M. Gambetta, L. S. Bishop, B. R. Johnson, D. I. Schuster, J. Majer, A. Blais, L. Frunzio, S. M. Girvin, and R. J. Schoelkopf. "Demonstration of two-qubit algorithms with a superconducting quantum processor." *Nature*, **460**, 240–244 (2009). Cited on page 4.
- [Didier18] N. Didier, E. A. Sete, M. P. da Silva, and C. Rigetti. "Analytical modeling of parametrically-modulated transmon qubits." *Phys. Rev. A*, **97**, 022330 (2018). Cited on page 19.
- [Dinc19] F. Dinc and A. M. Branczyk. "Non-markovian super-superradiance in a linear chain of up to 100 qubits." *Phys. Rev. Research*, **1**, 032042 (2019). Cited on page 181.
- [Dinc20] F. Dinc, L. E. Hayward, and A. M. Branczyk. "Multi-dimensional super- and subradiance in waveguide quantum electrodynamics." *arXiv:2003.04906* (2020). Cited on page 106.

- [DiVincenzo00] D. P. DiVincenzo. “The physical implementation of quantum computation.” *Fortschritte der Physik*, **48**, 771–783 (2000). Cited on pages 22 and 125.
- [Dolan77] G. J. Dolan. “Offset masks for lift-off photoprocessing.” *Applied Physics Letters*, **31**, 337–339 (1977). Cited on page 14.
- [Dressel14] J. Dressel and A. N. Korotkov. “Avoiding loopholes with hybrid bell-leggett-garg inequalities.” *Phys. Rev. A*, **89**, 012125 (2014). Cited on page 180.
- [Duan04] L.-M. Duan and H. J. Kimble. “Scalable photonic quantum computation through cavity-assisted interactions.” *Phys. Rev. Lett.* (2004). Cited on page 181.
- [Duan10] L.-M. Duan and C. Monroe. “Colloquium: Quantum networks with trapped ions.” *Rev. Mod. Phys.*, **82**, 1209–1224 (2010). Cited on page 87.
- [Duan11] L.-M. Duan. “Entanglement detection in the vicinity of arbitrary dicke states.” *Phys. Rev. Lett.*, **107**, 180502 (2011). Cited on page 182.
- [Dutt07] M. V. G. Dutt, L. Childress, L. Jiang, E. Togan, J. Maze, F. Jelezko, A. S. Zibrov, P. R. Hemmer, and M. D. Lukin. “Quantum register based on individual electronic and nuclear spin qubits in diamond.” *Science*, **316**, 1312–1316 (2007). Cited on page 125.
- [Eddins19] A. Eddins, J. M. Kreikebaum, D. M. Toyli, E. M. Levenson-Falk, A. Dove, W. P. Livingston, B. A. Levitan, L. C. G. Govia, A. A. Clerk, and I. Siddiqi. “High-efficiency measurement of an artificial atom embedded in a parametric amplifier.” *Phys. Rev. X*, **9**, 011004 (2019). Cited on page 74.
- [Egger18] D. Egger, M. Werninghaus, M. Ganzhorn, G. Salis, A. Fuhrer, P. Müller, and S. Filipp. “Pulsed reset protocol for fixed-frequency superconducting qubits.” *Phys. Rev. Applied*, **10**, 044030 (2018). Cited on pages 125, 126 and 127.
- [Eichler11] C. Eichler, D. Bozyigit, C. Lang, M. Baur, L. Steffen, J. M. Fink, S. Filipp, and A. Wallraff. “Observation of two-mode squeezing in the microwave frequency domain.” *Phys. Rev. Lett.*, **107**, 113601 (2011). Cited on page 173.
- [Eichler14a] C. Eichler, Y. Salathe, J. Mlynek, S. Schmidt, and A. Wallraff. “Quantum-limited amplification and entanglement in coupled nonlinear resonators.” *Phys. Rev. Lett.*, **113**, 110502 (2014). Cited on page 74.

- [Eichler14b] C. Eichler and A. Wallraff. “Controlling the dynamic range of a Josephson parametric amplifier.” *EPJ Quantum Technology*, **1**, 2 (2014). Cited on page 128.
- [Einstein35] A. Einstein, B. Podolsky, and N. Rosen. “Can quantum-mechanical description of physical reality be considered complete?” *Phys. Rev.*, **47**, 777–780 (1935). Cited on pages 2 and 49.
- [Eintein71] A. Eintein. *Letter from Einstein to Max Born, 3 March 1947*. Walker, New York (1971). Cited on page 49.
- [Eisert00] J. Eisert, K. Jacobs, P. Papadopoulos, and M. B. Plenio. “Optimal local implementation of nonlocal quantum gates.” *Phys. Rev. A*, **62**, 052317 (2000). Cited on page 2.
- [Ekert91] A. K. Ekert. “Quantum cryptography based on bell’s theorem.” *Phys. Rev. Lett.*, **67**, 661–663 (1991). Cited on page 3.
- [Elder20] S. S. Elder, C. S. Wang, P. Reinhold, C. T. Hann, K. S. Chou, B. J. Lester, S. Rosenblum, L. Frunzio, L. Jiang, and R. J. Schoelkopf. “High-fidelity measurement of qubits encoded in multilevel superconducting circuits.” *Phys. Rev. X*, **10**, 011001 (2020). Cited on page 126.
- [Elkouss16] D. Elkouss and S. Wehner. “(Nearly) optimal P values for all Bell inequalities.” *npj Quantum Information*, **2**, 16026 (2016). Cited on pages 61, 62 and 162.
- [Elzerman04] J. M. Elzerman, R. Hanson, L. H. W. van Beveren, L. M. K. Vandersypen, and L. P. Kouwenhoven. “Single-shot read-out of an individual electron spin in a quantum dot.” *Nature*, **430**, 431 (2004). Cited on page 125.
- [Eriksson09] J. Eriksson, E. Ollila, and V. Koivunen. “Statistics for complex random variables revisited.” In “2009 IEEE International Conference on Acoustics, Speech and Signal Processing,” 3565–3568 (2009). Cited on page 71.
- [Estalote77] E. A. Estalote and K. G. Ramanathan. “Low-temperature emissivities of copper and aluminum.” *J. Opt. Soc. Am.*, **67**, 39–44 (1977). Cited on page 90.
- [Fan18] L. Fan, C.-L. Zou, R. Cheng, X. Guo, X. Han, Z. Gong, S. Wang, and H. X. Tang. “Superconducting cavity electro-optics: A platform for coherent photon conversion between superconducting and photonic circuits.” *Science Advances*, **4** (2018). Cited on pages 144 and 182.

- [Farhi01] E. Farhi, J. Goldstone, S. Gutmann, J. Lapan, A. Lundgren, and D. Preda. “A quantum adiabatic evolution algorithm applied to random instances of an np-complete problem.” *Science*, **292**, 472–475 (2001). Cited on page 2.
- [Ferreira20] V. S. Ferreira, J. Banker, A. Sipahigil, M. H. Matheny, A. J. Keller, E. Kim, M. Mirhosseini, and O. Painter. “Collapse and revival of an artificial atom coupled to a structured photonic reservoir.” *arXiv:2001.03240* (2020). Cited on page 181.
- [Feynman82] R. P. Feynman. “Simulating physics with computers.” *Int. J. Theor. Phys.*, **21**, 467–488 (1982). Cited on page 1.
- [Fickett82] F. R. Fickett. “Electrical and magnetic properties of internally oxidised copper and dilute copper-iron alloys.” *Journal of Physics F: Metal Physics*, **12**, 1753–1769 (1982). Cited on pages 104 and 113.
- [Fine82] A. Fine. “Hidden variables, joint probability, and the bell inequalities.” *Phys. Rev. Lett.*, **48**, 291–295 (1982). Cited on page 54.
- [Forsch19] M. Forsch, R. Stockill, A. Wallucks, I. Marinković, C. Gärtner, R. A. Norte, F. van Otten, A. Fiore, K. Srinivasan, and S. Gröblacher. “Microwave-to-optics conversion using a mechanical oscillator in its quantum ground state.” *Nature Physics* (2019). Cited on page 144.
- [Fowler10] A. G. Fowler, D. S. Wang, C. D. Hill, T. D. Ladd, R. Van Meter, and L. C. L. Hollenberg. “Surface code quantum communication.” *Phys. Rev. Lett.*, **104**, 180503 (2010). Cited on pages 101, 178 and 181.
- [Fowler13] A. G. Fowler. “Coping with qubit leakage in topological codes.” *Phys. Rev. A*, **88**, 042308 (2013). Cited on page 126.
- [Foxen18] B. Foxen, J. Y. Mutus, E. Lucero, R. Graff, A. Megrant, Y. Chen, C. Quintana, B. Burkett, J. Kelly, E. Jeffrey, Y. Yang, A. Yu, K. Arya, R. Barends, Z. Chen, B. Chiaro, A. Dunsworth, A. Fowler, C. Gidney, M. Giustina, T. Huang, P. Klimov, M. Neeley, C. Neill, P. Roushan, D. Sank, A. Vainsencher, J. Wenner, T. C. White, and J. M. Martinis. “Qubit compatible superconducting interconnects.” *Quantum Science and Technology*, **3**, 014005 (2018). Cited on pages 4 and 143.
- [Freedman72] S. J. Freedman and J. F. Clauser. “Experimental test of local hidden-variable theories.” *Phys. Rev. Lett.*, **28**, 938–941 (1972). Cited on pages 3 and 179.

- [Froissart81] M. Froissart. “Constructive generalization of bell’s inequalities.” *Il Nuovo Cimento B (1971-1996)*, **64**, 241–251 (1981). Cited on page 54.
- [Gallego10] R. Gallego, N. Brunner, C. Hadley, and A. Acín. “Device-independent tests of classical and quantum dimensions.” *Phys. Rev. Lett.*, **105**, 230501 (2010). Cited on pages 3 and 56.
- [Gambetta06] J. Gambetta, A. Blais, D. I. Schuster, A. Wallraff, L. Frunzio, J. Majer, M. H. Devoret, S. M. Girvin, and R. J. Schoelkopf. “Qubit-photon interactions in a cavity: Measurement-induced dephasing and number splitting.” *Phys. Rev. A*, **74**, 042318 (2006). Cited on page 103.
- [Gambetta07] J. Gambetta, W. A. Braff, A. Wallraff, S. M. Girvin, and R. J. Schoelkopf. “Protocols for optimal readout of qubits using a continuous quantum non-demolition measurement.” *Phys. Rev. A*, **76**, 012325–11 (2007). Cited on page 126.
- [Gambetta08] J. Gambetta, A. Blais, M. Boissonneault, A. A. Houck, D. I. Schuster, and S. M. Girvin. “Quantum trajectory approach to circuit QED: Quantum jumps and the zeno effect.” *Phys. Rev. A*, **77**, 012112 (2008). Cited on pages 69, 72, 74, 75 and 76.
- [Gambetta11a] J. M. Gambetta, A. A. Houck, and A. Blais. “Superconducting qubit with Purcell protection and tunable coupling.” *Phys. Rev. Lett.*, **106**, 030502 (2011). Cited on page 167.
- [Gambetta11b] J. M. Gambetta, F. Motzoi, S. T. Merkel, and F. K. Wilhelm. “Analytic control methods for high-fidelity unitary operations in a weakly nonlinear oscillator.” *Phys. Rev. A*, **83**, 012308–13 (2011). Cited on pages 22 and 25.
- [Gao18] Y. Y. Gao, B. J. Lester, Y. Zhang, C. Wang, S. Rosenblum, L. Frunzio, L. Jiang, S. M. Girvin, and R. J. Schoelkopf. “Programmable interference between two microwave quantum memories.” *Phys. Rev. X*, **8**, 021073 (2018). Cited on page 180.
- [Gao19] Y. Y. Gao, B. J. Lester, K. Chou, L. Frunzio, M. H. Devoret, L. Jiang, S. M. Girvin, and R. J. Schoelkopf. “Entanglement of bosonic modes through an engineered exchange interaction.” *Nature*, **566**, 509–512 (2019). Cited on page 180.
- [Gardiner85] C. W. Gardiner and M. J. Collett. “Input and output in damped quantum systems: Quantum stochastic differential equations and the master equation.” *Phys. Rev. A*, **31**, 3761–3774 (1985). Cited on page 70.

- [Gardiner93] C. W. Gardiner. “Driving a quantum system with the output field from another driven quantum system.” *Physical Review Letters*, **70**, 2269–2272 (1993). Cited on page 208.
- [Gasparinetti16] S. Gasparinetti, S. Berger, A. A. Abdumalikov, M. Pechal, S. Filipp, and A. J. Wallraff. “Measurement of a vacuum-induced geometric phase.” *Sci. Adv.*, **2**, e1501732 (2016). Cited on pages 40, 41 and 130.
- [Geerlings13] K. Geerlings, Z. Leghtas, I. M. Pop, S. Shankar, L. Frunzio, R. J. Schoelkopf, M. Mirrahimi, and M. H. Devoret. “Demonstrating a driven reset protocol for a superconducting qubit.” *Phys. Rev. Lett.*, **110**, 120501 (2013). Cited on pages 125, 126, 127 and 149.
- [Gerry90] C. C. Gerry and J. H. Eberly. “Dynamics of a raman coupled model interacting with two quantized cavity fields.” *Phys. Rev. A*, **42**, 6805–6815 (1990). Cited on page 41.
- [Gershenfeld97] N. Gershenfeld and I. Chuang. “Bulk spin resonance quantum computation.” *Science*, **275**, 350–356 (1997). Cited on page 4.
- [Gill03a] R. D. Gill. “Accardi contra bell (cum mundi): The impossible coupling.” *Lecture Notes-Monograph Series*, **42**, 133–154 (2003). Cited on page 61.
- [Gill03b] R. D. Gill. “Time, finite statistics, and bell’s fifth position.” *arXiv:quant-ph/0301059* (2003). Cited on pages 61 and 62.
- [Girvin09] S. M. Girvin, M. H. Devoret, and R. J. Schoelkopf. “Circuit QED and engineering charge-based superconducting qubits.” *Phys. Scr.*, **T137**, 014012 (2009). Cited on page 17.
- [Girvin14] S. M. Girvin. “Circuit QED: superconducting qubits coupled to microwave photons.” In M. Devoret, B. Huard, R. Schoelkopf, and L. F. Cugliandolo editors, “Quantum Machines: Measurement and Control of Engineered Quantum Systems: Lecture Notes of the Les Houches Summer School: Volume 96, July 2011,” Oxford University Press (2014). Cited on page 9.
- [Gisin99] N. Gisin and B. Gisin. “A local hidden variable model of quantum correlation exploiting the detection loophole.” *Phys. Lett. A*, **260**, 323 – 327 (1999). Cited on page 61.
- [Giustina15] M. Giustina, M. A. M. Versteegh, S. Wengerowsky, J. Handsteiner, A. Hochrainer, K. Phelan, F. Steinlechner, J. Kofler, J. Larsson, C. Abellán, W. Amaya, V. Pruneri, M. W. Mitchell, J. Beyer, T. Gerrits, A. E. Lita, L. K. Shalm, S. W. Nam, T. Scheidl, R. Ursin, B. Wittmann, and A. Zeilinger.

- “A significant-loop-hole-free test of bell’s theorem with entangled photons.” [arXiv:1511.03190 \(2015\)](#). Cited on pages 3, 65, 66, 69, 162 and 180.
- [Göppl08] M. Göppl, A. Fragner, M. Baur, R. Bianchetti, S. Filipp, J. M. Fink, P. J. Leek, G. Puebla, L. Steffen, and A. Wallraff. “Coplanar waveguide resonators for circuit quantum electrodynamics.” *J. Appl. Phys.*, **104**, 113904 (2008). Cited on pages 11 and 12.
- [Gottesman99] D. Gottesman and I. L. Chuang. “Demonstrating the viability of universal quantum computation using teleportation and single-qubit operations.” *Nature*, **402**, 390–393 (1999). Cited on pages 2 and 69.
- [Grajcar08] M. Grajcar, S. H. W. van der Ploeg, A. Izmailkov, E. Il’ichev, H.-G. Meyer, A. Fedorov, A. Shnirman, and G. Schön. “Sisyphus cooling and amplification by a superconducting qubit.” *Nat. Phys.*, **4**, 612–616 (2008). Cited on page 126.
- [Grover96] L. K. Grover. “A fast quantum mechanical algorithm for database search.” In “Proceedings of the twenty-eighth annual ACM symposium on Theory of computing,” 212–219. ACM, Philadelphia, Pennsylvania, United States (1996). Cited on page 2.
- [Hacohen-Gourgy16] S. Hacohen-Gourgy, L. S. Martin, E. Flurin, V. V. Ramasesh, K. B. Whaley, and I. Siddiqi. “Quantum dynamics of simultaneously measured non-commuting observables.” *Nature*, **538**, 491–494 (2016). Cited on page 143.
- [Hall10] M. J. W. Hall. “Local deterministic model of singlet state correlations based on relaxing measurement independence.” *Phys. Rev. Lett.*, **105**, 250404 (2010). Cited on page 57.
- [Hanson07] R. Hanson, L. P. Kouwenhoven, J. R. Petta, S. Tarucha, and L. M. K. Vandersypen. “Spins in few-electron quantum dots.” *Rev. Mod. Phys.*, **79**, 1217–1265 (2007). Cited on page 4.
- [Haroche89] S. Haroche and D. Kleppner. “Cavity quantum electrodynamics.” *Physics Today*, **42**, 24–30 (1989). Cited on page 33.
- [Haroche92] S. Haroche. *Fundamental Systems in Quantum Optics*, chapter Cavity quantum electrodynamics. Elsevier, New York (1992). Cited on pages 33 and 38.
- [Haroche20] S. Haroche, M. Brune, and J. M. Raimond. “From cavity to circuit quantum electrodynamics.” *Nature Physics* (2020). Cited on page 33.

- [Harrow09] A. W. Harrow, A. Hassidim, and S. Lloyd. “Quantum algorithm for linear systems of equations.” *Phys. Rev. Lett.*, **103**, 150502 (2009). Cited on page 1.
- [Hease20] W. Hease, A. Rueda, R. Sahu, M. Wulf, G. Arnold, H. G. L. Schwefel, and J. M. Fink. “Cavity quantum electro-optics: Microwave-telecom conversion in the quantum ground state.” *arXiv:2005.12763* (2020). Cited on pages 87, 144 and 182.
- [Heinsoo18] J. Heinsoo, C. K. Andersen, A. Remm, S. Krinner, T. Walter, Y. Salathé, S. Gasparinetti, J.-C. Besse, A. Potočnik, A. Wallraff, and C. Eichler. “Rapid high-fidelity multiplexed readout of superconducting qubits.” *Phys. Rev. Appl.*, **10**, 034040 (2018). Cited on pages 39, 69 and 79.
- [Heiss04] W. D. Heiss. “Exceptional points of non-hermitian operators.” *Journal of Physics A: Mathematical and General*, **37**, 2455 (2004). Cited on pages 133 and 204.
- [Hensen15] B. Hensen, H. Bernien, A. E. Dreau, A. Reiserer, N. Kalb, M. S. Blok, J. Ruitenbergh, R. F. L. Vermeulen, R. N. Schouten, C. Abellan, W. Amaya, V. Pruneri, M. W. Mitchell, M. Markham, D. J. Twitchen, D. Elkouss, S. Wehner, T. H. Taminiau, and R. Hanson. “Loophole-free bell inequality violation using electron spins separated by 1.3 kilometres.” *Nature*, **526**, 682–686 (2015). Cited on pages 3, 65, 66, 69, 162 and 180.
- [Higginbotham18] A. P. Higginbotham, P. S. Burns, M. D. Urmey, R. W. Peterson, N. S. Kampel, B. M. Brubaker, G. Smith, K. W. Lehnert, and C. A. Regal. “Harnessing electro-optic correlations in an efficient mechanical converter.” *Nature Physics*, **14**, 1038 (2018). Cited on pages 144 and 182.
- [Hill97] S. Hill and W. K. Wootters. “Entanglement of a pair of quantum bits.” *Phys. Rev. Lett.*, **78**, 5022– (1997). Cited on page 47.
- [Hofmann12] J. Hofmann, M. Krug, N. Ortegel, L. Gérard, M. Weber, W. Rosenfeld, and H. Weinfurter. “Heralded entanglement between widely separated atoms.” *Science*, **337**, 72–75 (2012). Cited on pages 4 and 144.
- [Hong20] S. S. Hong, A. T. Papageorge, P. Sivarajah, G. Crossman, N. Dider, A. M. Polloreno, E. A. Sete, S. W. Turkowski, M. P. da Silva, and B. R. Johnson. “Demonstration of a parametrically-activated entangling gate protected from flux noise.” *Phys. Rev. A*, **101**, 012302 (2020). Cited on page 141.

- [Hood00] C. J. Hood, T. W. Lynn, A. C. Doherty, A. S. Parkins, and H. J. Kimble. “The atom-cavity microscope: Single atoms bound in orbit by single photons.” *Science*, **287**, 1447–1453 (2000). Cited on page 33.
- [Horodecki95] R. Horodecki, P. Horodecki, and M. Horodecki. “Violating bell inequality by mixed spin-12 states: necessary and sufficient condition.” *Physics Letters A*, **200**, 340 – 344 (1995). Cited on pages 62 and 64.
- [Houck08] A. A. Houck, J. A. Schreier, B. R. Johnson, J. M. Chow, J. Koch, J. M. Gambetta, D. I. Schuster, L. Frunzio, M. H. Devoret, S. M. Girvin, and R. J. Schoelkopf. “Controlling the spontaneous emission of a superconducting transmon qubit.” *Phys. Rev. Lett.*, **101**, 080502 (2008). Cited on pages 11, 27 and 37.
- [Huang21a] S. Huang, B. Lienhard, G. Calusine, A. Vepsäläinen, J. Braumüller, D. K. Kim, A. J. Melville, B. M. Niedzielski, J. L. Yoder, B. Kannan, T. P. Orlando, S. Gustavsson, and W. D. Oliver. “Microwave package design for superconducting quantum processors.” *PRX Quantum*, **2** (2021). Cited on page 27.
- [Huang21b] Z. Huang, P. S. Mundada, A. Gyenis, D. I. Schuster, A. A. Houck, and J. Koch. “Engineering dynamical sweet spots to protect qubits from 1/f noise.” *Physical Review Applied*, **15** (2021). Cited on page 176.
- [Hyllus05] P. Hyllus, O. Gühne, D. Bruß, and M. Lewenstein. “Relations between entanglement witnesses and bell inequalities.” *Phys. Rev. A*, **72**, 012321 (2005). Cited on page 53.
- [Ilves20] J. Ilves, S. Kono, Y. Sunada, S. Yamazaki, M. Kim, K. Koshino, and Y. Nakamura. “On-demand generation and characterization of a microwave time-bin qubit.” *npj Quantum Information*, **6**, 34 (2020). Cited on page 87.
- [Jaynes63] E. Jaynes and F. Cummings. “Comparison of quantum and semiclassical radiation theories with application to the beam maser.” *Proceedings of the IEEE*, **51**, 89–109 (1963). Cited on page 32.
- [Jeffrey14] E. Jeffrey, D. Sank, J. Y. Mutus, T. C. White, J. Kelly, R. Barends, Y. Chen, Z. Chen, B. Chiaro, A. Dunsworth, A. Megrant, P. J. J. O’Malley, C. Neill, P. Roushan, A. Vainsencher, J. Wenner, A. N. Cleland, and J. M. Martinis. “Fast accurate state measurement with superconducting qubits.” *Phys. Rev. Lett.*, **112**, 190504 (2014). Cited on pages 39, 69, 74, 79 and 82.

- [Jelezko04] F. Jelezko, T. Gaebel, I. Popa, A. Gruber, and J. Wrachtrup. “Observation of coherent oscillations in a single electron spin.” *Phys. Rev. Lett.*, **92**, 076401 (2004). Cited on pages 4 and 125.
- [Jiang20] W. Jiang, C. J. Sarabalis, Y. D. Dahmani, R. N. Patel, F. M. Mayor, T. P. McKenna, R. Van Laer, and A. H. Safavi-Naeini. “Efficient bidirectional piezo-optomechanical transduction between microwave and optical frequency.” *Nature Communications*, **11**, 1166 (2020). Cited on page 182.
- [Jin15] X. Y. Jin, A. Kamal, A. P. Sears, T. Gudmundsen, D. Hover, J. Miloshi, R. Slattery, F. Yan, J. Yoder, T. P. Orlando, S. Gustavsson, and W. D. Oliver. “Thermal and residual excited-state population in a 3d transmon qubit.” *Phys. Rev. Lett.*, **114**, 240501 (2015). Cited on page 135.
- [Johnson12] J. E. Johnson, C. Macklin, D. H. Slichter, R. Vijay, E. B. Weingarten, J. Clarke, and I. Siddiqi. “Heralded state preparation in a superconducting qubit.” *Phys. Rev. Lett.*, **109**, 050506 (2012). Cited on pages 125 and 126.
- [Josephson62] B. D. Josephson. “Possible new effects in superconductive tunnelling.” *Physics Letters*, **1**, 251–253 (1962). Cited on pages 4, 14 and 15.
- [Josephson74] B. D. Josephson. “The discovery of tunnelling supercurrents.” *Rev. Mod. Phys.*, **46**, 251–254 (1974). Cited on page 4.
- [Jozsa03] R. Jozsa and N. Linden. “On the role of entanglement in quantum-computational speed-up.” *Proceedings of the Royal Society of London A: Mathematical, Physical and Engineering Sciences*, **459**, 2011–2032 (2003). Cited on page 2.
- [Jurcevic20] P. Jurcevic, A. Javadi-Abhari, L. S. Bishop, I. Lauer, D. F. Bogorin, M. Brink, L. Capelluto, O. Günlük, T. Itoko, N. Kanazawa, A. Kandala, G. A. Keefe, K. Krsulich, W. Landers, E. P. Lewandowski, D. T. McClure, G. Nannicini, A. Narasgond, H. M. Nayfeh, E. Pritchett, M. B. Rothwell, S. Srinivasan, N. Sundaresan, C. Wang, K. X. Wei, C. J. Wood, J.-B. Yau, E. J. Zhang, O. E. Dial, J. M. Chow, and J. M. Gambetta. “Demonstration of quantum volume 64 on a superconducting quantum computing system.” *arXiv:2008.08571* (2020). Cited on pages 4, 87, 126 and 141.
- [Kandala17] A. Kandala, A. Mezzacapo, K. Temme, M. Takita, M. Brink, J. M. Chow, and J. M. Gambetta. “Hardware-efficient variational quantum eigensolver for small molecules and quantum magnets.” *Nature*, **549**, 242–246 (2017). Cited on page 4.

- [Kandala19] A. Kandala, K. Temme, A. D. Córcoles, A. Mezzacapo, J. M. Chow, and J. M. Gambetta. “Error mitigation extends the computational reach of a noisy quantum processor.” *Nature*, **567**, 491–495 (2019). Cited on pages 4 and 143.
- [Katz08] N. Katz, M. Neeley, M. Ansmann, R. C. Bialczak, M. Hofheinz, E. Lucero, A. O’Connell, H. Wang, A. N. Cleland, J. M. Martinis, and A. N. Korotkov. “Reversal of the weak measurement of a quantum state in a superconducting phase qubit.” *Phys. Rev. Lett.*, **101**, 200401 (2008). Cited on page 180.
- [ÅkeLarsson99] J. Åke Larsson. “Modeling the singlet state with local variables.” *Physics Letters A*, **256**, 245–252 (1999). Cited on page 61.
- [Kelly14] J. Kelly, R. Barends, B. Campbell, Y. Chen, Z. Chen, B. Chiaro, A. Dunsworth, A. G. Fowler, I.-C. Hoi, E. Jeffrey, A. Megrant, J. Mutus, C. Neill, P. J. J. O’Malley, C. Quintana, P. Roushan, D. Sank, A. Vainsencher, J. Wenner, T. C. White, A. N. Cleland, and J. M. Martinis. “Optimal quantum control using randomized benchmarking.” *Phys. Rev. Lett.*, **112**, 240504 (2014). Cited on page 126.
- [Kenny21] J. Kenny, H. Mallubhotla, and R. Joynt. “Magnetic noise from metal objects near qubit arrays.” *Phys. Rev. A*, **103**, 062401 (2021). Not cited.
- [Kent05] A. Kent. “Causal quantum theory and the collapse locality loophole.” *Phys. Rev. A*, **72**, 012107 (2005). Cited on page 60.
- [Kessler17] M. Kessler and R. Arnon-Friedman. “Device-independent randomness amplification and privatization.” *arXiv:1705.04148* (2017). Cited on pages 3 and 180.
- [Khalfin85] L. A. Khalfin and B. S. Tsirelson. “Quantum and quasi-classical analogs of bell inequalities.” *Symposium on the Foundations of Modern Physics (ed. Lahti et al.; World Sci. Publ.)*, 441–460 (1985). Cited on page 52.
- [Khaneja05] N. Khaneja, T. Reiss, C. Kehlet, T. Schulte-Herbrüggen, and S. J. Glaser. “Optimal control of coupled spin dynamics: design of {NMR} pulse sequences by gradient ascent algorithms.” *Journal of Magnetic Resonance*, **172**, 296–305 (2005). Cited on page 25.
- [Kim21] E. Kim, X. Zhang, V. S. Ferreira, J. Banker, J. K. Iverson, A. Sipahigil, M. Bello, A. González-Tudela, M. Mirhosseini, and O. Painter. “Quantum electrodynamics in a topological waveguide.” *Physical Review X*, **11** (2021). Cited on pages 40, 106 and 181.

- [Kimble08] H. J. Kimble. “The quantum internet.” *Nature*, **453**, 1023–1030 (2008). Cited on pages 87 and 182.
- [Kitaev03] A. Y. Kitaev. “Fault-tolerant quantum computation by anyons.” *Annals of Physics*, **303**, 2 – 30 (2003). Cited on pages 2 and 69.
- [Kjaergaard20] M. Kjaergaard, M. E. Schwartz, J. Braumüller, P. Krantz, J. I.-J. Wang, S. Gustavsson, and W. D. Oliver. “Superconducting qubits: Current state of play.” *Annual Review of Condensed Matter Physics*, **11**, 369–395 (2020). Cited on page 16.
- [Knill98] E. Knill, R. Laflamme, and W. H. Zurek. “Resilient quantum computation.” *Science*, **279**, 342–345 (1998). Cited on pages 2 and 69.
- [Koch07] J. Koch, T. M. Yu, J. Gambetta, A. A. Houck, D. I. Schuster, J. Majer, A. Blais, M. H. Devoret, S. M. Girvin, and R. J. Schoelkopf. “Charge-insensitive qubit design derived from the Cooper pair box.” *Phys. Rev. A*, **76**, 042319 (2007). Cited on pages 4, 17, 19, 21, 32, 76, 128 and 205.
- [Kofler06] J. Kofler, T. Paterek, and i. c. v. Brukner. “Experimenter’s freedom in bell’s theorem and quantum cryptography.” *Phys. Rev. A*, **73**, 022104 (2006). Cited on page 57.
- [Kok07] P. Kok, W. J. Munro, K. Nemoto, T. C. Ralph, J. P. Dowling, and G. J. Milburn. “Linear optical quantum computing with photonic qubits.” *Rev. Mod. Phys.*, **79**, 135–174 (2007). Cited on page 3.
- [Kono18] S. Kono, K. Koshino, Y. Tabuchi, A. Noguchi, and Y. Nakamura. “Quantum non-demolition detection of an itinerant microwave photon.” *Nature Physics* (2018). Cited on pages 39 and 181.
- [Krinner19] S. Krinner, S. Storz, P. Kurpiers, P. Magnard, J. Heinsoo, R. Keller, J. Lütolf, C. Eichler, and A. Wallraff. “Engineering cryogenic setups for 100-qubit scale superconducting circuit systems.” *EPJ Quantum Technology*, **6**, 2 (2019). Cited on pages 4, 101, 143 and 182.
- [Krinner20] S. Krinner, P. Kurpiers, B. Royer, P. Magnard, I. Tsitsilin, J.-C. Besse, A. Remm, A. Blais, and A. Wallraff. “Demonstration of an all-microwave controlled-phase gate between far-detuned qubits.” *Phys. Rev. Appl.*, **14**, 044039 (2020). Cited on pages 76 and 141.
- [Kurpiers17] P. Kurpiers, T. Walter, P. Magnard, Y. Salathe, and A. Wallraff. “Characterizing the attenuation of coaxial and rectangular microwave-frequency

- waveguides at cryogenic temperatures.” *EPJ Quantum Technology*, **4**, 8 (2017). Cited on pages 87, 122 and 181.
- [Kurpiers18] P. Kurpiers, P. Magnard, T. Walter, B. Royer, M. Pechal, J. Heinsoo, Y. Salathé, A. Akin, S. Storz, J.-C. Besse, S. Gasparinetti, A. Blais, and A. Wallraff. “Deterministic quantum state transfer and remote entanglement using microwave photons.” *Nature*, **558**, 264–267 (2018). Cited on pages 26, 39, 41, 43, 44, 45, 46, 47, 79, 87, 101, 141, 144, 146, 155, 174, 179, 182, 193 and 194.
- [Kurpiers19a] P. Kurpiers. *Quantum Networks with Superconducting Circuits*. Ph.D. thesis, ETH Zurich (2019). Cited on pages 193 and 194.
- [Kurpiers19b] P. Kurpiers, M. Pechal, B. Royer, P. Magnard, T. Walter, J. Heinsoo, Y. Salathé, A. Akin, S. Storz, J.-C. Besse, S. Gasparinetti, A. Blais, and A. Wallraff. “Quantum communication with time-bin encoded microwave photons.” *Phys. Rev. Appl.*, **12**, 044067 (2019). Cited on pages 48, 92, 130 and 178.
- [Lacroix20] N. Lacroix, C. Hellings, C. K. Andersen, A. Di Paolo, A. Remm, S. Lazar, S. Krinner, G. J. Norris, M. Gabureac, J. Heinsoo, A. Blais, C. Eichler, and A. Wallraff. “Improving the performance of deep quantum optimization algorithms with continuous gate sets.” *PRX Quantum*, **1**, 110304 (2020). Cited on page 4.
- [Lambert20] N. J. Lambert, A. Rueda, F. Sedlmeir, and H. G. L. Schwefel. “Coherent conversion between microwave and optical photons—an overview of physical implementations.” *Advanced Quantum Technologies*, **3**, 1900077 (2020). Cited on page 182.
- [Larsson14] J.-A. Larsson. “Loopholes in Bell inequality tests of local realism.” *J. Phys. A: Math. Theor.*, **47**, 424003 (2014). Cited on pages 3, 56, 57 and 160.
- [Lauk20] N. Lauk, N. Sinclair¹, S. Barzanjeh, J. P. Covey¹, M. Saffman, M. Spiropulu¹, and C. Simon. “Perspectives on quantum transduction.” *Quantum Science and Technology*, **5**, 020501 (2020). Cited on page 182.
- [Le Sage21] G. P. Le Sage and R. Stringfellow. “3d printed, self-temperature compensated microwave cavity notch filters.” *IEEE Access*, **9**, 32969–32978 (2021). Cited on page 122.
- [Lee99] J. Lee, H. Lee, W. Kim, J. Lee, and J. Kim. “Suppression of coupled-slotline mode on CPW using air-bridges measured by picosecond photoconductive sampling.” *Microwave and Guided Wave Letters, IEEE [see also IEEE*

- Microwave and Wireless Components Letters*, **9**, 265–267 (1999). Cited on page 13.
- [Leek09] P. J. Leek, S. Filipp, P. Maurer, M. Baur, R. Bianchetti, J. M. Fink, M. Göppl, L. Steffen, and A. Wallraff. “Using sideband transitions for two-qubit operations in superconducting circuits.” *Phys. Rev. B*, **79**, 180511 (2009). Cited on page 40.
- [Lei20] C. U. Lei, L. Krayzman, S. Ganjam, L. Frunzio, and R. J. Schoelkopf. “High coherence superconducting microwave cavities with indium bump bonding.” *Applied Physics Letters*, **116**, 154002 (2020). Cited on pages 4 and 143.
- [Leibfried03] D. Leibfried, R. Blatt, C. Monroe, and D. Wineland. “Quantum dynamics of single trapped ions.” *Rev. Mod. Phys.*, **75**, 281–324 (2003). Cited on page 4.
- [Lescanne20] R. Lescanne, M. Villiers, T. Peronnin, A. Sarlette, M. Delbecq, B. Huard, T. Kontos, M. Mirrahimi, and Z. Leghtas. “Exponential suppression of bit-flips in a qubit encoded in an oscillator.” *Nature Physics* (2020). Cited on page 40.
- [Leung19] N. Leung, Y. Lu, S. Chakram, R. K. Naik, N. Earnest, R. Ma, K. Jacobs, A. N. Cleland, and D. I. Schuster. “Deterministic bidirectional communication and remote entanglement generation between superconducting qubits.” *npj Quantum Information*, **5**, 18 (2019). Cited on pages 40, 48, 87, 101, 144 and 178.
- [Li18] M.-H. Li, C. Wu, Y. Zhang, W.-Z. Liu, B. Bai, Y. Liu, W. Zhang, Q. Zhao, H. Li, Z. Wang, L. You, W. J. Munro, J. Yin, J. Zhang, C.-Z. Peng, X. Ma, Q. Zhang, J. Fan, and J.-W. Pan. “Test of local realism into the past without detection and locality loopholes.” *Phys. Rev. Lett.*, **121**, 080404 (2018). Cited on page 57.
- [Lienhard20] J. H. Lienhard, IV and J. H. Lienhard, V. *A Heat Transfer Textbook*. Phlogiston Press, Cambridge, MA, 5th edition (2020). Version 5.10. Cited on pages 90, 92 and 98.
- [Liu16] Y. Liu, S. Shankar, N. Ofek, M. Hatridge, A. Narla, K. M. Sliwa, L. Frunzio, R. J. Schoelkopf, and M. H. Devoret. “Comparing and combining measurement-based and driven-dissipative entanglement stabilization.” *Phys. Rev. X*, **6**, 011022 (2016). Cited on page 126.

- [Lloyd13] S. Lloyd, M. Mohseni, and P. Rebentrost. “Quantum algorithms for supervised and unsupervised machine learning.” *arXiv:1307.0411* (2013). Cited on page 1.
- [Lounasmaa74] O. V. Lounasmaa. *Experimental Principles and Methods Below 1 K*. Academic Press (1974). Cited on page 88.
- [Lucero10] E. Lucero, J. Kelly, R. C. Bialczak, M. Lenander, M. Mariantoni, M. Neeley, A. D. O’Connell, D. Sank, H. Wang, M. Weides, J. Wenner, T. Yamamoto, A. N. Cleland, and J. M. Martinis. “Reduced phase error through optimized control of a superconducting qubit.” *Phys. Rev. A*, **82**, 042339 (2010). Cited on page 25.
- [Mabuchi02] H. Mabuchi and A. C. Doherty. “Cavity quantum electrodynamics: Coherence in context.” *Science*, **298**, 1372–1377 (2002). Cited on page 33.
- [Macklin15] C. Macklin, K. O’Brien, D. Hover, M. E. Schwartz, V. Bolkhovskiy, X. Zhang, W. D. Oliver, and I. Siddiqi. “A near-quantum-limited Josephson traveling-wave parametric amplifier.” *Science*, **350**, 307–310 (2015). Cited on page 74.
- [Magnard18] P. Magnard, P. Kurpiers, B. Royer, T. Walter, J.-C. Besse, S. Gasparinetti, M. Pechal, J. Heinsoo, S. Storz, A. Blais, and A. Wallraff. “Fast and unconditional all-microwave reset of a superconducting qubit.” *Phys. Rev. Lett.*, **121**, 060502 (2018). Cited on pages 19, 41, 43, 125, 126, 127 and 179.
- [Magnard20] P. Magnard, S. Storz, P. Kurpiers, J. Schär, F. Marxer, J. Lütolf, T. Walter, J.-C. Besse, M. Gabureac, K. Reuer, A. Akin, B. Royer, A. Blais, and A. Wallraff. “Microwave quantum link between superconducting circuits housed in spatially separated cryogenic systems.” *Phys. Rev. Lett.*, **125**, 260502 (2020). Cited on pages 13, 41, 44, 79, 101, 122, 144 and 179.
- [Mallet09] F. Mallet, F. R. Ong, A. Palacios-Laloy, F. Nguyen, P. Bertet, D. Vion, and D. Esteve. “Single-shot qubit readout in circuit quantum electrodynamics.” *Nat. Phys.*, **5**, 791–795 (2009). Cited on page 69.
- [Mariantoni11a] M. Mariantoni, H. Wang, R. C. Bialczak, M. Lenander, E. Lucero, M. Neeley, A. D. O’Connell, D. Sank, M. Weides, J. Wenner, T. Yamamoto, Y. Yin, J. Zhao, J. M. Martinis, and A. N. Cleland. “Photon shell game in three-resonator circuit quantum electrodynamics.” *Nat. Phys.*, **7**, 287–293 (2011). Cited on page 40.

- [Mariantoni11b] M. Mariantoni, H. Wang, T. Yamamoto, M. Neeley, R. C. Bialczak, Y. Chen, M. Lenander, E. Lucero, A. D. O’Connell, D. Sank, M. Weides, J. Wenner, Y. Yin, J. Zhao, A. N. Korotkov, A. N. Cleland, and J. M. Martinis. “Implementing the quantum von Neumann architecture with superconducting circuits.” *Science*, **334**, 61–65 (2011). Cited on page 125.
- [Marlow11] W. A. Marlow. “Design of Multilayer Insulation for the Multipurpose Hydrogen Test Bed.” Technical report, NASA (2011). Cited on page 121.
- [Marquardt02] E. D. Marquardt, J. P. Le, and R. Radebaugh. “Cryogenic material properties database.” *Cryocoolers 11*, 681–687 (2002). Cited on page 108.
- [Mattle96] K. Mattle, H. Weinfurter, P. G. Kwiat, and A. Zeilinger. “Dense coding in experimental quantum communication.” *Phys. Rev. Lett.*, **76**, 4656–4659 (1996). Cited on page 2.
- [Mayers98] D. Mayers and A. Yao. “Quantum cryptography with imperfect apparatus.” In “Proceedings 39th Annual Symposium on Foundations of Computer Science (Cat. No.98CB36280),” 503–509 (1998). Cited on pages 3 and 55.
- [McEwen21] M. McEwen, D. Kafri, Z. Chen, J. Atalaya, K. J. Satzinger, C. Quintana, P. V. Klimov, D. Sank, C. Gidney, A. G. Fowler, F. Arute, K. Arya, B. Buckley, B. Burkett, N. Bushnell, B. Chiaro, R. Collins, S. Demura, A. Dunsworth, C. Erickson, B. Foxen, M. Giustina, T. Huang, S. Hong, E. Jeffrey, S. Kim, K. Kechedzhi, F. Kostritsa, P. Laptev, A. Megrant, X. Mi, J. Mutus, O. Naaman, M. Neeley, C. Neill, M. Niu, A. Paler, N. Redd, P. Roushan, T. C. White, J. Yao, P. Yeh, A. Zalcman, Y. Chen, V. N. Smelyanskiy, J. M. Martinis, H. Neven, J. Kelly, A. N. Korotkov, A. G. Petukhov, and R. Barends. “Removing leakage-induced correlated errors in superconducting quantum error correction.” *Nature Communications* (2021). Cited on pages 125, 126 and 127.
- [McKague09] M. McKague. “Device independent quantum key distribution secure against coherent attacks with memoryless measurement devices.” *New Journal of Physics*, **11**, 103037 (2009). Cited on pages 3 and 55.
- [McKay15] D. C. McKay, R. Naik, P. Reinhold, L. S. Bishop, and D. I. Schuster. “High-contrast qubit interactions using multimode cavity qed.” *Phys. Rev. Lett.*, **114**, 080501 (2015). Cited on page 10.
- [McKay17] D. C. McKay, C. J. Wood, S. Sheldon, J. M. Chow, and J. M. Gambetta. “Efficient z gates for quantum computing.” *Phys. Rev. A*, **96**, 022330 (2017). Cited on pages 24 and 25.

- [McKenna20] T. P. McKenna, J. D. Witmer, R. N. Patel, W. Jiang, R. Van Laer, P. Arrangoiz-Arriola, E. A. Wollack, J. F. Herrmann, and A. H. Safavi-Naeini. “Cryogenic microwave-to-optical conversion using a triply-resonant lithium niobate on sapphire transducer.” *arXiv:2005.00897* (2020). Cited on page 182.
- [McRae20] C. R. H. McRae, R. E. Lake, J. L. Long, M. Bal, X. Wu, B. Jugdersuren, T. H. Metcalf, X. Liu, and D. P. Pappas. “Dielectric loss extraction for superconducting microwave resonators.” *Applied Physics Letters*, **116**, 194003 (2020). Cited on page 10.
- [Minev19] Z. K. Mineev, S. O. Mundhada, S. Shankar, P. Reinhold, R. Gutiérrez-Jáuregui, R. J. Schoelkopf, M. Mirrahimi, H. J. Carmichael, and M. H. Devoret. “To catch and reverse a quantum jump mid-flight.” *Nature*, **570**, 200–204 (2019). Cited on page 143.
- [Mirhosseini18] M. Mirhosseini, E. Kim, V. S. Ferreira, M. Kalae, A. Sipahigil, A. J. Keller, and O. Painter. “Superconducting metamaterials for waveguide quantum electrodynamics.” *Nat. Comm.*, **9**, 3706 (2018). Cited on page 181.
- [Mirhosseini19] M. Mirhosseini, E. Kim, X. Zhang, A. Sipahigil, P. B. Dieterle, A. J. Keller, A. Asenjo-Garcia, D. E. Chang, and O. Painter. “Cavity quantum electrodynamics with atom-like mirrors.” *Nature* (2019). Cited on page 181.
- [Mirhosseini20] M. Mirhosseini, A. Sipahigil, M. Kalae, and O. Painter. “Superconducting qubit to optical photon transduction.” *Nature*, **588**, 599–603 (2020). Cited on pages 87, 144 and 182.
- [Moehring07] D. L. Moehring, P. Maunz, S. Olmschenk, K. C. Younge, D. N. Matsukevich, L. M. Duan, and C. Monroe. “Entanglement of single-atom quantum bits at a distance.” *Nature*, **449**, 68–71 (2007). Cited on pages 4 and 144.
- [Monroe95a] C. Monroe, D. M. Meekhof, B. E. King, W. M. Itano, and D. J. Wineland. “Demonstration of a fundamental quantum logic gate.” *Phys. Rev. Lett.*, **75**, 4714–4717 (1995). Cited on page 4.
- [Monroe95b] C. Monroe, D. M. Meekhof, B. E. King, S. R. Jefferts, W. M. Itano, D. J. Wineland, and P. Gould. “Resolved-sideband raman cooling of a bound atom to the 3d zero-point energy.” *Phys. Rev. Lett.*, **75**, 4011–4014 (1995). Cited on page 125.
- [Monroe14] C. Monroe, R. Raussendorf, A. Ruthven, K. R. Brown, P. Maunz, L.-M. Duan, and J. Kim. “Large-scale modular quantum-computer architecture

- with atomic memory and photonic interconnects.” *Phys. Rev. A*, **89**, 022317 (2014). Cited on page 180.
- [Montanaro16] A. Montanaro. “Quantum algorithms: an overview.” *npj Quantum Information*, **2**, 15023 (2016). Cited on page 2.
- [Morin19] O. Morin, M. Körber, S. Langenfeld, and G. Rempe. “Deterministic shaping and reshaping of single-photon temporal wave functions.” *Phys. Rev. Lett.*, **123**, 133602 (2019). Cited on page 43.
- [Motzoi09] F. Motzoi, J. M. Gambetta, P. Rebentrost, and F. K. Wilhelm. “Simple pulses for elimination of leakage in weakly nonlinear qubits.” *Phys. Rev. Lett.*, **103**, 110501 (2009). Cited on pages 19, 22, 25, 149 and 167.
- [Murch12] K. W. Murch, U. Vool, D. Zhou, S. J. Weber, S. M. Girvin, and I. Siddiqi. “Cavity-assisted quantum bath engineering.” *Phys. Rev. Lett.*, **109**, 183602 (2012). Cited on page 126.
- [Murta19] G. Murta, S. B. van Dam, J. Ribeiro, R. Hanson, and S. Wehner. “Towards a realization of device-independent quantum key distribution.” *Quantum Science and Technology*, **4**, 035011 (2019). Cited on pages 3, 55, 178 and 180.
- [Musilova05] V. Musilova, P. Hanzelka, T. Kralik, and A. Srnka. “Low temperature radiative properties of materials used in cryogenics.” *Cryogenics*, **45**, 529–536 (2005). Cited on page 90.
- [Naik17] R. K. Naik, N. Leung, S. Chakram, P. Groszkowski, Y. Lu, N. Earnest, D. C. McKay, J. Koch, and D. I. Schuster. “Random access quantum information processors.” *Nature Communications*, **8**, 1904 (2017). Cited on page 40.
- [Nakamura99] Y. Nakamura, Y. A. Pashkin, and J. S. Tsai. “Coherent control of macroscopic quantum states in a single-Cooper-pair box.” *Nature*, **398**, 786–788 (1999). Cited on pages 4 and 17.
- [Negnevitsky18] V. Negnevitsky, M. Marinelli, K. K. Mehta, H.-Y. Lo, C. Flühmann, and J. P. Home. “Repeated multi-qubit readout and feedback with a mixed-species trapped-ion register.” *Nature*, **563**, 527–531 (2018). Cited on page 181.
- [Nickerson13] N. H. Nickerson, Y. Li, and S. C. Benjamin. “Topological quantum computing with a very noisy network and local error rates approaching one percent.” *Nature Communications*, **4**, 1756 (2013). Cited on page 181.

- [Nickerson14] N. H. Nickerson, J. F. Fitzsimons, and S. C. Benjamin. “Freely scalable quantum technologies using cells of 5-to-50 qubits with very lossy and noisy photonic links.” *Phys. Rev. X*, **4**, 041041 (2014). Cited on pages 143, 178 and 181.
- [Nickerson15] N. Nickerson. *Practical fault-tolerant quantum computing*. Ph.D. thesis, Imperial College London (2015). Cited on page 101.
- [Nielsen05] M. A. Nielsen and C. M. Dawson. “Fault-tolerant quantum computation with cluster states.” *Phys. Rev. A*, **71**, 042323 (2005). Cited on page 40.
- [Nielsen11] M. A. Nielsen and I. L. Chuang. *Quantum Computation and Quantum Information*. Cambridge University Press, New York, NY, USA, 10th edition (2011). Cited on page 23.
- [Nieto-Silleras14] O. Nieto-Silleras, S. Pironio, and J. Silman. “Using complete measurement statistics for optimal device-independent randomness evaluation.” *New Journal of Physics*, **16**, 013035 (2014). Cited on pages 3 and 55.
- [Ofek16] N. Ofek, A. Petrenko, R. Heeres, P. Reinhold, Z. Leghtas, B. Vlastakis, Y. Liu, L. Frunzio, S. M. Girvin, L. Jiang, M. Mirrahimi, M. H. Devoret, and R. J. Schoelkopf. “Extending the lifetime of a quantum bit with error correction in superconducting circuits.” *Nature*, **536**, 441–445 (2016). Cited on pages 4 and 143.
- [O’Malley16] P. J. J. O’Malley, R. Babbush, I. D. Kivlichan, J. Romero, J. R. McClean, R. Barends, J. Kelly, P. Roushan, A. Tranter, N. Ding, B. Campbell, Y. Chen, Z. Chen, B. Chiaro, A. Dunsworth, A. G. Fowler, E. Jeffrey, E. Lucero, A. Megrant, J. Y. Mutus, M. Neeley, C. Neill, C. Quintana, D. Sank, A. Vainsencher, J. Wenner, T. C. White, P. V. Coveney, P. J. Love, H. Neven, A. Aspuru-Guzik, and J. M. Martinis. “Scalable quantum simulation of molecular energies.” *Phys. Rev. X*, **6**, 031007 (2016). Cited on page 4.
- [Otterbach17] J. S. Otterbach, R. Manenti, N. Alidoust, A. Bestwick, M. Block, B. Bloom, S. Caldwell, N. Didier, E. S. Fried, S. Hong, P. Karalekas, C. B. Osborn, A. Papageorge, E. C. Peterson, G. Prawiroatmodjo, N. Rubin, C. A. Ryan, D. Scarabelli, M. Scheer, E. A. Sete, P. Sivarajah, R. S. Smith, A. Staley, N. Tezak, W. J. Zeng, A. Hudson, B. R. Johnson, M. Reagor, M. P. da Silva, and C. Rigetti. “Unsupervised Machine Learning on a Hybrid Quantum Computer.” *arXiv:1712.05771* (2017). Cited on page 141.
- [Owens18] C. Owens, A. LaChapelle, B. Saxberg, B. M. Anderson, R. Ma, J. Simon, and D. I. Schuster. “Quarter-flux hofstadter lattice in a qubit-compatible

- microwave cavity array.” *Phys. Rev. A*, **97**, 013818 (2018). Cited on page 181.
- [Paik11] H. Paik, D. I. Schuster, L. S. Bishop, G. Kirchmair, G. Catelani, A. P. Sears, B. R. Johnson, M. J. Reagor, L. Frunzio, L. I. Glazman, S. M. Girvin, M. H. Devoret, and R. J. Schoelkopf. “Observation of high coherence in Josephson junction qubits measured in a three-dimensional circuit QED architecture.” *Phys. Rev. Lett.*, **107**, 240501 (2011). Cited on page 4.
- [Parma14] V. Parma. “Cryostat design.” *CAS - CERN Accelerator School: Course on Superconductivity for Accelerators* (2014). Cited on pages 92 and 121.
- [Pashkin03] Y. A. Pashkin, T. Yamamoto, O. Astafiev, Y. Nakamura, D. V. Averin, and J. S. Tsai. “Quantum oscillations in two coupled charge qubits.” *Nature*, **421**, 823–826 (2003). Cited on page 4.
- [Pearle70] P. M. Pearle. “Hidden-variable example based upon data rejection.” *Phys. Rev. D*, **2**, 1418–1425 (1970). Cited on pages 61 and 180.
- [Pechal14] M. Pechal, L. Huthmacher, C. Eichler, S. Zeytinoğlu, A. A. Abdumalikov Jr., S. Berger, A. Wallraff, and S. Filipp. “Microwave-controlled generation of shaped single photons in circuit quantum electrodynamics.” *Phys. Rev. X*, **4**, 041010 (2014). Cited on pages 41, 43, 44, 87, 127 and 130.
- [Pechal16a] M. Pechal. *Microwave photonics in superconducting circuits*. Ph.D. thesis, ETH Zurich (2016). Cited on pages 193, 194 and 195.
- [Pechal16b] M. Pechal, J.-C. Besse, M. Mondal, M. Oppliger, S. Gasparinetti, and A. Wallraff. “Superconducting switch for fast on-chip routing of quantum microwave fields.” *Phys. Rev. Appl.*, **6**, 024009 (2016). Cited on page 180.
- [Penrose98] R. Penrose. “Quantum computation, entanglement and state reduction.” *Philosophical Transactions of the Royal Society of London. Series A: Mathematical, Physical and Engineering Sciences*, **356**, 1927–1939 (1998). Cited on page 2.
- [Pfaff17] W. Pfaff, C. J. Axline, L. D. Burkhardt, U. Vool, P. Reinhold, L. Frunzio, L. Jiang, M. H. Devoret, and R. J. Schoelkopf. “Controlled release of multiphoton quantum states from a microwave cavity memory.” *Nat. Phys.* (2017). Cited on pages 43, 87 and 180.
- [Pichler17] H. Pichler, S. Choi, P. Zoller, and M. D. Lukin. “Universal photonic quantum computation via time-delayed feedback.” *Proceedings of the National*

- Academy of Sciences*, **114**, 11362–11367 (2017). Cited on pages 106 and 181.
- [Pirandola16] S. Pirandola and S. L. Braunstein. “Physics: Unite to build a quantum internet.” *Nature*, **532** (2016). Cited on page 87.
- [Pironio05] S. Pironio. “Lifting bell inequalities.” *Journal of Mathematical Physics*, **46**, 062112 (2005). Cited on page 52.
- [Pironio09] S. Pironio, A. Acín, N. Brunner, N. Gisin, S. Massar, and V. Scarani. “Device-independent quantum key distribution secure against collective attacks.” *New Journal of Physics*, **11**, 045021 (2009). Cited on pages 3 and 55.
- [Pitowsky86] I. Pitowsky. “The range of quantum probability.” *Journal of Mathematical Physics*, **27**, 1556–1565 (1986). Cited on page 52.
- [Planat19] L. Planat, R. Dassonneville, J. P. Martínez, F. Foroughi, O. Buisson, W. Hasch-Guichard, C. Naud, R. Vijay, K. Murch, and N. Roch. “Understanding the saturation power of josephson parametric amplifiers made from squid arrays.” *Phys. Rev. Applied*, **11**, 034014 (2019). Cited on page 74.
- [Pobell06] F. Pobell. *Matter and Methods at Low Temperatures*. Springer, 3rd edition, (2006). Cited on page 110.
- [Pope13] J. E. Pope and A. Kay. “Limited measurement dependence in multiple runs of a bell test.” *Phys. Rev. A*, **88**, 032110 (2013). Cited on page 58.
- [Popescu94] S. Popescu and D. Rohrlich. “Quantum nonlocality as an axiom.” *Foundations of Physics*, **24**, 379–385 (1994). Cited on page 52.
- [Pozar12] D. M. Pozar. *Microwave Engineering*. Wiley & Sons, Inc., New Jersey, USA, 4th edition (2012). Cited on pages 10, 11, 12, 122, 181, 182, 183, 184, 185 and 186.
- [Premaratne17] S. P. Premaratne, F. C. Wellstood, and B. S. Palmer. “Characterization of coherent population-trapped states in a circuit-qed Λ system.” *Phys. Rev. A*, **96**, 043858 (2017). Cited on page 126.
- [Preskill18] J. Preskill. “Quantum Computing in the NISQ era and beyond.” *Quantum*, **2**, 79 (2018). Cited on pages 4 and 143.
- [Purcell46] E. M. Purcell. “Spontaneous emission probabilities at radio frequencies.” *Phys. Rev.*, **69**, 681–681 (1946). Cited on page 38.

- [Raimond01] J. M. Raimond, M. Brune, and S. Haroche. “Manipulating quantum entanglement with atoms and photons in a cavity.” *Rev. Mod. Phys.*, **73**, 565–582 (2001). Cited on page 33.
- [Ramanathan18] R. Ramanathan, M. Horodecki, S. Pironio, K. Horodecki, and P. Horodecki. “Generic randomness amplification schemes using hardy paradoxes.” *arXiv:1810.11648* (2018). Cited on page 180.
- [Rastall85] P. Rastall. “Locality, bell’s theorem, and quantum mechanics.” *Foundations of Physics*, **15**, 963–972 (1985). Cited on page 52.
- [Rauch18] D. Rauch, J. Handsteiner, A. Hochrainer, J. Gallicchio, A. S. Friedman, C. Leung, B. Liu, L. Bulla, S. Ecker, F. Steinlechner, R. Ursin, B. Hu, D. Leon, C. Benn, A. Ghedina, M. Cecconi, A. H. Guth, D. I. Kaiser, T. Scheidl, and A. Zeilinger. “Cosmic Bell test using random measurement settings from high-redshift quasars.” *Phys. Rev. Lett.*, **121**, 080403 (2018). Cited on page 57.
- [Raussendorf01] R. Raussendorf and H. J. Briegel. “A one-way quantum computer.” *Phys. Rev. Lett.*, **86**, 5188–5191 (2001). Cited on page 2.
- [Reagor13] M. Reagor, H. Paik, G. Catelani, L. Sun, C. Axline, E. Holland, I. M. Pop, N. A. Masluk, T. Brecht, L. Frunzio, M. H. Devoret, L. I. Glazman, and R. J. Schoelkopf. “Reaching 10 ms single photon lifetimes for superconducting aluminum cavities.” *Appl. Phys. Lett.*, **102**, 192604 (2013). Cited on pages 4, 122 and 181.
- [Reagor16] M. Reagor, W. Pfaff, C. Axline, R. W. Heeres, N. Ofek, K. Sliwa, E. Holland, C. Wang, J. Blumoff, K. Chou, M. J. Hatridge, L. Frunzio, M. H. Devoret, L. Jiang, and R. J. Schoelkopf. “Quantum memory with millisecond coherence in circuit QED.” *Phys. Rev. B*, **94**, 014506 (2016). Cited on page 122.
- [Rebentrost18] P. Rebentrost and S. Lloyd. “Quantum computational finance: quantum algorithm for portfolio optimization.” *arXiv:1811.03975* (2018). Cited on page 2.
- [Reed10a] M. D. Reed, L. DiCarlo, B. R. Johnson, L. Sun, D. I. Schuster, L. Frunzio, and R. J. Schoelkopf. “High-fidelity readout in circuit quantum electrodynamics using the Jaynes-Cummings nonlinearity.” *Phys. Rev. Lett.*, **105**, 173601–4 (2010). Cited on pages 4, 69, 74 and 82.

- [Reed10b] M. D. Reed, B. R. Johnson, A. A. Houck, L. DiCarlo, J. M. Chow, D. I. Schuster, L. Frunzio, and R. J. Schoelkopf. “Fast reset and suppressing spontaneous emission of a superconducting qubit.” *Appl. Phys. Lett.*, **96**, 203110 (2010). Cited on pages 125, 126 and 127.
- [Reed12] M. D. Reed, L. DiCarlo, S. E. Nigg, L. Sun, L. Frunzio, S. M. Girvin, and R. J. Schoelkopf. “Realization of three-qubit quantum error correction with superconducting circuits.” *Nature*, **482**, 382–385 (2012). Cited on page 125.
- [Reichardt13] B. W. Reichardt, F. Unger, and U. Vazirani. “Classical command of quantum systems.” *Nature*, **496**, 456–460 (2013). Cited on page 3.
- [Reiher17] M. Reiher, N. Wiebe, K. M. Svore, D. Wecker, and M. Troyer. “Elucidating reaction mechanisms on quantum computers.” *Proceedings of the National Academy of Sciences*, **114**, 7555–7560 (2017). Cited on pages 1, 143 and 182.
- [Reiserer14] A. Reiserer, N. Kalb, G. Rempe, and S. Ritter. “A quantum gate between a flying optical photon and a single trapped atom.” *Nature*, **508**, 237–240 (2014). Cited on page 181.
- [Reiserer15] A. Reiserer and G. Rempe. “Cavity-based quantum networks with single atoms and optical photons.” *Rev. Mod. Phys.*, **87**, 1379–1418 (2015). Cited on page 3.
- [Reuer21] K. Reuer, J. Besse, L. Wernli, P. Magnard, P. Kurpiers, G. J. Norris, A. Wallraff, and C. Eichler. “Realization of a universal quantum gate set for itinerant microwave photons.” *arXiv:2106.03481* (2021). Cited on page 181.
- [Rhode&Schwarz16] Rhode&Schwarz. “Generating multiple phase coherent signals - aligned in phase and time.” Technical Report 1GP108_1E, Rhode & Schwarz (2016). Cited on page 169.
- [Ristè12a] D. Ristè, C. C. Bultink, K. W. Lehnert, and L. DiCarlo. “Feedback control of a solid-state qubit using high-fidelity projective measurement.” *Phys. Rev. Lett.*, **109**, 240502 (2012). Cited on pages 125 and 126.
- [Ristè12b] D. Ristè, J. G. van Leeuwen, H.-S. Ku, K. W. Lehnert, and L. DiCarlo. “Initialization by measurement of a superconducting quantum bit circuit.” *Phys. Rev. Lett.*, **109**, 050507 (2012). Cited on pages 74, 125, 126 and 127.

- [Robert21] A. Robert, P. K. Barkoutsos, S. Woerner, and I. Tavernelli. “Resource-efficient quantum algorithm for protein folding.” *npj Quantum Information*, **7**, 38 (2021). Cited on page 1.
- [Rogers14] L. J. Rogers, K. D. Jahnke, M. H. Metsch, A. Sipahigil, J. M. Binder, T. Teraji, H. Sumiya, J. Isoya, M. D. Lukin, P. Hemmer, and F. Jelezko. “All-optical initialization, readout, and coherent preparation of single silicon-vacancy spins in diamond.” *Phys. Rev. Lett.*, **113**, 263602 (2014). Cited on page 125.
- [Rosario Hamann18] A. Rosario Hamann, C. Müller, M. Jerger, M. Zanner, J. Combes, M. Pletyukhov, M. Weides, T. M. Stace, and A. Fedorov. “Nonreciprocity realized with quantum nonlinearity.” *Phys. Rev. Lett.*, **121**, 123601 (2018). Cited on page 181.
- [Rosenblum77] S. Rosenblum, W. Steyert, and F. Fickett. “A simple method for producing high conductivity copper for low temperature applications.” *Cryogenics*, **17**, 645–647 (1977). Cited on pages 104 and 113.
- [Rosenblum18] S. Rosenblum, P. Reinhold, M. Mirrahimi, L. Jiang, L. Frunzio, and R. J. Schoelkopf. “Fault-tolerant detection of a quantum error.” *Science*, **361**, 266–270 (2018). Cited on page 41.
- [Rosenfeld17] W. Rosenfeld, D. Burchardt, R. Garthoff, K. Redeker, N. Ortegel, M. Rau, and H. Weinfurter. “Event-ready bell test using entangled atoms simultaneously closing detection and locality loopholes.” *Phys. Rev. Lett.*, **119**, 010402 (2017). Cited on page 180.
- [Rowe01] Rowe, Kielpinski, Meyer, Sackett, Itano, Monroe, and Wineland. “Experimental violation of a Bell’s inequality with efficient detection.” *Nature*, **409** (2001). Cited on pages 3 and 179.
- [Roy15] A. Roy, Z. Leghtas, A. D. Stone, M. Devoret, and M. Mirrahimi. “Continuous generation and stabilization of mesoscopic field superposition states in a quantum circuit.” *Phys. Rev. A*, **91**, 013810 (2015). Cited on page 74.
- [Saffman16] M. Saffman. “Quantum computing with atomic qubits and Rydberg interactions: Progress and challenges.” *arXiv:1605.05207* (2016). Cited on page 3.
- [Salathé15] Y. Salathé, M. Mondal, M. Oppliger, J. Heinsoo, P. Kurpiers, A. Potočnik, A. Mezzacapo, U. Las Heras, L. Lamata, E. Solano, S. Filipp, and A. Wallraff. “Digital quantum simulation of spin models with circuit quantum electrodynamics.” *Phys. Rev. X*, **5**, 021027 (2015). Cited on page 69.

- [Salathé18] Y. Salathé, P. Kurpiers, T. Karg, C. Lang, C. K. Andersen, A. Akin, S. Krinner, C. Eichler, and A. Wallraff. “Low-latency digital signal processing for feedback and feedforward in quantum computing and communication.” *Phys. Rev. Appl.*, **9**, 034011 (2018). Cited on pages 125, 126 and 127.
- [Salerno97] L. J. Salerno and P. Kittel. “Thermal Contact Conductance.” Technical report, NASA (1997). Cited on pages 94, 97, 116, 118 and 119.
- [Sank16] D. Sank, Z. Chen, M. Khezri, J. Kelly, R. Barends, B. Campbell, Y. Chen, B. Chiaro, A. Dunsworth, A. Fowler, and et al. “Measurement-induced state transitions in a superconducting qubit: Beyond the rotating wave approximation.” *Physical Review Letters*, **117**, 190503 (2016). Cited on pages 74, 82, 83, 84 and 126.
- [Santha86] M. Santha and U. V. Vazirani. “Generating quasi-random sequences from semi-random sources.” *Journal of Computer and System Sciences*, **33**, 75–87 (1986). Cited on page 58.
- [Santos96] E. Santos. “Unreliability of performed tests of bell’s inequality using parametric down-converted photons.” *Physics Letters A*, **212**, 10–14 (1996). Cited on page 61.
- [Scheidl10] T. Scheidl, R. Ursin, J. Kofler, S. Ramelow, X.-S. Ma, T. Herbst, L. Ratschbacher, A. Fedrizzi, N. K. Langford, T. Jennewein, and A. Zeilinger. “Violation of local realism with freedom of choice.” *Proceedings of the National Academy of Sciences*, **107**, 19708–19713 (2010). Cited on page 57.
- [Schindler11] P. Schindler, J. T. Barreiro, T. Monz, V. Nebendahl, D. Nigg, M. Chwalla, M. Hennrich, and R. Blatt. “Experimental repetitive quantum error correction.” *Science*, **332**, 1059–1061 (2011). Cited on page 125.
- [Schrödinger35] E. Schrödinger. “Discussion of probability relations between separated systems.” *Mathematical Proceedings of the Cambridge Philosophical Society*, **31**, 555–563 (1935). Cited on page 2.
- [Schreier08] J. A. Schreier, A. A. Houck, J. Koch, D. I. Schuster, B. R. Johnson, J. M. Chow, J. M. Gambetta, J. Majer, L. Frunzio, M. H. Devoret, S. M. Girvin, and R. J. Schoelkopf. “Suppressing charge noise decoherence in superconducting charge qubits.” *Phys. Rev. B*, **77**, 180502 (2008). Cited on page 128.

- [Schuster08] I. Schuster, A. Kubanek, A. Fuhrmanek, T. Puppe, P. W. H. Pinkse, K. Murr, and G. Rempe. “Nonlinear spectroscopy of photons bound to one atom.” *Nat. Phys.*, **4**, 382–385 (2008). Cited on page 4.
- [Serniak18] K. Serniak, M. Hays, G. de Lange, S. Diamond, S. Shankar, L. D. Burkhardt, L. Frunzio, M. Houzet, and M. H. Devoret. “Hot nonequilibrium quasiparticles in transmon qubits.” *Phys. Rev. Lett.*, **121**, 157701 (2018). Cited on page 149.
- [Sete14] E. A. Sete, J. M. Gambetta, and A. N. Korotkov. “Purcell effect with microwave drive: suppression of qubit relaxation rate.” *Phys. Rev. B*, **89**, 104516 (2014). Cited on pages 40 and 79.
- [Sete15] E. A. Sete, J. M. Martinis, and A. N. Korotkov. “Quantum theory of a bandpass purcell filter for qubit readout.” *Phys. Rev. A*, **92**, 012325 (2015). Cited on page 39.
- [Shalm15] L. K. Shalm, E. Meyer-Scott, B. G. Christensen, P. Bierhorst, M. A. Wayne, M. J. Stevens, T. Gerrits, S. Glancy, D. R. Hamel, M. S. Allman, K. J. Coakley, S. D. Dyer, C. Hodge, A. E. Lita, V. B. Verma, C. Lambrocco, E. Tortorici, A. L. Migdall, Y. Zhang, D. R. Kumor, W. H. Farr, F. Marsili, M. D. Shaw, J. A. Stern, C. Abellán, W. Amaya, V. Pruneri, T. Jennewein, M. W. Mitchell, P. G. Kwiat, J. C. Bienfang, R. P. Mirin, E. Knill, and S. W. Nam. “Strong loophole-free test of local realism.” *Phys. Rev. Lett.*, **115**, 250402 (2015). Cited on pages 3, 65, 66, 69, 162 and 180.
- [Sheldon16] S. Sheldon, E. Magesan, J. M. Chow, and J. M. Gambetta. “Procedure for systematically tuning up cross-talk in the cross-resonance gate.” *Phys. Rev. A*, **93**, 060302(R) (2016). Cited on page 141.
- [Shnirman97] A. Shnirman, G. Schön, and Z. Hermon. “Quantum manipulations of small josephson junctions.” *Phys. Rev. Lett.*, **79**, 2371–2374 (1997). Cited on page 17.
- [Shor95] P. W. Shor. “Scheme for reducing decoherence in quantum computer memory.” *Phys. Rev. A*, **52**, R2493–R2496 (1995). Cited on pages 2 and 69.
- [Shor97] P. W. Shor. “Polynomial-time algorithms for prime factorization and discrete logarithms on a quantum computer.” *SIAM Journal on Scientific and Statistical Computing*, **26**, 1484 (1997). Cited on pages 1 and 2.

- [Simon92] N. Simon, E. Drexler, and R. Reed. “Properties of copper and copper alloys at cryogenic temperatures.” *NIST Monograph*, **177** (1992). Cited on pages 112, 117 and 118.
- [Simons01] R. N. Simons. *Coplanar waveguide circuits, components and systems*. Wiley Series in Microwave and Optical Engineering. Wiley Inter-Science (2001). Cited on page 12.
- [Slichter12] D. H. Slichter, R. Vijay, S. J. Weber, S. Boutin, M. Boissonneault, J. M. Gambetta, A. Blais, and I. Siddiqi. “Measurement-induced qubit state mixing in circuit QED from up-converted dephasing noise.” *Phys. Rev. Lett.*, **109**, 153601 (2012). Cited on pages 82 and 126.
- [Somoroff21] A. Somoroff, Q. Ficheux, R. A. Mencia, H. Xiong, R. V. Kuzmin, and V. E. Manucharyan. “Millisecond coherence in a superconducting qubit.” *arXiv:2103.08578* (2021). Cited on page 4.
- [Stark14] J. Stark. “Beobachtungen über den Effekt des elektrischen Feldes auf Spektrallinien I. Quereffekt.” *Annalen der Physik*, **43**, 965–982 (1914). Cited on page 24.
- [Steane96] A. M. Steane. “Error correcting codes in quantum theory.” *Phys. Rev. Lett.*, **77**, 793–797 (1996). Cited on page 2.
- [Steffen13] L. Steffen, Y. Salathe, M. Oppliger, P. Kurpiers, M. Baur, C. Lang, C. Eichler, G. Puebla-Hellmann, A. Fedorov, and A. Wallraff. “Deterministic quantum teleportation with feed-forward in a solid state system.” *Nature*, **500**, 319–322 (2013). Cited on pages 4 and 180.
- [Steffen14] A. Steffen, A. Alberti, W. Alt, N. Belmechri, S. Hild, M. Karski, A. Widera, and D. Meschede. “Digital atom interferometer with single particle control on a discretized spacetime geometry.” *arXiv:1404.3994* (2014). Cited on page 69.
- [Sundaresan19] N. M. Sundaresan, R. Lundgren, G. Zhu, A. V. Gorshkov, and A. A. Houck. “Interacting qubit-photon bound states with superconducting circuits.” *Phys. Rev. X*, **9**, 011021 (2019). Cited on page 181.
- [Tamarat95] P. Tamarat, B. Lounis, J. Bernard, M. Orrit, S. Kummer, R. Kettner, S. Mais, and T. Basche. “Pump-probe experiments with a single-molecule-ac-stark effect and nonlinear-optical response.” *Phys. Rev. Lett.*, **75**, 15141517 (1995). Cited on page 24.

- [Tan17a] K. Y. Tan, M. Partanen, R. E. Lake, J. Govenius, S. Masuda, and M. Mötönen. “Quantum-circuit refrigerator.” *Nature Communications*, **8**, 15189 (2017). Cited on page 126.
- [Tan17b] T. R. Tan, Y. Wan, S. Erickson, P. Bierhorst, D. Kienzler, S. Glancy, E. Knill, D. Leibfried, and D. J. Wineland. “Chained bell inequality experiment with high-efficiency measurements.” *Phys. Rev. Lett.*, **118**, 130403 (2017). Cited on page 180.
- [Tan20] E. Y.-Z. Tan, C. C.-W. Lim, and R. Renner. “Advantage distillation for device-independent quantum key distribution.” *Phys. Rev. Lett.*, **124**, 020502 (2020). Cited on pages 178 and 180.
- [Tseng99] C. H. Tseng, S. Somaroo, Y. Sharf, E. Knill, R. Laflamme, T. F. Havel, and D. G. Cory. “Quantum simulation of a three-body-interaction hamiltonian on an nmr quantum computer.” *Phys. Rev. A*, **61**, 012302– (1999). Cited on page 4.
- [Urbaszek13] B. Urbaszek, X. Marie, T. Amand, O. Krebs, P. Voisin, P. Maletinsky, A. Högele, and A. İmamoğlu. “Nuclear spin physics in quantum dots: An optical investigation.” *Rev. Mod. Phys.*, **85**, 79–133 (2013). Cited on page 4.
- [Vaidman01] L. Vaidman. “Tests of bell inequalities.” *Physics Letters A*, **286**, 241–244 (2001). Cited on page 57.
- [Valenzuela06] S. O. Valenzuela, W. D. Oliver, D. M. Berns, K. K. Berggren, L. S. Levitov, and T. P. Orlando. “Microwave-induced cooling of a superconducting qubit.” *Science*, **314**, 1589–1592 (2006). Cited on pages 125, 126 and 127.
- [Valery21] J. A. Valery, S. Chowdhury, G. Jones, and N. Didier. “Dynamical sweet spot engineering via two-tone flux modulation of superconducting qubits.” *arXiv:2104.07835* (2021). Cited on page 176.
- [Vandersypen01] L. M. K. Vandersypen, M. Steffen, G. Breyta, C. S. Yannoni, M. H. Sherwood, and I. L. Chuang. “Experimental realization of Shor’s quantum factoring algorithm using nuclear magnetic resonance.” *Nature*, **414**, 883 (2001). Cited on page 4.
- [vanEnk07] S. J. van Enk, N. Lütkenhaus, and H. J. Kimble. “Experimental procedures for entanglement verification.” *Phys. Rev. A*, **75**, 052318 (2007). Cited on page 156.

- [vanLoo13] A. van Loo, A. Fedorov, K. Lalumière, B. Sanders, A. Blais, and A. Wallraff. “Photon-mediated interactions between distant artificial atoms.” *Science*, **342**, 1494–1496 (2013). Cited on page 143.
- [Vazirani12] U. Vazirani and T. Vidick. “Certifiable quantum dice.” *Philosophical Transactions of the Royal Society A: Mathematical, Physical and Engineering Sciences*, **370**, 3432–3448 (2012). Cited on page 3.
- [Vazirani14] U. Vazirani and T. Vidick. “Fully device-independent quantum key distribution.” *Phys. Rev. Lett.*, **113**, 140501 (2014). Cited on pages 3 and 55.
- [Vergis86] A. Vergis, K. Steiglitz, and B. Dickinson. “The complexity of analog computation.” *Mathematics and Computers in Simulation*, **28**, 91–113 (1986). Cited on page 1.
- [Vermersch17] B. Vermersch, P-O. Guimond, H. Pichler, and P. Zoller. “Quantum state transfer via noisy photonic and phononic waveguides.” *Phys. Rev. Lett.*, **118**, 133601 (2017). Cited on pages 101, 144, 178 and 180.
- [Verstraete02] F. Verstraete and M. M. Wolf. “Entanglement versus bell violations and their behavior under local filtering operations.” *Phys. Rev. Lett.*, **89**, 170401 (2002). Cited on pages 3, 53 and 55.
- [Vion02] D. Vion, A. Aassime, A. Cottet, P. Joyez, H. Pothier, C. Urbina, D. Esteve, and M. H. Devoret. “Manipulating the quantum state of an electrical circuit.” *Science*, **296**, 886–889 (2002). Cited on page 4.
- [Vool17] U. Vool and M. Devoret. “Introduction to quantum electromagnetic circuits.” *International Journal of Circuit Theory and Applications*, **45**, 897–934 (2017). Cta.2359. Cited on page 16.
- [Wallraff04] A. Wallraff, D. I. Schuster, A. Blais, L. Frunzio, R.-S. Huang, J. Majer, S. Kumar, S. M. Girvin, and R. J. Schoelkopf. “Strong coupling of a single photon to a superconducting qubit using circuit quantum electrodynamics.” *Nature*, **431**, 162–167 (2004). Cited on pages 4, 33, 69 and 87.
- [Walter15] S. Walter and F. Marquardt. “Dynamical gauge fields in optomechanics.” *arXiv:1510.06754* (2015). Cited on page 66.
- [Walter17] T. Walter, P. Kurpiers, S. Gasparinetti, P. Magnard, A. Potočnik, Y. Salathé, M. Pechal, M. Mondal, M. Oppliger, C. Eichler, and A. Wallraff. “Rapid, high-fidelity, single-shot dispersive readout of superconducting qubits.”

- Phys. Rev. Appl.*, **7**, 054020 (2017). Cited on pages 19, 39, 45, 69, 74, 75, 77, 78, 79, 82, 83, 126, 127, 128, 140, 149, 151, 173 and 179.
- [Wan20] K. Wan, S. Choi, I. H. Kim, N. Shutty, and P. Hayden. “Fault-tolerant qubit from a constant number of components.” *arXiv:2011.08213* (2020). Cited on page 106.
- [Wang15] C. Wang, C. Axline, Y. Y. Gao, T. Brecht, Y. Chu, L. Frunzio, M. H. Devoret, and R. J. Schoelkopf. “Surface participation and dielectric loss in superconducting qubits.” *Applied Physics Letters*, **107**, 162601 (2015). Cited on page 27.
- [Wang16] C. Wang, Y. Y. Gao, P. Reinhold, R. W. Heeres, N. Ofek, K. Chou, C. Axline, M. Reagor, J. Blumoff, K. M. Sliwa, L. Frunzio, S. M. Girvin, L. Jiang, M. Mirrahimi, M. H. Devoret, and R. J. Schoelkopf. “A Schrödinger cat living in two boxes.” *Science*, **352**, 1087–1091 (2016). Cited on page 126.
- [Wang21] C. Wang, X. Li, H. Xu, Z. Li, J. Wang, Z. Yang, Z. Mi, X. Liang, T. Su, C. Yang, G. Wang, W. Wang, Y. Li, M. Chen, C. Li, K. Linghu, J. Han, Y. Zhang, Y. Feng, Y. Song, T. Ma, J. Zhang, R. Wang, P. Zhao, W. Liu, G. Xue, Y. Jin, and H. Yu. “Transmon qubit with relaxation time exceeding 0.5 milliseconds.” *arXiv:2105.09890* (2021). Cited on page 4.
- [Wei21] K. X. Wei, E. Magesan, I. Lauer, S. Srinivasan, D. F. Bogorin, S. Carnevale, G. A. Keefe, Y. Kim, D. Klaus, W. Landers, N. Sundaresan, C. Wang, E. J. Zhang, M. Steffen, O. E. Dial, D. C. McKay, and A. Kandala. “Quantum crosstalk cancellation for fast entangling gates and improved multi-qubit performance.” *arXiv:2106.00675* (2021). Cited on page 176.
- [Weihs98] G. Weihs, T. Jennewein, C. Simon, H. Weinfurter, and A. Zeilinger. “Violation of bell’s inequality under strict einstein locality conditions.” *Phys. Rev. Lett.*, **81**, 5039–5043 (1998). Cited on pages 3, 56 and 179.
- [Wen69] C. Wen. “Coplanar waveguide: A surface strip transmission line suitable for nonreciprocal gyromagnetic device applications.” *IEEE Trans. Microwave Theory Tech.*, **17**, 1087–1090 (1969). Cited on page 12.
- [Wendin17] G. Wendin. “Quantum information processing with superconducting circuits: a review.” *Rep. Prog. Phys.*, **80**, 106001 (2017). Cited on page 16.
- [Wenner11] J. Wenner, R. Barends, R. C. Bialczak, Y. Chen, J. Kelly, E. Lucero, M. Mariantoni, A. Megrant, P. J. J. O’Malley, D. Sank, A. Vainsencher,

- H. Wang, T. C. White, Y. Yin, J. Zhao, A. N. Cleland, and J. M. Martinis. “Surface loss simulations of superconducting coplanar waveguide resonators.” *Appl. Phys. Lett.*, **99**, 113513 (2011). Cited on page 27.
- [Wenner13] J. Wenner, Y. Yin, Y. Chen, R. Barends, B. Chiaro, E. Jeffrey, J. Kelly, A. Megrant, J. Y. Mutus, C. Neill, P. J. J. O’Malley, P. Roushan, D. Sank, A. Vainsencher, T. C. White, A. N. Korotkov, A. N. Cleland, and J. M. Martinis. “Catching shaped microwave photons with 99.4efficiency.” *arXiv:1311.1180* (2013). Cited on page 87.
- [Werninghaus21] M. Werninghaus, D. J. Egger, F. Roy, S. Machnes, F. K. Wilhelm, and S. Filipp. “Leakage reduction in fast superconducting qubit gates via optimal control.” *npj Quantum Information*, **7**, 14 (2021). Cited on page 25.
- [White16] T. C. White, J. Y. Mutus, J. Dressel, J. Kelly, R. Barends, E. Jeffrey, D. Sank, A. Megrant, B. Campbell, Y. Chen, Z. Chen, B. Chiaro, A. Dunsworth, I.-C. Hoi, C. Neill, P. J. J. O’Malley, P. Roushan, A. Vainsencher, J. Wenner, A. N. Korotkov, and J. M. Martinis. “Preserving entanglement during weak measurement demonstrated with a violation of the Bell–Leggett–Garg inequality.” *npj Quantum Information*, **2**, 15022 (2016). Cited on page 180.
- [Wolfowicz21] G. Wolfowicz, F. J. Heremans, C. P. Anderson, S. Kanai, H. Seo, A. Gali, G. Galli, and D. D. Awschalom. “Quantum guidelines for solid-state spin defects.” *Nature Reviews Materials* (2021). Cited on page 4.
- [Woodcraft05] A. L. Woodcraft. “Recommended values for the thermal conductivity of aluminium of different purities in the cryogenic to room temperature range, and a comparison with copper.” *Cryogenics*, **45**, 626 – 636 (2005). Cited on pages 110 and 113.
- [Woodcraft09] A. L. Woodcraft and A. Gray, editors. *A low temperature thermal conductivity database. AIP Conference Proceedings*. 1185. 681-684. 10.1063/1.3292433. (2009). Cited on page 108.
- [Woods19] W. Woods, G. Calusine, A. Melville, A. Sevi, E. Golden, D. Kim, D. Rosenberg, J. Yoder, and W. Oliver. “Determining interface dielectric losses in superconducting coplanar-waveguide resonators.” *Phys. Rev. Applied*, **12**, 014012 (2019). Cited on page 27.
- [Wootters98] W. K. Wootters. “Entanglement of formation of an arbitrary state of two qubits.” *Phys. Rev. Lett.*, **80**, 2245–2248 (1998). Cited on page 47.

- [Wu97] Y. Wu and X. Yang. “Effective two-level model for a three-level atom in the ξ configuration.” *Phys. Rev. A*, **56**, 2443–2446 (1997). Cited on page 41.
- [Xiang17] Z.-L. Xiang, M. Zhang, L. Jiang, and P. Rabl. “Intracavity quantum communication via thermal microwave networks.” *Physical Review X*, **7**, 011035 (2017). Cited on pages 66, 87, 95, 101, 103, 144, 178 and 180.
- [Yamamoto03] T. Yamamoto, Y. A. Pashkin, O. Astafiev, Y. Nakamura, and J. S. Tsai. “Demonstration of conditional gate operation using superconducting charge qubits.” *Nature*, **425**, 941–944 (2003). Cited on page 4.
- [Yin13] Y. Yin, Y. Chen, D. Sank, P. J. J. O’Malley, T. C. White, R. Barends, J. Kelly, E. Lucero, M. Mariantoni, A. Megrant, C. Neill, A. Vainsencher, J. Wenner, A. N. Korotkov, A. N. Cleland, and J. M. Martinis. “Catch and release of microwave photon states.” *Phys. Rev. Lett.*, **110**, 107001 (2013). Cited on page 40.
- [Yurke96] B. Yurke, M. L. Roukes, R. Movshovich, and A. N. Pargellis. “A low-noise series-array Josephson junction parametric amplifier.” *Appl. Phys. Lett.*, **69**, 3078–3080 (1996). Cited on pages 73 and 128.
- [Zeytinoğlu15] S. Zeytinoğlu, M. Pechal, S. Berger, A. A. Abdumalikov Jr., A. Wallraff, and S. Filipp. “Microwave-induced amplitude- and phase-tunable qubit-resonator coupling in circuit quantum electrodynamics.” *Phys. Rev. A*, **91**, 043846 (2015). Cited on pages 40, 41, 42, 43, 130, 140, 195 and 204.
- [Zhang21] H. Zhang, S. Chakram, T. Roy, N. Earnest, Y. Lu, Z. Huang, D. Weiss, J. Koch, and D. I. Schuster. “Universal fast-flux control of a coherent, low-frequency qubit.” *Physical Review X*, **11** (2021). Cited on page 140.
- [Zhong19] Y. P. Zhong, H.-S. Chang, K. J. Satzinger, M.-H. Chou, A. Bienfait, C. R. Conner, . Dumur, J. Grebel, G. A. Peairs, R. G. Povey, D. I. Schuster, and A. N. Cleland. “Violating bell’s inequality with remotely connected superconducting qubits.” *Nature Physics* (2019). Cited on pages 40, 101, 144, 178 and 181.
- [Zhong21] Y. Zhong, H.-S. Chang, A. Bienfait, t. Dumur, M.-H. Chou, C. R. Conner, J. Grebel, R. G. Povey, H. Yan, D. I. Schuster, and A. N. Cleland. “Deterministic multi-qubit entanglement in a quantum network.” *Nature*, **590**, 571–575 (2021). Cited on pages 48, 87, 101 and 144.
- [Zhou20] Y. Zhou, E. M. Stoudenmire, and X. Waintal. “What limits the simulation of quantum computers?” *Physical Review X*, **10** (2020). Cited on page 2.

- [Zhou21] Y. Zhou, Z. Zhang, Z. Yin, S. Huai, X. Gu, X. Xu, J. Allcock, F. Liu, G. Xi, Q. Yu, H. Zhang, M. Zhang, H. Li, X. Song, Z. Wang, D. Zheng, S. An, Y. Zheng, and S. Zhang. “Rapid and unconditional parametric reset protocol for tunable superconducting qubits.” *arXiv:2103.11315* (2021). Cited on pages 125, 126 and 127.

List of Publications

- 1.* *Microwave Quantum Link between Superconducting Circuits Housed in Spatially Separated Cryogenic Systems*,
P. Magnard, S. Storz, P. Kurpiers, J. Schär, F. Marxer, J. Lütolf, T. Walter, J.-C. Besse, M. Gabureac, K. Reuer, A. Akin, B. Royer, A. Blais, and A. Wallraff
[Phys. Rev. Lett. 125, 260502 \(2020\)](#), also in [arXiv:2008.01642](#)
- 2.* *Fast and Unconditional All-Microwave Reset of a Superconducting Qubit*,
P. Magnard, P. Kurpiers, B. Royer, T. Walter, J.-C. Besse, S. Gasparinetti, M. Pechal, J. Heinsoo, S. Storz, A. Blais, and A. Wallraff,
[Phys. Rev. Lett. 121, 060502 \(2018\)](#), also in [arXiv:1801.07689](#)
- 3.* *Deterministic quantum state transfer and remote entanglement using microwave photons*,
P. Kurpiers*, **P. Magnard***, T. Walter, B. Royer, M. Pechal, J. Heinsoo, Y. Salathe, A. Akin, S. Storz, J.-C. Besse, S. Gasparinetti, A. Blais, and A. Wallraff,
[Nature 558, 264-267 \(2018\)](#), also in [arXiv:1712.08593](#)
4. *Realization of a Universal Quantum Gate Set for Itinerant Microwave Photons*,
K. Reuer, J.-C. Besse, L. Wernli, **P. Magnard**, P. Kurpiers, G. J. Norris, A. Wallraff, C. Eichler
[arXiv:2106.03481](#)
5. *Realizing a Deterministic Source of Multipartite-Entangled Photonic Qubits*,
J.-C. Besse, K. Reuer, M. C. Collodo, A. Wulff, L. Wernli, A. Copetudo, D. Malz, **P. Magnard**, A. Akin, M. Gabureac, G. J. Norris, J. I. Cirac, A. Wallraff, C. Eichler
[Nature Communications 11, 4877 \(2020\)](#), also in [arXiv:2005.07060](#)
6. *Demonstration of an All-Microwave Controlled-Phase Gate between Far Detuned Qubits*,
S. Krinner, P. Kurpiers, B. Royer, **P. Magnard**, I. Tsitsilin, J.-C. Besse, A. Remm, A. Blais, A. Wallraff,
[Phys. Rev. Applied 14, 044039 \(2020\)](#), also in [arXiv:2006.10639](#)
7. *Quantum Communication with Time-Bin Encoded Microwave Photons*,
P. Kurpiers, M. Pechal, B. Royer, **P. Magnard**, T. Walter, J. Heinsoo, Y. Salathe, A. Akin, S. Storz, J.-C. Besse, S. Gasparinetti, A. Blais, and A. Wallraff,
[Phys. Rev. Applied 12, 044067 \(2019\)](#), also in [arXiv:1811.07604](#)

8. *Engineering Cryogenic Setups for 100-qubit Scale Superconducting Circuit Systems*,
S. Krinner, S. Storz, P. Kurpiers, **P. Magnard**, J. Heinsoo, R. Keller, J. Luetolf, C. Eichler,
A. Wallraff,
[EPJ Quantum Technology](#) **6**, 2 (2019), also in [arXiv:1806.07862](#)
9. *Challenging local realism with human choices*,
The BIG Bell Test Collaboration,
[Nature](#) **557**, 212-216 (2018), also in [arXiv:1805.04431](#)
10. *Rapid High-Fidelity Single-shot Dispersive Readout of Superconducting Qubits*,
T. Walter, P. Kurpiers, S. Gasparinetti, P. Magnard, A. Potočnik, Y. Salathé, M. Pechal, M. Mondal,
M. Oppliger, C. Eichler, A. Wallraff,
[Phys. Rev. Applied](#) **7**, 054020 (2017), also in [arXiv:1701.06933](#)
11. *Characterizing the Attenuation of Coaxial and Rectangular Microwave-Frequency Waveguides at Cryogenic Temperatures*,
P. Kurpiers, T. Walter, **P. Magnard**, Y. Salathe, A. Wallraff,
[EPJ Quantum Technology](#) **4**, 8 (2017), also in [arXiv:1612.07977](#)

Acknowledgements

I have spent almost six years working in the Qudev Lab as a Ph.D. student. There I met a lot of incredible people whom I worked and interacted with. I would like to take the time to thank them for everything they have brought to me during this time in terms of research skills, physics insights and on a personal level.

My first thanks go to my professor *Andreas Wallraff*. I learned many lessons under your supervision such as being paranoid about what can go wrong in order to make a design right, valuing working solutions more than not-yet-implemented upgrades, or writing papers with the mindset of a critical reader. I also enjoyed your initiatives to make the group a nice place to be in: recurring football games, annual ski trips, cryogenic barbecues, aperos, group concerts and so on.

I would also like to thank the other professors who helped me during these years. Thank you *Prof. Yiwen Chu* for co-examining my Ph.D thesis. I really enjoyed all our interactions, and I have been impressed by how rapidly you have set up your lab to release first quality publications. Thank you *Prof. Alexandre Blais* for always being available and enthusiastic to discuss our fresh results or fresh thoughts. These discussions always boosted both my motivation and my research. Finally, thanks you *Prof. Renato Renner* and *Nicolas Sangouard* for your explanations on Bell test analyzes and *device independence*.

I had the chance to work in a large scale project, the SuperQuNet project, together with many great people who made crucial contributions. *Philipp Kurpiers*, as the earliest and most senior member of the team, I owe a lot. You essentially taught me how to do practical experimental physics. It was such a pleasure to work with you, for almost five years. You were always here to give help like supervising my students during long absences or debugging hardware. *Simon Storz*, the list of what you gave to the team is large: SweepSpot, an average seventeen hours of work per week on the projects, even when you were not the "main contributor", and making the loophole-free Bell test happen. You have a great talent in human and project management which I could really appreciate when you took over the main project in my final year. *Josua Schär*, from day one you have amazed me with your genius gift for mechanics. The infrastructure and the hat-building skills of the lab improved thanks to your 3D printing skills. Your relentless efforts to build and debug the cryogenics and electronics were crucial to the project. *Anatoly Kulikov*, thanks a lot for your critical review of the final chapters my thesis. We just briefly overlapped in the team, but I am sure you will do great as the first SuperQuNet postdoc. *Theo Walter*, I loved spending the first three years of my

PhD with you. I'll always remember your excitement for each project, your relaxed attitude, your crazy board games, and your mad ski-jumping and goal-keeping skills. Thank you for all that. Your death was a huge blow. To me, and to everyone in the lab. However, the memories of you have kept pushing me until today. *Janis Lütolf*, you were the mastermind and executive leader behind the realization of the cryogenic link. Let me give you a big thanks, together with *Melvin Frey*, *Raphael Keller*, *Alain Fauqueix*, *Niti Kohli* and *Reto Schlater* for your involvement in designing, purchasing, prototyping, moving and repeatedly assembling and disassembling cryogenic links. I really loved the team spirit which emanated during the hundreds of hours spent with you guys, Philip, Simon and Josua, assembling various cryogenics prototypes.

I would also like to give particular thanks to other lab members and people who I collaborated with. To *Baptiste Royer*, who worked the theory of photon emission and absorption and the resulting master simulations of all our experiments. To *Sebastian Krinner*, for the many projects we have worked on together, like fast fluxed readout, fg-ge gates, or cryogenics, but also for leading our football team several times to the Boltzmann cup final! To *Jean-Claude Besse*, for making so many Josephson junctions for our projects. Going to conferences and working on photon emission with you was also a great pleasure. To *Marek Pechal*, who taught me how to shape photons and how to work with non-Hermitian Hamiltonians. To *Mihai Gabureac*, for the numerous wafers which you deposited and etched for us. To *Kevin Reuer*, for the amazing FPGA firmware you made, and kept improving over the years. To *Fabian Marxer* and *Elias Portoles*, for the nice friendship which stemmed from supervising you guys. To *Kadir Akin*, for your amazing FPGA firmwares. I loved co-supervising with you. To *Christian Kraglund Andersen*, for the numerous inspiring discussions about fundamental physics. To *Johannes Hermann*, for the switch PCB designs and inspiring microwave engineering discussions. To *Gabriella Strahm*, *Francesca Bay* and *Cindy Donati*, for your invaluable support with administration, organizing events and dealing with invoices.

Unfortunately, I cannot write one full sentence for all the people who played an important role for me during this time. *Christopher Eichler*, *Markus Oppliger*, *Simone Gasparinetti*, *Anton Potočník*, *Johannes Heinsoo*, *Yves Salathé*, *Matthias Stammeier*, *Anna Stockklauser*, *Michele Collodo*, *Sébastien Garcia*, *Pasquale Scarlino*, *David van Woerkom*, *Stefania Lazăr*, *Graham Norris*, *Ants Remm*, *Adrian Beckert*, *Bradley Mitchell*, *Robin Buijs*, *Jonas Butscher*, *Wang Zhiren*, *Grégoire Noël*, *Leon Raabe*, *Hangxi Li*, *Andrés Rosario Hamman*, *Christoph Hellings*, *James O'Sullivan*, *Ekaterina Al-Tavil*, *Dante Colao Zanuz*, *Michael Kershbaum*, *Colin Scarato*, *François Swiadek*, *Nathan Lacroix*, *Adrian Copetudo*, *Yongxin Song*, *Bahadır Dönmez*: let me thank each and every one of you for your presence, your friendship, and for the great moments spent with you. You all contributed making these six years in Qudev awesome.

I'd like to also thank my Zurich friends, *Clara and Alex* (a.k.a. *Lala et Lolo*), *Charlotte and Valentin*, *Henry and Myriam*, *Laura and Alexis*, *Kevin Towa*, *Alice Vanel*, *Sabine and Alvaro*, and *Florian*, for all the exceptional moments we had together.

My parents also deserve big thanks, for keeping encouraging me throughout the thesis.

Last but not least, I would like to thank my wife, *Claude*, for her invaluable presence and support, for the piece of life we have written together during our time in Zurich.

Curriculum Vitae

Name	Paul Magnard
Date of birth	31.03.1992
Citizenship	French

Education

09.2015 – 06.2021	Ph.D. studies, ETH Zürich
09.2014 – 06.2015	Master of Advanced Studies in Physics, University of Cambridge
09.2012 – 06.2015	Grande École d'Ingénieur, École Centrale Paris
09.2010 – 07.2012	Classes Préparatoires MPSI/MP, Lycée Sainte-Geneviève
09.2007 – 07.2010	Baccalauréat Scientifique, Lycée Charlemagne, Paris

Professional Experience

09.2015 – 06.2021	Research and teaching assistant (Prof. Wallraff), ETH Zürich
01.2015 – 05.2015	Research assistant (Prof. Atatüre), University of Cambridge, UK
07.2014 – 08.2014	Research intern (Prof. Wallraff), ETH Zürich
07.2015 – 08.2015	Labour intern, SBM Offshore, Rio de Janeiro, Brasil

